



**HAL**  
open science

# Rashba-Dresselhaus spin-orbit coupling in topological physics and exciton-polariton fluids

Pavel Kokhanchik

► **To cite this version:**

Pavel Kokhanchik. Rashba-Dresselhaus spin-orbit coupling in topological physics and exciton-polariton fluids. Optics [physics.optics]. Université Clermont Auvergne, 2024. English. NNT : 2024UCFA0138 . tel-04956439

**HAL Id: tel-04956439**

**<https://theses.hal.science/tel-04956439v1>**

Submitted on 19 Feb 2025

**HAL** is a multi-disciplinary open access archive for the deposit and dissemination of scientific research documents, whether they are published or not. The documents may come from teaching and research institutions in France or abroad, or from public or private research centers.

L'archive ouverte pluridisciplinaire **HAL**, est destinée au dépôt et à la diffusion de documents scientifiques de niveau recherche, publiés ou non, émanant des établissements d'enseignement et de recherche français ou étrangers, des laboratoires publics ou privés.

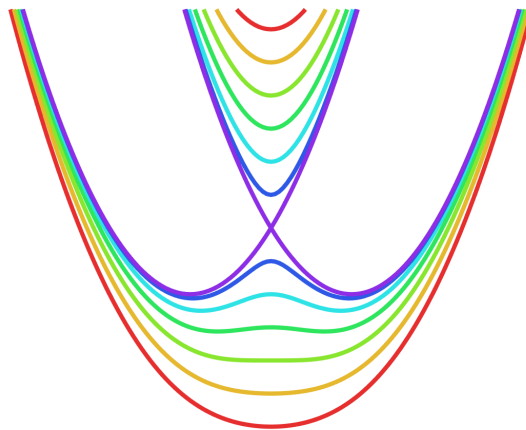


UNIVERSITÉ CLERMONT AUVERGNE  
ÉCOLE DOCTORALE DES SCIENCES FONDAMENTALES  
INSTITUT PASCAL, CNRS

# Rashba-Dresselhaus spin-orbit coupling in topological physics and exciton-polariton fluids

PHD THESIS

PAVEL KOKHANCHIK



**Supervisors:** Prof. Dmitry Solnyshkov, Université Clermont Auvergne, IUF  
Dr. Guillaume Malpuech, Université Clermont Auvergne, CNRS

**Reviewers:** Prof. Michał Matuszewski, Institute of Physics, Polish Academy of Sciences  
Dr. Grazia Salerno, School of Science, Aalto University  
Dr. Pierre Delplace, Ecole Normale Supérieure de Lyon, CNRS

**Examiners:** Dr. Alberto Amo, Université de Lille, CNRS, **jury president**  
Dr. Hai Son Nguyen, Institut des Nanotechnologies de Lyon, ECL

Clermont-Ferrand, 5 December 2024

---



Additional degrees of freedom enrich the physics of systems and provide the supplementary control knobs necessary for achieving applications. For example, by including the *electron spin* in the description of electron transport in solids, the whole field of spintronics has emerged, which now counts many applications, such as magnetic memory storage devices, magnetic sensors, spin-polarized LEDs and lasers, spin transistors, etc. In the domain of Topological Physics, the inclusion of the spin gave rise to the quantum spin Hall insulators and superconductors, Weyl semimetals, and other interesting topological phases of matter.

The core of many of these effects lies in the *spin-orbit coupling*, the link between electron spin and its motion. Generically, electronic spin-orbit coupling is described by a superposition of *Rashba* and *Dresselhaus* contributions. Under proper fabrication and tuning of parameters, these two contributions can be balanced, giving rise to a particular regime of *Rashba-Dresselhaus spin-orbit coupling (RDSOC)*. It turns out that the same type of balanced spin-orbit coupling is possible to realize in photonics and atomic gases, where the role of spin is played by the *light polarization* in the case of photons and *two hyperfine levels* in the case of atoms. The investigation of possible effects originating from RDSOC is the main scope of this theoretical thesis.

First, we investigate how the incorporation of RDSOC can induce or modify the *topology* of different systems. We start by constructing a proper generic *tight-binding* description of lattices in the presence of RDSOC. We distinguish two regimes provided by RDSOC: tunneling amplitude and phase control regimes. The first allows us to demonstrate the topology control of the *Su-Schrieffer-Heeger* chain. The second paves the way towards realization of the *Harper-Hofstadter model*. We then extend our study to non-Hermitian systems. By adding a non-Hermiticity into the system, the tunneling becomes *non-reciprocal*. In the case of a monomer chain, it gives rise to the *spin non-Hermitian skin effect*, where the monomer chain splits into two orthogonally-polarized copies, each realizing the *Hatano-Nelson model*. A similar effect happens for an SSH chain with RDSOC, with the addition of *anomalous bulk-boundary correspondence*.

In this thesis, we focus on a particular realization of the RDSOC in a *nematic liquid crystal planar microcavity*. This system provides a fine tunability of band structure, vast engineering capabilities, including lithography, it possesses all the advantages of photonic systems, such as direct access to the eigenstates, light-matter coupling, unique nonlinear properties, and, finally, it offers a path towards non-Hermitian physics due to the open nature of photonic systems. We show that the effects suggested above can be realized in the liquid crystal microcavities, and some of them *have already been realized* after our proposals.

Finally, we devote the last part of this thesis to the description of *exciton-polariton fluids* under RDSOC. We suggest a new approach for the *strong coupling* confirmation in a system with a tunable band structure. We apply this approach to the experimental results obtained in a hybrid liquid crystal – organic polymer microcavity. We further investigate this system in the condensed regime, demonstrating and studying the stripe phase of the

polariton fluid, a hallmark of the *supersolidity*.

Des degrés de liberté supplémentaires enrichissent la physique des systèmes et fournissent les leviers de contrôle supplémentaires nécessaires à la réalisation d'applications. Par exemple, en incluant *le spin de l'électron* dans la description du transport électronique dans les solides, tout le domaine de la spintronique a émergé, lequel compte désormais de nombreuses applications, telles que les dispositifs de stockage de mémoire magnétique, les capteurs magnétiques, les DEL et lasers polarisés en spin, les transistors à spin, etc. Dans le domaine de la physique topologique, l'inclusion du spin a donné naissance aux isolants et supraconducteurs de Hall quantique de spin, aux semi-métaux de Weyl, ainsi qu'à d'autres phases topologiques intéressantes de la matière.

Le cœur de nombreux de ces effets réside dans le *couplage spin-orbite*, le lien entre le spin de l'électron et son mouvement. En général, le couplage spin-orbite électronique est décrit par une superposition des contributions de *Rashba* et de *Dresselhaus*. Sous une fabrication et un réglage appropriés des paramètres, ces deux contributions peuvent être équilibrées, donnant lieu à un régime particulier de *couplage spin-orbite de Rashba-Dresselhaus (RDSOC)*. Il se trouve que le même type de couplage spin-orbite équilibré peut être réalisé dans les systèmes photoniques et les gaz atomiques, où le rôle du spin est joué par la *polarisation de la lumière* dans le cas des photons et par *deux niveaux hyperfins* dans le cas des atomes. L'étude des effets possibles provenant du RDSOC est l'objectif principal de cette thèse théorique.

Tout d'abord, nous examinons comment l'incorporation du RDSOC peut induire ou modifier la *topologie* de différents systèmes. Nous commençons par construire une description générique et appropriée des *liaisons fortes* dans des réseaux en présence de RDSOC. Nous distinguons deux régimes fournis par le RDSOC : les régimes de contrôle de l'amplitude et de la phase des coefficients de couplage. Le premier nous permet de démontrer le contrôle topologique de la chaîne de *Su-Schrieffer-Heeger*. Le second ouvre la voie à la réalisation du *modèle de Harper-Hofstadter*. Nous élargissons ensuite notre étude aux systèmes non-Hermitiens. En introduisant la non-Hermiticité dans le système, l'effet tunnel devient *non-réciproque*. Dans le cas d'une chaîne de monomères, cela donne lieu à *l'effet de peau non-Hermitien de spin*, où la chaîne de monomères se divise en deux copies orthogonalement polarisées, chacune réalisant le *modèle de Hatano-Nelson*. Un effet similaire se produit pour une chaîne SSH avec RDSOC, conduisant à une *correspondance anormale entre le volume et les bords*.

Dans cette thèse, nous nous concentrons sur une réalisation particulière du RDSOC dans une *microcavité planaire à cristaux liquides nématiques*. Ce système offre une grande flexibilité de la structure de bande, de vastes capacités d'ingénierie, y compris par lithographie, il possède tous les avantages des systèmes photoniques, tels que l'accès direct aux états propres, le couplage lumière-matière, des propriétés non linéaires uniques et, enfin, il offre une voie vers la physique non-Hermitienne en raison de la nature ouverte des systèmes photoniques. Nous montrons que les effets suggérés ci-dessus peuvent être réalisés dans des microcavités avec cristaux liquides, et certains *ont déjà été réalisés* après nos propositions.

Enfin, nous consacrons la dernière partie de cette thèse à la description des *fluides d'exciton-polaritons* sous RDSOC. Nous proposons une nouvelle approche pour confirmer le *couplage fort* dans un système à structure de bande modulable. Nous appliquons cette approche aux résultats expérimentaux obtenus dans une microcavité hybride cristaux liquides-polymère organique. Nous poursuivons l'étude de ce système dans le régime condensé, en démontrant et en étudiant la phase « stripes » du fluide polaritonique, une caractéristique emblématique de la *supersolidité*.

## Acknowledgements

The three years of PhD is certainly a challenging period of time, and I would like to thank the people who were close to me during this time and who helped me to pass through all the difficulties. First of all, this Thesis would not be possible without my supervisors, Dmitry and Guillaume. I would like to thank them for giving me an opportunity to work in their team, which is, at the same time, an opportunity to explore the life abroad, in France. I am also grateful for the time they spent on educating me and sharing with me their knowledge, and for all the good moments we had in our lab. I would like to thank Dmitry for always being available and kind, and always trying to listen to me and ameliorate my life, both inside and outside of the lab.

I would like to thank my colleagues with whom we were working side-by-side and shared some very memorable moments. Thank you Charly for your advices and for your openness that helped us to easily and quickly get along. Thank you as well for helping me to immerse in the life in Clermont. Thank you Ismael for the constant support and for the time you devoted on helping me with my work and daily life challenges. It was really nice to work together with you on various projects and simply to have in your face a person who perfectly understands me. Thank you both for lovely evenings and great conferences that we had together. With some people I was working less, but it does not mean that I less appreciate our time spent together. Thank you Matthieu for the interesting conversations you always initiated during our lunches together. Thank you Olga for your cheerfulness and positive spirit. Thank you all the colleagues who moved the TopoLight collaboration forward, especially, Jacek, Marcin, Thilo, Darius, Rafał and Helgi with whom I had a pleasure to work closely. I would also like to express my gratitude to the people of Institut Pascal and Université Clermont Auvergne for their hospitality.

Конечно же, особую часть в моей жизни занимают моя семья и мои друзья. Они придают мне силы на новые свершения, и их поддержка по-настоящему дорога мне. Спасибо, Настя, за то, что ты всегда рядом и разделяешь со мной как радостные, так и грустные моменты. Несомненно, переезд, адаптация и жизнь в другой стране были бы гораздо сложнее без тебя. Спасибо всем моим друзьям, которые, несмотря на большое расстояние между нами и на различные трудности, находят время и желание, чтобы поддерживать наше общение, регулярно встречаться, и забываемо проводить время вместе. Спасибо Даниилу и Кате, после вашего переезда в Клермон жизнь стала существенно веселее. Последнее, но не менее важное, – спасибо моим родителям за безусловную любовь, поддержку, заботу, и за свободу данную мне в выборе профессионального и жизненного пути, без чего этой Диссертации также могло бы и не быть.

Clermont-Ferrand, 4 October 2024

*Pavel Kokhanchik*



<b>Abstract</b>	<b>1</b>
<b>Résumé</b>	<b>3</b>
<b>Acknowledgements</b>	<b>5</b>
<b>I Introduction</b>	<b>11</b>
<b>1 Optical microcavities</b>	<b>13</b>
1.1 Weak coupling regime . . . . .	14
1.1.1 Planar microcavity structure . . . . .	14
1.1.2 Photon dispersion . . . . .	14
1.1.3 Spinor model for photon and Stokes vector . . . . .	15
1.1.4 TE-TM spin-orbit coupling . . . . .	17
1.1.5 Birefringence . . . . .	20
1.1.6 Combination of TE-TM SOC and birefringence . . . . .	21
1.2 Strong coupling regime . . . . .	22
1.2.1 Exciton-polariton . . . . .	22
1.2.2 Polariton condensation . . . . .	25
1.2.3 Polariton superfluidity . . . . .	26
1.2.4 Gross-Pitaevskii equation . . . . .	28
<b>2 Topological photonics and topological models</b>	<b>31</b>
2.1 Topological photonics . . . . .	31
2.2 Artificial gauge fields in topological photonics . . . . .	34
2.3 Topological models . . . . .	36
2.3.1 Su–Schrieffer–Heeger model and winding number . . . . .	36
2.3.2 Harper-Hofstadter model and Chern number . . . . .	40
2.4 Non-Hermitian effects . . . . .	43
2.4.1 Non-Hermitian skin effect . . . . .	44
2.4.2 Anomalous bulk-boundary correspondence . . . . .	46
<b>3 Rashba-Dresselhaus spin-orbit coupling</b>	<b>49</b>
3.1 Overview . . . . .	49
3.2 RDSOC in liquid crystal microcavities . . . . .	52
3.2.1 Nematic liquid crystal microcavity . . . . .	52
3.2.2 (N,N+1) resonant regime . . . . .	53
3.2.3 Minimal coupling representation . . . . .	57
3.2.4 Cholesteric liquid crystal and optical activity . . . . .	59

<b>II</b>	<b>Results</b>	<b>63</b>
<b>4</b>	<b>RDSOC in weakly-coupled systems</b>	<b>65</b>
4.1	RDSOC in tight-binding approximation . . . . .	66
4.2	SSH topology control . . . . .	67
4.2.1	Tight-binding model . . . . .	67
4.2.2	Reduced model and topological transition . . . . .	69
4.2.3	Topology switching in continuous realistic photonic model . . . . .	71
4.2.4	Period doubling in both models . . . . .	74
4.3	Continuous tunneling control between individual sites . . . . .	76
4.3.1	General idea . . . . .	76
4.3.2	Realization in nematic liquid crystal microcavity . . . . .	78
4.3.3	<i>sp</i> coupling by RDSOC on a single site . . . . .	80
4.3.4	Tunneling control between two sites mediated by RDSOC . . . . .	82
4.3.5	Tunneling inversion and topological transition . . . . .	84
4.3.6	Discussion . . . . .	85
4.4	1D tunable lattice in cholesteric liquid crystal microcavity . . . . .	85
4.4.1	Microcavity scheme . . . . .	86
4.4.2	CLC-induced photonic 1D potential . . . . .	86
4.4.3	CLC-induced photonic spin-orbit coupling . . . . .	90
4.4.4	Spin-orbit coupling approximation by RDSOC . . . . .	91
4.5	Perspectives for 2D lattice models . . . . .	93
4.5.1	HH model in tunneling phase control regime . . . . .	94
4.5.2	XY Hamiltonian in tunneling amplitude control regime . . . . .	95
4.6	1D non-Hermitian models with RDSOC . . . . .	96
4.6.1	Hatano-Nelson tight-binding model . . . . .	96
4.6.2	Non-Hermitian SSH tight-binding model . . . . .	100
4.6.3	NHSE in continuous realistic photonic model . . . . .	101
4.6.4	NHSE in continuous realistic electronic model . . . . .	104
<b>5</b>	<b>RDSOC in strongly-coupled systems</b>	<b>107</b>
5.1	Microcavity scheme and MeLPPP properties . . . . .	107
5.2	Strong coupling . . . . .	109
5.2.1	Experimental results . . . . .	109
5.2.2	Photonic mass extraction . . . . .	111
5.2.3	Tavis-Cummings model with inhomogeneous broadening . . . . .	111
5.3	Condensation . . . . .	115
5.3.1	Condensate polarization control . . . . .	115
5.3.2	Polariton stripes . . . . .	118
	<b>Conclusion and perspectives</b>	<b>123</b>

Appendices	127
A 8x8 DT Hamiltonian and perturbation theory	129
B Tight-binding model for ULH	131
C Publications	133
D Conference presentations	135
Bibliography	161
Abbreviations	163
Index	165



I

**Introduction**



## Contents

<b>1.1 Weak coupling regime</b> . . . . .	<b>14</b>
1.1.1 Planar microcavity structure . . . . .	14
1.1.2 Photon dispersion . . . . .	14
1.1.3 Spinor model for photon and Stokes vector . . . . .	15
1.1.4 TE-TM spin-orbit coupling . . . . .	17
1.1.5 Birefringence . . . . .	20
1.1.6 Combination of TE-TM SOC and birefringence . . . . .	21
<b>1.2 Strong coupling regime</b> . . . . .	<b>22</b>
1.2.1 Exciton-polariton . . . . .	22
1.2.2 Polariton condensation . . . . .	25
1.2.3 Polariton superfluidity . . . . .	26
1.2.4 Gross-Pitaevskii equation . . . . .	28

Optical microcavity [1, 2], or microresonator, has proven to be a powerful platform for studying diverse physics. Thanks to their small cavity volume  $V$  and high quality factor  $Q$ , the microcavity density of states is significantly modified with respect to the density of states of free space or conventional resonators: it shows narrow sparsely distributed quasi-equidistant peaks. This gives rise to one of the fundamental microcavity effects, *Purcell effect*, stating that the spontaneous emission of an atom is altered (enhanced or suppressed) as a function of available microcavity states to decay.

Another fundamental phenomenon appearing in the optical microcavities is the pronounced enhancement in the light-matter interaction, known as *strong coupling* between a cavity mode and a cavity atom resonance. The strong coupling appears when the field-atom coupling strength (half *Rabi frequency*) exceeds the total dissipation of the cavity-atom system, and it results in the new entangled eigenstates between the cavity field and atom.

Unique properties of microcavities and these two principle phenomena allowed microcavities to find their use in numerous research domains including non-linear photonics, cavity quantum electrodynamics, optical sensing, cavity optomechanics, topological photonics, non-Hermitian physics, and to give rise to remarkable technologies, such as VCSEL and single-photon source [3].

Depending on the desired properties, microcavities can have different realizations: Fabry-Perot resonators, whispering gallery resonators, and photonic crystals. In this Thesis, we will focus exclusively on planar Fabry-Perot microcavities. Section 1.1 is devoted to the mathematical description of photonic modes in the weak coupling regime, while Sec. 1.2 discusses the strong light-matter coupling regime.

## 1.1 Weak coupling regime

### 1.1.1 Planar microcavity structure

Fabry-Perot, or more precisely, *planar microcavity*, is formed by a pair of parallelly aligned mirrors. Those mirrors are commonly metal layers or *distributed Bragg reflectors* (DBRs). Metallic mirrors are efficient in infrared and beyond, while their  $Q$  factor is limited in the visible range by the material absorption. This is not the case for DBRs. A single DBR constitutes the alternating layers of two dielectric materials. The target optical length of each layer is  $\lambda_c/4$ , where  $\lambda_c$  is the desired central wavelength of the reflectivity stopband. The number of layers and the material refractive index contrast control the Bragg mirror stopband width and  $Q$  factor. Since the dielectric materials do not show strong absorption in the visible range,  $Q$  factors are significantly increased with respect to metallic mirrors. Therefore, the DBR  $Q$  factor is mostly a trade-off between the increasing number of DBR layers and the capability to reduce their roughness and surface cracking. DBR mirrors provide a huge advantage in terms of engineering the desired reflectivity spectrum, which is not the case for metallic mirrors where the reflectivity spectrum is fixed by the material.

Microcavity based on DBR mirrors can be viewed as a 1D photonic crystal with the cavity being a defect. In DBR-based microcavity, the cavity mode length is limited by a deep penetration of the electric field inside the DBR mirrors, which should be taken into account when analyzing any effect depending on the mode volume, such as the strong coupling, for example. For the metallic mirror, the penetration length is normally sub-wavelength. Often, a microcavity is designed to have a wedge, the spatially dependent cavity width in a selected direction. This allows one to control the cavity mode frequency by moving the excitation spot along the sample. This is especially crucial when the cavity mode needs to be finely tuned to a resonance of material filling the microcavity.

### 1.1.2 Photon dispersion

Due to the light confinement along the microcavity growth axis  $z$ , the photonic modes become discrete. The anchoring of the electric field node at the *ideal* mirror interface implies  $k_{z,N}L_c = N\pi$ , where  $k_{z,N}$  is the projection of the cavity photon wavevector  $\mathbf{k} = (k_x, k_y, k_z)$  on the  $z$  axis,  $L_c$  is the cavity length,  $n_c$  is the cavity material refractive index, and  $N$  is the mode number. For small transverse wavevector component  $\mathbf{k}_\perp = (k_x, k_y)$  with respect to  $k_{z,N}$ , it is easy to show that the cavity photon dispersion is parabolic in  $\mathbf{k}_\perp$  (i.e. the cavity photon acquires an effective mass):

$$E_N(\mathbf{k}_\perp) = \hbar\omega_c = \hbar\frac{c}{n_c}\sqrt{k_{z,N}^2 + \mathbf{k}_\perp^2} \approx \hbar\frac{c}{n_c}k_{z,N}\left(1 + \frac{\mathbf{k}_\perp^2}{2k_{z,N}^2}\right) = E_{N,0} + \frac{\hbar^2\mathbf{k}_\perp^2}{2m_N}, \quad 1.1$$

where  $E_{N,0} = m_N(c/n_c)^2$  is the  $N$ th cavity mode energy at  $\mathbf{k}_\perp = 0$  (typically in the range of 1–3 eV),  $m_N = \hbar n_c k_{z,N}/c$  is the effective cavity photon mass (typically  $10^{-6}$ – $10^{-5}m_e$ , where  $m_e$  is the electron mass),  $\omega_c$  is the photon angular frequency (further frequency),  $\hbar$

is the reduced Planck constant, and  $c$  is the speed of light. It is worth noting explicitly that the cavity photon mass  $m_N$  depends on the mode number  $N$ , cavity length  $L_c$ , and cavity material refractive index  $n_c$ . This will be crucial for understanding the tunable multimode dispersion of liquid crystal microcavities discussed extensively in this Thesis.

If mirrors are not ideal, and more particularly, if each mirror is a DBR consisting of  $N$  pairs of layers, then the microcavity eigenfrequency has both real and imaginary parts. The real part  $\omega$  defines the frequency at which one can observe a transmission (reflection) peak (dip) for light illuminating the cavity, while the imaginary part  $\gamma$  defines the spectral width of this peak. The eigenmode frequency is modified with respect to  $\omega_c$  according to the formula [4]:

$$\omega(\varphi) = \frac{L_c \omega_c(\varphi) + L_{DBR}(\varphi) \omega_s(\varphi)}{L_c + L_{DBR}(\varphi)}, \quad 1.2$$

where  $\varphi$  is the incidence angle of the light from a medium outside the cavity with the refractive index  $n_0$ . As one can see, the cavity eigenfrequency becomes a weighted average of the perfect cavity eigenfrequency  $\omega_c$  and the mirror stopband center frequency  $\omega_s$ . The weights (coefficients) are the resonator layer length  $L_c$  and the effective DBR length  $L_{DBR}$ , respectively. The latter is defined as an additional (to  $L_c$ ) increase of the distance between *ideal* mirrors which would create the same phase shift for a wave as under reflection at *non-ideal* DBRs. The exact formulas for the components entering the Eq. 1.2 can be found in [4]. One noticeable property of the Eq. 1.2 is that the eigenfrequency of a realistic cavity  $\omega$  approximately coincides with the eigenfrequency of an ideal one  $\omega_c$  when the latter is tuned to the center of the mirror stopband  $\omega_s$ . Therefore, when the mode is in the vicinity of the stopband center, Eq. 1.1 provides a good approximation for the cavity eigenfrequency.

The imaginary part of the eigenfrequency  $\gamma$ , inversely proportional to the cavity photon lifetime  $\tau$ , is defined as [4]:

$$\gamma(\varphi) \approx \frac{c(1 - R(\varphi))}{2n_c(L_c + L_{DBR}(\varphi)) \cos \varphi_c}, \quad 1.3$$

where  $R$  is the mirror reflectivity, and  $\varphi_c$  is the incidence angle of the light inside the cavity layer, related to the  $\varphi$  by the Snell law:

$$n_0 \sin \varphi = n_c \sin \varphi_c. \quad 1.4$$

There are two noticeable properties of the Eq. 1.3. Firstly, the photon lifetime increases with reflectivity, going to infinity ( $\gamma = 0$ ) at  $R = 1$  (ideal mirrors), as expected. Secondly, the lifetime is angle-dependent.

### 1.1.3 Spinor model for photon and Stokes vector

The Eq. 1.1 is scalar, in other words, it does not take into account the *polarization degree of freedom* of the photon. We now turn to the discussion of how to represent the polarization of the photon mathematically and be able to describe various effects involving light polarization.

The polarized state of the photon can be decomposed, for example, on the circular polarization components  $c_{\pm}$  as  $|\psi\rangle = c_+|+\rangle + c_-|-\rangle$ , where  $|\pm\rangle$  are  $\pm$  circular polarization eigenstates. This polarized state is usually written in the form of a two-component vector in the basis of circular polarization  $(|+\rangle |-\rangle)^T$ :  $|\psi\rangle = (c_+ c_-)^T$ .

In the circular polarization basis, every Hamiltonian appears as 2x2 matrix. Since Pauli matrices  $\boldsymbol{\sigma} = \{\sigma_x, \sigma_y, \sigma_z\}$  together with the identity matrix  $\sigma_0$  form a basis for 2x2 matrix space, we can rewrite any Hamiltonian  $H$  as:

$$H = E_0\sigma_0 + \boldsymbol{\Omega} \cdot \boldsymbol{\sigma}, \quad 1.5$$

where  $E_0$  is the polarization-independent energy, and  $\boldsymbol{\Omega} = \{\Omega_x, \Omega_y, \Omega_z\}$  decomposition coefficients which are real for the Hermitian Hamiltonian. We can now introduce a new quantity called *Stokes vector*  $\mathbf{S} = \{S_x, S_y, S_z\}$ , or *Stokes parameters*, being extremely useful for the geometric interpretation of a photon state and for understanding the physical meaning of the decomposition coefficients  $\boldsymbol{\Omega}$ . Stokes vector is simply the expectation value of Pauli matrix vector:  $\mathbf{S} = \langle \boldsymbol{\sigma} \rangle$ . Namely, in the circular polarization basis:

$$S_x = 2\text{Re}[c_+^*c_-], \quad S_y = -2\text{Im}[c_+^*c_-], \quad S_z = |c_+|^2 - |c_-|^2. \quad 1.6$$

Stokes vector components  $S_{x,y,z}$  quantify the degree of polarization between horizontal-vertical (HV), diagonal-antidiagonal (DA), and positive-negative circular (+-) polarizations, respectively. Note, that the Stokes vector is automatically normalized  $\mathbf{S}^2 = S_x^2 + S_y^2 + S_z^2 = 1$  if the state  $|\psi\rangle$  is normalized. Otherwise, it can be easily done by dividing each component of the Stokes vector by  $S_0 = \langle \sigma_0 \rangle = |c_+|^2 + |c_-|^2$ .

The pure state of the polarized light, therefore, can be graphically represented as the Stokes vector on the surface of a unit sphere, which is called the *Poincaré sphere*, and constitutes the analog of the Bloch sphere in solid-state physics (see Fig. 1.1). The poles of the Poincaré sphere correspond to the states of circular polarization (north +, south -), while linearly polarized states lie within the equator; all other points on the sphere are elliptically polarized.

Now, we can understand better the physical meaning of the decomposition coefficients  $\boldsymbol{\Omega}$ . Using the definition of the Stokes vector  $\mathbf{S}$  and the Schrödinger equation with Hamiltonian 1.5, one can obtain:

$$\frac{\partial \mathbf{S}}{\partial t} = \frac{2}{\hbar} \boldsymbol{\Omega} \times \mathbf{S}. \quad 1.7$$

In general, this whole mathematical description reminds strongly the one of the spin- $\frac{1}{2}$  particle, therefore, it is reasonable to call the Stokes vector the photon *pseudospin*. Furthermore, the Eq. 1.7 describes the precession of the pseudospin  $\mathbf{S}$  about the vector  $\boldsymbol{\Omega}$ , so  $\boldsymbol{\Omega}$  plays a role of an *effective magnetic field*. The frequency of this precession is  $\frac{2}{\hbar}|\boldsymbol{\Omega}|$ .

The transformation from the circularly polarized basis +- to the linear one, either HV

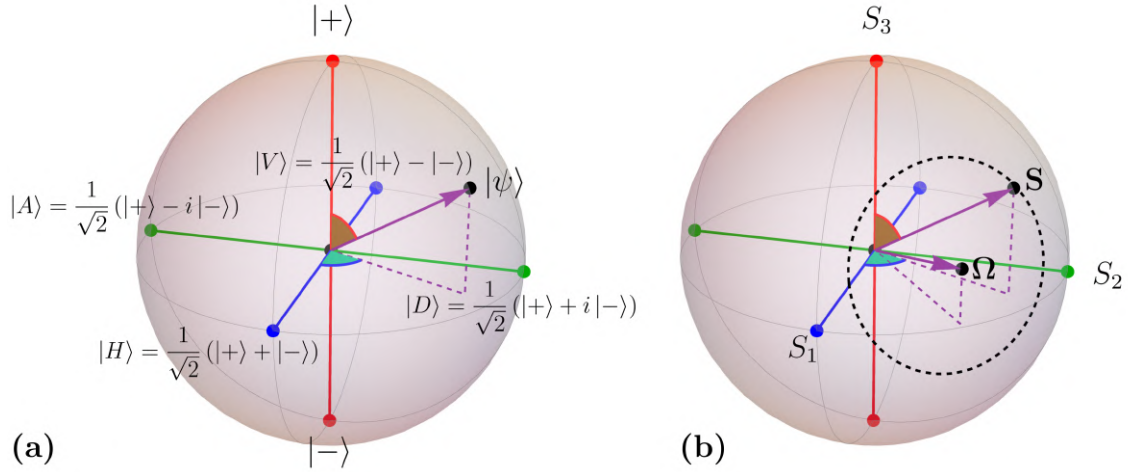


Figure 1.1: **Poincaré sphere.** (a) Polarized state  $|\psi\rangle$  on a sphere (purple arrow); the sphere is fully defined by two circularly polarized basis states  $|+\rangle$  and  $|-\rangle$ ; (b) Pseudospin  $\mathbf{S}$  on a sphere (purple arrow) which precesses around the effective magnetic field  $\mathbf{\Omega}$  (another purple arrow); the precession trajectory on a surface of the sphere is shown by the black dashed line; note that the states having orthogonal orientation of the electric field in real space ( $H$  and  $V$ , for example) correspond to the counter-oriented pseudospins  $\mathbf{S}$  on the Poincaré sphere.

or DA, can be easily performed with the use of corresponding transformation matrices:

$$T_{+ \rightarrow HV} = \frac{1}{\sqrt{2}} \begin{pmatrix} 1 & 1 \\ 1 & -1 \end{pmatrix}, T_{+ \rightarrow AD} = \frac{1}{\sqrt{2}} \begin{pmatrix} 1 & i \\ 1 & -i \end{pmatrix}. \quad 1.8$$

The formulas 1.6 change in this case and involve new spinor components ( $c_{H,V}$  or  $c_{A,D}$ ).

### 1.1.4 TE-TM spin-orbit coupling

Though sometimes the orthogonal polarizations of light can be decoupled and considered separately, in most cases different polarizations are involved in an intricate way, producing various polarization patterns in real and reciprocal space. The coupling (link) between polarization (pseudospin) and light propagation direction received the name of *photonic (pseudo)spin-orbit coupling* (SOC), in analogy with atomic spin-orbit coupling, where the spin of electron couples to its orbital motion inside the atom.

According to the *Fresnel equations*, as soon as we have a refractive index gradient in our system, we can distinguish between two waves,  $s$  and  $p$ , or in more contemporary terminology, between TE and TM polarizations of light. These TE and TM polarizations have different reflection and transmission coefficients, and they are the solution (eigenmodes) of Maxwell's wave equation. In general, the more pronounced the refractive index gradients in the system of interest and the bigger the angles of incidence of light to gradient direction, the stronger the emerging difference between reflection and transmission of these two modes.

In microcavities with DBRs, due to the presence of a refractive index gradient along the cavity growth axis, the difference appears between the effective DBR length  $L_{DBR}(\varphi)$  and

the stopband center frequency  $\omega_s(\varphi)$  for TE and TM modes of the cavity (see Eq. 1.2). Consequently, the cavity eigenfrequency  $\omega$  is different for TE and TM modes as well. The difference between them is the *TE-TM splitting* term  $\Delta_{TE-TM}$ , which can be written as [4]:

$$\Delta_{TE-TM} = \omega_{TE}(\varphi_c) - \omega_{TM}(\varphi_c) \approx \frac{L_c L_{DBR}(0)}{(L_c + L_{DBR}(0))^2} \frac{2 \cos \varphi_c \sin^2 \varphi_c}{1 - 2 \cos^2 \varphi_c} (\omega_c(0) - \omega_s(0)), \quad 1.9$$

where  $\varphi_c$  is the incidence angle of the light inside the cavity layer. This formula utilizes a strong approximation of close values for  $n_1$ ,  $n_2$  and  $n_c$ , where  $n_1$  and  $n_2$  are the refractive indices of the DBR layers. However, it provides a good intuition for the TE-TM splitting behavior. As one can see, the splitting is proportional to the detuning between the perfect cavity mode frequency  $\omega_c(0)$  and the stopband center frequency  $\omega_s(0)$ , therefore, allowing for the splitting sign change. By considering small angles of incidence  $\varphi$  and utilizing the Eq. 1.4, we can easily show that  $\Delta_{TE-TM} \propto \varphi^2 \propto k_{\perp}^2$ . This proportionality is typically used for constructing effective Hamiltonians with TE-TM SOC term, since it provides a good enough precision. Without any approximations, the formula for the TE-TM splitting Eq. 1.9 will contain higher order contributions in  $k_{\perp}$ , but all of them will be even in  $k_{\perp}$ , and the leading one ( $k_{\perp}^2$ ) will still be dominant for realistic microcavities.

The angular dependence of the TE-TM SOC term ensures the invariance of the microcavity under rotation around  $z$  axis (Fig. 1.2(d)). In terms of the effective magnetic field defined in Eq. 1.5, TE-TM SOC in circular polarization basis can be written as [5]:

$$\mathbf{\Omega}(\mathbf{k}_{\perp}) = (\Delta_{TE-TM}(k_{\perp}) \cos 2\theta, \Delta_{TE-TM}(k_{\perp}) \sin 2\theta, 0), \quad 1.10$$

where  $\theta = \arctan k_y/k_x$  is the in-plane propagation angle of the light. The effective field direction in reciprocal space for the fixed  $k_{\perp}$  is depicted in Fig. 1.2(c), where color corresponds to the in-plane angle of the field with respect to the  $k_x$  axis.

Together with the microcavity photon kinetic energy term Eq. 1.1, the Hamiltonian of a microcavity photon including TE-TM SOC in the circular polarization basis reads as:

$$H_{TE-TM} = \begin{pmatrix} E_0 + \frac{\hbar^2 k_{\perp}^2}{2m} & \gamma k_{\perp}^2 e^{-2i\theta} \\ \gamma k_{\perp}^2 e^{2i\theta} & E_0 + \frac{\hbar^2 k_{\perp}^2}{2m} \end{pmatrix}, \quad 1.11$$

where we have omitted the mode number  $N$  (Eq. 1.1) since we consider two orthogonally polarized longitudinal modes of the same number  $N$ .

The  $k_{\perp}^2$  dependence of TE-TM SOC results in the two energy bands  $E_{\pm}(k_{\perp}) = E_0 + \frac{\hbar^2 k_{\perp}^2}{2m} \pm \gamma k_{\perp}^2$  with different effective masses:  $m_{TM,TE}^{-1} = m^{-1} \pm 2\gamma/\hbar^2$  (see Fig. 1.2(a,b), notice that  $\mathbf{k}_{\perp} = (k_x, k_y)$ ). The corresponding eigenstates are  $\psi_{\pm} = \frac{1}{\sqrt{2}}(1 \pm e^{2i\theta})^T$ . Therefore, the Stokes vectors of these eigenstates (Eq. 1.6):  $\mathbf{S}_{\pm} = (\pm \cos 2\theta, \pm \sin 2\theta, 0)$ . By comparing  $\mathbf{S}_{\pm}$  with Eq. 1.10, we see that the higher energy pseudospin  $\mathbf{S}_{+}$  is co-aligned with the effective field, while lower energy pseudospin  $\mathbf{S}_{-}$  is counter-aligned.

If an optical microcavity is excited resonantly under a non-zero angle, in general, the excitation propagates along the cavity, and its pseudospin precesses according to Eq. 1.7.

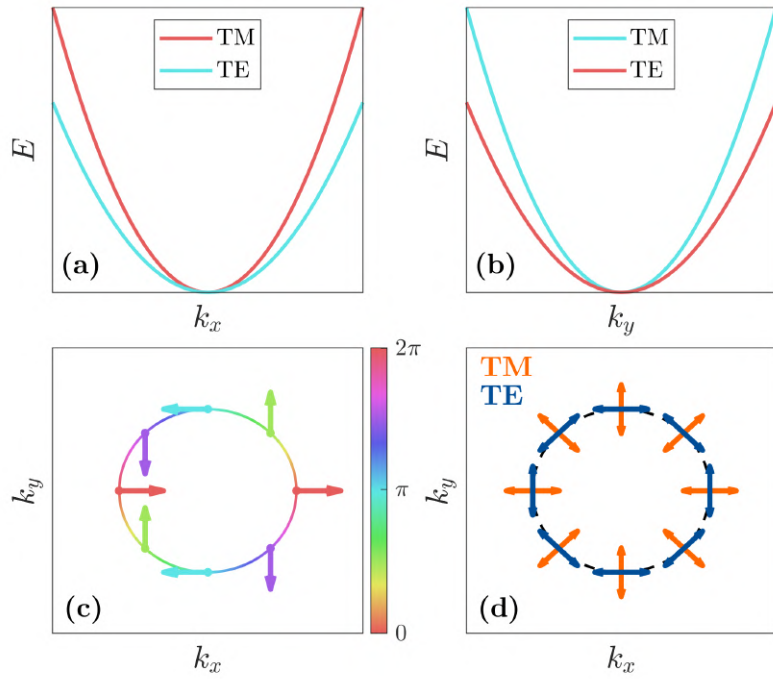


Figure 1.2: **TE-TM SOC**. Energy bands of Hamiltonian [1.11](#) along (a)  $k_x$  and (b)  $k_y$ ; TE or TM mode polarization depends on propagation direction; TM mode has higher energy; (c) effective TE-TM magnetic field (Eq. [1.10](#)) acting on polarization pseudospin for the fixed value of  $k_{\perp}$ ; color in (a-c) represents the angle between effective field direction and  $k_x$  axis; (d) TE and TM mode linear polarization for the fixed value of  $k_{\perp}$ ; color is used to distinguish between the two modes.

Due to the Rayleigh scattering, all other states at fixed  $k_{\perp}$  will be populated as well. In combination with a double-winding structure of effective TE-TM field (see Eq. 1.10 and Fig. 1.2), it gives rise to a four-lobe polarization structure in real space. This effect has been discovered in 2005 [6] and has been named *Optical Spin Hall Effect* (OSHE) in analogy with electronic spin Hall effect, where electrons propagating in opposite directions have different spin (two-lobe spin structure).

### 1.1.5 Birefringence

Another property widespread in optical microcavities is optical anisotropy, or *birefringence*. The optical anisotropy is the difference between refractive indices for different polarizations of light which results, for example, in the double refraction effect happening when the light strikes a birefringent material. In optical microcavities, plenty of sources of both linear and circular optical birefringence can exist and coexist, including stress (deformation), patterning or structuring, nonlinear effects (Pockels or Kerr effect), orientation of anisotropic molecules, molecular chirality, and material magnetic properties (Faraday effect).

In this section, we focus uniquely on the linear birefringence of uniaxial materials, since nematic liquid crystals studied extensively in this Thesis are such materials. Uniaxial materials have a single direction governing the behavior of the light propagating inside the material known as the material optic axis. In the case of nematic liquid crystals, this direction is equivalent to the *molecular director*, a preferential orientation of rod-like LC molecules. The light polarized along this axis propagates with *extraordinary refractive index*, while the orthogonal polarization is characterized by *ordinary refractive index*.

If the optic axis coincides with  $x$  or  $y$  of a bare planar microcavity, the birefringence translates itself into quantization energy (Eq. 1.1) difference between  $x$ - and  $y$ -polarized modes, which we will often refer to as  $H$  and  $V$  polarizations, respectively. This difference is simply described by the effective field  $\Omega = (\delta, 0, 0)$ , where  $\delta = (E_{N,0}^H - E_{N,0}^V)/2$ . It is crucial to note, that we consider here a small birefringence that keeps orthogonal  $H$  and  $V$  modes of number  $N$  close to each other in comparison with the cavity free spectral range (distance between modes of consecutive numbers). If this is not the case, the Hamiltonian often should be written in an extended basis taking into account possible coupling mechanisms between cavity modes. The case of a large birefringence on the order of the free spectral range will be considered in Sec. 3.2.

The Hamiltonian of microcavity photon including birefringence, therefore, reads in circular polarization basis as:

$$H_{HV} = \begin{pmatrix} E_0 + \frac{\hbar^2 k_{\perp}^2}{2m} & \delta \\ \delta & E_0 + \frac{\hbar^2 k_{\perp}^2}{2m} \end{pmatrix}, \quad 1.12$$

where we used subscript  $HV$  standing for  $HV$  linear splitting, the term we will use occasionally. The corresponding energy bands are  $E_{H,V}(k_{\perp}) = E_0 + \frac{\hbar^2 k_{\perp}^2}{2m} \pm \delta$  (see Fig. 1.3(a,b)) and eigenstates are  $\psi_{\pm} = \frac{1}{\sqrt{2}}(1, \pm 1)^T$ . The pseudospin is simply aligned along  $x$ :  $\mathbf{S}_{\pm} = (\pm 1, 0, 0)$ .

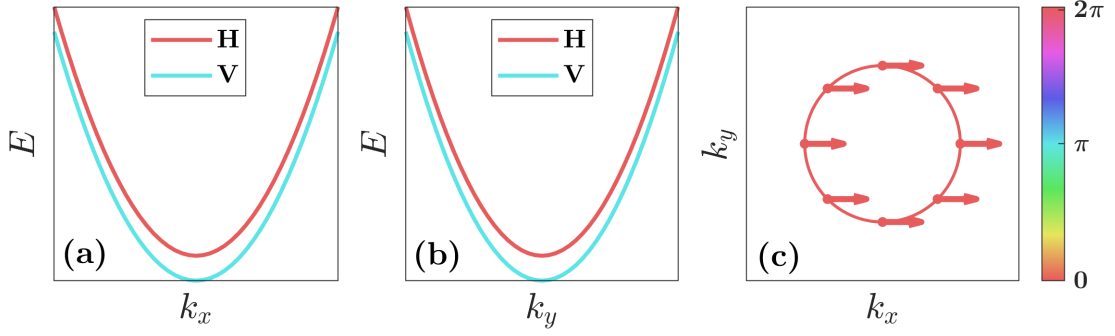


Figure 1.3: **Birefringence.** Energy bands of Hamiltonian 1.12 along (a)  $k_x$  and (b)  $k_y$ ; the H ( $x$ -polarized) mode has a higher energy than the V ( $y$ -polarized) mode; (c) effective magnetic field of birefringence acting on polarization pseudospin for the fixed value of  $k_\perp$ ; color represents the angle between effective field direction and  $k_x$  axis.

### 1.1.6 Combination of TE-TM SOC and birefringence

As one can notice, the birefringence term is quite trivial and does not produce any remarkable effect. The combination of TE-TM SOC and birefringence, though, provides us with a qualitatively new behavior, which is worth discussing in more detail. The Hamiltonian combines two effective fields:

$$\Omega(\mathbf{k}_\perp) = \left( \delta + \gamma k_\perp^2 \cos 2\theta, \gamma k_\perp^2 \sin 2\theta, 0 \right), \quad 1.13$$

and, therefore, reads in circular polarization basis as:

$$H_{TE-TM+HV} = \begin{pmatrix} E_0 + \frac{\hbar^2 k_\perp^2}{2m} & \delta + \gamma k_\perp^2 e^{-2i\theta} \\ \delta + \gamma k_\perp^2 e^{2i\theta} & E_0 + \frac{\hbar^2 k_\perp^2}{2m} \end{pmatrix}. \quad 1.14$$

The energy bands are defined as  $E_\pm(k_\perp) = E_0 + \frac{\hbar^2 k_\perp^2}{2m} \pm [\delta^2 + \gamma^2 k_\perp^4 + 2\delta\gamma k_\perp^2 \cos 2\theta]^{1/2}$  (see Fig. 1.4(a,b)), and corresponding eigenstates can be written as  $\psi_\pm = \frac{1}{\sqrt{2}}(1 \pm e^{i\theta'})^T$  with  $\theta' = \arg(\delta + \gamma k_\perp^2 e^{2i\theta})$ .

Contrary to parabolic band crossing (Fig. 1.2(a,b)) with eigenstate winding 2 (Fig. 1.2(c)), the combined case of TE-TM SOC and birefringence demonstrates two linear crossings at degeneracy points  $\mathbf{k}_\perp^0 = (0, \pm\sqrt{\delta/\gamma})$  (Fig. 1.4(a,b)) with eigenstate winding 1 around each of them (Fig. 1.4(c)). These two points are tilted *Dirac points*, sometimes referred as *diabolic points*. The linear crossings characteristic for Dirac cones can be easily verified by Taylor expansion of effective field, energies and eigenstates around the degeneracy points  $\mathbf{k}_\perp^0 = (q_x, q_y \pm \sqrt{\delta/\gamma})$ :

$$\Omega(\mathbf{q}) \approx 2\sqrt{\delta\gamma}(\mp q_y, \pm q_x, 0), \quad 1.15$$

$E_\pm(q) \approx \pm 2\sqrt{\delta\gamma}q$ ,  $\psi_\pm \approx \frac{1}{\sqrt{2}}(1 \pm e^{i(\theta_q \pm \pi/2)})^T$ , where  $\mathbf{q} = (q_x, q_y)$ ,  $\theta_q = \arctan q_y/q_x$ , and  $\pm$  ( $\mp$ ) in Eq. 1.15 and  $\pm$  before  $\pi/2$  correspond to different Dirac points  $\mathbf{k}_\perp^0 = (0, \pm\sqrt{\delta/\gamma})$ , respectively.

The ingredients discussed in this Section will appear throughout this Thesis. The spinor formalism and eigensystem analysis along with terminology of polarization, effective

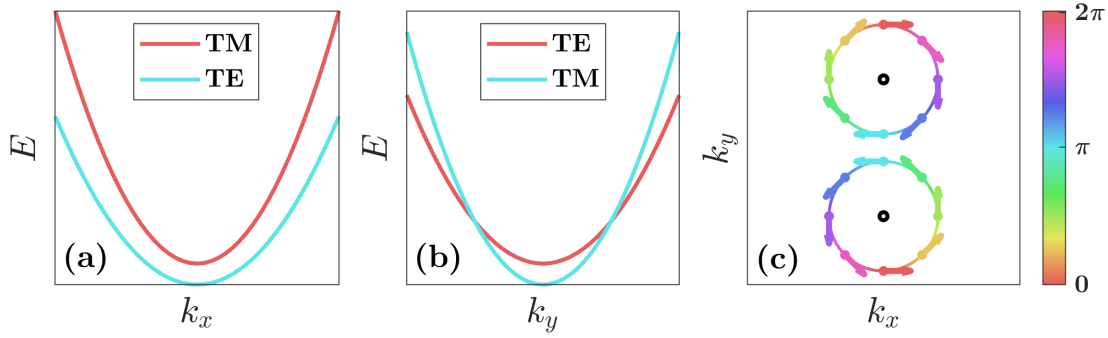


Figure 1.4: **Combination of TE-TM SOC and birefringence.** Energy bands of Hamiltonian 1.13 along (a)  $k_x$  and (b)  $k_y$ ; two tilted Dirac cones are visible at non-zero  $k_y$  in (b); (c) combined effective magnetic field of TE-TM SOC and birefringence acting on polarization pseudospin around Dirac points (black dots)  $\mathbf{k}_\perp^0 = (0, \pm\sqrt{\delta/\gamma})$ ; color represents the angle between effective field direction and  $k_x$  axis.

field, and pseudospin form a toolkit for understanding this Thesis. More details about the winding number, and topology in general, will be given in Ch. 2.

## 1.2 Strong coupling regime

The strong light-matter coupling allows us to significantly enrich the scope of fundamental physical phenomena and technological applications. Among various material excitations, we will focus only on *exciton*, a bound state of an electron and a hole. By experiencing the strong coupling with a photon, they create a part-light part-matter quasi-particle called *exciton-polariton*. This Thesis will be partially devoted to studying the novel effects engaging these fascinating quasiparticles.

### 1.2.1 Exciton-polariton

Excitation of a valence electron to a conduction band leaves a vacation in the valence band, called *electron hole*. An electron hole, being positively charged, interacts with an electron through Coulomb interaction thus forming a bound state resembling a hydrogen atom, called exciton. Exciton, therefore, is a chargeless quasiparticle that, however, can transfer energy. Since electron and hole are both fermions, the created exciton is a *composite boson*.

Excitons have diverse physical properties, but it is common to distinguish two main classes. *Wannier-Mott excitons* are hydrogen-like states having their size (radius) much larger than the crystal unit cell and typical binding energies of the order of tens meV. Wannier-Mott excitons usually appear in inorganic semiconductors and they are strongly sensitive to confinement potentials, in other words, their properties may vary significantly in 3D, 2D, or 1D structures. Another class, *Frenkel excitons*, is distinguished by smaller exciton sizes of the order of a single unit cell and larger binding energies, typically hundreds of meV. Frenkel excitons are common for some insulators and organic semiconductors.

Excitons give rise to narrow optical resonances at the energies lying inside the bandgap.

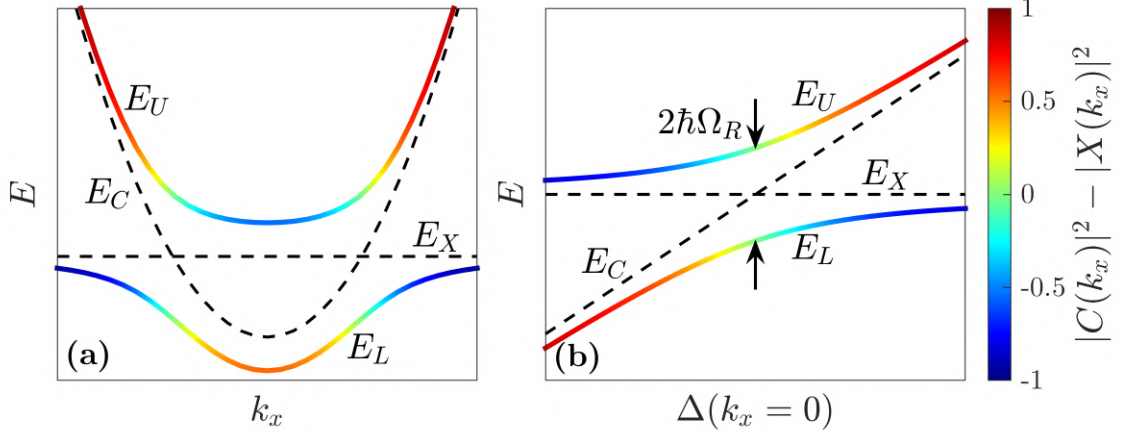


Figure 1.5: **Common exciton-polariton plots.** Energy of upper  $E_U$  and lower  $E_L$  polariton branches (a) along wavevector  $k_x$  (dispersion) and (b) versus detuning  $\Delta(k_x = 0)$  (solid colored lines); polariton branches visibly differ from bare cavity photon  $E_C$  and exciton  $E_X$  modes (dashed black lines), notably, by an apparent anticrossing in place of crossing of the bare modes; color represents the photon-exciton polarization, where 1 (-1) corresponds to a pure photonic (excitonic) mode.

They are detectable in reflection, transmission, absorption, or photoluminescence measurements. Due to the low binding energies, these measurements should be performed at low temperatures for Wannier-Mott excitons. On the contrary, Frenkel excitons are often measurable at room temperature, which we will benefit from in our studies described in Ch. 5.

The process of the light-matter interaction between a cavity photon and an exciton can be viewed as follows: a cavity photon with wavevector  $\mathbf{k}$  and energy  $E$  is absorbed by a material, creating an exciton with the same wavevector and energy; next, exciton emits a photon, which after reflection on microcavity mirror gets reabsorbed by the material. In that way, the light-matter interaction is enhanced by several orders of magnitude in comparison with free space photon propagation.

In the second quantization formalism, according to the dipole and rotating wave approximations, the Hamiltonian describing the light-matter coupling in  $\mathbf{k}$ -space can be written as [2, 7] (Jaynes-Cummings model [8]):

$$H = \sum_{\mathbf{k}} E_C(\mathbf{k}) a_{\mathbf{k}}^{C\dagger} a_{\mathbf{k}}^C + \sum_{\mathbf{k}} E_X(\mathbf{k}) a_{\mathbf{k}}^{X\dagger} a_{\mathbf{k}}^X + \sum_{\mathbf{k}} \hbar\Omega_R (a_{\mathbf{k}}^{C\dagger} a_{\mathbf{k}}^X + a_{\mathbf{k}}^{X\dagger} a_{\mathbf{k}}^C), \quad 1.16$$

where  $a_{\mathbf{k}}^C$  ( $a_{\mathbf{k}}^{C\dagger}$ ) and  $a_{\mathbf{k}}^X$  ( $a_{\mathbf{k}}^{X\dagger}$ ) are cavity photon and exciton annihilation (creation) operators, respectively;  $E_C(\mathbf{k})$  and  $E_X(\mathbf{k})$  are photon and exciton dispersions, respectively;  $\Omega_R$  is the Rabi frequency accounting for conversion of a cavity photon into an exciton. The dispersion of a photon  $E_C(\mathbf{k})$  is given by Eq. 1.1. The dispersion of an exciton  $E_X(\mathbf{k})$  in the cases of our interest can be well approximated by a constant since the exciton effective mass is several orders larger than the one of a cavity photon. The Rabi frequency is proportional to the product of the exciton electric dipole moment and the local amplitude (at the position of an exciton) of the cavity photon electric field.

Both photon and exciton annihilation operators  $a_{\mathbf{k}}^C$  and  $a_{\mathbf{k}}^X$  obey the bosonic algebra in the low excitation density limit:

$$[a_{\mathbf{k}}, a_{\mathbf{q}}] = [a_{\mathbf{k}}^\dagger, a_{\mathbf{q}}^\dagger] = 0, \quad [a_{\mathbf{k}}, a_{\mathbf{q}}^\dagger] = \delta_{\mathbf{k}, \mathbf{q}}. \quad 1.17$$

The Hamiltonian 1.16 can be diagonalized by constructing a linear superposition of photon and exciton annihilation operators. This transformation, often referred to as *Hopfield transformation* [9], can be written as:

$$a_{\mathbf{k}}^L = X(\mathbf{k})a_{\mathbf{k}}^X - C(\mathbf{k})a_{\mathbf{k}}^C, \quad 1.18a$$

$$a_{\mathbf{k}}^U = C(\mathbf{k})a_{\mathbf{k}}^X + X(\mathbf{k})a_{\mathbf{k}}^C. \quad 1.18b$$

New basis annihilation operators  $a_{\mathbf{k}}^L$  and  $a_{\mathbf{k}}^U$  describe so-called lower and upper *exciton-polaritons* (or simply *polaritons*), the new quasiparticles being the eigenstates of the system and combining properties of a photon and an exciton. A polariton is a boson since its constituents are, and the operators  $a_{\mathbf{k}}^L$  and  $a_{\mathbf{k}}^U$  obey the bosonic algebra as well. How much a polariton is photonic-like or excitonic-like is defined by real-valued coefficients of transformation  $X(\mathbf{k})$  and  $C(\mathbf{k})$ , called *Hopfield coefficients*. The Hamiltonian 1.16 after applying the transformation 1.18 reads as:

$$H = \sum_{\mathbf{k}} E_U(\mathbf{k})a_{\mathbf{k}}^{U\dagger}a_{\mathbf{k}}^U + \sum_{\mathbf{k}} E_L(\mathbf{k})a_{\mathbf{k}}^{L\dagger}a_{\mathbf{k}}^L, \quad 1.19$$

where  $E_U(\mathbf{k})$  and  $E_L(\mathbf{k})$  are upper and lower polariton dispersions, respectively, defined as:

$$E_{U,L}(\mathbf{k}) = \frac{1}{2}(E_C(\mathbf{k}) + E_X(\mathbf{k})) \pm \sqrt{(\hbar\Omega_R)^2 + \frac{1}{2}(E_C(\mathbf{k}) - E_X(\mathbf{k}))^2}. \quad 1.20$$

Many of the hallmarks of polaritons are embedded in Eq. 1.20. We plot the dispersion along  $k_x$  of the upper and lower polariton branches (UPB and LPB) in Fig. 1.5(a). The *anticrossing* characteristic for polaritons appears in the spectrum Fig. 1.5(a) at  $k_x$  where bare cavity photon and exciton modes cross. One can also introduce a *photon-exciton detuning* between cavity and exciton modes as:

$$\Delta(\mathbf{k}) = E_C(\mathbf{k}) - E_X(\mathbf{k}). \quad 1.21$$

When plotting UPB and LPB versus detuning  $\Delta(k_x = 0)$  an anticrossing appears as well at  $\Delta = 0$  (Fig. 1.5(b)). At the position of anticrossing, the distance between UPB and LPB is minimal and equal  $2\hbar\Omega_R$ . It is also crucial to note, that the effective mass of both UPB and LPB is detuning-dependent  $m_{U,L} = m_{U,L}(\Delta(k_x = 0))$ , the fact which we will use in the Ch. 5. The strong light-matter coupling regime is achieved when the Rabi frequency  $\Omega_R$  exceeds the loss imbalance between the exciton and the photon.

## 1.2.2 Polariton condensation

As already mentioned earlier, polaritons are bosons, so it is natural to expect that they demonstrate canonical bosonic effects such as *Bose-Einstein condensation (BEC)* and *superfluidity*. Moreover, as a platform to study these effects, they possess significant advantages over other bosonic platforms. For example, microcavity polariton effective mass is typically 4-5 orders less than the electron mass which allows to obtain BEC at higher temperature (lower density) contrary to dilute gases of atoms [10, 11] or excitons [12]. Also, the properties of exciton-polariton condensate such as coherence, polarization, and distribution function are easily accessible in the experiment thanks to photons escaping the cavity and transferring this information. At the same time, since microcavity polaritons have a short lifetime in order of ps, they are intrinsically an open system. Therefore, the condensation process is generally *non-equilibrium*, and it is defined by an interplay between high energy exciton reservoir formation by the pump, scattering rate towards lower energy polariton states, and the loss of polaritons. This creates additional challenges and requires sometimes a more careful analysis of the condensation process. However, at the same time, the non-equilibrium nature of exciton-polaritons enriches their physics.

Regardless of the resemblance to the exact thermal equilibrium, there are some properties that the polariton ground state should demonstrate to be called a polariton condensate [13]. Mainly, it is an establishment of *long-range order (spatial coherence)* and *spontaneous symmetry breaking* over the excitation spot size. The macroscopic state of the condensate in real space is described by the classical single-particle wavefunction  $\psi(\mathbf{r})$  equivalent in this case to the quantum matter field. The system Hamiltonian is unchanged under an arbitrary transformation of the wavefunction phase (global gauge invariance). At phase transition, the wavefunction spontaneously chooses a phase throughout the condensate thus breaking the gauge symmetry. In this case, the *condensate order parameter* reads as [14, 2]:

$$\psi(\mathbf{r}) = \sqrt{n(\mathbf{r})}e^{i\theta(\mathbf{r})}, \quad 1.22$$

where  $n(\mathbf{r})$  is the condensate density, and  $\theta(\mathbf{r})$  is the global condensate phase.

Along with spatial coherence, the condensate of exciton-polaritons demonstrates an enhanced *temporal coherence* at the phase transition [13]. It can be directly probed by means of interferometry, or implicitly appear as an abrupt condensate linewidth narrowing at phase transition.

The crucial distinctive feature being achievable in the experiment is the *polariton distribution function*. An ideal Bose gas after the condensation onset is characterized by a macroscopically occupied ground state and excited states following the Bose-Einstein distribution with the temperature of the lattice. Polariton condensate shows two key differences. First, as a consequence of the non-equilibrium nature of polaritons, the effective temperature of the distribution is higher than the one of the lattice. Second, due to the interaction between polaritons, at high pumping densities, the microscopic occupation of the ground state is typically "smeared" across the low-energy states [15, 13].

Finally, one of the polariton condensation hallmarks is the *energy blueshift*. It appears during the typical experimental analysis of the microcavity: measurement of the density

dependence. The origins of the blueshift are the *phase space filling* and interactions between polaritons. The phase space filling is a consequence of the composite structure of an exciton, which combines an electron and a hole, both following the Fermi statistics and obeying the Pauli exclusion principle. At high pumping densities, excitons fill most of the available phase space, thus preventing further excitations, which effectively results in the Rabi splitting reduction, and can even lead to the collapse of the strong coupling back to the weak coupling regime. Polariton-polariton interaction is realized through matter part (excitons) and is mathematically described by the terms of type  $V_{\mathbf{q}} a_{\mathbf{k}+\mathbf{q}}^{X\dagger} a_{\mathbf{k}'-\mathbf{q}}^{X\dagger} a_{\mathbf{k}}^X a_{\mathbf{k}'}^X$ . For a condensate state, the interaction is, therefore, proportional to  $n^2$ . This term starts to grow after condensation onset and results in the energy renormalization of the condensate state with the shift towards higher energies (lower wavelengths).

### 1.2.3 Polariton superfluidity

*Superfluidity* is tightly bound with the phenomenon of Bose-Einstein condensation, such that the difference between the two is not always clear [14]. Superfluids can propagate without energy dissipation since they do not show any mechanical viscosity. The first observation of superfluidity was achieved in 1938 simultaneously by Allen and Misener [16] and Kapitsa [17]. Several years later, Landau has explained this phenomenon [18] and formulated a concise yet powerful criterion for superfluidity. He has defined a maximum velocity at which a weak impurity can travel through the superfluid without friction, the *Landau critical velocity* [7]:

$$v_c = \min_{\mathbf{k}} [\omega(\mathbf{k})/k]. \quad 1.23$$

This criterion received the name of *Landau criterion* and it is formulated in a perturbative manner, i.e., for a weak impurity.

Shortly after the demonstration of polariton BEC [13], several experiments demonstrating polariton superfluidity have been performed [19, 20] reinforced by numerous theoretical studies [21, 22, 23, 24]. The general idea of distinct experiments is to induce a polariton flow with velocity  $v$  which hits a defect naturally present in a microcavity (Fig. 1.6). If the polariton flow moves fast  $v > v_c$  (left column in Fig. 1.6), it scatters on the defect. The resulting density pattern forms a Mach-Cherenkov cone originating from the interference of an incident plane wave and scattered spherical wave. Because of an apparent similarity with sound, this regime is also called *supersonic*, where  $v_c$  plays a role of polariton sound velocity. If the regime is *subsonic*  $v < v_c$  (right column in Fig. 1.6), then the polariton cloud is superfluid and travels without friction only creating small local density oscillations near the surface of the defect. The transition from one regime to another in the experiment is usually achieved through pumping density control. A low-density pump creates non-interacting polaritons, which, when injected under an angle, are normally in a supersonic regime. With increasing pumping density, interactions start to play a role and modify the excitation spectrum of the polariton fluid bringing it into a superfluid regime.

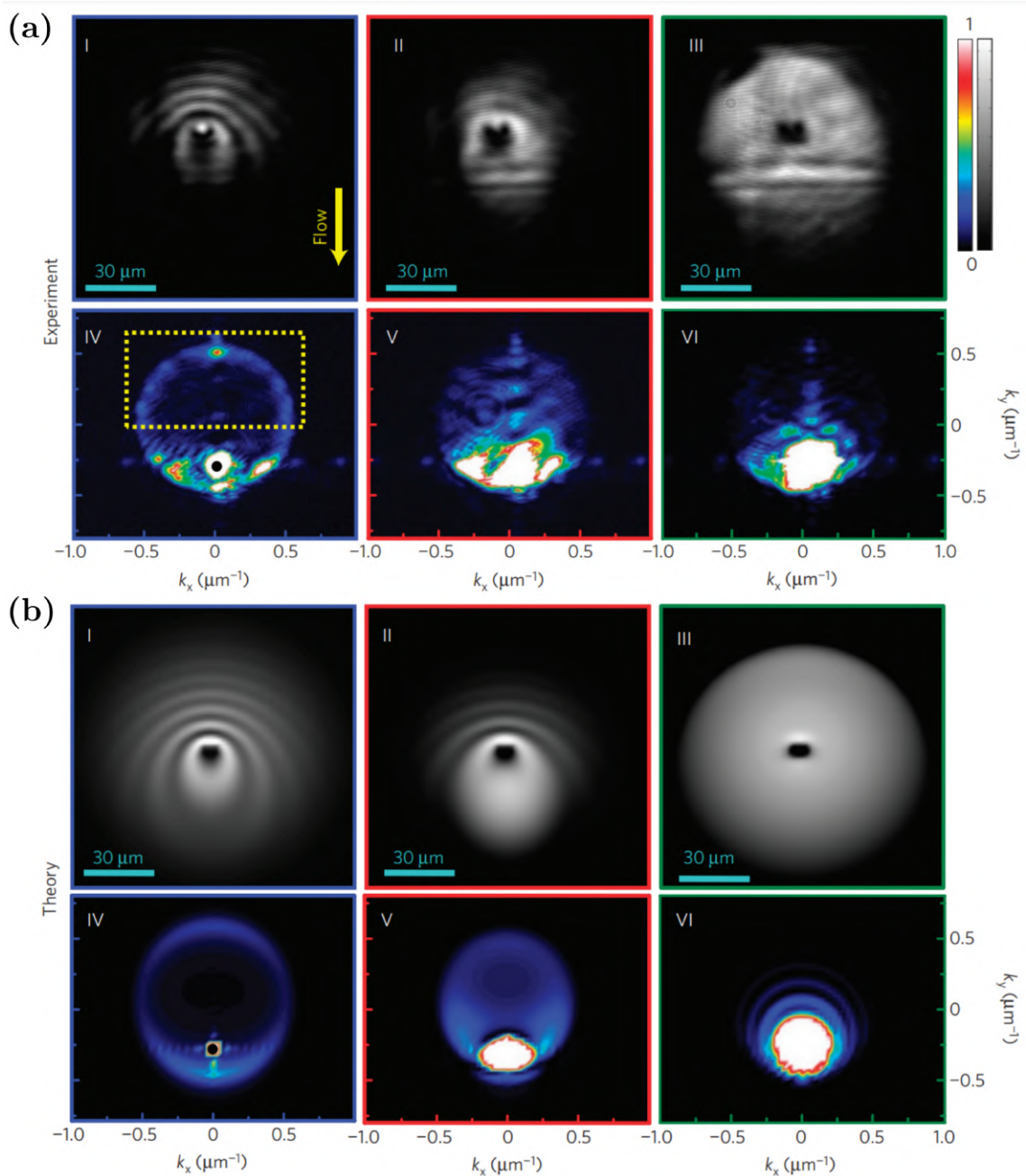


Figure 1.6: **Polariton superfluidity.** (a) *Experimental and (b) numerical polariton density in real (first row) and reciprocal (second row) space for a polariton flow hitting the defect; columns correspond to different polariton densities (excitation intensities) increasing from left to right; low-density limit shows supersonic behavior of polaritons (left column), while high-density limit represents the polariton superfluid (subsonic regime). Adopted from [19].*

### 1.2.4 Gross-Pitaevskii equation

The powerful tool for explaining the spatial dynamics of condensate is the nonlinear Schrödinger equation including interactions between the particles of Bose gas. This equation was first written by Gross [25] and Pitaevskii [26] in order to describe quantum vortices in liquid helium. Since then, it has been commonly used to simulate phenomena involving BEC and it is referred to as the *Gross-Pitaevskii equation (GPE)*:

$$i\hbar \frac{\partial \psi(\mathbf{r}, t)}{\partial t} = -\frac{\hbar^2}{2m} \nabla^2 \psi(\mathbf{r}, t) + V_{ext}(\mathbf{r})\psi(\mathbf{r}, t) + g|\psi(\mathbf{r}, t)|^2\psi(\mathbf{r}, t), \quad 1.24$$

where  $\psi(\mathbf{r}, t)$  is the condensate wavefunction defined in Eq. 1.22,  $m$  is the particle mass,  $V_{ext}$  is an external potential, and  $g$  is a constant of interaction. This model provides a good quantitative agreement only in the limit of high density (low temperature) when the condensate mode dominates over all other modes.

One can notice that Eq. 1.24 is written for thermodynamic limit and does not account for a driven-dissipative nature of polaritons. There exist two commonly used generalizations of GPE differing by the pumping configuration [7]. The first one describes the case of *coherent pumping*, where the pumping laser is tuned *resonantly* or *quasiresonantly* with respect to the LPB, and in which condensate inherits the coherence properties from the pump. We skip the discussion of this case since it is not used in this Thesis. The second generalization describes the case of *incoherent pumping*, where the pumping laser is significantly blue-detuned with respect to the LPB (*non-resonant excitation*), and any information about its coherence is lost during the relaxation process. Typically, the relaxation takes place in two steps. First, hot excitons relax towards the region near the inflection point of LPB (see Fig. 1.5(a)) through the exciton-polariton and phonon-polariton scattering mechanisms. There, polaritons accumulate due to the lack of final lower energy states. Due to this accumulation, this region is often called a *bottleneck region*. In the second step, this bottleneck effect is overcome by polariton-polariton scattering. In this scattering process, one polariton relaxes towards the bottom of the LPB while the second one is excited at high  $\mathbf{k}_\perp$  in agreement with energy and momentum conservation laws. This relaxation process is further undergoing a bosonic stimulation due to the bosonic nature of polaritons if the population of the ground state is of order 1 [7].

In order to describe the two-step relaxation process, an introduction of an additional bottleneck *polariton reservoir*  $n_R(\mathbf{r}, t)$  has been suggested [27]. The scattering rate from the polariton reservoir towards the condensate state  $\psi(\mathbf{r}, t)$  is generally described by the monotonically growing function  $R[n_R]$  (in the simplest case  $R[n_R] = Rn_R$ ). The polariton dissipation rate is  $\gamma_{LPB}$ . In this case, the generalized GPE reads as:

$$i\hbar \frac{\partial \psi(\mathbf{r}, t)}{\partial t} = \left[ -\frac{\hbar^2}{2m_{LPB}} \nabla^2 + V_{ext}(\mathbf{r}) + g|\psi(\mathbf{r}, t)|^2 \right] \psi(\mathbf{r}, t) + \frac{i}{2} \left[ R[n_R(\mathbf{r}, t)] - \gamma_{LPB} \right] \psi(\mathbf{r}, t), \quad 1.25$$

where  $m_{LPB}$  is the LPB mass, and  $g$  is the polariton-polariton interaction strength. The

reservoir dynamics, in its turn, is defined by the pumping power  $P(\mathbf{r}, t)$ , scattering into the condensate, and decay of reservoir polaritons  $\gamma_R$ . Therefore, the reservoir equation is typically written as follows:

$$\frac{\partial n_R(\mathbf{r}, t)}{\partial t} = P(\mathbf{r}, t) - R[n_R(\mathbf{r}, t)]|\psi(\mathbf{r}, t)|^2 - \gamma_R n_R(\mathbf{r}, t). \quad 1.26$$

In the limit of fast reservoir dynamics, the adiabatic approximation can be used:  $\partial_t n_R(\mathbf{r}, t) \approx 0$ . In this case, the generalized GPE [1.25](#), [1.26](#) can be rewritten as a single equation containing a nonlinear gain term saturating at high condensate density (using  $R[n_R] = Rn_R$ ):

$$i\hbar \frac{\partial \psi(\mathbf{r}, t)}{\partial t} = \left[ -\frac{\hbar^2}{2m_{LPB}} \nabla^2 + V_{ext}(\mathbf{r}) + g|\psi(\mathbf{r}, t)|^2 \right] \psi(\mathbf{r}, t) + \frac{i}{2} \left[ \frac{RP(\mathbf{r}, t)}{\gamma_R + R|\psi(\mathbf{r}, t)|^2} - \gamma_{LPB} \right] \psi(\mathbf{r}, t). \quad 1.27$$

This equation is often called the *complex Ginzburg-Landau equation* for the polariton condensate. We will utilize a modified version of this equation in [Ch. 5](#) in order to simulate the polariton stripe phase under non-resonant excitation.



Contents

---

<b>2.1 Topological photonics</b> . . . . .	<b>31</b>
<b>2.2 Artificial gauge fields in topological photonics</b> . . . . .	<b>34</b>
<b>2.3 Topological models</b> . . . . .	<b>36</b>
2.3.1 Su–Schrieffer–Heeger model and winding number . . . . .	36
2.3.2 Harper-Hofstadter model and Chern number . . . . .	40
<b>2.4 Non-Hermitian effects</b> . . . . .	<b>43</b>
2.4.1 Non-Hermitian skin effect . . . . .	44
2.4.2 Anomalous bulk-boundary correspondence . . . . .	46

---

It is generally accepted that the Topological Physics, a domain combining the physics and the *topology*, the field of mathematics studying conserved properties under continuous transformations, emerged in 1980 with the demonstration of a remarkable effect nowadays known as *Quantum Hall Effect* [28]. The experiment showed the exact quantization of Hall conductance and was soon after crowned with a Nobel Prize in physics in 1985. To be more precise, the work Ref. [28] did not explain the effect in terms of topology, and the first topology-related explanation appeared only in two years [29]. There, the conductance was explicitly defined in terms of a global system invariant obtained by the integration of valence band wavefunctions over the whole unit cell, the quantity that later received the name *Chern invariant*, or *Chern number*. Several years later, a graphene-based model was proposed [30] which does not require a magnetic field but still demonstrates the quantization of Hall conductivity. The effect is now widely known as the *Anomalous Quantum Hall Effect*, where "anomalous" simply underlines the absence of a magnetic field. These works laid the foundation for the field of Topological Physics, which since then has grown exponentially and become omnipresent in physical systems.

In this Chapter, we shortly review the field of topological photonics and introduce the concept of *gauge field*. We will have a closer look at several canonical topological models, both Hermitian and non-Hermitian, and introduce their topological invariants.

## 2.1 Topological photonics

In 2005 the concept of topology was extended to the field of photonics [31, 32, 33] in the seminal works of Haldane and Raghu [34, 35]. They made a key observation that the band structure and its topology do not exclusively belong to the quantum system, but they are rather the properties of waves in periodic systems. They suggested a photonic system showing nontrivial topology based on a 2D photonic crystal built of dielectric rods breaking the time-reversal symmetry by the Faraday effect. Furthermore, they predicted the existence of the unidirectional propagating photonic *edge modes* robust against backscattering and localization by impurities. They thus confirmed theoretically the *bulk-boundary*

*correspondence* [36, 37] between the topology of the bulk states, defined by the Chern invariant, and the number of the chiral edge states which has been already remarked in electronic systems. Quickly after these theoretical studies, a realistic experimental platform based on 2D gyromagnetic microwave photonic crystal was proposed [38], and an experiment was conducted [39] fully confirming all predictions.

In the following, the domain of Topological Photonics was growing actively. If initially the research in photonic systems mostly confirmed the topological physics known from electronics, later the topological photonics caught up and became an equivalently advanced field. This is certainly linked with significant advantages provided by photonics. Photonic systems can be engineered in a diverse and precise manner. One of such powerful engineering approaches is the *Floquet engineering* which makes use of the periodic temporal dynamics of a Hamiltonian in order to realize an effective time-independent topologically nontrivial Hamiltonian. For the first time in photonics, this approach was utilized to construct the *Floquet Chern insulator* by breaking the *time-reversal symmetry* (*TRS*) and obtaining a propagating topologically-protected edge state in a femtosecond-laser written photonic honeycomb lattice constructed out of helical waveguides [40]. Later, the framework of Floquet engineering allowed to create photonic Weyl points [41], photonic *parity-time-symmetric* (*PT-symmetric*) crystals [42], anomalous Floquet topological insulators [43, 44] and a photonic topological Anderson insulator [45], for example. In addition to laser-written waveguide arrays, quantum walks in bulk optics is another popular approach [46] for Floquet engineering.

A broad range of different degrees of freedom in engineered photonic systems also proposes an extension towards higher dimensional topological models through *synthetic dimensions*. These degrees of freedom might be frequency [47, 48], mode structure [49], or orbital angular momentum [50, 51]. One of their major advantage is an opportunity to realize long-range couplings in a synthetic photonic lattice. Probably, the most fascinating consequence of synthetic dimensions is the ability to access 4D topological models and invariants [47, 52]. Synthetic dimensions have been already used to demonstrate experimentally a topological insulator [49].

Moreover, unique nonlinear optical effects and the open nature of photonic systems allow us to extend the topological physics into previously unexplored domains of nonlinear [53] and non-Hermitian [54] topological physics. The inclusion of nonlinear and non-Hermitian terms into a system description automatically generates plenty of intriguing questions: how are topological transitions modified, is the robustness enhanced or broken, are there any genuinely nonlinear or non-Hermitian topological phases without analogs in linear Hermitian systems. Various photonic setups allow us to find answers to these questions. Numerous works in photonics cover the topology of nonlinear systems, including soliton dynamics in topological systems [55, 56, 57, 58, 59], self-induced topological transitions [60] and nonlinearity-induced topological edge state tuning [61] in the Su–Schrieffer–Heeger chain, and second-order topological insulators [62]. In non-Hermitian topological photonics, researchers investigate mostly topological surface states in *PT*-symmetric systems with balanced gain and loss [63, 64], photonic Fermi-arcs and exceptional points [65] and different types of topological lasing: unidirectional [66] and

single-mode lasing in PT-symmetric systems [67, 68].

Finally, photonics also provides us with a rich diversity of hybrid systems thanks to the interaction of light with various material excitations, therefore opening the whole field of topological polaritonics. Among different hybrid modes, we are especially interested in microcavity exciton-polaritons and what new they can bring to topology. First of all, they can undergo BEC with an establishment of a global coherent state, as discussed in Sec. 1.2.2. This property allowed for one of the first realizations of a topological laser that was based on the Su–Schrieffer–Heeger chain [69, 70] in this case. This laser is attractive not only because of its topological protection, but also thanks to the low threshold typical for polariton condensates. Secondly, exciton-polaritons are strongly sensible to the magnetic field thanks to their excitonic fraction, thus providing a powerful tool to break the TRS. This property allowed to realize the anomalous Hall effect [71, 72] and a polaritonic topological insulator [73, 74, 75]. Importantly for this thesis, the TE-TM SOC played a central role in the realization of both these effects. Finally, polariton-polariton interactions capable of producing a huge Kerr nonlinearity open a way towards nonlinear topological phases with a potential to achieve strongly correlated phases of light in the quantum regime. So far, there are mostly theoretical works in this direction. For example, the topological protection of the valley Hall effect was demonstrated by utilizing the coupling between vortex (a nonlinear excitation of a polariton fluid) and valley degrees of freedom [76]. Other works make use of a spatial pattern of an excitation laser in order to induce a nontrivial topology for the nonlinear polariton fluid excitation spectrum under resonant [77] and non-resonant [78] excitation conditions. One more powerful approach for generation of a nontrivial topology in an initially trivial lattice is to optically-induce the Zeeman splitting (effective magnetic field) between circularly-polarized polaritonic modes. This is an alternative way to achieve the Chern insulator, as has been shown in quasi-resonant [79] and non-resonant [80] excitation schemes. Again, in the last case, the TE-TM SOC brings the contribution without which the system would not be a Chern insulator.

The expectation for technological impact is high in photonics. The new concepts of light confinement should result in optical devices with high control of electromagnetic fields. The topological protection of the edge states promises a large set of robust energy-efficient optical isolators, simulators, and lasers operating from microwave to optical frequencies. For more details, we refer you to a nicely captured evolution of the field in several review articles [31, 32, 33].

In this thesis, we will have a particular focus on the topology induced by a relatively new type of photonic spin-orbit coupling, recently engineered in a planar microcavity system [81] and called the *Rashba-Dresselhaus spin-orbit coupling (RDSOC)*. The detailed description of this SOC will be provided in Ch. 3. Here, we simply underline a couple of crucial points about this SOC. As we have seen by now, TE-TM SOC lies the foundation for a majority of exciting topological effects in optical microcavities. The RDSOC is fundamentally different from the TE-TM SOC. First of all, it is essentially a 1D SOC, therefore, it does not show any winding. It is also linear in wavevector, which makes it a *gauge field*. This is particularly important since gauge fields bring a lot of diverse

topological effects as we review in the next Sec. 2.2. And finally, in photonic microcavities, the RDSOC appears along with a linear polarization splitting term which gives rise to the polarization mixing and is responsible for many exciting effects which we discover in this Thesis.

## 2.2 Artificial gauge fields in topological photonics

With the development of physics, and especially with the advancement of its mathematical formalism, the omnipresence of the *gauge fields* along with gauge symmetries, potentials, and invariance is becoming more obvious [82]. Probably, the Aharonov-Bohm effect [83] is the first evidence that the gauge field is a wider and more fundamental concept than the real field. The gauge-dependent electromagnetic potentials, which were believed to have no physical meaning and direct consequences, have been shown to play an explicit role in quantum interference.

While in some systems gauge fields and potentials appear naturally, like in the case of an electron in the electromagnetic field, in other cases, the system should be properly engineered in order to obtain so-called *artificial gauge fields*. In both cases, the Hamiltonian can be written in a *minimal coupling form*:

$$H = H(\mathbf{p} - \mathbf{A}), \quad 2.1$$

where gauge potential  $\mathbf{A}$  can depend on spatial coordinates, time, internal degrees of freedom, etc:  $\mathbf{A} = \mathbf{A}(\mathbf{r}, t, \sigma)$ . The corresponding gauge field is a curl of the potential:  $\mathbf{B} = \nabla \times \mathbf{A}$ . The transition from a continuous space Hamiltonian in the minimal coupling form (Eq. 2.1) to a lattice in *tight-binding approximation* can be performed through Peierls transformation. In this case, the gauge potential appears as the *Peierls phase* between lattice sites.

The concept of gauge field is closely linked with the topology, but according to our knowledge, this link is not yet fully understood. For example, the *Berry curvature*, the quantity defining the topology of most systems, is itself a gauge field (but not necessary represented by Eq. 2.1), while the *Berry connection* is a gauge potential. Even leaving the Berry curvature out of the brackets, the artificial gauge field appearing in the minimal coupling form of the Hamiltonian is often responsible for the emergence of topological effects.

We are mostly interested in gauge-field-related topological effects in photonics. It turns out that many photonic topological settings, even initially formulated in the form of Maxwell's equations, can be reformulated in the minimal coupling form Hamiltonian 2.1 [84], thus confirming the role played by an artificial gauge field. One of them is the already discussed proposal by Haldane and Raghu [34, 35] and its following realization in a gyromagnetic photonic crystal [38, 39]. Another one is a photonic crystal based on the bianisotropic metamaterial [85], which constitutes the so-called  $\mathbb{Z}_2$  *topological insulator*. For this insulator, the TRS is not broken, and the total Chern number (topological invariant) is equal to zero. However, there is still a pair of counter-propagating orthogonally

polarized edge states, with associated *spin Chern numbers*, which appear thanks to the vectorial nature of light polarization. This effect is equivalent to the *Quantum Spin Hall Effect* in electronics.

Numerous other platforms and frameworks involve gauge fields and potentials in an explicit way. One of them is an array of coupled ring resonators [86, 87, 88]. In this case, the vectorial nature of the state (pseudospin) originates from the clockwise and counter-clockwise propagating modes of each ring resonator, which are consequently coupled to each other with a path-length-dependent phase. When the mixing between different pseudospins is absent, they can be split out with each of them realizing a celebrated *Harper-Hofstadter model* [89, 90], with the Hofstadter butterfly spectrum. The model, therefore, does not require breaking the TRS, but as with any topological model, to keep its robustness, it should stay in the same universality class, which in this case means keeping the pseudospin-flipping scattering negligible.

Another approach to achieve nontrivial topology in the form of artificial gauge field-induced Landau levels is to use a strained photonic lattice [91, 92, 93, 94]. Contrary to the unstrained lattice, the artificial gauge potential is spatially dependent which gives rise to a non-zero curl (artificial gauge field). No matter what platform is used, a lattice of coupled waveguides [91], semiconductor micropillars [92, 93] or a silicon photonic crystal [94], all works report propagating chiral edge states, again in pairs formed by opposite polarizations, since the TRS is conserved.

The next framework widely utilized is *Floquet engineering*: construction of a periodically modulated in time system which after natural averaging appearing in evolution or detection results in a time-independent effective topologically-nontrivial Hamiltonian. The realizations may be various [95, 96, 97], but the most known is in the form of coupled helical (spiral) waveguides [40]. The role of time is played there by waveguide propagation coordinate  $z$ . The waveguide position oscillations periodic along  $z$  are associated with artificial gauge potential after averaging. As a result, TRS is broken, and a unique propagation direction of the edge states has been confirmed experimentally.

Another crucial framework strongly enriching topological physics is *synthetic dimensions*. As stated earlier, it allows to extend the system towards 3D, 4D, or even more dimensions by means of numerous system's degrees of freedom. These degrees of freedom can be frequency eigenmodes of ring resonators [47] or their chirality [98], transverse modes of waveguide lattice [49], time-bins [99], optical angular momentum modes in a free space cavity [50], frequency modes of nonlinear waveguide [100], etc. The exploitation of synthetic dimension is the only way to access four-dimensional topological physics [47, 52] which promises new interesting phenomena not present in 2D [101].

We can also look from the point of view of physical phenomena that can be associated with gauge fields and find a diversity of them in photonics. In addition to what has been already mentioned, gauge fields play a central role in 3D photonic topological insulators [102, 103], light guiding [104, 105], non-Abelian Harper-Hofstadter model [106], Klein tunneling [107], Weyl points [108] and exceptional rings [109], exceptional points and Fermi arcs [65], and many other effects.

Certainly, plenty of other paradigms and platforms combining gauge fields and non-

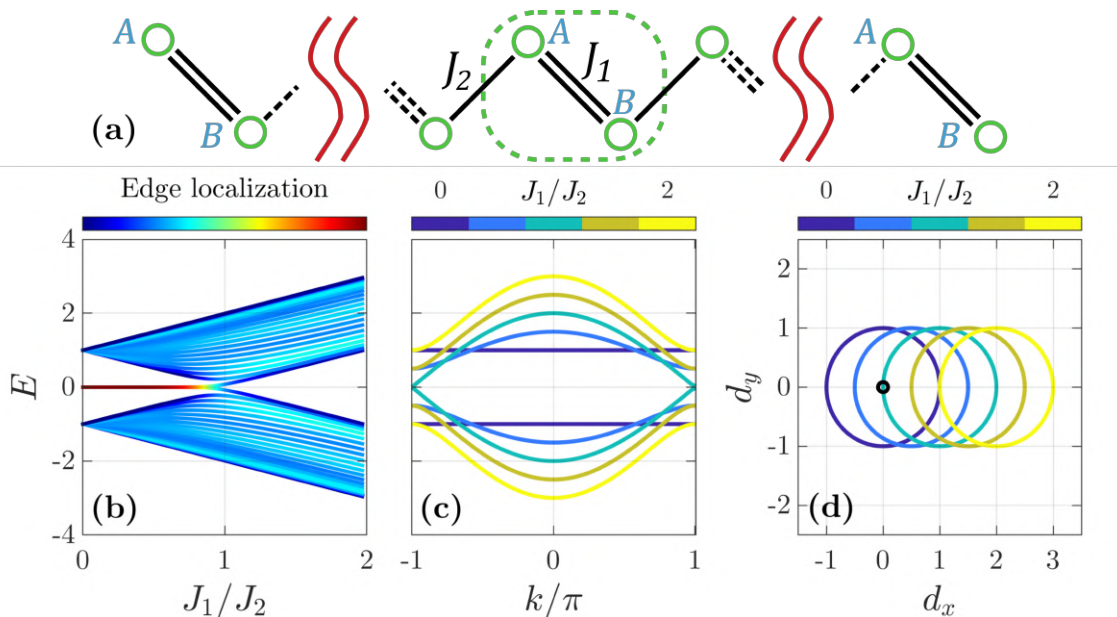


Figure 2.1: **SSH model.** (a) Scheme of a finite SSH chain; unit cell (green dashed line) contains two lattice sites (A and B);  $J_1$  and  $J_2$  are intracell and intercell couplings, respectively; (b) spectrum of the finite SSH chain depending on the coupling ratio  $J_1/J_2$ ; color represents the edge localization; (c) dispersion of the infinite SSH chain for several values of ratio  $J_1/J_2$  (different colors); (d) trajectories of the field vector  $\mathbf{d}$  in  $(d_x, d_y)$  plane for different values of ratio  $J_1/J_2$  (different colors); trajectories circumventing the origin (small black circle) have non-zero winding.

trivial topology exist. The last but not least platform that is worth mentioning here is an optical microcavity, where an artificial gauge field for photons or polaritons is usually realized through the spin-orbit coupling. The combination of the TE-TM SOC and material birefringence gives rise to the Dresselhaus- [110, 111] or Rashba-type [112, 113] SOC in the vicinity of a Dirac point. Another approach utilizes the magnetoelectric Stark effect for polaritons to realize a tunable gauge potential [114]. This platform is of particular interest for this Thesis. We will demonstrate in Ch. 4 new topological models emerging from a gauge field associated with the Rashba-Dresselhaus spin-orbit coupling in liquid crystal microcavities. Contrary to finely engineered gauge fields in different platforms described above, this SOC naturally appears in a nematic liquid crystal microcavity in the course of molecular rotation. Therefore, it provides us with a nice playground for demonstrating various gauge-field-induced effects.

## 2.3 Topological models

### 2.3.1 Su–Schrieffer–Heeger model and winding number

We start with the simplest topological model known, the *Su–Schrieffer–Heeger (SSH) chain* [115]. This model was suggested to describe the electron band structure and soliton formation in polyacetylene. It is quite often an introductory model in textbooks on topological physics since it allows to establish many concepts of topological physics in a

simple and vivid way. The model is depicted in Fig. 2.1(a). The chain is defined by two staggered coupling coefficients  $J_1$  and  $J_2$ . The unit cell of the chain contains two atoms, which we mark as A and B. The Hamiltonian of the chain is [116]:

$$H = \sum_n J_1 a_{n,B}^\dagger a_{n,A} + J_2 a_{n,B}^\dagger a_{n+1,A} + h.c., \quad 2.2$$

where  $a_{n,\sigma}^\dagger$  ( $a_{n,\sigma}$ ) is a creation (annihilation) operator of a photon at  $n$ th unit cell and  $\sigma = \{A, B\}$  lattice site. The spectrum of the Hamiltonian 2.2 (chain of 20 unit cells) is demonstrated in Fig. 2.1(b) as a function of the coupling ratio  $J_1/J_2$ . One can clearly observe that most of the states form two bands. These bands are separated by a bandgap which changes its size depending on the ratio  $J_1/J_2$ . For small ratios, two additional states are present inside the bandgap at zero energy. When the ratio reaches the value of 1, the bandgap closes. For bigger ratios, it opens again but without any states inside the bandgap.

These bandgap states are *edge states* of the chain. It is easy to verify by writing the edge state as  $|\psi\rangle = (c_{1,A} \ c_{1,B} \ \dots \ c_{N,A} \ c_{N,B})^T$  in the basis of single site localized states  $a_{n,\sigma}^\dagger |0\rangle = |n, \sigma\rangle$  and by calculating the edge localization degree accordingly:

$$EL = \sum_{n=\{i_{edges}\}} |c_{n,A}|^2 + |c_{n,B}|^2. \quad 2.3$$

We show the edge localization degree 2.3 as a color in Fig. 2.1(b), where we utilized 3 unit cells from each edge as  $\{i_{edges}\}$ . As one can see, the  $EL$  for bandgap states is close to one contrary to smaller values for the delocalized bulk states forming the bands. If the chain is long enough for two edges to be decoupled, each edge state is localized on the lattice sites of a single type: A sites for the state on the left edge and B sites for the state on the right edge (see Fig. 2.1(a)). When the ratio approaches 1, the edge states continuously delocalize into the bulk states (in the case of a finite chain).

The bandgap states are not only edge-localized but also *topologically protected* states. The protection stems from the famous *bulk-boundary correspondence* [36, 37, 117] which links the number of edge states with the quantized topological invariant of the system. The topological invariant, in its turn, is defined *in the bulk* by the symmetry class of the Hamiltonian. Ten different symmetry classes of the Hermitian systems were introduced by Altland and Zirnbauer [118]. These symmetry classes are built upon three fundamental symmetry operations: *time-reversal symmetry (TRS)*, *particle-hole symmetry (PHS)*, and *chiral symmetry (CS)*. Initially, these classes were discussed in the context of electronic systems, from where symmetries names appear. Nowadays, it is understood that the Altland-Zirnbauer classification is more fundamental and can be applied to many different platforms (photonic, for example), therefore, it is better not to interpret these names literally, but rather consider these symmetries as pure mathematical properties of the Hamiltonian.

It is worth noting that the symmetry class is defined not by the symmetries of the Hamiltonian itself, but rather by the symmetries which we *impose* on the system. In other

words, the Hamiltonian of an ideal unperturbed system can have several symmetries, but when the perturbation kicks in, it breaks some of them. Those symmetries that are robust against the allowed perturbations define the genuine symmetry class of the system. In the case of the SSH chain, typically, the chiral symmetry is imposed which is defined as:

$$\Gamma^{-1}H\Gamma = -H, \quad 2.4$$

with CS operator  $\Gamma$  being unitary  $\Gamma\Gamma^\dagger = 1$  and Hermitian  $\Gamma = \Gamma^\dagger$ . The CS operator  $\Gamma$  satisfying these properties is easy to construct for the SSH chain:

$$\Gamma = P_A - P_B = \sum_n a_{n,A}^\dagger a_{n,A} - a_{n,B}^\dagger a_{n,B}, \quad 2.5$$

with the projection operator  $P_A$  ( $P_B$ ) on lattice sites A (B). In Hermitian systems, CS is identical to *sublattice symmetry (SLS)* [119]. This name is widely used for SSH since it is more intuitive: it underlines the bipartite nature of the lattice which originates from the lattice couplings connecting only sites of different types.

In addition to the symmetry class, the imposed symmetries define the constraints on eigenvalues and eigenvectors. For SSH, application of the CS operator on the eigenstate  $|\psi_n\rangle$  with eigenvalue  $E_n$  reveals that each eigenstate  $|\psi_n\rangle$  possesses a chiral-symmetric partner  $\Gamma|\psi_n\rangle$  with eigenvalue  $-E_n$ :

$$H\Gamma|\psi_n\rangle = -\Gamma H|\psi_n\rangle = -E_n\Gamma|\psi_n\rangle. \quad 2.6$$

For the edge states having  $E_n = 0$ , the localization on lattice sites of a single type (A or B) can be proved:

$$HP_{A/B}|\psi_n\rangle = \frac{1}{2}H(\sigma_0 \pm \Gamma)|\psi_n\rangle = 0. \quad 2.7$$

Eq. 2.7 automatically indicates that the edge state is a chiral-symmetric partner of itself:  $\Gamma|\psi_n\rangle = \pm|\psi_n\rangle$ .

Until now, we have been working with a finite SSH chain, i.e. under *open boundary condition (OBC)*, possessing two edges and thus corresponding to the "boundary" constituent of the bulk-boundary correspondence. In order to address the "bulk" constituent, we have to rewrite the Hamiltonian 2.2 under *periodic boundary condition (PBC)*:

$$H = \sum_n J_1 a_{n,B}^\dagger a_{n,A} + J_2 a_{n,B}^\dagger a_{(n+1 \bmod N),A} + h.c., \quad 2.8$$

where difference appears only as mod  $N$  in subscript. Now, the system has the translation symmetry and wavevector  $k$  is a good quantum number. Therefore, the discrete Fourier transform can be applied to change from the real space basis  $|n, \sigma\rangle$  to the reciprocal space one  $|k, \sigma\rangle$ :

$$|n, \sigma\rangle = \frac{1}{\sqrt{N}} \sum_n e^{-ink} |k, \sigma\rangle. \quad 2.9$$

Then, the Hamiltonian 2.8 reads in the basis of the sublattice degree of freedom ( $|A\rangle |B\rangle$ )<sup>T</sup>

as:

$$H(k) = \langle k | H | k \rangle = \begin{pmatrix} 0 & J_1 + J_2 e^{-ik} \\ J_1 + J_2 e^{ik} & 0 \end{pmatrix} = d_x(k)\sigma_x + d_y(k)\sigma_y, \quad 2.10$$

with effective field vector components  $d_x(k) = J_1 + J_2 \cos k$  and  $d_y(k) = J_2 \sin k$ . The dispersion of the bulk Hamiltonian 2.10 is simply defined analytically as a length of the field vector  $E(k) = d(k) = \sqrt{(d_x(k))^2 + (d_y(k))^2}$ . The dispersion is shown in Fig. 2.1(c) with the ratio  $J_1/J_2$  as a parameter. At zero ratio the bands are flat since different dimers of the chain are completely decoupled (dark blue line, regime of full dimerization  $J_2 = 0$ ). When ratio starts to increase (light blue line), the bands bend and approach each other at the edges of the *Brillouin zone* (BZ). At ratio 1 (green line), the gap between the bands closes. While increasing ratio even more, the gap reopens and increases (dark and light yellow lines).

The topological invariant of the SSH chain is convenient to define geometrically by looking at the evolution of the field vector  $\mathbf{d}$  in  $(d_x, d_y)$  plane while  $k$  is moving along the BZ (Fig. 2.1(d)). The amount of times that the vector  $\mathbf{d}$  encircles the origin (black dot) is a topological invariant called the *winding number* [120]. For small ratios  $J_1/J_2 < 1$  it is equal to one (dark and light blue lines), for big ratios  $J_1/J_2 > 1$  it is equal to zero (dark and light yellow lines), and, finally, for exact equality  $J_1 = J_2$  it is ill-defined since the  $\mathbf{d}$  trajectory crosses the origin (green line). As one can easily notice, OBC spectra, PBC spectra and field vector trajectories (Figs. 2.1(a,b,c), respectively) are well consistent with each other. The presence of the localized edge states at  $J_1/J_2 < 1$  coincides with the nonzero winding number. This correspondence is indeed the bulk-boundary correspondence. In case of the SSH chain, winding number indicates the amount of edge states on a single edge. Since there are two edges in our chain, the total number of edge states is doubled.

The fact that the winding number is a good topological invariant is strongly related to the symmetries (and, therefore, the symmetry class) of the system. The CS ensures the absence of  $\sigma_z$  term in the Hamiltonian, which forces the field vector  $\mathbf{d}$  to stay inside the  $(d_x, d_y)$  plane. Therefore, in order to transform the system from topologically nontrivial phase (dark blue line in Fig. 2.1(d)) to topologically trivial phase (light yellow line in Fig. 2.1(d)) the trajectory of  $\mathbf{d}$  must cross the origin. The intersection with the origin implies the closure of the gap and, consequently, non-adiabatic Hamiltonian phase transition. If one lifts the requirement of CS, then the phase transition can be performed adiabatically (without crossing the origin and closing the gap) by means of  $\sigma_z$  term which takes the  $\mathbf{d}$  trajectory out of plane [116].

As a final note on this model, we discuss another topological invariant which is equivalent to the winding number in the case of SSH chain. This invariant is the *Zak phase*  $\gamma_n(BZ)$  defined for the bulk reciprocal space eigenstate  $|\phi_n(k)\rangle$  as [121]:

$$\gamma_n(BZ) = i \int_{BZ} \langle \phi_n(k) | \frac{\partial}{\partial k} | \phi_n(k) \rangle. \quad 2.11$$

If normalized to  $2\pi$ , it gives precisely the same result as the winding number: 1 for  $J_1/J_2 < 1$  and 0 for  $J_1/J_2 > 1$ . In case of SSH chain the calculation of both invariants is useless since they give the same result, but considering a different system, especially a higher

dimensional system, the difference becomes pronounced and fundamental. The winding number is a so-called  $\mathbb{Z}$  invariant in the system with *odd* number of dimensions [119]. The Zak phase in its turn is a special case of the Berry phase  $\gamma_n(\mathcal{C})$ , the geometric phase acquired by the eigenstate during the adiabatic evolution in the parameter space. Berry phase is inextricably linked with Berry curvature, Berry connection and Chern number, which we already mentioned before in this Thesis and which we will discuss in more details in the next Sec. 2.3.2. Contrary to the winding number, the Chern number is  $\mathbb{Z}$  invariant in the system with *even* number of dimensions. As one can remark once again, the SSH model in some sense marries these invariants.

Since the SSH is one of the simplest topological models to study and realize experimentally, it is not surprising that it has plenty of realizations in photonics. The SSH chain was utilized for the first realization of *exciton-polariton topological laser* [69, 70]. Instead of varying the distance between chain sites, this realization utilizes the anisotropic coupling between localized  $p$ -orbital states: the difference between  $\sigma$  and  $\pi$  bonds. Since the pillars are arranged in a zigzag manner,  $\sigma$  and  $\pi$  bonds interchange along the chain making the system equivalent to the SSH. Other experimental realizations of polaritonic SSH have appeared later in different geometry [122], at room temperature [123, 124], under electrical injection [125] and in the regime of condensate ballistic coupling [126].

Other realizations of SSH involve optically induced potential in nonlinear crystal [127], quantum walks in free-space optical system [46] and based on orbital angular momentum of light beams [128], plasmonic [129] and dielectric [130, 131] nanoparticles forming a zigzag chain, arrays of plasmonic [132, 133, 134] and dielectric waveguides [135, 134, 136], chain of microwave resonators [137], array of silicon Mach-Zehnder interferometers [138]. Most of these realizations, once fabricated, do not allow tunability of the model parameters. We will address this issue by proposing a tunable photonic SSH configuration in Sec. 4.2.

### 2.3.2 Harper-Hofstadter model and Chern number

The next system which we discuss in detail is an electron in a 2D lattice under a perpendicular homogeneous magnetic field (Fig. 2.2(a)). For the first time this model was studied by Harper [89], and latter in more details by Hofstadter [90]. The significant contribution of both studies resulted in the currently widely used model name, *Harper-Hofstadter (HH) model*. The model played a crucial role for understanding the quantization of the Hall conductance since the integer Chern numbers characterizing the Hall conductance emerge naturally while solving the model *analytically*. It also reproduces the Landau levels in a continuous limit.

Initially, the HH model is formulated for charged spinless non-interacting fermions. The Hamiltonian of the model can be written in a compact way as [139]:

$$H = t(T_x + T_y) + h.c., \quad 2.12$$

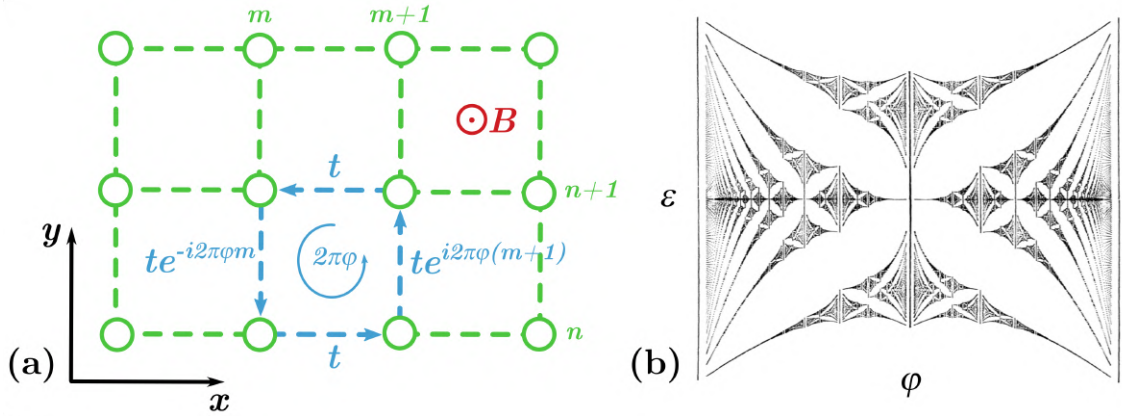


Figure 2.2: **Harper-Hofstadter model.** (a) Scheme of the model: segment of the infinite square lattice built out of lattice sites with coordinates  $(x, y) = (m, n)$  (green circles) connected by lattice couplings  $t$  along  $x$  direction and  $te^{i2\pi\varphi m}$  along positive  $y$  direction (blue dashed lines and text); the Peierls phase along  $y$  is created thanks to the perpendicular magnetic field  $B$  (red circle) and the use of Landau gauge; the total phase acquired while moving along the lattice plaquette is  $2\pi\varphi$  (blue looped arrow); (b) the spectrum of HH model  $\epsilon$  versus magnetic flux per plaquette  $\varphi$  showing the famous Hofstadter butterfly (adopted from the original work of Hofstadter [9]).

where  $T_x$  and  $T_y$  are translation operators in the presence of the magnetic field:

$$T_x = \sum_{m,n} a_{m+1,n}^\dagger a_{m,n} e^{i\theta_{m,n}^x}, \quad T_y = \sum_{m,n} a_{m,n+1}^\dagger a_{m,n} e^{i\theta_{m,n}^y}. \quad 2.13$$

The phase  $\theta_{m,n}^x$  and  $\theta_{m,n}^y$  originate from the vector potential  $\mathbf{A}$  and can be obtained through *Peierls substitution*:

$$\theta_{m,n}^x = \frac{e}{\hbar} \int_m^{m+1} A_x dx, \quad \theta_{m,n}^y = \frac{e}{\hbar} \int_n^{n+1} A_y dy. \quad 2.14$$

It is simple to verify that the total phase accumulated while encircling a lattice plaquette (lattice curl), sometimes called the *Aharonov-Bohm phase*, is linked with the flux per lattice plaquette  $\varphi$ :

$$\text{rot}_{mn}\theta = \frac{e}{\hbar} \oint_{mn} \mathbf{A} \cdot d\mathbf{l} = 2\pi \frac{e}{\hbar} \int_{mn} B dS = 2\pi \frac{\varphi}{\varphi_0}, \quad 2.15$$

where  $\varphi_0 = h/e$  is the quantum of magnetic flux. Now, when the model is introduced (Fig. 2.2(a)), we will briefly discuss several remarkable properties of this model. For further analysis, we restrict ourselves to Landau gauge  $\mathbf{A} = (0, Bx, 0) = (0, 2\pi\varphi m, 0)$ . Therefore,  $\theta_{m,n}^x = 0$  and  $\theta_{m,n}^y = 2\pi\varphi m$ .

The Hamiltonian is not diagonal in the basis of eigenstates of translation operators since they do not commute:  $[T_x, T_y] \neq 0$ . New operators which diagonalize the Hamiltonian are called *magnetic translation operators* and they deal with the presence of Peierls

phase induced by the magnetic field:

$$\hat{T}_x = \sum_{m,n} a_{m+1,n}^\dagger a_{m,n} e^{i2\pi n\varphi}, \quad \hat{T}_y = \sum_{m,n} a_{m,n+1}^\dagger a_{m,n}. \quad 2.16$$

These operators do not commute and they form so-called *magnetic translation algebra*:

$$\hat{T}_x \hat{T}_y = e^{i2\pi\varphi} \hat{T}_y \hat{T}_x. \quad 2.17$$

In the case of *rational* flux per plaquette  $\varphi = p/q$ , these operators can be used to construct a new,  $q$  times increased *magnetic unit cell* under translation by 1 lattice constant along  $y$  and  $q$  lattice constants along  $x$ :  $[\hat{T}_x^q, \hat{T}_y] = 0$ . Therefore, the *magnetic Brillouin zone*  $\mathbb{T}^2$  is reduced by  $q$ :  $0 \leq k_x \leq 2\pi/q$ ,  $0 \leq k_y \leq 2\pi$ . Because of this shrinking of the BZ, the spectrum of the model acquires  $q$ -fold degeneracy at different  $k_y$  wavevectors.

Making use of the reduced magnetic BZ, the state of the system can be written as a superposition of  $q$  states localized on the "sites" in momentum space ( $k_x = k_x^0 + 2\pi\varphi m$ ,  $m = 0, \dots, q-1$ ):

$$|\phi\rangle = \sum_{m=0}^{q-1} c_m a_{k_x^0 + 2\pi\varphi m, k_y}^\dagger. \quad 2.18$$

The spectrum and eigenstates of the HH model are then defined by *Harper equation*:

$$\varepsilon c_m = (E/t)c_m = 2 \cos(k_x^0 + 2\pi\varphi m) c_m + (e^{-ik_y} c_{m-1} + e^{ik_y} c_{m+1}). \quad 2.19$$

The resulting spectrum  $\varepsilon$  as a function of the magnetic flux per plaquette  $\varphi$  is shown in Fig. 2.2(b) and it forms a fractal pattern widely known as *Hofstadter butterfly*. The Landau levels can be reproduced by going in the continuous limit  $\varphi \rightarrow 0$ .

Probably, the most striking result emerging from this model is the quantization of Hall conductance. If the Fermi level is placed inside the  $r$ th gap, then three positive integers  $r, p, q$  can be linked by *Diophantine equation* [29]:

$$r = qs_r + pt_r, \quad 2.20$$

with the constraints of integer  $s_r, t_r$  and  $|t_r| \leq q/2$ ,  $0 \leq r \leq q$ . The Hall conductance  $\sigma_{xy}$  in this case reads as (*TKNN formula*):

$$\sigma_{xy} = \frac{e^2}{h} t_r. \quad 2.21$$

This is an extremely simple and elegant formula confirming the quantization of the Hall conductance. But so far it did not involve the topology explicitly. In other words, the geometrical properties of the eigenstates in Hilbert space are not explicitly used for derivation of this formula. In order to build a link with the topology, we need to start from another end and discuss the general properties of bands in Hilbert space.

In 1984, Berry [140] realized that under adiabatic evolution of the eigenstate  $|n(\mathbf{R})\rangle$  in the parameter space  $\mathbf{R}$ , the state acquires not only a dynamical phase, but also an additional *geometric phase*  $\gamma_n(\mathcal{C})$  defined uniquely by the eigenstate  $|n(\mathbf{R})\rangle$  and trajectory

$\mathcal{C}$  in the parameter space  $\mathbf{R}$ . This concept has received the name of *Berry phase* and is probably the most important concept in topological band theory. Berry phase is by definition a gauge phase. It has associated gauge potential  $\mathcal{A}_n(\mathbf{R})$  and gauge field  $\mathbf{\Omega}_n(\mathbf{R})$  called *Berry connection* and *Berry curvature*, respectively, and defined as:

$$\mathcal{A}_n(\mathbf{R}) = i \langle n(\mathbf{R}) | \nabla_{\mathbf{R}} | n(\mathbf{R}) \rangle, \quad 2.22$$

$$\mathbf{\Omega}_n(\mathbf{R}) = \nabla_{\mathbf{R}} \times \mathcal{A}_n. \quad 2.23$$

As one can see, these quantities are pure derivatives from a single band state  $|n(\mathbf{R})\rangle$ , and therefore can be viewed as geometric characteristics of this band.

In case of 2D electron Bloch band, the Berry curvature integrated over the whole BZ gives an integer number of a pure geometric nature, called the *band Chern number*  $C_n$ . And here the link between the mathematics and physics comes. The sum of Chern numbers  $C_n$  for all occupied bands (below Fermi level in  $r$ th gap) is exactly equal to  $t_r$ , which is called the *gap Chern number*:

$$t_r = \sum_{n=1}^r C_n. \quad 2.24$$

We showed here how a simple model such as the Harper-Hofstadter model brings us to the striking result linking the topology, a purely mathematical concept, with the Hall conductance, an observable physical quantity. The transport in this system appears through the topologically protected edge states according to the bulk-boundary correspondence. These states are unidirectional as a consequence of the TRS breaking. One of the results of this Thesis is a possible realization scheme of a TRS-conserving yet topological version of the HH model in a liquid crystal microcavity which we will address in more detail in Sec. 4.5.

## 2.4 Non-Hermitian effects

Up to this moment, we were discussing the effects which can be described in terms of Hermitian Hamiltonians ( $H = H^\dagger$ ). The non-Hermitian Hamiltonians ( $H \neq H^\dagger$ ) for a long time were not seriously considered, since the non-Hermiticity mostly originating from the system losses was perceived as detrimental for the system. Nevertheless, every physical system is an open system by some extent, and often the exchange with the environment can not be neglected. The non-Hermitian Hamiltonians provide a simple and intuitive description of the system in this case.

The formalism of non-Hermitian Hamiltonians has first appeared in the works of Moiseyev [141], where they were applied to describe atomic and molecular resonances. We can say that the interest for non-Hermitian Hamiltonians started to grow quickly after the study made by Bender and Boettcher [142], where they suggested parity-time symmetric non-Hermitian Hamiltonians having *real* spectra, thus building a bridge between Hermitian and non-Hermitian Hamiltonian formalisms. Nowadays, parity-time symmetric

non-Hermitian Hamiltonians are often used to describe the systems with balanced gain and loss [143, 144].

In the following, the classification of topological phases of matter was extended to the non-Hermitian Hamiltonians [119]. The concept of bandgap was split on point and line bandgaps in complex energy plane, new symmetries, topological classes and invariants were defined. This mathematical extension was supported by purely non-Hermitian phenomena which have emerged in physical systems [54]. Today, several promising applications built on the non-Hermitian Hamiltonian formalism are already realized; they count enhanced sensing [145, 146, 147], unidirectional visibility [148, 149] and lasing [150], and single-mode lasing [67, 68].

### 2.4.1 Non-Hermitian skin effect

One of non-Hermitian phenomena is the *non-Hermitian skin effect (NHSE)* [151]. The core feature of the effect is the localization of *all* eigenstates of a finite system on its edge. The number of localized states here is proportional to the system volume, contrary to the Hermitian systems where it is proportional to the system surface area at most. The states of the system are called *skin states* by drawing inspiration from the electromagnetic skin effect where the current density concentrates near the surface of a conductor.

First, the non-Hermitian skin effect is a genuinely non-Hermitian topological effect characterized by the *complex spectral winding number* [152]:

$$w_{E_b} = \frac{1}{2\pi} \oint_{BZ} \frac{d}{dz} \arg[H(z) - E_b] dz, \quad 2.25$$

where  $z = e^{ik}$  is the BZ in a complex plane,  $H(z)$  is the tight-binding Hamiltonian under PBC, and  $E_b$  is a complex energy reference point. If there exists a point  $E_b$  with non-zero winding, then the non-Hermitian skin effect is present. Second, the effect can appear even for a single band Hamiltonian, which is not the case for Hermitian systems, where for nontrivial Hermitian topology at least two bands are required.

A single-band system where the NHSE takes place is the *Hatano-Nelson (HN) model* [153]. The model is a 1D chain with non-reciprocal hopping coefficients  $t^+$  and  $t^-$ . The single-particle Hamiltonian of the chain is:

$$H = \sum_n t^+ a_{n+1}^\dagger a_n + t^- a_n^\dagger a_{n+1}, \quad 2.26$$

where  $a_n$  ( $a_n^\dagger$ ) is the annihilation (creation) operator for a particle at lattice site  $n$ , as usual. All eigenstates of the chain are localized at one side (Fig. 2.3(a,b)). The spectrum of the chain forms a loop in the complex energy plane (Fig. 2.3(c)):

$$E(k) = (t^- + t^+) \cos k + i(t^- - t^+) \sin k, \quad 2.27$$

therefore, having non-zero winding number  $w_{E_b=0}$ . The winding sign, and, hence, the localization edge is defined by  $\text{sign}(|t^-| - |t^+|)$ .

Another approach providing the complementary information about the NHSE is the

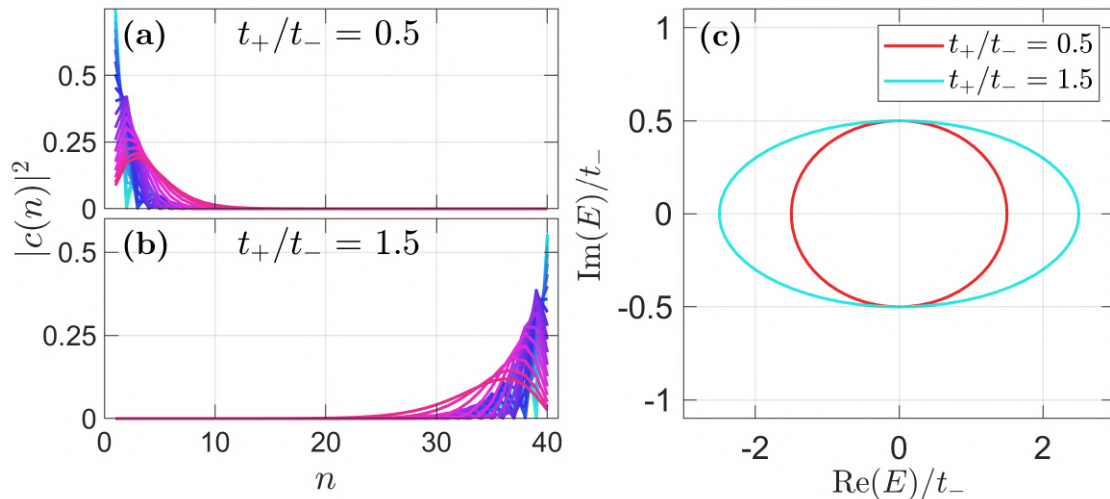


Figure 2.3: **HN model.** Density of all eigenstates in real space for (a)  $t_+ < t_-$  and (b)  $t_+ > t_-$ ; color corresponds to the state number; (c) complex spectra of HN model for two different ratios  $t_+/t_-$ ; red (blue) color corresponds to the positive (negative) spectral winding Eq. 2.25; the simulations are performed for a finite HN chain of 40 sites.

construction of *generalized Brillouin zone (GBZ)*. The necessity to substitute normal BZ appears when we perform a transition from bulk (PBC) to finite system (OBC). Initially delocalized states pile up at the edge of the system under the system truncation which contradicts to the postulate we use to apply the bulk-boundary correspondence: the introduction of the border does not change the bulk topology. Therefore, the topology should be redefined under OBC. Starting from this intuition, Yokomizo and Murakami suggested how to construct this GBZ [154]. As a result of this construction for a system in mind, one can visualize the GBZ in a complex plane as:  $z = r(k)e^{ik}$ ,  $r(k) \in \mathbb{R}$ ,  $k \in [0, 2\pi]$ . The pre-factor  $r$  originates from the non-Hermitian nature of Hamiltonian and captures the exponential growth ( $r(k) > 1$ ) or decay ( $r(k) < 1$ ) of the eigenstate. The predictions of the NHSE by the winding number and GBZ are equivalent despite the completely different approaches: the first is based on the spectrum under PBC while the second utilizes the complex wavevectors originating from OBC [155].

The first experimental realizations of NHSE appeared mostly in acoustics [156, 157], mechanics [158, 159, 160, 161], electrical circuits [162, 163, 164, 165], and cold atoms [166]. Several theoretical suggestions were done in the field of photonics and they are mainly based on coupled ring resonators [167, 168, 169, 170], exciton-polariton lattices [171, 172, 173, 174], array of chirally coupled atoms [175] and photonic crystals [176, 177, 178, 179]. Experimental realizations of NHSE in photonics are not numerous and involve only discrete-time quantum walks in coupled optical fiber loops [180] and bulk optics [181, 182, 183], synthetic frequency dimension in an optical ring resonator [184, 185], and a single realization in a real space utilizing a chain of active ring resonators [186]. The key ingredient for achieving the NHSE in a simple 1D model is the non-reciprocity of couplings, though in 2D there was a suggestion how to realize it with gain and loss only [187]. Therefore, most of proposals and experimental realizations resort to the complicated setups, elaborated fabrication techniques, and use of synthetic dimensions. In the

Sec. 4.6, we suggest a way how to realize tunable non-reciprocal couplings and the NHSE in real space which is applicable to several platforms.

### 2.4.2 Anomalous bulk-boundary correspondence

Another effect which often (but not always) accompanies the NHSE is the *anomalous bulk-boundary correspondence*. Basically, the topological transition with an edge state appearance happens at the set of system parameters not expected from Hermitian topological invariant calculated for Bloch bands of the system. The effect was initially observed for a Creutz ladder [188], which is equivalent to the *non-Hermitian SSH* chain (Fig. 2.4(a)) under similarity transformation. The Hamiltonian of the non-Hermitian SSH chain can be written in this case as:

$$H = \sum_n t_1^+ a_{n,B}^\dagger a_{n,A} + t_1^- a_{n,A}^\dagger a_{n,B} + t_2^- a_{n,B}^\dagger a_{n+1,A} + t_2^+ a_{n+1,A}^\dagger a_{n,B}, \quad 2.28$$

where  $t_{1,2}^+$  and  $t_{1,2}^-$  are staggered non-reciprocal couplings along positive and negative directions of the chain, respectively,  $a_{n,\sigma}$  ( $a_{n,\sigma}^\dagger$ ) is the annihilation (creation) operator for a particle at lattice site  $n$  and sublattice type  $\sigma = \{A, B\}$ .

The spectrum of Hamiltonian 2.28 is complex. Its absolute value, real part and complex part are shown separately in Fig. 2.4(b,c,d) as a function of the reciprocal part  $t_1$  of intracell coupling ( $t_1^\pm = t_1 \pm \gamma/2$ ). Here, the specific case of reciprocal intercell coupling  $t_2^\pm = t_2$  is considered in order to distil the result. As one can easily see, the transition happens at  $t_1/t_2 \neq 1$ , contrary to what expected from Hermitian topology (see Fig. 2.1).

An extension of topological classification towards non-Hermitian systems [152, 119] allowed to define a proper topological invariant for this system and restore the bulk-boundary correspondence. In analogy with Hermitian SSH, the *non-Hermitian winding number* predicts correctly the transition. It is defined as:

$$W = \oint \frac{dk}{4\pi i} \text{tr} \left[ \mathcal{S} H^{-1}(k) \frac{dH(k)}{dk} \right], \quad 2.29$$

under the SLS  $\mathcal{S}$  that is conserved (and not CS):

$$\mathcal{S} H(k) \mathcal{S}^{-1} = -H(k). \quad 2.30$$

Another approach makes use of biorthogonal quantum mechanics [189] and defines a topological invariant in real space called *biorthogonal polarization* [190]. Biorthogonal quantum mechanics operates with both right and left eigenstates of the Hamiltonian:

$$H |\psi_{R,i}\rangle = E_i |\psi_{R,i}\rangle, \quad H^\dagger |\psi_{L,i}\rangle = E_i^* |\psi_{L,i}\rangle. \quad 2.31$$

Then, the biorthogonal polarization  $P$  makes use of localized nature of zero-energy topological mode and is defined as:

$$P = 1 - \lim_{N \rightarrow \infty} \frac{\sum_n \langle \psi_{L,0} | n \Pi_n | \psi_{0,R} \rangle}{N}, \quad 2.32$$

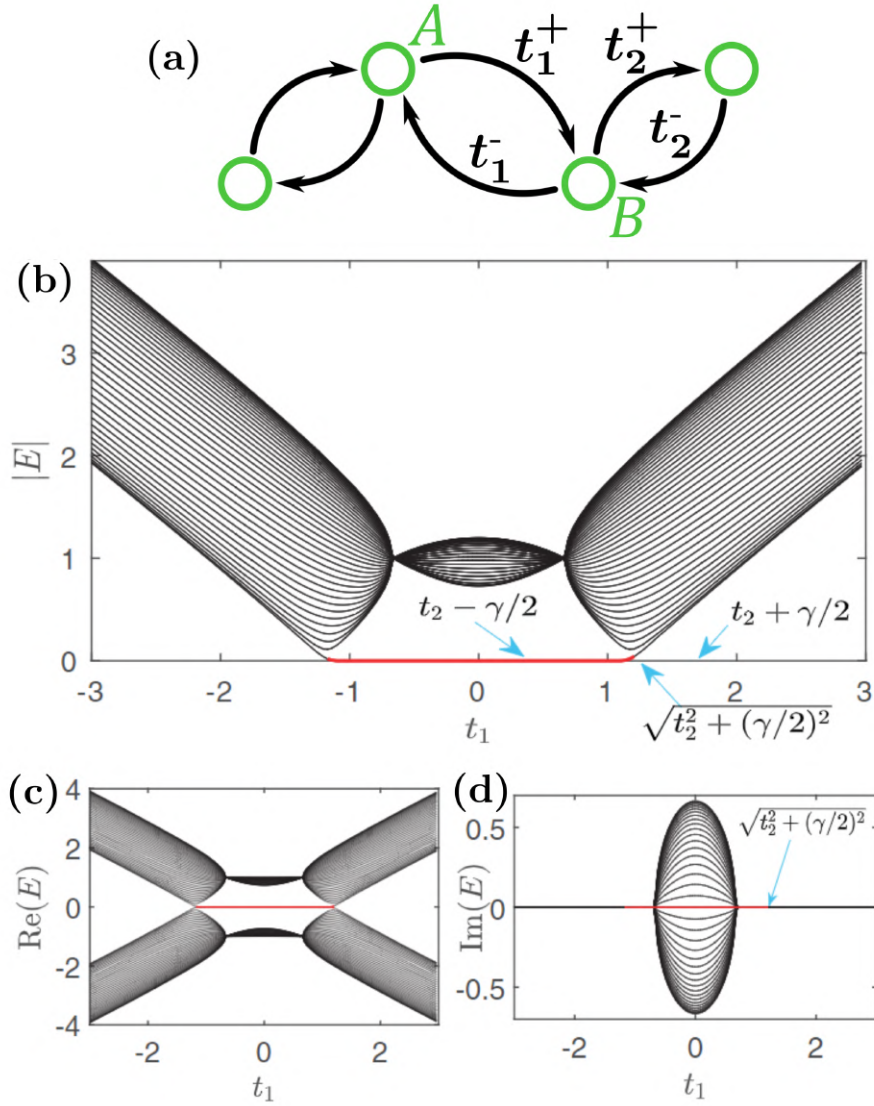


Figure 2.4: **Non-Hermitian SSH model.** (a) Segment of a non-Hermitian SSH chain; the chain is defined by non-reciprocal intracell  $t_1^\pm$  and intercell  $t_2^\pm$  couplings; (b) absolute value, (c) real part and (d) imaginary part of complex spectrum of the finite non-Hermitian SSH chain depending on the reciprocal part of intracell tunneling  $t_1$  (special case of  $t_1^\pm = t_1 \pm \gamma/2$ ,  $t_2^\pm = t_2 = 1$ ,  $\gamma = 4/3$ ); red solid lines mark a topologically protected zero-energy mode; the topological transitions happens at  $t_1/t_2 \neq 1$  contrary to Hermitian SSH (Fig. 2.1); panels (b,c,d) are adopted from [151].

where  $N$  is a system size, subscript 0 indicates the zero-energy state, and  $\Pi_n$  is a projection operator onto the unit cell  $n$ , which in the case of non-Hermitian SSH [2.28](#) reads as  $\Pi_n = a_{n,A}^\dagger a_{n,A} + a_{n,B}^\dagger a_{n,B}$ . The invariant is generalizable to higher-order boundary states, multiple boundary states and systems without analytical solutions.

Contents

---

<b>3.1 Overview</b> . . . . .	<b>49</b>
<b>3.2 RDSOC in liquid crystal microcavities</b> . . . . .	<b>52</b>
3.2.1 Nematic liquid crystal microcavity . . . . .	52
3.2.2 (N,N+1) resonant regime . . . . .	53
3.2.3 Minimal coupling representation . . . . .	57
3.2.4 Cholesteric liquid crystal and optical activity . . . . .	59

---

In this Chapter, we will cover the central concept of this Thesis, the *Rashba-Dresselhaus spin-orbit coupling (RDSOC)*. In Sec. 3.1, we will start by reviewing the historical development of this SOC in different systems and discussing the theoretical works studying various RDSOC-induced effects. In Sec. 3.2, we cover a particular platform of *liquid crystal (LC) microcavity* which constitutes a nice playground for the physics of spin-orbit coupling.

### 3.1 Overview

In 1955, Dresselhaus calculated [191] the electronic bands of a zinc blende structure from the symmetry considerations in order to explain the properties of InSb observed in experiment. Due to the *bulk inversion asymmetry (BIA)*, the dispersion of the bulk material demonstrates the band splitting originating from the spin-orbit coupling and proportional to the third power of wavevector components  $H_D \propto k_x^i k_y^j k_z^l$ ,  $i + j + l = 3$ . For 2D material lacking inversion symmetry, the confinement along  $z$  axis allows to isolate a leading term linear in  $\mathbf{k}$ , nowadays typically called the *Dresselhaus spin-orbit coupling*:

$$H_D = \boldsymbol{\Omega}_D \cdot \boldsymbol{\sigma} = \beta(k_x \sigma_x - k_y \sigma_y), \tag{3.1}$$

where  $\sigma_i$  is the  $i$ th Pauli matrix, and  $\beta$  is the strength of the SOC. The band structure of a massive particle with Dresselhaus SOC  $H_D$  and the pseudospin structure  $\mathbf{S}$  (co- and counter-aligned with the effective field  $\boldsymbol{\Omega}_D$ ) are shown in Fig. 3.1(a,d), respectively.

Four years later, in 1959, Rashba and Sheka have discovered a similar band splitting in bulk wurtzite lattice having uniaxial symmetry [192] (see Supplementary Materials of [193] for english version). Some years later, Bychkov and Rashba realized [194] that this type of SOC is typical for many 2D material samples having an asymmetric confinement (surfaces and heterostructures), or the *structure inversion symmetry (SIA)*. For these materials *Rashba spin-orbit coupling* is commonly written as:

$$H_R = \boldsymbol{\Omega}_R \cdot \boldsymbol{\sigma} = \alpha(k_y \sigma_x - k_x \sigma_y), \tag{3.2}$$

where  $\alpha$  is the strength of the SOC. The band structure of a massive particle with Rashba SOC  $H_R$  and the pseudospin structure  $\mathbf{S}$  (co- and counter-aligned with the effective field  $\boldsymbol{\Omega}_R$ ) are shown in Fig. 3.1(b,e), respectively. Nowadays, the *Rashba effect*, and especially

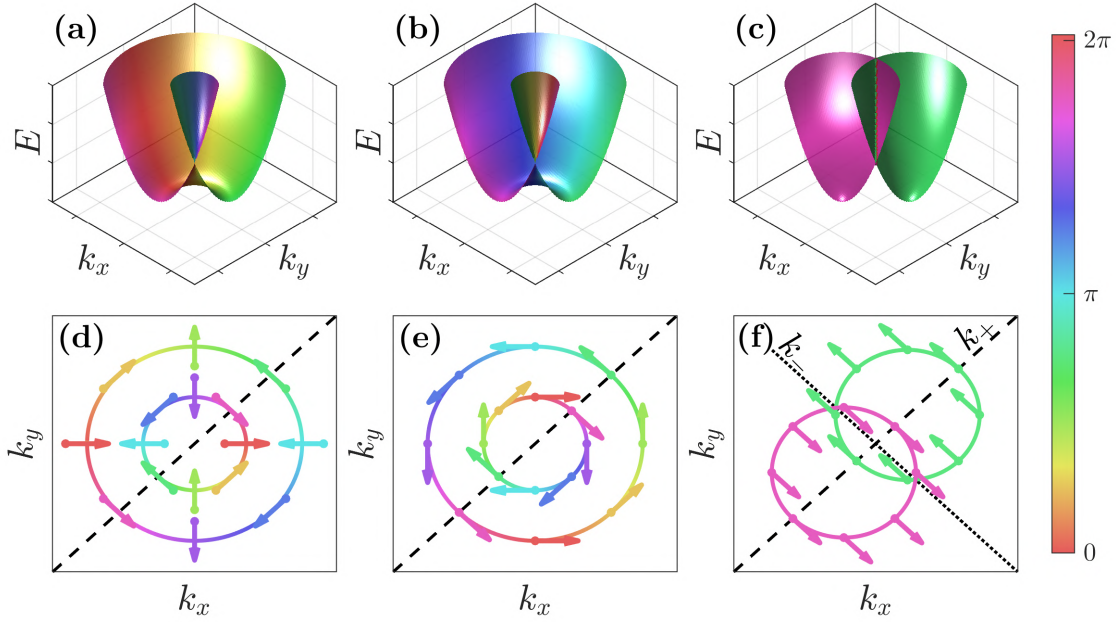


Figure 3.1: **Rashba and Dresselhaus SOCs.** Dispersion cut for a massive particle with (a) Dresselhaus, (b) Rashba and (c) Rashba-Dresselhaus SOC; the pseudospin structure at constant energy cut of the dispersions (a,b,c): (d) Dresselhaus, (e) Rashba and (f) Rashba-Dresselhaus SOC; dashed line shows the cut axis for panels (a,b,c); dashed and dotted lines are  $k_+$  and  $k_-$  coordinate axes, respectively, which simplify  $H_{RD}$  Hamiltonian Eq. 3.3; color represents the in-plane pseudospin orientation (Eq. 1.6).

its tunability by applied electric field, is one of the foundational effects for the field of spintronics [195], it plays a pivotal role in Spin Hall Effect [196] and Quantum Spin Hall Effect [197] and it has potential to be applied in Topological quantum computing through realization of Majorana fermions [198, 199, 200, 201].

Rashba and Dresselhaus dispersions are identical (for  $\alpha = \beta$ ) and they show an extrema circle at nonzero  $k$ , a fingerprint of these SOCs. However, the eigenstate behavior is different for them: the effective field of Dresselhaus SOC  $\Omega_D$  demonstrates the winding of -1, while the winding of Rashba field  $\Omega_R$  is 1.

In general, the Hamiltonian of a 2D electron gas is then written as:

$$H = \frac{\hbar^2 \mathbf{k}^2}{2m} \sigma_0 + H_R + H_D, \quad 3.3$$

where the first term is the kinetic energy of the lattice electron with effective mass  $m$ . An interesting change in the bands and eigenstates appears when both contributions are balanced:  $\alpha = \beta$  (Fig. 3.1(c)) [202]. In this case, there are two degenerate bands shifted oppositely along a certain direction of the reciprocal space. Each band shows a unique pseudospin direction (Fig. 3.1(c,f)). To clarify the result, the Hamiltonian 3.3 can be transformed into a different basis by  $U = \frac{1}{\sqrt{2}} \left[ 1 + \frac{i}{\sqrt{2}} (\sigma_x + \sigma_y) \right]$  along with the spatial coordinate transformation  $k_{\pm} = \frac{1}{\sqrt{2}} (k_y \pm k_x)$  (see dashed and dotted lines in Fig. 3.1(f)).

We, therefore, obtain the Hamiltonian with *Rashba-Dresselhaus SOC*:

$$H_{RD} = \frac{\hbar^2 \mathbf{k}^2}{2m} \sigma_0 - 2\alpha k_+ \sigma_z. \quad 3.4$$

Since Hamiltonian 3.4 is diagonal, one easily obtains two energy bands  $E_{\pm} = \hbar^2 k^2 / 2m \mp 2\alpha k_+$  for  $|+\rangle = (1 \ 0)^T$  and  $|-\rangle = (0 \ 1)^T$  eigenstates. The shift between two minima of parabolic bands along  $k_+$  axis is  $Q_+ = 4m\alpha/\hbar^2$ . The shift along  $k_-$  is absent:  $Q_- = 0$ .

The same Hamiltonian 3.4 (as in the rotated basis) emerges in [110] semiconductor quantum wells of zinc-blende structure (GaAs, for example). The uniform eigenstate spin structure of Hamiltonians 3.3 and 3.4 ensures an enhanced spin lifetime [203, 204]. By using this effect, it was suggested to realize a nonballistic spin field effect transistor [205, 206]. Later, the SU(2) symmetry of the Hamiltonian 3.4 was discovered which led to the prediction [202] and the following experimental observation [207, 208] of the *persistent spin helix*, stable in-plane pattern of spin stripes. Interestingly, Ref. [202] interpreted mathematically the persistent spin helix as a "manifestation of a non-Abelian flux in the ground state of the Hamiltonian". We will discuss it in more details in Sec. 3.2.3.

In 2011, following the theoretical proposal of 2009 [209], RDSOC was engineered in an atomic system [210] with the use of ultracold atomic gas of neutral bosonic  $^{87}\text{Rb}$  particles. Two spin states of the ground electronic manifold were used as basis states for a two-level system. By dressing these two states with a pair of lasers, the authors realized the next Hamiltonian:

$$H = \frac{\hbar^2 \mathbf{k}^2}{2m} \sigma_0 + \frac{\Omega}{2} \sigma_z + \frac{\delta}{2} \sigma_y + 2\alpha k_x \sigma_y, \quad 3.5$$

where the first term is the atom kinetic energy with effective mass  $m$ , the second and the third terms play a role of Zeeman magnetic fields along  $z$  and  $y$  axes, respectively, and the last term is the RDSOC. All effective fields can be independently controlled in this system. The same SOC was afterwards realized in fermionic atomic gases [211, 212]. Later, the control over the RDSOC magnitude was achieved through amplitude-modulated Raman coupling of spin states [213]. As a consequence of Dirac-like dispersion structure of Hamiltonian 3.5 near  $\mathbf{k} = 0$ , the *Zitterbewegung* oscillations were observed [214, 215]. In this case, they constitute the synchronized trembling particle motion in real space and spin oscillations due to the interference between eigenstates of the Hamiltonian. Following the theoretical proposals [216, 217], the Spin Hall Effect and spin field effect transistor were realized in atomic gas by utilizing spatial variation of RDSOC while moving along finite-size inhomogeneous Raman laser profile [218]. Various phases of atomic BEC under RDSOC were studied as well [210, 219].

Since RDSOC is essentially a 1D SOC, it is not easy to engineer many different topological phases. Nevertheless, some studies do exist. Two-legs ladder, with each leg playing a role of pseudospin, was studied in tight-binding approximation and its equivalence with the Hofstadter model was claimed [220]. Other works studied an SSH chain with RDSOC, but did not obtain any crucial changes with respect to the conventional SSH [221, 222].

Among photonic systems, the main platform allowing to engineer the RDSOC is a planar microcavity filled with highly birefringent material. These can be the microcavities

filled with liquid crystals [81], organic materials [223, 224, 225], or hybrid microcavities having a combination of liquid crystals and perovskites, for example [226, 227, 228]. While the dispersion of cavities containing the LC is tunable by external voltage, it is not the case for organic materials. With the use of these setups in the RDSOC regime, sometimes in combination with emitting materials, many exciting results have already been obtained, including optical persistent spin helix [229], lasing [230, 224], tunable Berry curvature [231, 227], partially inspired by the theoretical proposal [232], electrical switching of lasing polarization [233], manipulation of exciton-polariton propagation [226], polarized electroluminescence from light emitting diode [225, 234], 1D electrically tunable photonic lattice [235], polariton spin Hall effect [228], Zitterbewegung oscillations [236], polariton stripe phase [237], electrically tunable polariton vortex pairs with locked spin and orbital angular momentum [238], with many of these effects happening in the strong light-matter coupling regime [226, 227, 224, 233, 239, 228, 236, 237, 238].

The tunability of optical LC microcavities can bring us beyond the RDSOC regime, where different physics appear, such as tunable optical spin Hall effect [240], meron polarization textures [241] and tunable exceptional points [242]. We will pay a special attention to this platform and discuss it in more detail in the next Sec. 3.2. The RDSOC was observed as well in photonic metamaterials [243, 244], but has not been extensively studied there.

## 3.2 RDSOC in liquid crystal microcavities

### 3.2.1 Nematic liquid crystal microcavity

A *nematic LC microcavity* is a system where the RDSOC can appear as a dominant contribution to the dispersion [81], contrary to organic materials and perovskites. The scheme of a typical system is shown in Fig. 3.2(a). The microcavity is usually formed by two DBRs. The space between DBRs is filled with nematic LC, and its rotation plane is fixed by an orientation layer deposited on a DBR. In order to achieve electrical control over the LC molecular director orientation, two ITO electrodes are deposited on the outer parts of the DBRs. Depending on the LC used, at zero voltage director can be oriented along  $x$  or along  $z$  axis (see Fig. 3.2(a)). Under applied voltage  $V$ , the director rotates in the  $xz$  plane. In the course of this rotation,  $x$ -polarized mode experiences a continuous change of its refractive index  $n_x(V)$ , while the refractive index of  $y$ -polarized mode  $n_y$  stays unperturbed:

$$n_y = n_o, \quad n_x(V) = \frac{n_o n_e}{\sqrt{n_o^2 \cos^2 \theta(V) + n_e^2 \sin^2 \theta(V)}}, \quad 3.6$$

where  $n_o$  and  $n_e$  are ordinary and extraordinary refractive indices of LC, respectively,  $\theta(V)$  is a voltage-dependent angle of LC director rotation counted from the  $x$  axis. In the spectrum, LC rotation results in the energy change for  $x$ -polarized mode, and constant band structure for  $y$  polarization. If the microcavity is thick enough, the free spectral range of the modes is reduced, and by having big enough anisotropy of the LC one can achieve

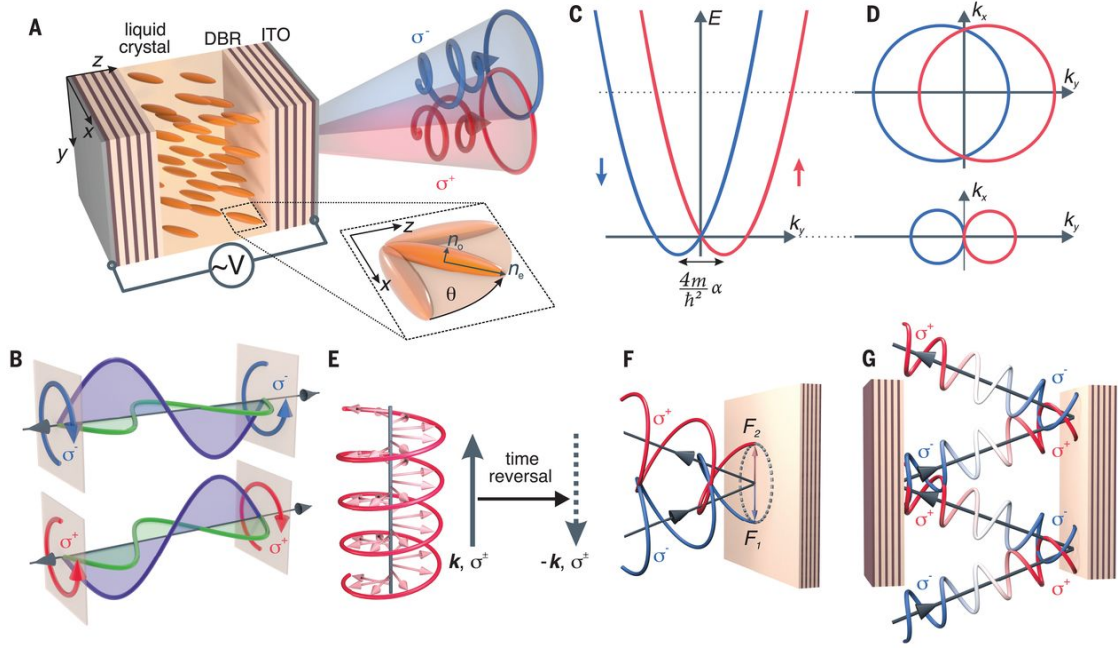


Figure 3.2: **Nematic LC microcavity and photonic RDSOC.** (a) Scheme of nematic LC microcavity; LC director rotates in  $xz$  plane under an applied voltage  $V$ ; (b) eigenmodes of the LC microcavity as a superposition of two linearly polarized standing waves formed by the traveling waves with different phase velocities; (c) dispersion of the Hamiltonian 3.7 for  $k_x = 0$ ; (d) isoenergetic lines of the Hamiltonian 3.7 in  $\mathbf{k}_\perp$  space; (e) TRS transformation of light in free space; (f) circular polarization inversion upon mirror reflection; (g) microcavity bulk acting on the eigenmode as a  $\lambda/2$  waveplate; red (blue) color and notation  $\sigma^+$  ( $\sigma^-$ ) represent the right (left) circular polarization everywhere. Adopted from [81].

the resonant regime between longitudinal modes of different numbers and orthogonal linear polarizations. In the case of a resonance between modes of the *same parity* ( $N$  and  $N$ ,  $N$  and  $N+2$ , etc), the Hamiltonian of the system is often well approximated by TE-TM SOC Hamiltonian 1.14, though an additional mass anisotropy and non-Hermiticity may appear [81, 242].

### 3.2.2 (N,N+1) resonant regime

In the case of a resonance between modes of *different parities* ( $N$  and  $N+1$ ,  $N$  and  $N+3$ , etc), the Hamiltonian of the system is the *RDSOC Hamiltonian* written in the circular polarization basis as:

$$H = \frac{\hbar^2 k_x^2}{2m_x} \sigma_0 + \frac{\hbar^2 k_y^2}{2m_y} \sigma_0 + \mu_x k_x^2 \sigma_x + \mu_y k_y^2 \sigma_x - 2\alpha k_y \sigma_z + \delta \sigma_x, \quad (3.7)$$

where the first two terms are kinetic energy terms with anisotropic masses  $m_x$  and  $m_y$ , the third and fourth terms are polarization-dependent mass differences along  $k_x$  and  $k_y$  due to the mode number difference (see Eq. 1.1), the fifth term is the RDSOC with magnitude  $\alpha$  and aligned along  $k_y$  axis, and the last term is a *linear polarization splitting* between modes  $N_x = N$  and  $N_y = N + 1$  with  $\delta = (E_x - E_y)/2$ . The Rashba-Dresselhaus

parameter  $\alpha$  is a function of the birefringence of the liquid crystal  $\Delta n = n_e - n_o$ , the tilt angle of the liquid crystal director  $\theta(V)$ , and the mode numbers  $N_x$  and  $N_y$  (see more details in SM of [81]). In this Section, we restrict ourselves to the case  $\mu_x = \mu_y = 0$  and  $m_x = m_y = m$ . The Hamiltonian can be obtained rigorously by starting from the Maxwell's equations with the dielectric tensor of LC [81] (see also Ref. [245] for a nice derivation of Hamiltonian 3.7 from the point group symmetry):

$$\varepsilon = \begin{pmatrix} \varepsilon_o \sin^2 \theta + \varepsilon_e \cos^2 \theta & 0 & (\varepsilon_e - \varepsilon_o) \sin \theta \cos \theta \\ 0 & \varepsilon_o & 0 \\ (\varepsilon_e - \varepsilon_o) \sin \theta \cos \theta & 0 & \varepsilon_o \cos^2 \theta + \varepsilon_e \sin^2 \theta \end{pmatrix}, \quad 3.8$$

where  $\varepsilon_o = n_o^2$  and  $\varepsilon_e = n_e^2$  are the main values of the anisotropic dielectric tensor. We will not repeat here the whole derivation, but simply emphasize that the basis used in this derivation and in Eq. 3.7 is:

$$|\pm\rangle = \frac{1}{\sqrt{2}} (|x, N_x\rangle \pm i |y, N_y\rangle), \quad 3.9$$

$$|x, N_x\rangle = \frac{2}{\sqrt{L\varepsilon_x}} \sin\left(\frac{N_x\pi}{L}z\right), \quad |y, N_y\rangle = \frac{2}{\sqrt{L\varepsilon_o}} \sin\left(\frac{N_y\pi}{L}z\right), \quad 3.10$$

where  $\varepsilon_x = n_x^2$  (Eq. 3.6) and  $L$  is the cavity length along  $z$ . By looking at structure of the basis states  $|\pm\rangle$  (Fig. 3.2(b)), one can notice that the polarization of the light is circular (at  $\delta = 0$ ) only at the edges of the cavity, and, consequently, outside of the cavity, while inside it is generally *elliptical*. Since the measurements are usually performed outside of the cavity, the Hamiltonian 3.7 serves perfectly for understanding the dispersion, real space dynamics, polarization distributions, etc. However, once the medium inside the cavity is not uniform, and especially if some additional polarization-dependent composites (such as chiral absorbers, for example) are introduced, the Hamiltonian Eq. 3.7 should be revised.

The dispersion of the Hamiltonian 3.7 for the case of  $\delta = 0$  is shown in Fig. 3.2(c,d). The modes are split along  $k_y$  with already mentioned magnitude of splitting  $Q_y = 4m\alpha/\hbar^2$  (which was introduced as  $Q_+$  in the case of semiconductor electron gas due to the splitting along  $k_+$  direction). The mode shifted positively has a + polarization (right circular), while the mode shifted negatively has a - polarization (left circular). The isoenergetic lines are two circles (in case of  $m = m_x = m_y$ ). The bottom of the dispersion valleys has the energy  $E_0 = -\alpha Q_y/2$ .

A physical explanation why circularly polarized modes are the eigenmodes of the system is suggested in Fig. 3.2(e,f,g). When a circularly polarized light is reflected from the mirror, an inversion of its polarization  $\sigma$  and wavevector component  $k_z$  happens (Fig. 3.2(f)). After the reflection, the light propagates through the cavity which plays a role of  $\lambda/2$  waveplate at any angle of incidence. When light reaches an opposite side of the cavity, the polarization it had before the reflection is restored (Fig. 3.2(g)). Therefore, the process is repetitive and the considered mode is an eigenmode of the system. As underlined before, it has a circular polarization only at the moment of reflection. The presence

of the cavity mixing the modes of opposite  $\sigma$  and  $k_z$  effectively modifies the TRS transformation. In the free space, the TRS transformation for light writes as  $(\mathbf{k}, \sigma) \rightarrow (-\mathbf{k}, \sigma)$  (Fig. 3.2(e)). In the case of cavity modes, it is modified:  $(\mathbf{k}_\perp, k_z, \sigma) \rightarrow (-\mathbf{k}_\perp, k_z, -\sigma)$ , where  $\mathbf{k}_\perp$  is the in-plane wavevector component. Therefore, two eigenmodes of the LC microcavity are TRS partners of each other and the TRS is conserved [81].

Let us now have a closer look at  $\delta \neq 0$  case (Fig. 3.3). Then, the dispersion and the Stokes vector are defined as:

$$E(\mathbf{k}_\perp) = \frac{\hbar^2(k_x^2 + k_y^2)}{2m} \pm \sqrt{4k_y^2\alpha^2 + \delta^2}, \quad 3.11$$

$$\mathbf{S} = \left( \pm \frac{\text{sign}(\delta)}{\sqrt{1 + \eta^2}}, 0, \mp \frac{\eta}{\sqrt{1 + \eta^2}} \right), \quad \eta = \frac{2k_y\alpha}{|\delta|}, \quad 3.12$$

where the upper (lower) sign corresponds to the upper (lower) band. The full dispersion is shown in Fig. 3.3(a), where the color indicates the  $S_z$  component of the pseudospin (Eq. 1.6). Now, the polarizations are mixed by the *detuning term*  $\delta$ . Fig. 3.3 provides a pseudospin structure in reciprocal space for the lower eigenstate of the dispersion. White arrows indicate an in-plane pseudospin component  $\mathbf{S}_\perp = (S_x, S_y)$ , which is induced by  $\delta$ , and, therefore, has uniquely  $S_x \neq 0$ . The color shows  $S_z$  as in panel (a). The dependence of the dispersion  $E(0, k_y)$  on the detuning  $\delta$  is shown in Fig. 3.3(c). With increasing magnitude of detuning  $|\delta|$ , two valleys are continuously approaching each other and finally merge into a single valley typical for a microcavity mode at  $|\delta| = \alpha Q_y$  (grey dashed line in Fig. 3.3(c)). The valley positions are defined as:

$$k_\pm = \pm \sqrt{\left(\frac{2m_y\alpha}{\hbar^2}\right)^2 - \left(\frac{\delta}{2\alpha}\right)^2}, \quad 3.13$$

and, therefore, the  $\delta$ -dependent inter-valley distance is:

$$Q_y(\delta) = k_+ - k_- = \sqrt{Q_y^2 - (\delta/\alpha)^2}, \quad 3.14$$

where  $Q_y$  is actually  $Q_y(0)$ .

The isoenergetic levels of the two-valley dispersion ( $|\delta| = 0.25\alpha Q_y$ ) are depicted in Fig. 3.3(d). The bottom of two valleys (red dots) emerges at

$$E_{min} = E(0, k_\pm) = -\frac{\alpha Q_y}{2} - \frac{\delta^2}{2\alpha Q_y}. \quad 3.15$$

Then the circles near the bottom appear (yellow dots). They are not symmetric as in the  $\delta = 0$  case (Fig. 3.2(d)), so they start to deform (light green dots) until they touch (dark green dots). At this moment, we reach a gap at  $\mathbf{k}_\perp = 0$  (light blue dots), and start to cross the upper band afterwards (dark blue dots). By going further, the isoenergetic lines expand (purple dots) while slowly bending towards the typical circular shape (pink dots).

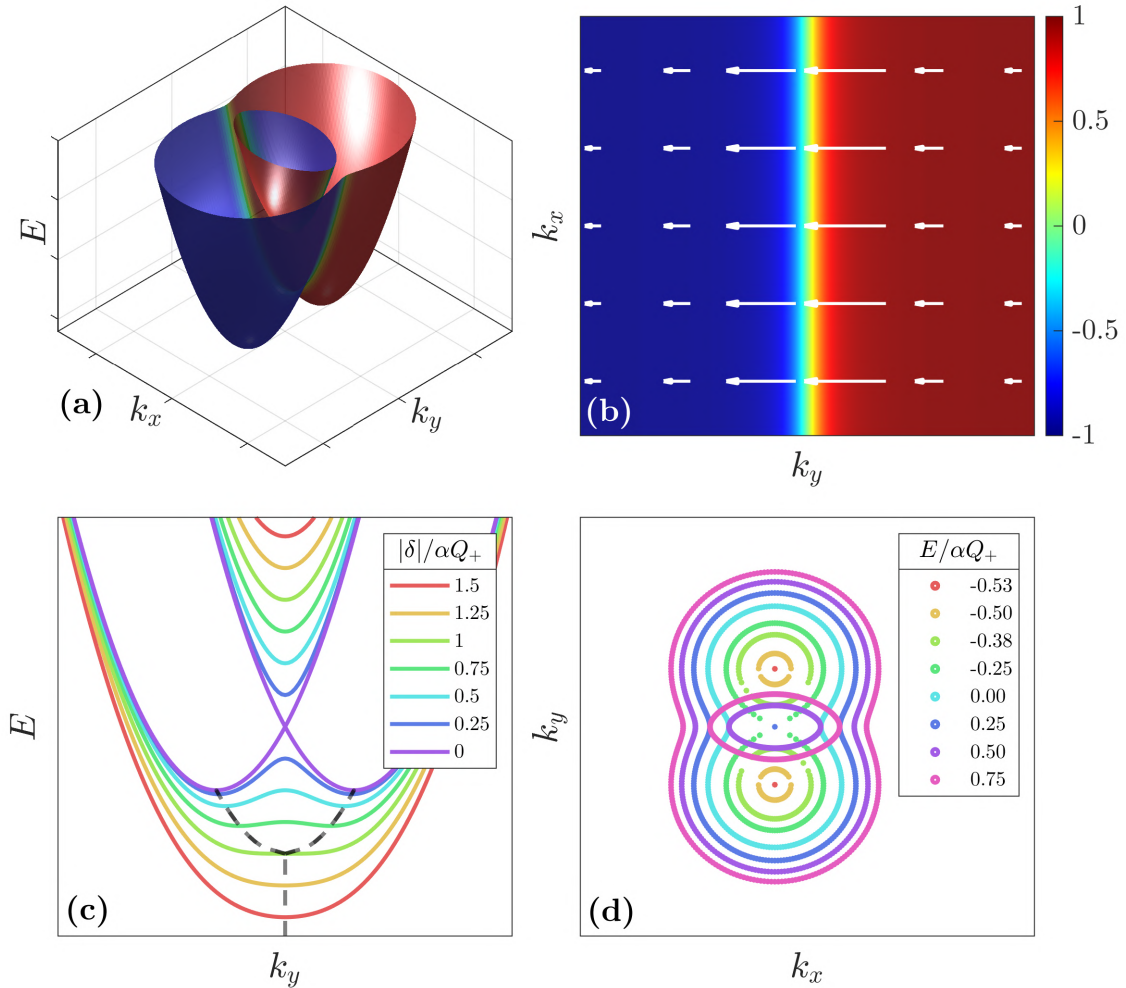


Figure 3.3: **Photonic RDSOC with nonzero detuning.** (a) Full dispersion of Hamiltonian 3.7; color shows  $S_z$  pseudospin component; two bands are split and two polarizations are mixed; (b) the pseudospin  $\mathbf{S}$  components in reciprocal space for the lower energy eigenstate; white lines show in-plane component  $\mathbf{S}_\perp$  while color visualizes the  $S_z$  component; (c) dispersion of Hamiltonian 3.7 along  $k_y$  for several magnitudes of detuning  $|\delta|$  (colored solid lines); dashed black line traces the trajectories of valleys  $k_\pm$  (Eq. 3.13) which merge at  $|\delta| = \alpha Q_y$ ; (d) isoenergetic lines of dispersion of the Hamiltonian 3.7 for several values of energy  $E$  (colored points).

### 3.2.3 Minimal coupling representation

The RDSOC Hamiltonian [3.7](#) can be rewritten in the minimal coupling representation:

$$H = \frac{p_x^2}{2m} \sigma_0 + \frac{(p_y \sigma_0 - A_{RD} \sigma_z)^2}{2m} + \delta \sigma_x + E_0 \sigma_0, \quad 3.16$$

where  $A_{RD} = 2m\alpha/\hbar = \hbar Q_y/2$  is the *vector potential* having opposite signs for different circular polarizations and  $E_0 = E_{min}(\delta = 0) = -\alpha Q_y/2$  (see also Eq. [3.15](#)). In fact, the vector potential  $A_{RD}$  is a *non-Abelian* vector potential forming a  $SU(2)$  field described by the Yang-Mills gauge theory. The Hamiltonian [3.16](#) can be treated in terms of  $SU(2) \times U(1)$  gauge theory unifying the Maxwell field  $U(1)$  governing the effective charge dynamics and Yang-Mills field responsible for pseudospin dynamics [\[246\]](#). The generic Hamiltonian of this theory reads as:

$$H = \frac{1}{2m} (\mathbf{p} - \frac{e}{c} \mathbf{A} - \eta \mathcal{A}^a \sigma^a)^2 + e A_0 + \mathcal{A}_0^a \sigma^a, \quad 3.17$$

where  $\mathbf{p} = \hbar \mathbf{k}$  is the momentum operator,  $A_\mu = (A_0, A_i)$  and  $\mathbb{A}_\mu = \mathcal{A}_\mu^a \sigma^a$  are the 4-vector potentials of Maxwell and Yang-Mills fields, respectively,  $\sigma^\mu = (\sigma^0, \sigma^a)$  is the 4-vector of identity matrix and Pauli matrices,  $e$  and  $\eta$  are quanta of effective charge and pseudospin, respectively, and we can easily assume  $e = \eta = \hbar = c = 1$  without losing generality for further results. Here and in the following in this Section we will utilize greek letters for indexes starting from zero  $\{0,1,2,3\}$  and latin letters for indexes starting from one  $\{1,2,3\}$ . The vector potentials define the field tensors of the Maxwell field  $F_{\mu\nu} = \partial_\mu A_\nu - \partial_\nu A_\mu$  and Yang-Mills field  $\mathbb{F}_{\mu\nu} = \mathcal{F}_{\mu\nu}^a \sigma^a$  with tensor components  $\mathcal{F}_{\mu\nu}^a = \partial_\mu \mathcal{A}_\nu^a - \partial_\nu \mathcal{A}_\mu^a - \varepsilon^{abc} \mathcal{A}_\nu^b \mathcal{A}_\mu^c$ , where  $\varepsilon^{abc}$  is the Levi-Civita symbol.

In the case of Hamiltonian [3.16](#), the non-zero components of vector potentials are:

$$A_0 = E_0, \quad \mathcal{A}_0^1 = \delta, \quad \mathcal{A}_2^3 = A_{RD}. \quad 3.18$$

They produce a single non-zero field tensor component:

$$\mathcal{F}_{20}^2 = -\mathcal{F}_{02}^2 = A_{RD} \delta. \quad 3.19$$

This component is a result of non-commutative nature of  $SU(2)$  group and it does not have any analog in  $U(1)$  gauge theory. We can also introduce a unified current tensor for the charge and spin in order to describe their full dynamics in real space. We first construct a 4-vector velocity operator  $v_\mu = v_\mu^\alpha \sigma^\alpha$  defined by the Heisenberg equation of motion:  $v_\mu = -\frac{i}{\hbar} [x_\mu, H]$ . We define as well the 4-spin operator as  $s^\alpha = \sigma^\alpha$ . In these notations, the unified current tensor is  $\mathbb{J} = J_\mu^\alpha \sigma^\alpha$  with tensor components  $J_\mu^\alpha = \frac{1}{2} \{v_\mu, s^\alpha\}$ , where the curly brackets indicate an anticommutator. In analogy with the continuity equation for charge, we can write a continuity-like equation governing the spin current dynamics:

$$\frac{\partial}{\partial x_\mu} \mathbb{J}_\mu + i [\mathbb{A}^\mu, \mathbb{J}_\mu], \quad 3.20$$

where  $\mathbb{A}^\mu = g^{\mu\nu} \mathbb{A}_\nu$ , and  $g^{\mu\nu}$  is the Minkowski metric tensor.

Finally, in analogy with the Lorentz force  $f_i = J_\mu^0 F_{\mu i} = J_0^0 E_i - \varepsilon_{ijk} J_j^0 B_k$ , where  $E_i$  and  $B_k$  are electric and magnetic fields along  $x_i$  and  $x_k$ , respectively, we can write an expression for the force induced by the Yang-Mills field acting on the spin 4-current:

$$f_i = J_\mu^a \mathcal{F}_{\mu i}^a = J_0^a \mathcal{E}_i^a - \varepsilon_{ijk} J_j^a \mathcal{B}_k^a, \quad 3.21$$

with the electric field  $\mathcal{E}_i^a$  and magnetic  $\mathcal{B}_k^a$  acting on the pseudospin current component  $J^a$  along  $x_i$  and  $x_k$ , respectively.

Now, equipped with this mathematical apparatus, we can discuss what kind of spin dynamics we expect for Hamiltonian 3.16. We will separate the effects originating from different terms. First, let us consider  $\mathcal{A}_0^1$  (see Eq. 3.18) term in the continuity equation Eq. 3.20. We obtain a system of equations:

$$\begin{aligned} \frac{\partial J_0^3}{\partial t} &= 2\delta J_0^2, \\ \frac{\partial J_0^2}{\partial t} &= -2\delta J_0^3. \end{aligned} \quad 3.22$$

This system of equations describes the *pseudospin density precession* in time with frequency  $2\delta$ . Since the effect is produced by  $\delta\sigma_x$  term, the pseudospin rotates around  $S_x$  vector in  $S_{yz}$  plane of the Poincare sphere (Fig. 1.1).

The next term of interest is  $\mathcal{A}_2^3 = A_{RD}$ , which under substitution in Eq. 3.20 results in:

$$\begin{aligned} \frac{\partial J_2^2}{\partial y} &= -2A_{RD} J_2^1, \\ \frac{\partial J_2^1}{\partial y} &= 2A_{RD} J_2^2. \end{aligned} \quad 3.23$$

This system of equations describes the real space oscillations of polarization current along  $y$  axis. The effect is produced by  $A_{RD}\sigma_z$  term of the Hamiltonian 3.16, and, therefore, oscillations happen between linearly polarized currents, in  $S_{xy}$  plane of the Poincare sphere (Fig. 1.1). The period of oscillations in real space is  $2\pi\hbar/2A_{RD} = 2\pi/Q_y$ . This effect is exactly the *persistent spin helix* already mentioned before (see Sec. 3.1). It was observed in a LC microcavity in the RDSOC regime [229, 230].

The last contribution for the dynamics originates from the non-Abelian field component  $\mathcal{F}_{02}^2 = -A_{RD}\delta$ . It produces an effective electric field  $\mathcal{E}_2^2 = -A_{RD}\delta$  for  $S_2$  component of pseudospin which results in the force acting on  $S_2$  along  $y$  axis:

$$f_2 = -A_{RD}\delta J_0^2. \quad 3.24$$

Since the eigenstates of the Hamiltonian 3.16 have  $S_y = 0$  over the whole  $k$  space (see Fig. 3.3(b)), it is impossible to decouple the spin force  $f_2$  Eq. 3.24 and the pseudospin precession Eq. 3.22. The combination of two effects results in the trembling motion of a particle, known as the *Zitterbewegung*, which was predicted for a slightly different configuration of LC microcavity [232], and only recently observed experimentally [236]. Another example of a recent experimental study of a similar non-Abelian gauge field can

be found in Ref. [113]. In Sec. 4.5, we will discuss how to go further and enrich system's physics by spatial variation of its parameters.

### 3.2.4 Cholesteric liquid crystal and optical activity

Another LC phase which will be of importance for this Thesis is a *cholesteric liquid crystal (CLC)*. This phase shows a twist of LC director along a specific direction in space with a spatial period of twist, typically called *pitch*  $p$ , that can vary from hundreds of nm to hundreds of  $\mu\text{m}$ . CLC is typically obtained by doping a nematic phase with a chiral material.

Let us revise the physics of light propagation in CLC. We choose the twist axis along  $z$  and fix the director orientation along  $x$  at  $z = 0$ . Then, the director vector has a form  $\mathbf{n}(\theta) = (\cos \theta, \sin \theta, 0)$ , where  $\theta = q_0 z$  is the director rotation angle in  $xy$  plane, and  $q = 2\pi/p$  is the pitch wavevector. Inside any  $z = \text{const}$  plane the director orientation is, therefore, uniform. The director structure in real space is depicted in Fig. 3.4(a), where the color represents the value of angle  $\theta(z)$ . Since  $\mathbf{n}$  and  $-\mathbf{n}$  are equivalent, the real, physical periodicity of the structure is  $p/2$ . The permittivity tensor in this case has a form:

$$\varepsilon(z) = \frac{\varepsilon_e + \varepsilon_o}{2} \begin{pmatrix} 1 & 0 \\ 0 & 1 \end{pmatrix} + \frac{\varepsilon_e - \varepsilon_o}{2} \begin{pmatrix} \cos 2q_0 z & \sin 2q_0 z \\ \sin 2q_0 z & -\cos 2q_0 z \end{pmatrix}. \quad 3.25$$

By introducing  $\varepsilon_{\pm} = (\varepsilon_e \pm \varepsilon_o)/2$  playing roles of average permittivity and anisotropy, respectively, and by solving the Maxwell's wave equation for the electric field and propagation along  $z$ , one can obtain the following system of equations [247]:

$$\begin{pmatrix} (k_z + q_0)^2 - k_0^2 \varepsilon_+ & -k_0^2 \varepsilon_- \\ -k_0^2 \varepsilon_- & (k_z - q_0)^2 - k_0^2 \varepsilon_+ \end{pmatrix} \begin{pmatrix} a_+ \\ a_- \end{pmatrix} = 0, \quad 3.26$$

where  $k_z$  is the wavevector component along  $z$ ,  $k_0 = \omega/c$ ,  $\omega$  is the wave frequency,  $c$  is the speed of light, and  $a_{\pm}$  are the amplitudes of circularly  $\pm$ -polarized plane waves utilized as the basis:

$$E_{\pm} = a_{\pm} \exp[i(k_z \pm q_0)z - i\omega t]. \quad 3.27$$

In order to have nontrivial solutions, the determinant of matrix in Eq. 3.26 has to be equal zero, which gives us a bi-quadratic equation for the dispersion  $\omega(k_z)$ :

$$(q_0^2 + k_z^2 - \varepsilon_+ k_0^2)^2 - 4q_0^2 k_z^2 - \varepsilon_-^2 k_0^4 = 0. \quad 3.28$$

By imposing  $\omega > 0$ , we draw two dispersion branches of Eq. 3.28 in Fig. 3.4(c). We are especially interested in the polarization texture of the eigenmodes. The Stokes vector can be written as:

$$\mathbf{S} = \left( S_{\perp} \cos 2q_0 z, S_{\perp} \sin 2q_0 z, \mp \frac{\eta}{\sqrt{1 + \eta^2}} \right), \quad S_{\perp} = \pm \frac{1}{\sqrt{1 + \eta^2}}, \quad \eta = \frac{2q_0 k_z}{k_0^2 \varepsilon_-}. \quad 3.29$$

It turns out, that there are two drastically different regimes for  $\mathbf{S}$ . At  $k_z \rightarrow 0$  and  $k_z \rightarrow \infty$  the eigenmodes are linearly polarized  $S_z = 0$ ,  $S_{\perp} \neq 0$ . This regime is called

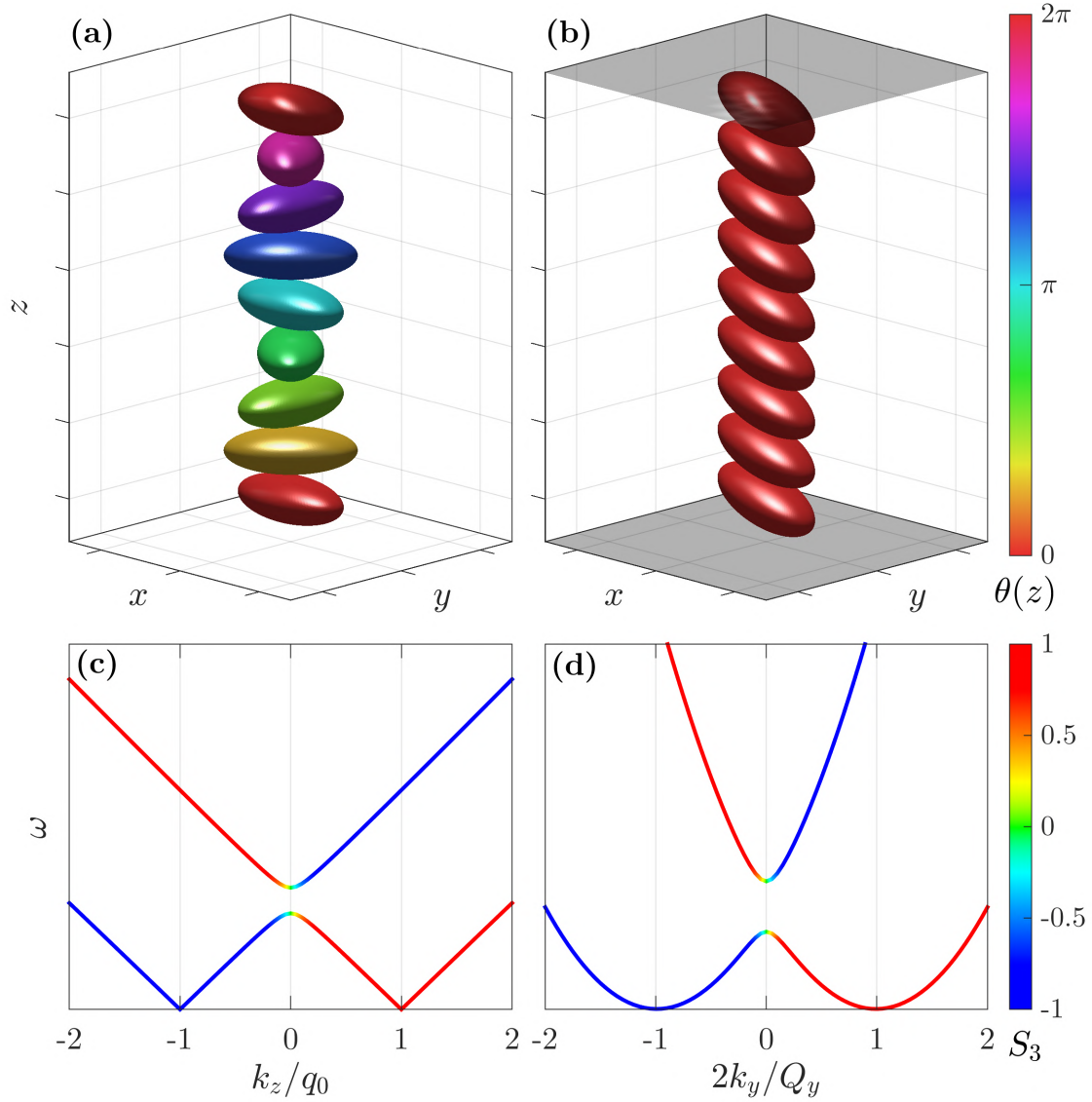


Figure 3.4: **Dispersion of CLC and RDSOC Hamiltonian.** (a) CLC aligned along  $z$  axis; the rotation of molecular director happens in  $xy$  plane and the angle of rotation  $\theta(z)$  is shown by the color; (b) nematic LC microcavity in the RDSOC regime; the director orientation is uniform over the space and obtained by rotation in  $xz$  plane; two black planes symbolize the microcavity mirrors; dispersion of (c) CLC and (d) nematic LC in the RDSOC regime; color depicts the circular polarization degree  $S_3$ ; an apparent similarity arises at low wavevectors, both for polarization and bands.

*Mauguin regime* and it is characterized by *waveguiding* of the eigenmodes by local director orientation: at each  $z$  plane, the orientation of the 1st (2nd) eigenmode linear polarization is parallel (perpendicular) to the director orientation, and, therefore, it propagates with  $n_e$  ( $n_o$ ) effective refractive index. The difference The gap between two bands at  $k_z = 0$  is defined by modes refractive indices as:  $\omega_+(0) = cq_0/n_o$ ,  $\omega_-(0) = cq_0/n_e$ .

Another regime emerges when  $\eta \rightarrow \infty$ . In real materials it covers a large range of frequencies since often  $\varepsilon_- \ll 1$ . In this regime, the polarization of eigenmodes is predominantly circular:  $S_z \approx \pm 1$ ,  $S_\perp \approx 0$ . Under these conditions, an incoming linearly polarized wave will quickly rotate, analogously to what happens in optically active materials. Therefore, this regime can be called *optically active regime*. The rotation angle  $\zeta$  for incoming linearly polarized light at frequency  $\omega$  is defined by effective refractive indices  $n_{1,2}$  of circular polarized eigenmodes as:

$$\zeta = \frac{1}{2}k_0(n_1 - n_2)d = \frac{\varepsilon_-^2 k_0^4}{8q_0(\varepsilon_+ k_0^2 - q_0^2)}, \quad k_0 n_{1,2} = k_z^{1,2} \mp q_0, \quad 3.30$$

where  $k_z^{1,2} = k_z(\omega)$  are two roots of the same group velocity of Eq. 3.28, and  $d$  is a light propagation distance. The full polarization structure of the eigenmodes is shown in Fig. 3.4(c), where color depicts  $S_z$  Stokes parameter (high  $k_z$  values characterized by linearly polarized eigenmodes are not shown).

In one of the first papers investigating the photonic RDSOC [223] the analogy has been drawn between RDSOC and optical activity. Indeed, as we discussed already, under RDSOC the rotation of polarization happens for the light propagating in microcavity plane along the direction of RDSOC  $k_y$ . We utilized the term persistent spin helix to describe this effect, however, this term is better suitable for electronics, and, especially, spintronics, where the spin control makes a central interest. In our case, the term *emergent optical activity* is a better fit, since it underlines the optical nature of the system, and at the same time points out that the system does not contain any optically active materials, and the effect *emerges* as a result of an interplay between material linear birefringence and cavity confinement.

A final remark can be done after comparing the band and eigenstate polarization structures for CLC and nematic LC microcavity in the RDSOC regime (compare left and right columns in Fig. 3.4). First of all, the polarization structures of the eigenstates demonstrate a pronounced similarity (compare also Eq. 3.29 and Eq. 3.12), except for the region of large  $k_z$  ( $k_y$ ) where we expect the difference (not shown in Fig. 3.4(c,d)). Also, the bands itself are quite similar at  $k_z < q_0$  ( $k_y < Q_y/2$ ) where the dispersion resembles the one of the massive Dirac Hamiltonian. This likeness implies that the RDSOC effective Hamiltonian 3.7 can be used in order to describe the CLC eigenmodes at low wavevectors  $k_z < q_0$ . This allows to facilitate the analytical analysis of CLC modes due to the pronounced simplicity of RDSOC mathematical description. It also allows us to apply all our knowledge about RDSOC while studying a novel, before unexplored system. We will utilize this analogy in Sec. 4.4 in order to explain the band and polarization structures of CLC microcavity in the *uniformly lying helix* configuration.





Results



**Contents**

---

<b>4.1 RDSOC in tight-binding approximation</b> . . . . .	<b>66</b>
<b>4.2 SSH topology control</b> . . . . .	<b>67</b>
4.2.1 Tight-binding model . . . . .	67
4.2.2 Reduced model and topological transition . . . . .	69
4.2.3 Topology switching in continuous realistic photonic model . . . . .	71
4.2.4 Period doubling in both models . . . . .	74
<b>4.3 Continuous tunneling control between individual sites</b> . . . . .	<b>76</b>
4.3.1 General idea . . . . .	76
4.3.2 Realization in nematic liquid crystal microcavity . . . . .	78
4.3.3 <i>sp</i> coupling by RDSOC on a single site . . . . .	80
4.3.4 Tunneling control between two sites mediated by RDSOC . . . . .	82
4.3.5 Tunneling inversion and topological transition . . . . .	84
4.3.6 Discussion . . . . .	85
<b>4.4 1D tunable lattice in cholesteric liquid crystal microcavity</b> . . . . .	<b>85</b>
4.4.1 Microcavity scheme . . . . .	86
4.4.2 CLC-induced photonic 1D potential . . . . .	86
4.4.3 CLC-induced photonic spin-orbit coupling . . . . .	90
4.4.4 Spin-orbit coupling approximation by RDSOC . . . . .	91
<b>4.5 Perspectives for 2D lattice models</b> . . . . .	<b>93</b>
4.5.1 HH model in tunneling phase control regime . . . . .	94
4.5.2 XY Hamiltonian in tunneling amplitude control regime . . . . .	95
<b>4.6 1D non-Hermitian models with RDSOC</b> . . . . .	<b>96</b>
4.6.1 Hatano-Nelson tight-binding model . . . . .	96
4.6.2 Non-Hermitian SSH tight-binding model . . . . .	100
4.6.3 NHSE in continuous realistic photonic model . . . . .	101
4.6.4 NHSE in continuous realistic electronic model . . . . .	104

---

In this chapter, we study in detail the lattice effects stemming from the RDSOC. We start with the discussion of RDSOC in tight-binding approximation in Sec. 4.1. We demonstrate how to control the topology of an SSH chain by RDSOC and we suggest a realistic realization of this effect in a nematic LC microcavity in Sec. 4.2. Next, we discuss how to control the tunneling between individual lattice sites in Sec. 4.3. The tunneling control was already realized experimentally in a nematic LC microcavity by our colleagues from IBM Research–Zurich and University of Warsaw, with the samples produced in the Warsaw Military University of Technology. We then turn to the discussion of 1D tunable lattices in CLC microcavities in Sec. 4.4. We suggest 2D lattice models for further studies and experimental realization in Sec. 4.5. Finally, we study non-Hermitian 1D models with RDSOC in Sec. 4.6, including HN and non-Hermitian SSH models in tight-binding approximation, and possible NHSE realizations in photonic and electronic settings.

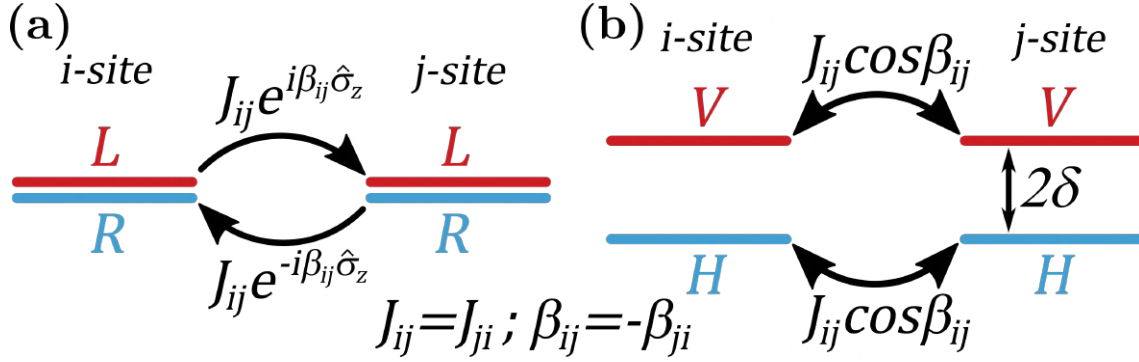


Figure 4.1: **Tunneling phase and amplitude control.** Regimes of (a) tunneling phase control ( $\delta \approx 0$ ) and (b) tunneling amplitude control (large  $\delta$ ).

#### 4.1 RDSOC in tight-binding approximation

As was mentioned earlier, the RDSOC Hamiltonian can be represented in the minimal coupling form Eq. 2.1, where RDSOC itself plays a role of *non-Abelian vector potential* (Eq. 3.18). In this case, the transformation from continuous Hamiltonian to tight-binding approximation can be done with the use of *Peierls substitution* [248]. Let us consider the coupling between two sites  $i$  and  $j$ , each hosting (pseudo)-spin-1/2 particles. We will use further the terminology from photonics when speaking about spin degree of freedom. If a link between sites has an angle  $\theta_{ij}$  with respect to the RDSOC direction, two circular polarizations (eigenmodes of  $\hat{\sigma}_z$ ) acquire opposite Peierls, or Aharonov-Bohm, phases  $\pm\beta_{ij}(\theta_{ij})$  while propagating along the link:

$$\beta_{ij}(\theta_{ij}) = \frac{\alpha_{ij}d_{ij}}{\hbar^2/2m} \cos \theta_{ij}, \quad 4.1$$

where  $d_{ij}$  is the link length,  $\alpha_{ij}$  is the RDSOC magnitude at the position of  $ij$  link,  $m$  is the particle effective mass, and  $\beta_{ij} = -\beta_{ji}$ . We will call  $\beta_{ij}$  the *RDSOC phase*. Therefore, the RDSOC Hamiltonian 2.1 of an arbitrary lattice in tight-binding approximation can be written as:

$$H_{lattice} = \sum_{i,j} J_{ij} e^{i\beta_{ij}\sigma_z} a_j^\dagger a_i + \sum_i \delta\sigma_x a_i^\dagger a_i, \quad 4.2$$

where  $a_i$  ( $a_i^\dagger$ ) is an annihilation (creation) operator for a particle at lattice site  $i$ , and  $J_{ij}$  is the tunneling coefficient between lattice sites  $i$  and  $j$ . By decoupling circular polarizations ( $\delta = 0$ ), one can control the tunneling phases of individual couplings using the RDSOC, if we assume that one can vary RDSOC amplitude  $\alpha_{ij}$  or direction  $\theta_{ij}$  at individual couplings. Therefore, the regime of absent or small  $\delta$  (with respect to  $|J_{ij}|$ ) can be called a *phase control regime* (Fig. 4.1(a)).

By going in the opposite limit of big  $\delta$  (in comparison with  $|J_{ij}|$ ), one obtains the eigenstates almost identical to *HV*-polarized eigenstates of  $\sigma_x$ . Therefore, it is useful to rewrite the generic Hamiltonian 4.2 in the *HV* basis:

$$H_{lattice} = \sum_{i,j} J_{ij} (\sigma_0 \cos \beta_{ij} + i\sigma_x \sin \beta_{ij}) a_j^\dagger a_i + \sum_i \delta\sigma_z a_i^\dagger a_i. \quad 4.3$$

As one can notice, the co-polarized tunneling is now proportional to  $\cos \beta_{ij}$ , contrary to  $e^{\pm i\beta_{ij}}$  in the phase control regime. It means, that by varying RDSOC amplitude  $\alpha_{ij}$  or direction  $\theta_{ij}$ , one now controls the tunneling amplitude of the individual couplings instead of phases. Therefore, we can call this limit the *amplitude control regime*. In order to verify and clarify this result, we can write an effective Hamiltonian for a single polarization in the perturbation theory *up to the 2nd order*. If we focus on  $V$  polarization, with energy  $\approx -\delta$ , then the effective Hamiltonian writes as:

$$H_{lattice,eff} = \sum_i -\delta a_i^\dagger a_i + \sum_{i,j} J_{ij} \cos \beta_{ij} a_j^\dagger a_i + \sum_{i,j,m} \frac{J_{im} J_{mj} \sin \beta_{im} \sin \beta_{mj}}{2\delta} a_j^\dagger a_i, \quad 4.4$$

where Pauli matrices are absent because we got rid of polarization degree of freedom by choosing a single  $V$  polarization. From Hamiltonian 4.4 it is evident that the co-polarized term of Eq. 4.3  $J_{ij} \cos \beta_{ij}$  contributes to the direct tunneling, while the cross-polarized term  $J_{ij} \sin \beta_{ij}$  contributes to a smaller order indirect (through the third site) tunneling change and the on-site energy shift. From the point of view of lattice engineering, both phase and amplitude control regimes are valuable, since some lattice models require phase control (Harper-Hofstadter model, for example) and other require amplitude control (SSH, for example).

## 4.2 SSH topology control

In this Section, we utilize the amplitude control regime in order to modify tunneling coefficients of the SSH model. Since the topological transition in an SSH happens when staggered tunnelings are balanced (see Sec. 2.3.1 and especially Fig. 2.1), the possibility of changing the ratio between the tunnelings via the RDSOC, allows us to suggest a reconfigurable SSH model.

### 4.2.1 Tight-binding model

The system which we consider is an SSH chain with a period  $d$ , shown in Fig. 4.2(a). Since normally RDSOC direction is uniform in real space in physical systems, we achieve the staggering between angles  $\theta_{ij}$  ( $\theta_1$  and  $\theta_2$ ) along the chain by zigzag geometry. These angles control the RDSOC phases  $\beta_1$  and  $\beta_2$  according to Eq. 4.1. The unit cell consists of two lattice sites  $A$  and  $B$ . Therefore, the generic Hamiltonian 4.2 reduces in  $k$ -space to a  $4 \times 4$  Hamiltonian which in the basis  $(|A_+\rangle |A_-\rangle |B_+\rangle |B_-\rangle)^T$  reads as:

$$H_{\sigma SSH}(k_x) = \begin{pmatrix} 0 & \delta & J_1 e^{i\beta_1} + J_2 e^{-i\beta_2} e^{-ik_x d} & 0 \\ \delta & 0 & 0 & J_1 e^{-i\beta_1} + J_2 e^{i\beta_2} e^{-ik_x d} \\ c.c. & 0 & 0 & \delta \\ 0 & c.c. & \delta & 0 \end{pmatrix}, \quad 4.5$$

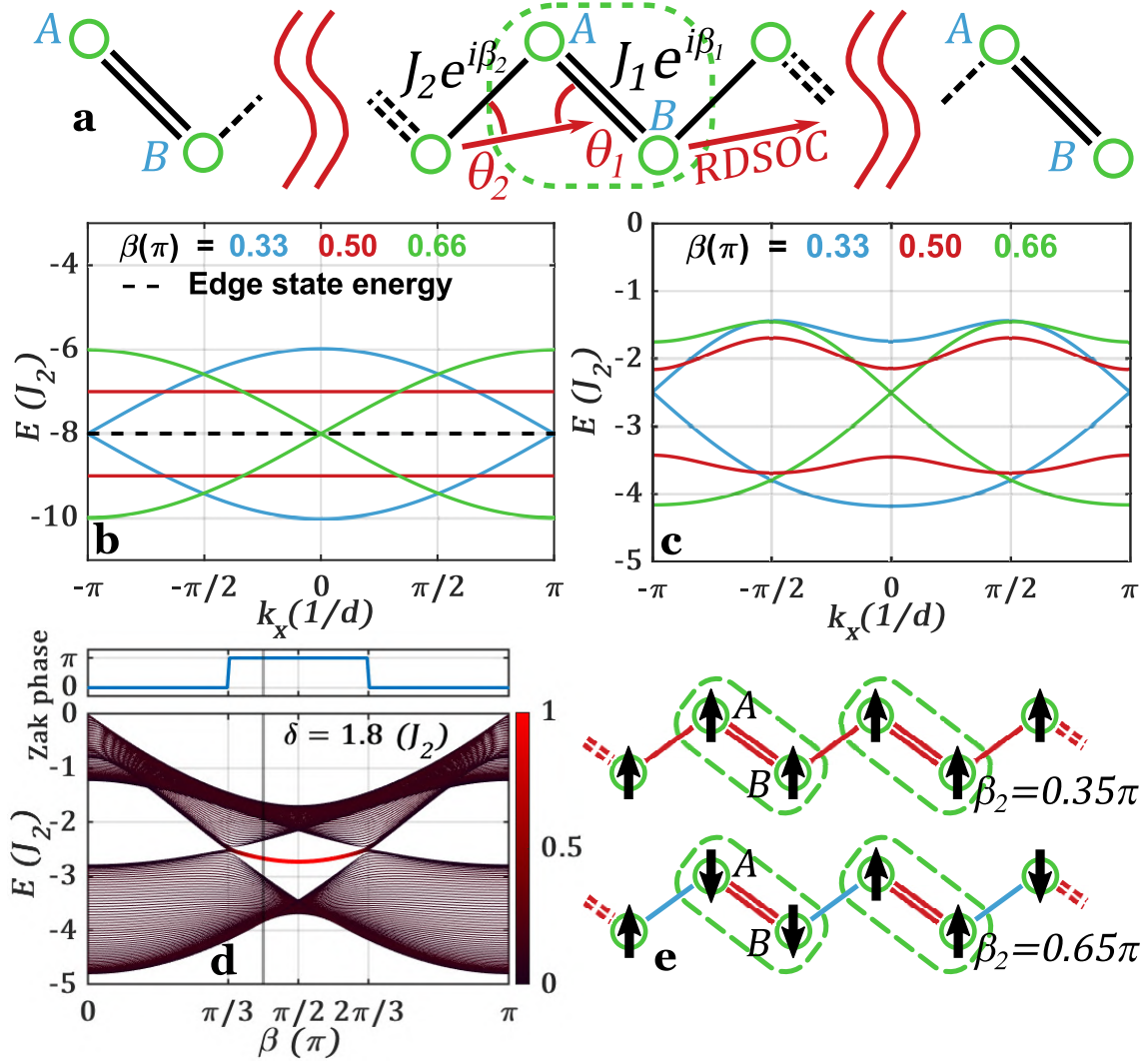


Figure 4.2: **Topology control in SSH with RDSOC.** (a) The scheme of SSH chain with RDSOC; RDSOC is uniform in space and staggering of the RDSOC phases  $\beta_{1,2}$  is achieved through zigzag geometry; the dispersion of (b) reduced Hamiltonian (Eq. 4.9,  $\delta = 8$ ) and (c) general spinful SSH Hamiltonian (Eq. 4.6,  $\delta = 1.8$ ) with staggered RDSOC for several values of  $\beta$  (for all values of  $\beta$  see SM Movie in [248]); (d) energy spectrum of a finite SSH chain and Zak phase of the corresponding bulk dispersion lowest band depending on the RDSOC phase  $\beta$  (the colorscale shows the edge localization); (e) SSH chain corresponding to ferro- (top) and antiferromagnetic (bottom) phases of TFIM: black arrows correspond to the ground state spin distribution; red (blue) lines show positive (negative) tunneling amplitudes.

where *c.c.* stands for a complex conjugate. Since we would like to study the big- $\delta$  limit, it is useful again to transform the Hamiltonian [4.5](#) into *HV* basis ( $|A_H\rangle |A_V\rangle |B_H\rangle |B_V\rangle$ )<sup>T</sup>:

$$H_{\sigma SSH}(k_x) = \begin{pmatrix} \delta & 0 & c_1 & ic_2 \\ 0 & -\delta & ic_2 & c_1 \\ c_1^* & -ic_2^* & \delta & 0 \\ -ic_2^* & c_1^* & 0 & -\delta \end{pmatrix}, \quad (4.6)$$

$$c_1 = \rho_1 e^{i\varphi_1} = J_1 \cos \beta_1 + J_2 \cos \beta_2 \cdot e^{-ik_x d},$$

$$c_2 = \rho_2 e^{i\varphi_2} = J_1 \sin \beta_1 - J_2 \sin \beta_2 \cdot e^{-ik_x d},$$

with the co-polarized and cross-polarized tunnelings  $c_1$  and  $c_2$  in the *HV* basis, respectively. The spectrum of the Hamiltonian [4.6](#) is then easily written using these notations:

$$E(k_x) = \pm \left[ \delta^2 + \rho_1^2 + \rho_2^2 \pm 2\rho_1 \sqrt{\delta^2 + \rho_2^2 \sin^2(\varphi_2 - \varphi_1)} \right]^{1/2}. \quad (4.7)$$

The four bands of the system are separated in two pairs, symmetric with respect to  $E = 0$  because of the CS of the model:

$$\Gamma H^\dagger(k_x) \Gamma^{-1} = -H(k_x), \quad \Gamma = s_z \otimes \sigma_0, \quad (4.8)$$

where  $s_z$  is the third Pauli matrix acting in the pseudospin subspace.

## 4.2.2 Reduced model and topological transition

If  $\delta \gg J_1, J_2$ , it is possible to use the effective Hamiltonian [4.4](#). In that case each pair of modes (upper and lower) is *H*- and *V*-polarized and described by a standard SSH Hamiltonian (up to the 1st order of perturbation theory) which for the lower *V*-polarized pair reads:

$$H_{SSH}(k_x) \approx \begin{pmatrix} -\delta & J_1 \cos \beta_1 + J_2 \cos \beta_2 e^{-ik_x d} \\ c.c. & -\delta \end{pmatrix}. \quad (4.9)$$

Thus, RDSOC modulates the tunneling amplitudes as  $J'_1 = J_1 \cos \beta_1$  and  $J'_2 = J_2 \cos \beta_2$ . Consequently, it allows, for example, to transform a monomer chain ( $J_1 = J_2$ ) into a dimer chain ( $J'_1 \neq J'_2$ ), or to swap the ratio between the tunnelings ( $J'_1/J'_2 > 1 \rightarrow J'_1/J'_2 < 1$ ), thereby, changing the chain topology, characterized by the Zak phase (Eq. [2.11](#)). In the spinless SSH [2.2](#), edge states exist if  $|J_1| < |J_2|$  (chain ending with a weak link). With RDSOC, the topology is nontrivial when:

$$|J_1 \cos \beta_1| < |J_2 \cos \beta_2|. \quad (4.10)$$

It turns out, that the condition [4.10](#) is valid in the general case of Eq. [4.6](#) and not only for high  $\delta$  Eq. [4.9](#). A topological transition occurs when  $J_1 \cos \beta_1 = \pm J_2 \cos \beta_2$ , which corresponds to the closing of the lowest gap in Eq. [4.7](#) ( $\rho_1 = 0$ ).  $J_1 \cos \beta_1 = J_2 \cos \beta_2$  case corresponds to a gap closing at the edges of the BZ ( $k_x = \pm\pi/d$ ), analogously to the spinless SSH, whereas  $J_1 \cos \beta_1 = -J_2 \cos \beta_2$  case corresponds to a gap closing at  $k_x = 0$ .

If a spinless SSH chain is topologically trivial ( $|J_1| > |J_2|$ ), the same chain with modulated RDSOC could be either nontrivial ( $|J'_1| < |J'_2|$ ) or trivial ( $|J'_1| > |J'_2|$ ), depending on the values of  $\beta_1$  and  $\beta_2$ .

For clarity of the analysis let us choose  $\beta_2 = 0$  and  $\beta_1 = \beta$ . Physically, this corresponds to a zigzag chain with  $90^\circ$  angle between neighboring links, and the RDSOC aligned parallel to one of these links. Fig. 4.2(b) shows the energy bands computed in the large- $\delta$  limit for the strong link  $J_1 = 2$  and weak link  $J_2 = 1$  and different values of  $\beta$ . It is worth to remark that we apply the notions of "strong" and "weak" links for an SSH chain without RDSOC. When RDSOC is present, physical tunnelings are  $J'_1$  and  $J'_2$ , and their relative strength can change according to the 4.10. The critical  $\beta$  values for which the band topology is changing are  $\pi/3$  and  $2\pi/3$  which corresponds to a gap closing at  $k_x = \pm\pi/d$  and  $k_x = 0$ , respectively. At these values, the ratio between genuine tunneling amplitudes of the system  $J'_1$  and  $J'_2$  crosses 1. In between these  $\beta$  values, a topological band gap is opened. The edge states lie in the middle of this gap because the reduced  $2 \times 2$  Hamiltonian 4.9 is equivalent to the spinless SSH, and, therefore, preserves the CS. Precisely at  $\beta = \pi/2$ , the RDSOC completely suppresses the co-polarized tunneling through the strong link  $J_1$ . The corresponding band gap reaches its maximum value  $2J_2$  and the bands are completely flat.

Fig. 4.2(c) shows the finite  $\delta$  case, where all four bands have to be taken into account (all parameters except  $\delta$  are the same as for Fig. 4.2(b)). For any  $\delta$ , the gap is again closing at  $k_x = \pm\pi/d$  for  $\beta = \pi/3$  and at  $k_x = 0$  for  $\beta = 2\pi/3$ . The maximal gap value is still at  $\beta = \pi/2$ , but it is smaller than  $2J_2$ . There is no symmetry within the spectrum of a single bands pair and the edge states are not at the center of the gap. All these features are summarized in Fig. 4.2(d) showing the energy spectrum versus  $\beta$  and the corresponding Zak phase of a finite chain. A trivial gap (zero Zak phase) is present from  $\beta = 0$  to  $\beta = \pi/3$  where the gap closes, then immediately reopens as a topological gap persisting for  $\beta \in [\pi/3; 2\pi/3]$  (color demonstrates the edge localization degree as in Eq. 2.3). The gap closes at  $\beta = 2\pi/3$  becoming topologically trivial again. For  $\delta < |J_1 \cos \beta|$ , the bands are overlapping in energy (not crossing). There is no real gap anymore, and therefore no protected edge states.

Another interesting possibility offered by the tuning of tunneling amplitudes is the implementation of the mapping between the Hamiltonian 4.9 and the *transverse-field Ising model* (TFIM) – the fundamental quantum many-body model describing the transition between ordered (ferro- or antiferromagnetic) and disordered (paramagnetic) phases [249, 250]. The TFIM Hamiltonian reads as:

$$H_{TFIM} = -J \sum_i \sigma_i^z \sigma_{i+1}^z - h \sum_i \sigma_i^x, \quad 4.11$$

where  $J$  is a coupling term,  $h$  is a transverse magnetic field and  $i$  is the site index. After applying the Jordan-Wigner transformation [251], the mapping between Hamiltonians 4.9 and 4.11 is:  $J = J_2 \cos \beta_2$ ,  $h = J_1 \cos \beta_1$ . As shown in Fig. 4.2(e), where the spin orientation on each site is given by the on-site phase of the wavefunction, the sign modulation of tunneling amplitudes provided by the RDSOC allows to achieve both ferro- and anti-

ferromagnetic configurations which is not the case in TFIM based on usual SSH. Thus, tunneling amplitude modulation by RDSOC gives access to the whole variety of TFIM configurations.

### 4.2.3 Topology switching in continuous realistic photonic model

Next, we turn to the discussion of realistic realization of SSH topology control (Eq. 4.10) based on a nematic LC microcavity with DBR patterning [252] which realises an in-plane potential. The zigzag SSH potential  $U(\mathbf{r})$  (equivalent for both pseudospins and defined in 2D real space  $\mathbf{r} = (x, y)$ ) is constructed out of Gaussian potential wells with 30 meV depth, 1  $\mu\text{m}$  FWHM and 1.53 (1.7)  $\mu\text{m}$  intra-cell (inter-cell) distance, respectively. The potential is shown in Fig. 4.3(a) with the RDSOC being oriented along the strong link of the zigzag chain. We perform a simulation beyond the tight-binding approximation by solving the stationary spinor Schrödinger equation with 2D Hamiltonian:

$$H_{2D} = -\frac{\hbar^2 \nabla_{\mathbf{r}}^2}{2m} \sigma_0 + 2i\alpha \frac{\partial}{\partial x} \sigma_z + \delta \sigma_x + U(\mathbf{r}) \sigma_0. \quad 4.12$$

The parameters of the simulation are typical for a nematic LC microcavity: the cavity photon mass  $m = 1.6 \cdot 10^{-5} m_e$ , where  $m_e$  is the free electron mass, the linear splitting  $\delta = 5.5$  meV, and Lorentzian broadening of states 0.5 meV in full-width half-maximum.

Fig. 4.3(c,e) shows the modes in the real and reciprocal spaces without RDSOC. The chain exhibits a clear band gap of 1 meV, but no edge states. Fig. 4.3(d,f) shows the case with non-zero RDSOC ( $\alpha = 1.62$  meV $\cdot\mu\text{m}$ ). A mode strongly localized on the edge appears within the gap (also see Fig. 4.3(b)). The asymmetry between the lower and upper bands is enhanced when going beyond the tight-binding model. However, the lowest band is flattened analogously to  $\beta = \pi/2$  case in the tight-binding model (Fig. 4.2(b,c,d)). In the experiment, the transition between two cases happens when one applies voltage, and, therefore, modifies  $\delta$ . In the case of ( $N, N$ ) mode resonance, the RDSOC is effectively zero, while in the case of modes  $N$  and  $N + 1$  close to the resonance, it has non-zero value. Therefore, by going from one resonant regime to another we can *switch the topology* of the model. The condition 4.10 does not depend on  $\delta$ , therefore, it does not allow to predict a continuous transition between different topological phases with changing  $\delta$  (voltage). However, we will discuss in Sec. 4.3 how to obtain a  $\delta$ -dependence and perform a similar continuous transition.

We extend our analysis and study how the TE-TM SOC (Sec. 1.1.4) affects the edge states. As we stated already in Sec. 1.1, TE-TM SOC is almost inevitable in DBR microcavities, therefore, it is natural to verify that its contribution does not destroy the nontrivial topology of the system. The extended Hamiltonian 4.12 with TE-TM SOC reads:

$$H_{2D}^{ext} = -\frac{\hbar^2 \nabla_{\mathbf{r}}^2}{2m} \sigma_0 + 2i\alpha \frac{\partial}{\partial x} \sigma_z + \delta \sigma_x - \gamma \left( \frac{\partial^2}{\partial x^2} - \frac{\partial^2}{\partial y^2} \right) \sigma_x - 2\gamma \frac{\partial^2}{\partial x \partial y} \sigma_y + U(\mathbf{r}) \sigma_0, \quad 4.13$$

where  $\gamma = \frac{\hbar^2}{2m} \gamma'$  is the TE-TM SOC magnitude. Fig. 4.4 demonstrates the band structure

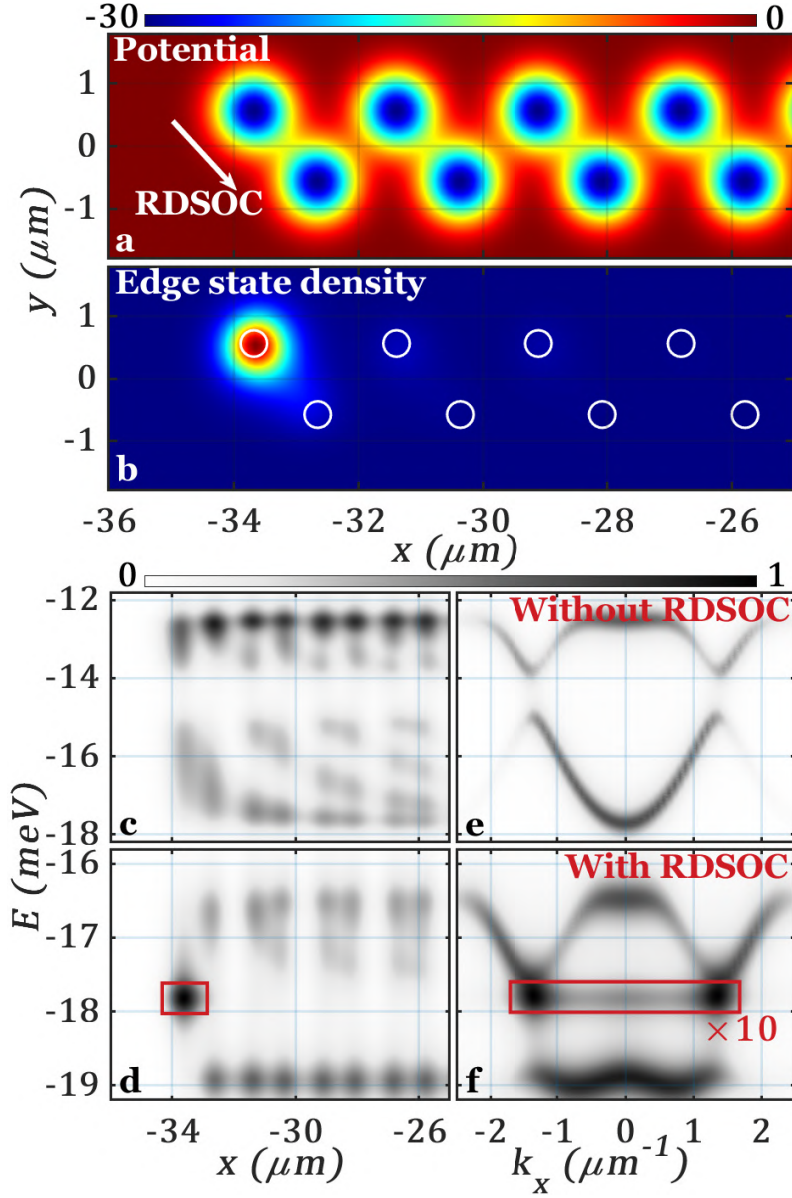


Figure 4.3: *SSH topology switching in a nematic LC microcavity.* (a) 2D zigzag SSH potential (in meV) constructed out of Gaussian wells with RDSOC aligned along strong link; (b) normalized edge state density; energy spectrum in real (c,d) and reciprocal (e,f) space in the absence (c,e) and presence (d,f) of RDSOC; the red rectangular highlights the edge state (in (f) intensity of the edge state is increased by 10x for visibility).

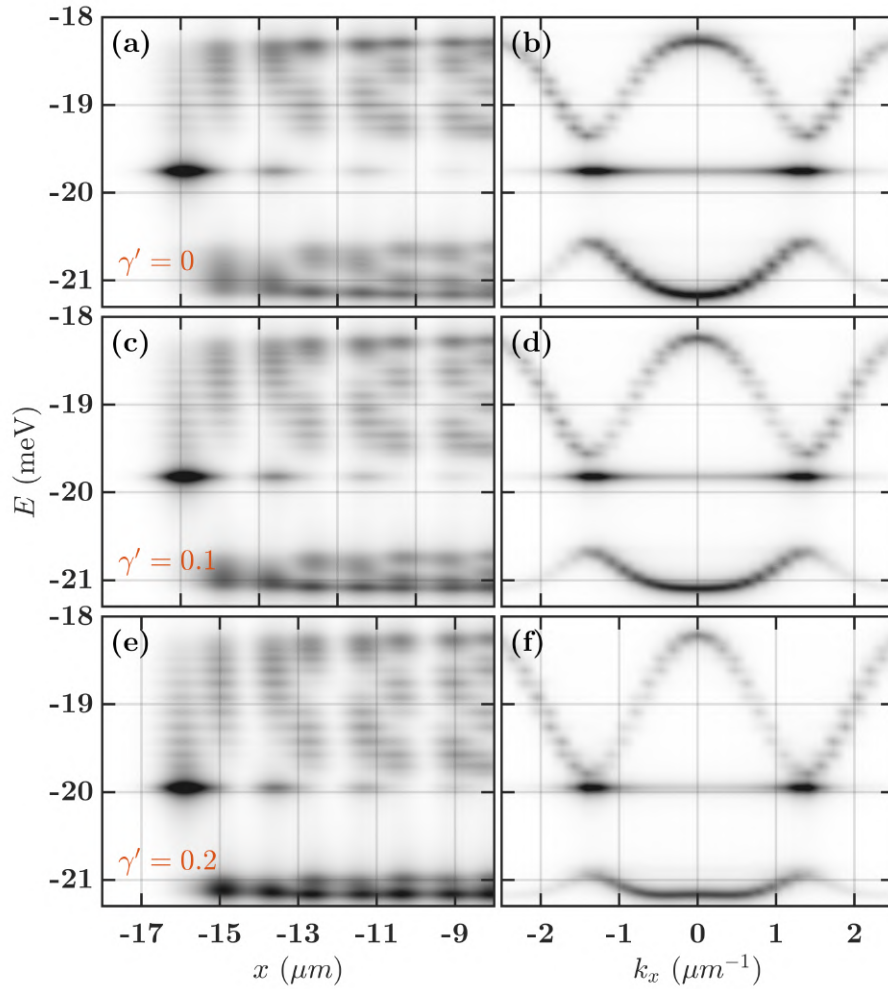
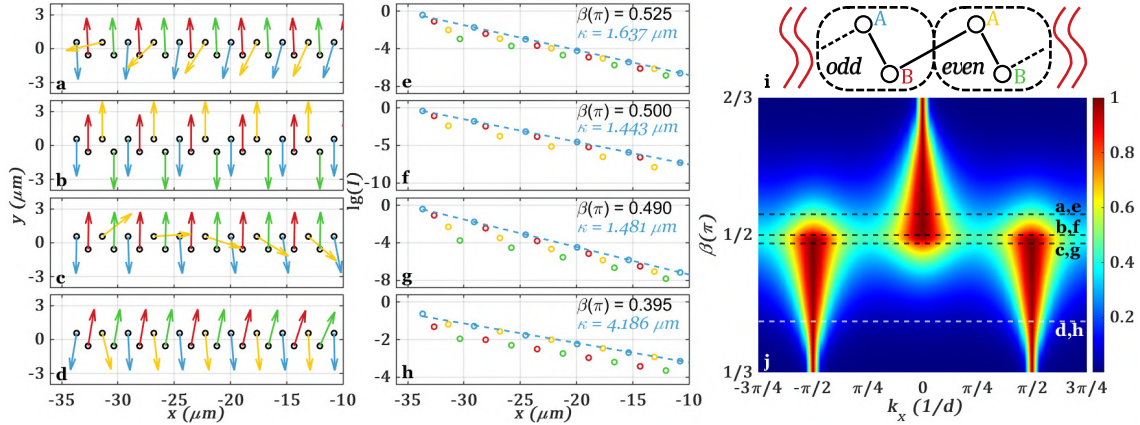


Figure 4.4: **SSH edge states in the presence of TE-TM SOC.** Energy spectrum of Hamiltonian 4.13 in (a,c,e) real and (b,d,e) reciprocal space for increasing magnitude of the TE-TM SOC  $\gamma'$  (rows from top to bottom); intensity of the edge state is increased by  $10x$  times for visibility, as in Fig. 4.3(e,f); the parameters are the same as for Fig. 4.3, except the chain is two times shorter, and  $\delta = 8.0$  meV.



**Figure 4.5: Edge state period doubling in tight-binding model.** The Stokes vector (a-d) and density decay (e-h) in real space of a finite SSH chain for different magnitudes of RDSOC  $\beta$ ;  $\kappa$  is an exponential decay length obtained by fitting the data (dashed lines); (i) the division of a unit cells into two types: odd and even; the colors of A-D letters correspond to the colors of arrows in (a-d) and dots in (e-h); (j) the edge state density (color) in reciprocal space depending on the RDSOC phase  $\beta$ .

in real (left column) and reciprocal (right column) space for different values of  $\gamma'$  (rows). As one can notice, with increasing TE-TM SOC the edge state slowly approaches the upper bands, and the asymmetry between the bands increases. However, for realistic values of TE-TM SOC used in these simulations, the state still stays inside the gap and its localization is evident.

#### 4.2.4 Period doubling in both models

In both cases, of tight-binding model Eq. 4.6 and of continuous model Eq. 4.12, we observe the period doubling of the edge state. We start by investigating the structure of the polarization and density of the edge state in the tight-binding model for the same parameters as for Fig. 4.2(d). Fig. 4.5(a-d) shows the in-plane Stokes vector at each site, and Fig. 4.5(e-h) shows the intensity distribution. The circular polarization degree of edge modes is zero. We divide all unit cells into odd and even (Fig. 4.5(i)). For small  $\beta$  there is no difference between Stokes vector behavior on odd and even unit cells, as one can see in Fig. 4.5(d,h). For  $\beta \approx \pi/2$ , we see a pronounced difference between odd and even unit cells (Fig. 4.5(c,g)). While all B sites are equivalent (red and green arrows), Stokes vector on odd and even A sites (blue and yellow arrows) rotates differently. The density behavior also shows four distinct spatial decay rates. For  $\beta = \pi/2$  (Fig. 4.5(b,f)), we have a specific edge state divided into orthogonally-polarized dimers; a single site terminates the chain. The density at even B lattice sites drops almost to zero (thus not visible in Fig. 4.5(f)). After crossing  $\beta = \pi/2$  value, the direction of polarization rotation at A sublattices changes (Fig. 4.5(a,e)), while B sublattices still do not rotate. For even larger  $\beta$ , the period doubling disappears.

The period doubling arises from a superposition of three components of the edge state wavefunction in reciprocal space for  $\beta \approx \pi/2$  (Fig. 4.5(j)). This occurs because the bulk energy bands exhibit almost equal gaps at the center and edges of the BZ (red line in

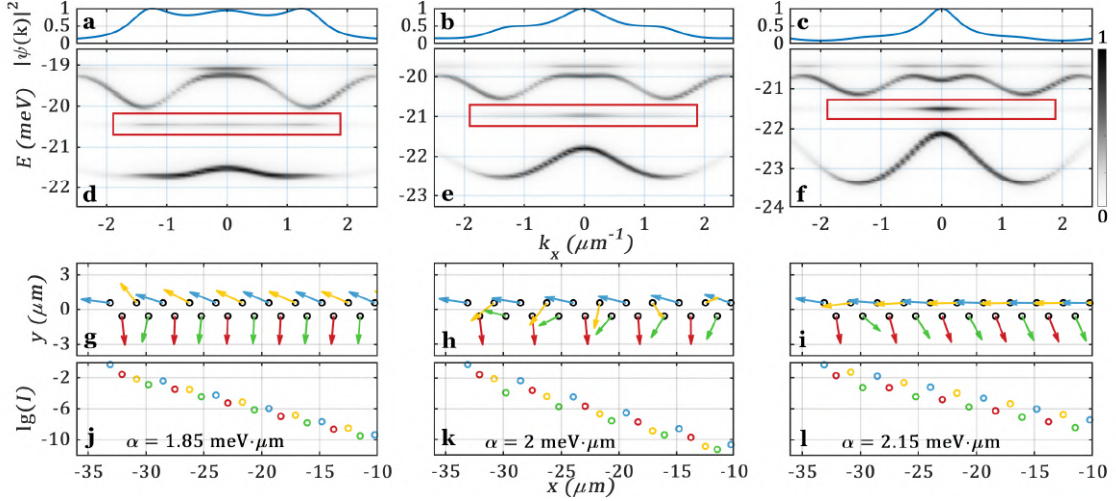


Figure 4.6: **Edge state period doubling in continuous model.** (a-c) Normalized edge state density distribution in reciprocal space, (d-f) spectrum of the lowest gap with the edge state marked by the red rectangle (edge state density is multiplied by 10, gray color scale shows normalized state density), (g-i) Stokes vector distribution in real space (averaged over FWHM region for each potential well) and (j-l) density decay in real space for different magnitudes of RDSOC constant  $\alpha$ ; parameters of the calculation are the same as for Fig. 4.3 with difference in  $\delta = 8$  meV and Lorentzian broadening of 0.1 meV FWHM (for better visibility).

Fig. 4.2(c)). The component located exactly in the middle of the BZ creates a constant phase distribution along the chain. The two components located exactly at the edges of the BZ create a phase distribution which jumps between each pair of neighboring unit cells. Thus, the linear combination of these three components creates an imbalance between odd and even unit cells, since in the former the components sum up constructively while in the latter the components sum up destructively. However, this superposition does not explain the difference between two sublattices inside each unit cell. The sublattice difference is created by the finite distribution of each of these three components in reciprocal space. It provides the necessary spatial decay rate and Stokes vector rotation inside each unit cell.

In the tight-binding approximation several assumptions are used: the chain is oriented along the  $x$  axis and all lattice sites have equal spacing, the tunneling between lattice sites does not depend on energy. In a realistic 2D implementation all these assumptions stop to hold, however, the period-doubling effect still can be observed, although with a slight difference in Stokes vector behavior and the edge state density distribution (Fig. 4.6). With increasing RDSOC, the period-doubling starts to appear at  $\alpha = 1.85$  meV  $\cdot$   $\mu$ m (first column of Fig. 4.6), acquires the most pronounced effect at  $\alpha = 2$  meV  $\cdot$   $\mu$ m (second column of Fig. 4.6) and finally vanishes at  $\alpha = 2.15$  meV  $\cdot$   $\mu$ m (third column of Fig. 4.6), similarly to what occurs around  $\beta = \pi/2$  in Fig. 4.5. Contrary to the tight-binding results, there are always two sets of sublattices of different type which rotate along the chain with distinct spatial rate. In Fig. 4.6(g-i) they are even A (yellow) and even B (green). The other two sets of sublattices stay unchanged. The density of the edge state still has three main components in reciprocal space (at the edges and at the center of the BZ), but now they become equal to each other rather on the onset of period-doubling (the first column

in Fig. 4.6). The density spatial decay (Fig. 4.6(j-l)) is in good correspondence with the tight-binding results. The pattern of polarization here, especially for the case of  $\beta = \pi/2$  reminds a persistent spin helix, but incorporated in a chain.

### 4.3 Continuous tunneling control between individual sites

As was mentioned in the previous Sec. 4.1, the tunneling in the effective Hamiltonian 4.9 does not depend on the detuning  $\delta$ , a single easily continuously tunable with voltage parameter of LC microcavity. As a result, it was only possible to make abrupt changes of topology by voltage, by turning the RDSOC on and off. More generally, it is so for any 1D model with *nearest-neighbor couplings only*, since in this case the last term in Eq. 4.4 contributes only to the on-site energy shift. Therefore, the tunneling can not be controlled by applied voltage according to Eq. 4.4. However, the following  $\delta$ -dependent terms emerge as the *3rd order perturbation theory correction*:

$$H_{lattice,eff} = \dots - \sum_{i,j,k,m} \frac{J_{ik}J_{km}J_{mj} \sin \beta_{ik} \cos \beta_{km} \sin \beta_{mj}}{4\delta^2} a_j^\dagger a_i + \dots \quad 4.14$$

Therefore, they provide a continuous control over effective tunneling. At the same time, we expect the 3rd order correction to be small, and thus make an experimental observation challenging. A workaround is necessary to get a correction of more leading order.

#### 4.3.1 General idea

Let us consider the case of two sites, which simplifies the mathematical description of the tunneling control. We will call this system a double trap (DT). The Hamiltonian 4.3 therefore can be written as 4x4 matrix in the basis combining polarization ( $HV$ ) and site (left/right) degrees of freedom ( $|V_s^l\rangle |V_s^r\rangle |H_s^l\rangle |H_s^r\rangle$ )<sup>T</sup>:

$$H = \begin{pmatrix} -\delta & -J \cos \beta & \mathbf{0} & iJ \sin \beta \\ -J \cos \beta & -\delta & -iJ \sin \beta & \mathbf{0} \\ \mathbf{0} & iJ \sin \beta & \delta & -J \cos \beta \\ -iJ \sin \beta & \mathbf{0} & -J \cos \beta & \delta \end{pmatrix}, \quad 4.15$$

where we have single tunneling amplitude  $J$  and RDSOC phase  $\beta$ , and subscript  $s$  underlines that we have a single localized state inside each trap which is typically called  $s$  state in analogy with atomic orbital notations. We inverted the sign of tunneling  $J \rightarrow -J$  since the tunneling between  $s$  states is negative, and it will be important for future considerations. Therefore, currently  $J > 0$ . According to the Hamiltonian 4.15, the cross-polarized inter-site transition is allowed (green terms), while cross-polarized intra-site one is prohibited (red terms). This is schematically depicted in Fig. 4.7(a). This happens because of the symmetry of RDSOC term, which mediates all cross-polarized transitions in this system. RDSOC term is linear in  $k_y$  (Eq. 3.7), and, consequently, it can couple only states of different symmetry (*symmetry selection rule*). Since we consider  $s$  states in both polarizations,  $s$  states located on the same site can not be coupled by the RDSOC, because

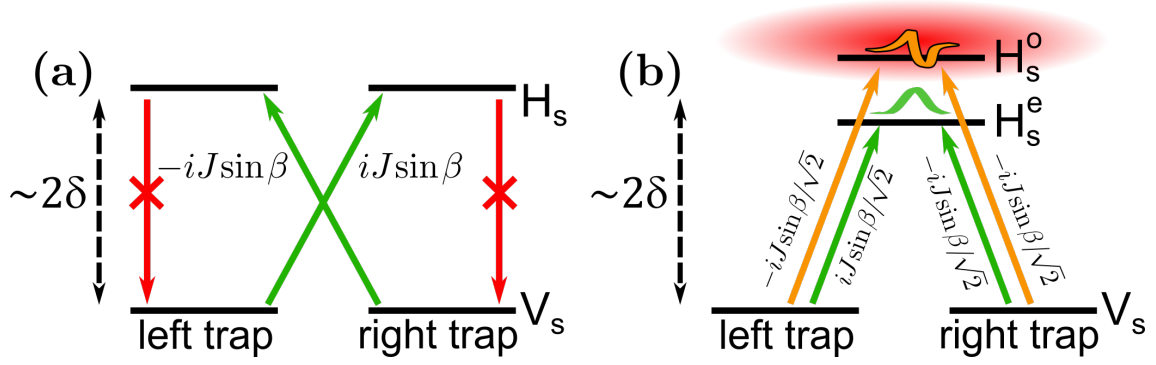


Figure 4.7: *Cross-polarized RDSOC-mediated transitions between  $s$  states of a double trap.* (a) Allowed (green) and prohibited (red) cross-polarized transitions between single-site  $s$  states; two-step transition from  $|V_s^l\rangle$  to  $|V_s^r\rangle$  is prohibited; (b) cross-polarized transitions between single-site  $s$  states of  $V$  polarization, and even-odd  $s$  states of  $H$  polarization (green and orange marker-like lines show the symmetry of state); all transitions are allowed, and two possible two-step paths from  $|V_s^l\rangle$  to  $|V_s^r\rangle$  (through  $|H_s^e\rangle$  (green) or  $|H_s^o\rangle$  (orange)) compensate each other, thus giving zero total change in tunneling (Eq. 4.4); however, if  $H_s^o$  state falls into the continuum (red cloud), the second-order transition through  $|H_s^e\rangle$  becomes unbalanced.

they share the same symmetry, while  $s$  states located at different sites can. Therefore, the two-step transition process from  $|V_s^l\rangle$  to  $|V_s^r\rangle$  through an intermediate state in  $H$  polarization, which is expected to change the tunneling, is prohibited.

The transitions depicted in Fig. 4.7 can be considered in another basis, where states in  $H$  polarization are already coupled, and form symmetric (even, superscript  $e$ ) and anti-symmetric (odd, superscript  $o$ ) two-site eigenstates (see green and orange marker-like lines in Fig. 4.7(b)). This basis is closer to reality, since now a perturbative approach is applied only for  $V$  polarization and its coupling to  $H$ , while inside  $H$  polarization the eigenstates are exact. The Hamiltonian 4.15 reads in this new basis  $(|V_s^l\rangle |V_s^r\rangle |H_s^e\rangle |H_s^o\rangle)^T$  as:

$$H = \begin{pmatrix} -\delta & -J \cos \beta & iJ \sin \beta / \sqrt{2} & -iJ \sin \beta / \sqrt{2} \\ -J \cos \beta & -\delta & -iJ \sin \beta / \sqrt{2} & -iJ \sin \beta / \sqrt{2} \\ -iJ \sin \beta / \sqrt{2} & iJ \sin \beta / \sqrt{2} & \delta - J \cos \beta & 0 \\ iJ \sin \beta / \sqrt{2} & iJ \sin \beta / \sqrt{2} & 0 & \delta + J \cos \beta \end{pmatrix}. \quad 4.16$$

In this basis, all four cross-polarized transitions are allowed. There are two different two-step paths which connect  $|V_s^l\rangle$  and  $|V_s^r\rangle$  states, through  $|H_s^e\rangle$  or  $|V_s^o\rangle$  states. The paths compensate each other because of sign difference in transition matrix elements (orange and green paths in Eq. 4.16 and Fig. 4.7(b)). However, if we imagine that the anti-symmetric state  $|V_s^o\rangle$ , which has a bigger energy, falls into the continuum (red cloud), this leaves us with the unbalanced two-step transition through  $|H_s^e\rangle$ . Therefore, the tunneling between  $s$  states in  $V$  polarization should acquire a change *already as the 2nd order correction*, contrary to Eq. 4.14. The Hamiltonian for 3-level system without  $|V_s^o\rangle$  can be easily

obtained by eliminating this state from Hamiltonian [4.16](#):

$$H = \begin{pmatrix} -\delta & -J \cos \beta & iJ \sin \beta / \sqrt{2} \\ -J \cos \beta & -\delta & -iJ \sin \beta / \sqrt{2} \\ -iJ \sin \beta / \sqrt{2} & iJ \sin \beta / \sqrt{2} & \delta - J \cos \beta \end{pmatrix}. \quad 4.17$$

The effective 2x2 Hamiltonian for  $V$  polarization is, therefore (up to the 2nd order corrections):

$$H_{eff} = \begin{pmatrix} -\left(\delta + \frac{J^2 \sin^2 \beta}{4\delta}\right) & -J \left(\cos \beta - \frac{J \sin^2 \beta}{4\delta}\right) \\ -J \left(\cos \beta - \frac{J \sin^2 \beta}{4\delta}\right) & -\left(\delta + \frac{J^2 \sin^2 \beta}{4\delta}\right) \end{pmatrix}. \quad 4.18$$

The non-diagonal terms proportional to  $\delta^{-1}$  are, therefore, the tunneling modification  $\Delta J$ . We call this result *the tunneling amplitude control technique*, since  $\Delta J$  can be controlled by detuning  $\delta$  which in its turn is simply controlled in experiment by voltage. Actually, the obtained result is quite general. It is based on (1) selection rules, which allow some transitions and prohibit the others, and (2) tunability of energy separation between the states of interest ( $V$ -polarized states) and intermediate states ( $H$ -polarized states). Therefore, it can be realized in different physical systems, using various types of inter-level (spin-orbit) couplings, and utilizing higher energy states, not necessarily  $s$  states.

### 4.3.2 Realization in nematic liquid crystal microcavity

In collaboration with IBM Research–Zurich, University of Warsaw, and Warsaw Military University of Technology, this proposal has been already realized in a nematic liquid crystal microcavity [\[253\]](#). The scheme of the cavity is shown in [Fig. 4.8\(a\)](#). In this realization, there are several differences with respect to the simplified model discussed in the previous [Section 4.3.1](#). First of all, the RDSOC-mediated tunneling control is realized through intermediate  $p$  states. Also, due to the refractive index difference for  $H$  and  $V$  ([Eq. 3.6](#)), the photonic potentials for  $H$  and  $V$  are different as well, and, consequently, the spectra of single-site localized states are different. Furthermore, the polarization mass difference terms ( $\mu_x$  and  $\mu_y$  in [Eq. 3.7](#)), originating from distinct longitudinal mode numbers ([Eq. 1.1](#)), can no longer be neglected. This mass difference for  $H$  and  $V$  photons results in unequal tunneling coefficients  $J$ . Finally, the RDSOC contribution is computed directly from the continuous Hamiltonian [3.7](#) by evaluating cross-polarized transition matrix elements between different localized states.

It will be useful to utilize the Hamiltonian [3.7](#) in  $HV$  basis, where we changed the RDSOC to be along  $k_x$  and to correspond to a new coordinate system ([Fig. 4.8\(a\)](#)). The Hamiltonian then reads:

$$H(k_x) = \frac{\hbar^2 k_x^2}{2M} \sigma_0 + \left( \frac{\hbar^2 k_x^2}{2m} + 2\alpha k_x \right) \sigma_x + \delta \sigma_{11}. \quad 4.19$$

with  $1/M = (1/m_H + 1/m_V)/2$ ,  $1/m = (1/m_H - 1/m_V)/2$ , where  $m_H$  ( $m_V$ ) is the mass of the  $H$ -( $V$ -)polarized mode, and  $\delta$  is the detuning between  $N$ th  $H$  (non-tunable) and  $(N + 1)$ th  $V$  (tunable) modes. Since only one mode is shifted by voltage in experiment,

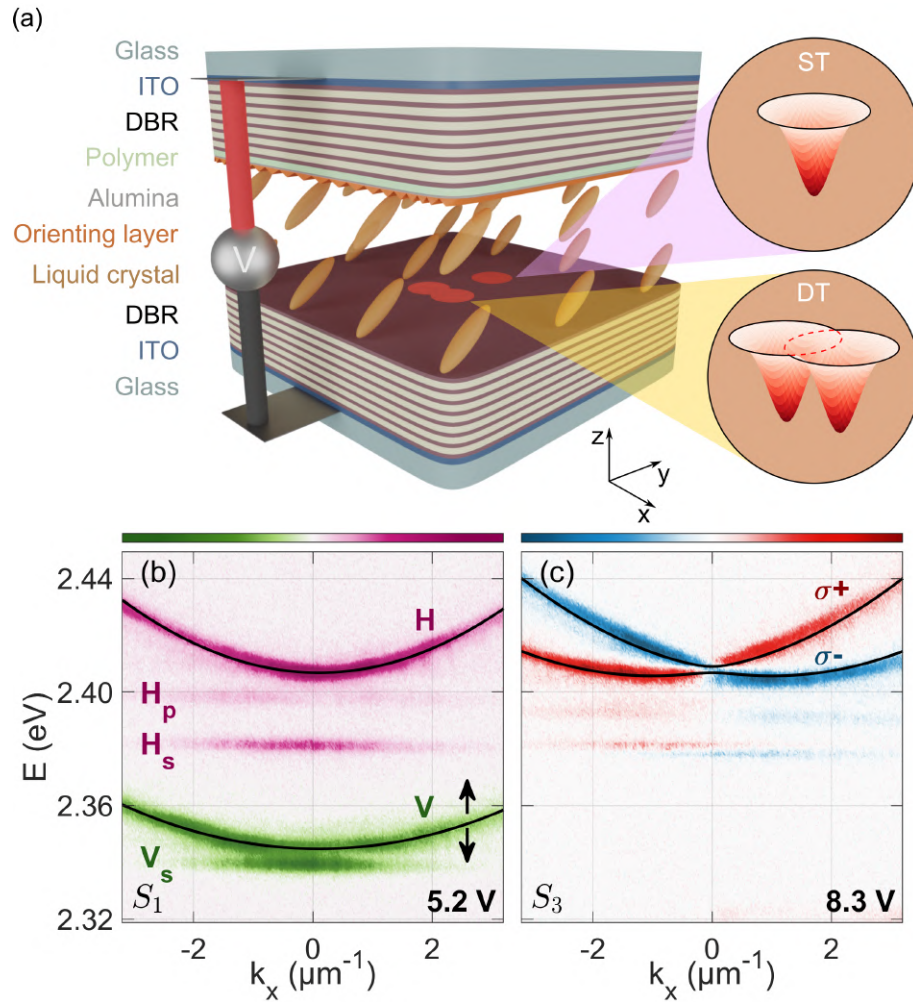


Figure 4.8: **Scheme of a nematic LC microcavity with potential traps and ST dispersion.** (a) Scheme of an LC microcavity with ST and DT potentials; experimentally measured dispersion of ST for (b) 5.2 V and (c) 8.3 V shown as  $S_1$  and  $S_3$  Stokes parameters, respectively; the data is nonlinearly transformed and saturated in order to enhance the visibility of localized states marked as  $|V_s\rangle$ ,  $|H_s\rangle$  and  $|H_p\rangle$ ; the colorbars are in a.u.; black solid lines show the fit of continuous modes ( $H$  and  $V$  in (b),  $+$  and  $-$  in (c)) by Hamiltonian 4.19; black double-headed arrow depicts the tunability of  $V$  mode. Adopted from [253].

the  $\sigma_x$  Pauli matrix next to the detuning  $\delta$  in Eq. 3.7 is substituted by  $\sigma_{11} = (\sigma_0 - \sigma_z)/2$ .

### 4.3.3 $sp$ coupling by RDSOC on a single site

We start by considering a single trap (ST) potential. In Fig. 4.8, we show the dispersion measured at the position of an ST for different voltages. At small voltages, the detuning  $\delta$  between the two linear polarizations is large, and therefore, the eigenmodes are predominantly linearly polarized. It is clearly visible when plotting the first Stokes parameter  $S_1$  (Fig. 4.8(b)). Along with continuous parabolic cavity modes, well described by the Hamiltonian 4.19, we observe the localized states. These states have discrete,  $k_x$ -independent energies below the corresponding continuous modes and show a node/antinode at  $k_x = 0$ , depending on the state symmetry. Due to the contrast in  $H$  and  $V$  effective refractive indices, the effective potential depth of the ST is different for  $H$  and  $V$ . As a result, a single localized state is observed for  $V$  ( $s$  state) and two localized states for  $H$  ( $s$  and  $p$  states).

For higher voltages (around 8.3 V), the  $V$  mode of  $(N + 1)$ th order approaches the  $H$  mode of  $N$ th order, and the RDSOC contribution  $2\alpha k_x$  starts to dominate over the splitting  $\delta$  between the linearly-polarized modes (Fig. 4.8(c)). In this regime, the eigenmodes are mostly circularly polarized and split along  $k_x$ , which is visible when plotting the third Stokes parameter  $S_3$ .

We measured the dispersion at the position of an ST for the set of voltages between 0 V and 11 V. The results are shown in Fig. 4.9(a) in an energy-voltage plot for a fixed angle of detection of  $-7^\circ$  corresponding to  $k_x = 1.49 \mu\text{m}^{-1}$  (which optimizes the simultaneous visibility of both  $s$  and  $p$  localized states). The tunability of the  $V$  mode (green) with voltage is well visible in this type of diagram. The experimental results can be reproduced by numerically solving the stationary Schrödinger equation with the Hamiltonian 4.19 as displayed in Fig. 4.9(b). From the experimentally measured total intensity in Fig. 4.9(c), one can infer that localized states anticross at the positions highlighted by black arrows, corroborated by numerical results (Fig. 4.9(d)). This anticrossing is a manifestation of RDSOC-mediated coupling between localized states of  $H$  and  $V$  of different symmetry. The absolute value of the matrix elements of this coupling can be generally written as  $\beta = |\langle H_l | 2\alpha k_x | V_{l'} \rangle|$ , with  $l(l') = \{s, p, \dots\}$  representing the quantum number of a localized state. While the  $|V_p\rangle$  state was not visible in Fig. 4.8(b), it appears when  $H$  and  $V$  are close to the resonance, and so it can couple with the other states which are always visible. Therefore, the tight-binding model for localized states of an ST in the basis  $(|H_s\rangle |H_p\rangle |V_s\rangle |V_p\rangle)^T$  can be written as:

$$H_{ST} = \begin{pmatrix} E_{H_s} & 0 & 0 & -i\beta_{ST,2} \\ 0 & E_{H_p} & i\beta_{ST,1} & 0 \\ 0 & -i\beta_{ST,1} & E_{V_s} + \delta & 0 \\ i\beta_{ST,2} & 0 & 0 & E_{V_p} + \delta \end{pmatrix}, \quad 4.20$$

where  $E_\varphi$  stands for the energy of localized  $|\varphi\rangle$  state. Two different coupling coefficients  $\beta_{ST,1(2)}$  give rise to two anticrossing points observed in Fig. 4.9(c,d). By diagonalizing

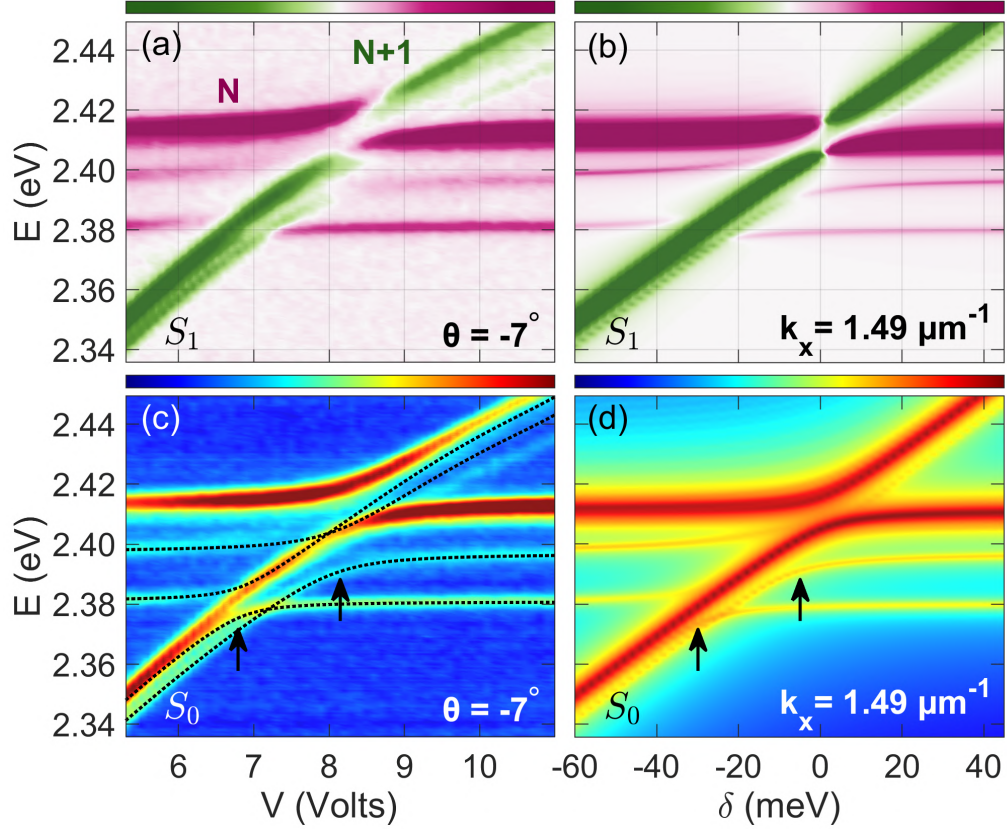


Figure 4.9: *Energy-voltage diagrams showing the near-resonant regime between  $N$ th  $H$  mode and  $(N + 1)$ th  $V$  mode in an  $ST$ . (a,c) Experimental and (b,d) numerical results represented as (a,b) linear polarization degree  $S_1$  and (c,d) total intensity  $S_0$ ; the detection angle of experimental data  $\theta = -7^\circ$  corresponds to  $k_x = 1.49 \mu\text{m}^{-1}$  of the numerical simulation; the data is nonlinearly transformed and saturated in order to enhance visibility of localized states; the colorbars are in a.u.; black arrows in (c,d) mark anticrossing points; black dotted lines in (c) show the energies obtained by diagonalizing tight-binding Hamiltonian [4.20](#). Adopted from [\[253\]](#).*

the tight-binding Hamiltonian [4.20](#), we obtain a good correspondence with experimental results (black dotted lines in Fig. [4.9\(c\)](#)). The parameters can be found in SM of [[253](#)].

#### 4.3.4 Tunneling control between two sites mediated by RDSOC

We now turn to the consideration of the DT potential. The dimensionality of Hamiltonian is 8 since it contains two polarizations, two sites, and two "orbitals" ( $s$  and  $p$ ). We write the full 8x8 Hamiltonian, perform its transformation and apply the perturbation theory in Appendix [A](#). Here, we discuss only the physical interpretation, very similar to the one of Sec. [4.3.1](#), and final formula.

The tunneling between sites contains both a first-order direct tunneling  $J_0$  and a second-order contribution due to RDSOC, as sketched in Fig. [4.10\(a,b\)](#). The RDSOC-mediated 2nd order transitions happen through the intermediate  $V_p$  ST states. In addition to the intra-site RDSOC-mediated  $sp$  transitions  $\beta'_2 \equiv \beta_{ST,2}$  discussed in the case of ST (Eq. [4.20](#)), inter-site  $sp$  transitions  $\beta'_3$  appear. The expression for the detuning-dependent effective tunneling between  $|H_s^l\rangle$  and  $|H_s^r\rangle$  states mediated by RDSOC through an intermediate  $|V_p\rangle$  states reads as:

$$J[\delta(V)] = J_0 - \frac{\beta_{DT,2}^2}{E_{V_p} - E_{H_s} + \delta(V)} \quad \text{4.21}$$

where  $\beta_{DT,2} = (\beta'_2 + \beta'_3)/\sqrt{2}$ ,  $\beta'_{2,3} = |\langle H_s^l | 2\alpha k_x | V_p^{l,r} \rangle|$  (see Fig. [4.10\(b\)](#)),  $E_{H_s}$  and  $E_{V_p}$  are the energies of ST  $|H_s\rangle$  and  $|V_p\rangle$  states, respectively (Eq. [4.20](#)). The voltage dependence of tunneling, analogous to Eq. [4.18](#), is evident.

We now present the comparison with the experimental results. The dispersions for negative and positive linear detunings  $\delta$  are shown in Fig. [4.10\(c,d\)](#), respectively. Now, each state of an ST is split into even and odd states, since the traps forming the DT are coupled by tunneling. For both  $H$  and  $V$  modes, we observe three localized states. The coupling between different localized states is described by the same matrix elements with  $\beta$  introduced above. Note that the energy splitting between  $|H_s^e\rangle$  and  $|H_s^o\rangle$  localized states is different for panels (c) and (d) in Fig. [4.10](#). Moreover, it changes continuously with voltage (Fig. [4.10\(g\)](#)). The effect is especially pronounced when approaching the resonance. At the same time, the polarization of the states is mostly conserved, which is confirmed by  $S_1$  both in the experiment (Fig. [4.10\(e\)](#)) and numerical simulation (Fig. [4.10\(f\)](#)). Since the uncoupled states in both traps are degenerate, the energy splitting between the DT states can be written as  $2J$ , where  $J$  is a tunneling coefficient. Therefore, this result can be interpreted as a continuous control of the tunneling amplitude by the applied voltage due to the RDSOC:  $J = J(V)$ .

The effective tunneling extracted from the experiment is shown as blue points in Fig. [4.10\(h\)](#), while the fitting of this data with  $J(\delta)$  (Eq. [4.21](#)) is illustrated by a solid black line. We, therefore, conclude that the hyperbolic dependence of the tunneling  $J$  on the detuning  $\delta$  (directly controlled by the voltage) given by Eq. [4.21](#) is confirmed by the experiment. The total change of  $J(\delta)$  is from  $0.7J_0$  to  $1.45J_0$ , exceeding a factor 2. This change is only possible if the absolute value of the RDSOC transition matrix element

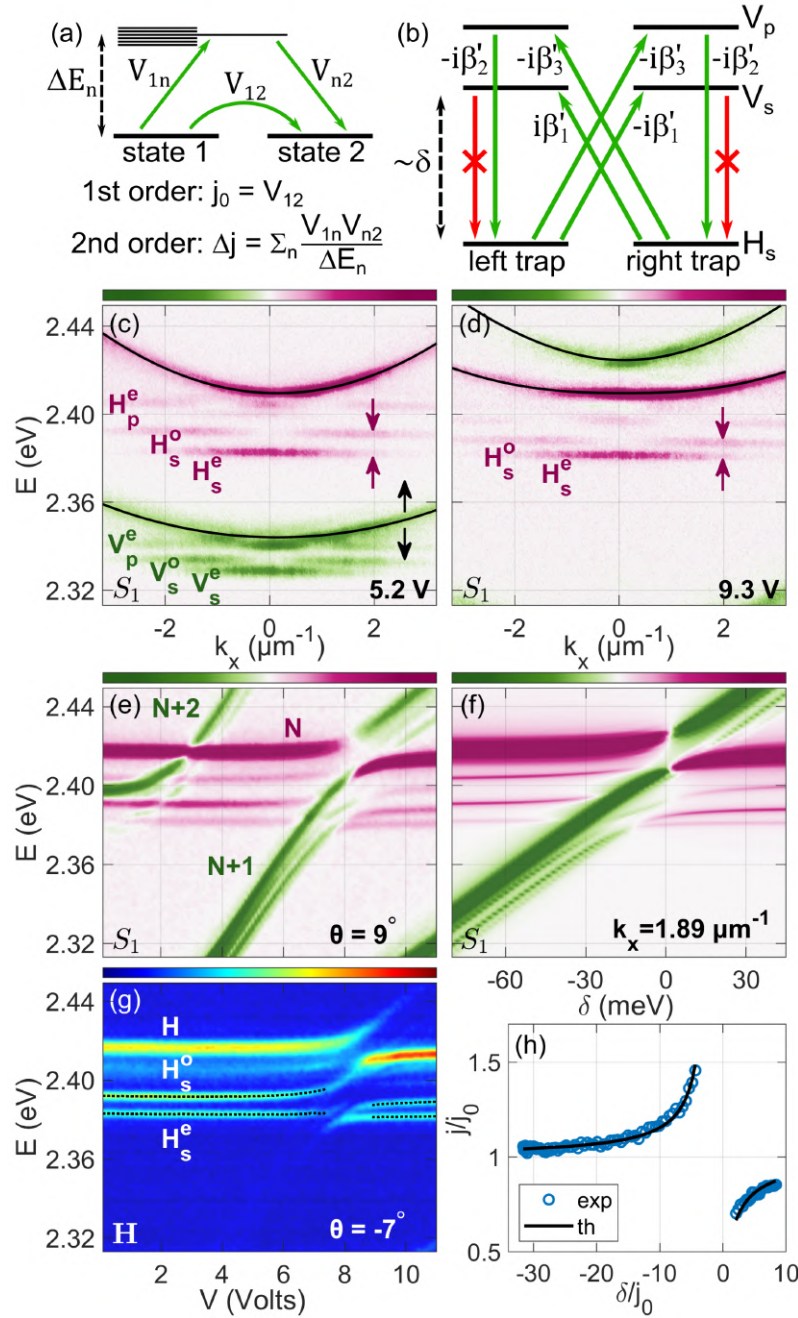


Figure 4.10: **Tunneling amplitude control in DT.** (a) Tunneling  $J_0$  and its change  $\Delta J$  as the first and the second order corrections of perturbation theory, respectively;  $V_{mn}$  is a matrix element of perturbation; (b) allowed (green) and prohibited (red) RDSOC-mediated transitions responsible for the tunneling control; experimentally measured dispersion of a DT for (c) 5.2 V and (d) 9.3 V shown as  $S_1$  Stokes parameter; black solid lines show the fit by Hamiltonian [4.19]; black double-headed arrow depicts the tunability of  $V$  mode; purple arrows mark the spectral distance between  $|H_s^e\rangle$  and  $|H_s^o\rangle$ ; (e,g) experimental and (f) numerical results represented as (e,f)  $S_1$  linear polarization degree and (g)  $H$ -polarized intensity; black dotted lines in (g) show the extracted energies of  $|H_s^e\rangle$  and  $|H_s^o\rangle$  localized states; the data in (c-g) is nonlinearly transformed and saturated in order to enhance the visibility of localized states; the colorbars are in a.u.; (h) effective coupling coefficient between  $|H_s^r\rangle$  and  $|H_s^l\rangle$  localized states extracted from the experiment (blue dots) and fitted by  $J(\delta)$  Eq. [4.21] (black line). See simulation parameters in SM of [253]. Adopted from [253].

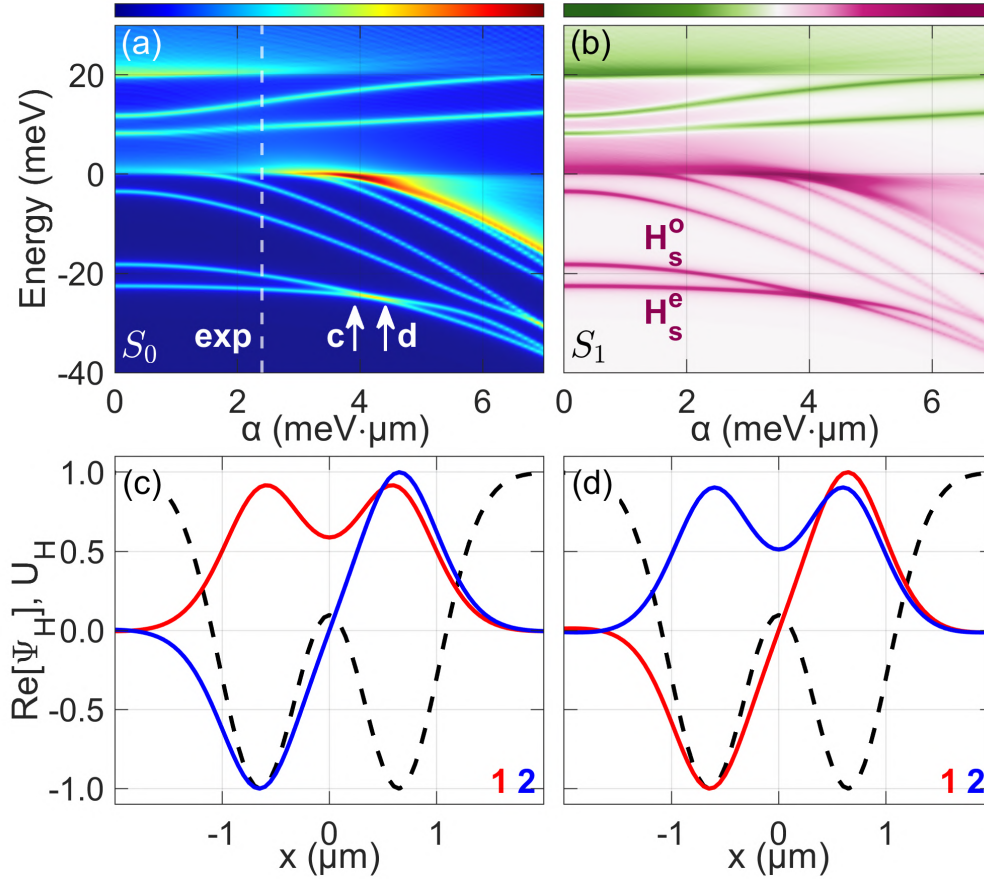


Figure 4.11: **Topological transition in DT.** Spectrum of a DT depending on RDSOC parameter  $\alpha$  showing a spectral inversion between  $|H_s^e\rangle$  and  $|H_s^o\rangle$  localized states in (a) total intensity  $S_0$  and (b) linear polarization degree  $S_1$ ; the colorbars are in a.u.; real part of H-polarized wavefunction component  $\text{Re}[\Psi_H]$  of the lowest (1, red) and the second lowest (2, blue) localized states (c) before and (d) after state inversion; black dashed line shows a potential  $U_H$  for H;  $\text{Re}[\Psi_H]$  and  $U_H$  units are normalized; white dashed line in (a) shows the experimental value of RDSOC parameter  $\alpha$  presented in Fig. 4.10; see parameters in SM of [253]. Adopted from [253].

$\beta_{DT,2}$  is non-zero. Thus, the RDSOC-mediated coupling between  $s$  and  $p$  states plays a crucial role in the control of the tunneling between two traps.

### 4.3.5 Tunneling inversion and topological transition

Another remarkable property of the effective tunneling  $J(\delta)$  is a minus sign allowing, in principle, to suppress the effective tunneling down to zero or even to invert its sign. The inversion of the tunneling sign is inextricably linked with a *topological transition* manifesting itself in the experiment as a spectral swap between  $e$  and  $o$  localized states. This transition is similar to the one observed in the first seminal works on the Quantum Spin Hall Effect in HgTe topological insulators [254]. The Quantum Spin Hall Effect in the HgTe quantum wells corresponds to the most well-known topological transition with the mass sign inversion in the Dirac Hamiltonian [255, 256], and our system corresponds to its 1D projection. In Fig. 4.11 we demonstrate this effect in numerical simulations.

Fig. 4.11(a,b) shows the evolution of the spectrum with increasing RDSOC constant  $\alpha$ . At  $\alpha \approx 4 \text{ meV}\cdot\mu\text{m}$ , the  $|H_s^e\rangle$  and  $|H_s^o\rangle$  localized states cross in energy. By looking at the structure of the lowest (1) and second lowest (2) states in real space before the crossing (Fig. 4.11(c)) and after the crossing (Fig. 4.11(d)), one can easily notice the inversion between the  $e$  and  $o$  states. At the same time, the polarization of these states is mostly conserved, as confirmed by the degree of linear polarization  $S_1$  (Fig. 4.11(b)).

In the demonstrated DT experiment (Fig. 4.10), the value of  $\alpha$  is  $2.4 \text{ meV}\cdot\mu\text{m}$ , which does not allow us to observe this topological transition experimentally (white dashed line in Fig. 4.11(a)). The simplest way to achieve it in future experiments is to utilize a LC material with higher birefringence.

### 4.3.6 Discussion

Along with an abundance of physical phenomena, microcavities allow studying various lattice models, often in the context of topological photonics. Nowadays, the most common techniques for lattice engineering in planar microcavities are micropillar etching [257, 5], where the tunneling in the presence of spin-orbit coupling has also been studied [258], and ballistical coupling [259]. Both of these techniques lack a simple tunability for the lattice tunnelings, and do not provide dynamical access to the transitions between different topological phases of the model, that our technique does. In the next Section 4.4, we will present another approach for lattice tunability based on CLC microcavity in a uniformly lying helix configuration [235], which has a different origin of tunability in comparison with the approach presented in this Section.

Our tunneling amplitude control technique can be further extended to the domains of strong light-matter interaction, non-linear physics, or non-Hermitian physics, since all necessary ingredients are available in nematic LC microcavities. Our technique is mathematically similar to the adiabatic elimination used to control coupling in photonic waveguide lattices [260] and atomic systems [261]: the full Hilbert space is reduced to an effective Hamiltonian exhibiting the desired coupling. The main advantage over the coupled waveguide system is the small spatial size of the DT system, allowing its efficient integrability. DT system presents the same miniaturisation advantage over another proposed implementation of coupling control based on Mach-Zehnder interferometers [262] and over artificial gauge field techniques of tunneling amplitude modulation based on bent waveguides [263].

## 4.4 1D tunable lattice in cholesteric liquid crystal microcavity

In this Section, we discuss the CLC embedded in microcavity and optical potential which it creates. This optical potential turns out to be tunable with external voltage and can exhibit a spin-orbit coupling having many similarities with RDSOC. We explain the origin of tunability and spin-orbit coupling, and describe the similarity with RDSOC. The experimental part was performed by our colleagues at University of Warsaw, and sample fabrication was done in Warsaw Military University of Technology.

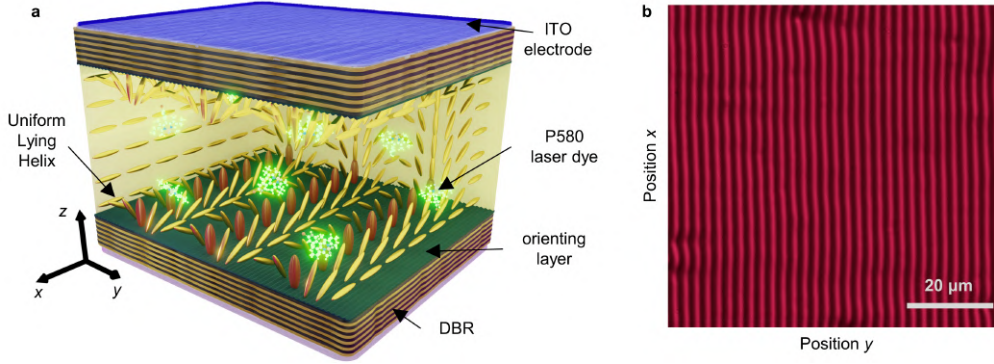


Figure 4.12: *CLC microcavity in ULH configuration.* (a) Scheme of the dye-doped optical microcavity with an embedded stabilized ULH structure; the rows of directors oriented vertically are colored in red to indicate the period of the lattice; (b) polarizing optical microscopy image of light transmitted through a ULH texture embedded inside LC microcavity. Adopted from [235].

#### 4.4.1 Microcavity scheme

The scheme of the microcavity used in experiment is presented in Fig. 4.12(a). The cavity is filled with a nematic LC and chiral dopant, which induces a CLC phase with a helical pitch  $p \approx 8 \mu\text{m}$  (Fig. 4.12(b)). Under homeotropic (perpendicular to the mirrors) anchoring, the mirror surfaces impose a topological frustration that induces a *uniformly lying helix* (ULH) configuration, with the axis of helix aligned parallel to the mirrors [264, 265, 266]. Doping of LC with an organic laser dye is important only for the experimental part of the work, so we will not discuss it here. Two different samples, showing some distinctions in physics, were prepared. Sample A, with a higher birefringence of the CLC mixture, was used in the first part of the work to demonstrate band structure tunability by external electric field. Sample B has a CLC mixture with lower birefringence but exhibits a deeper photonic potential thanks to the higher homogeneity along the cavity axis  $z$ . This sample demonstrates a photonic spin-orbit coupling absent in the sample A.

#### 4.4.2 CLC-induced photonic 1D potential

First, sample A was studied. Experiment is based on angle-resolved reflectivity spectroscopy. Without any voltage applied to the sample (Fig. 4.13(e,h)), the bandgap is visible only in  $H$  polarization, while in  $V$  polarization the spectrum remains gapless (within the spectrometer resolution and line broadening). The  $s$ -band is observed in  $H$  polarization (denoted  $H_s$ ,  $E \approx 2.1 \text{ eV}$ ). Under non-zero external voltage, an energy gap emerges in  $V$  polarization as well, as shown in Fig. 4.13(i,j), opening from 0 meV at 0.0 V to 20 meV at 3.7 V. The whole band structure in  $V$  polarization is shifted towards higher energies. The process of gap opening is reversible. We also observed the increase of the gap for  $H$  polarization, from 12 meV at 0.0 V to 25 meV at 3.7 V (Fig. 4.13(f,g)). Beside the symmetric  $s$ -band, another gap opens in  $H$  polarization for higher energies (around 2.14 eV), thus forming an additional anti-symmetric  $p$ -band (denoted  $H_p$ ).

The observed results can be explained by considering the combination of ULH-induced

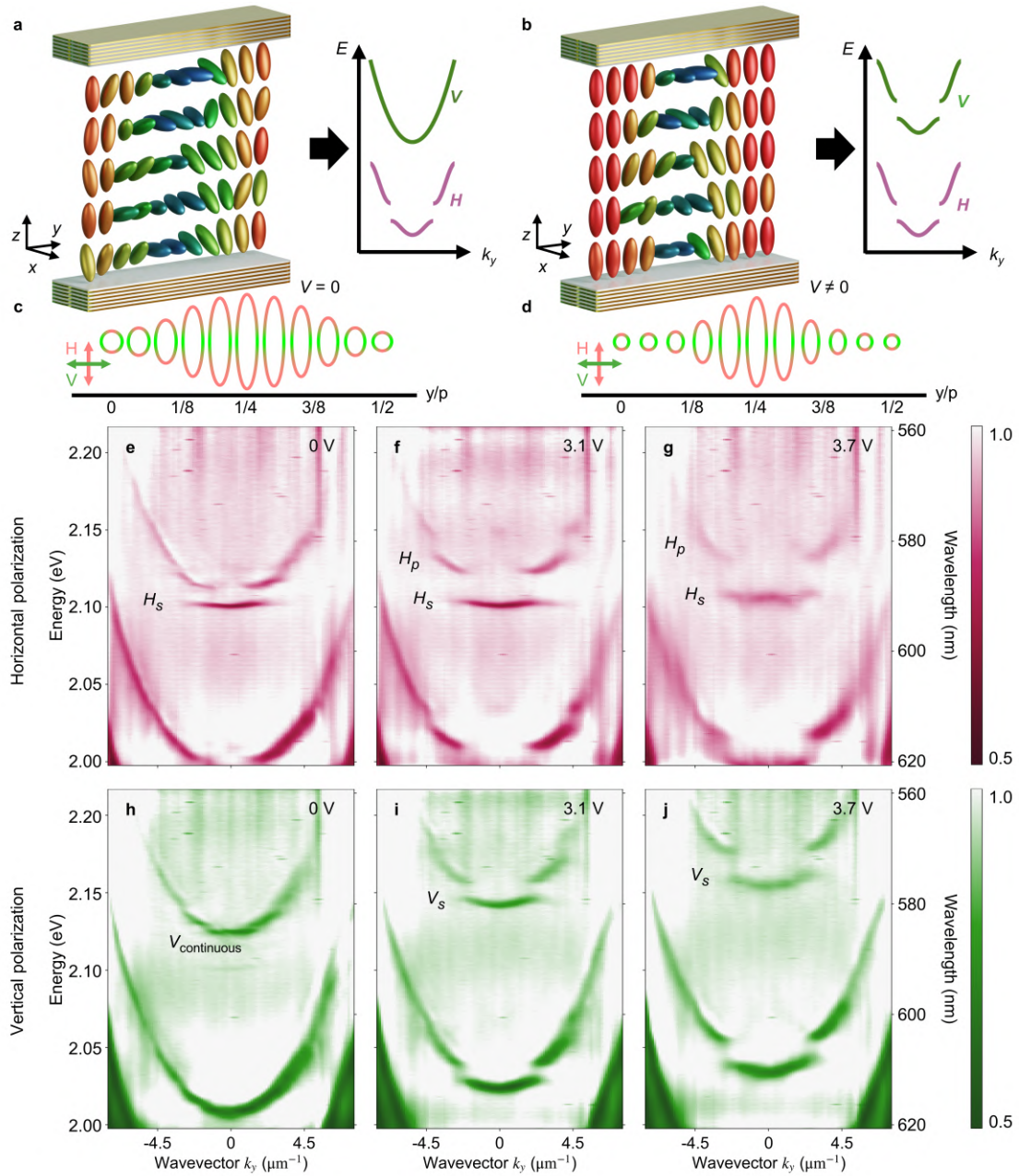


Figure 4.13: **Lattice tunability in ULH LC microcavity (sample A)**. Illustrative representation of the LC director arrangement inside the microcavity and the corresponding schematic dispersion relations of the horizontally- ( $H$ , pink) and vertically- ( $V$ , green) polarized modes for (a) zero and (b) non-zero voltage; effective refractive index ellipses for  $H$  and  $V$  polarizations showing periodical dependence along the ULH axis  $y$  over half-pitch  $p/2$  and obtained by averaging director distributions shown in (a) and (b) along microcavity axis  $z$  for (c) zero and (d) non-zero voltage, respectively; reflectivity spectra of (e-g)  $H$ - and (h-j)  $V$ -polarized band structures measured for different voltages (indicated in top right corners) applied to the sample A. Adopted from [235].

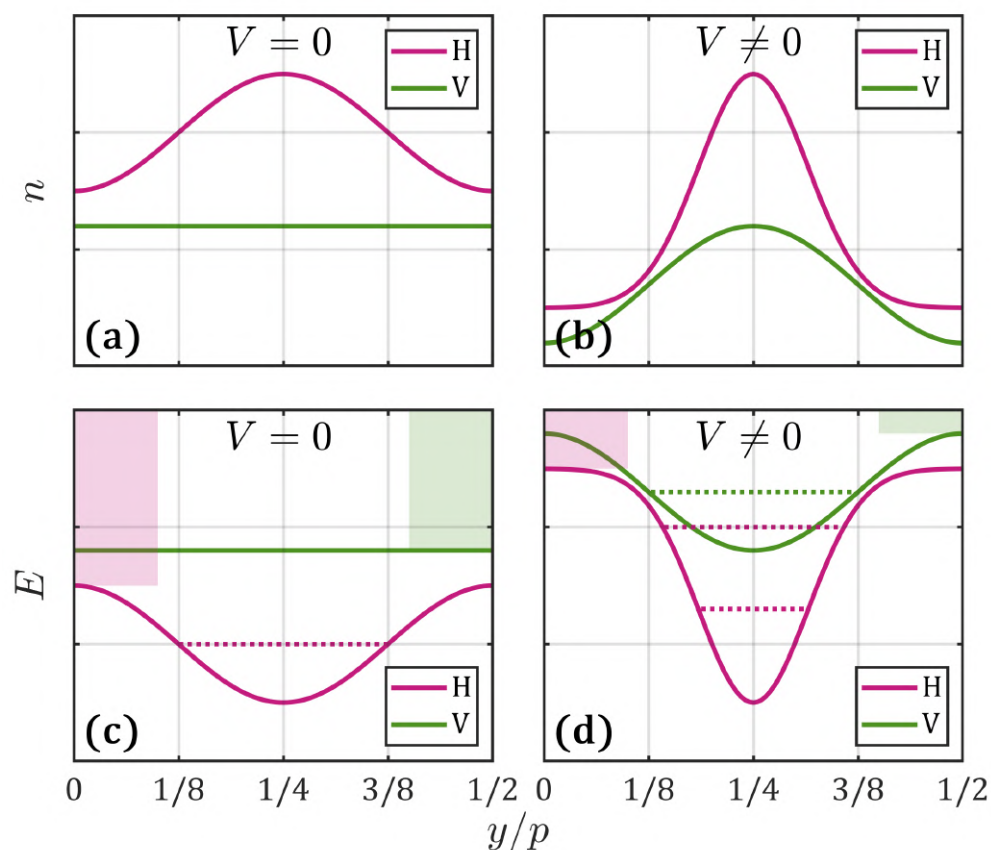


Figure 4.14: **Schematic dependence of refractive indices and corresponding potentials for sample A.** Refractive index real space dependence for (a) zero and (b) non-zero voltage; resulting periodic potentials for (c) zero and (d) non-zero voltage; pink and green colors correspond to H and V polarizations, respectively; dotted lines show single-well localized states and colored rectangles show the energy range of the continuum. Adopted from [235].

potential, *director fluctuations*, and so-called *dielectric effect* [267], governing director reorientation under applied field. Microcavity photons experience a potential defined by the effective refractive index obtained by averaging along  $z$  axis of the microcavity. This averaging can be easily performed for a known LC director distribution inside the microcavity. The ideal helix creates a perfectly uniform distribution of the director along the microcavity axis  $z$ . Its projection on microcavity plane  $x$ - $y$  shows a periodic variation of refractive index along  $y$  for one polarization ( $H$ ) and the absence of variation for another polarization ( $V$ ). In reality, the helix is not ideal, and the angular fluctuations [268] of molecules from ideal orientation occur (marked by color of ellipsoids in Fig. 4.13(a)). Under zero electric field, these fluctuations are randomly distributed and do not have any preferential direction. In general, their effect is a reduction of the effective refractive index contrast. In other words, if we now average the LC director distribution along  $z$  taking into account these fluctuations (Fig. 4.13(a)), the maximum (minimum) refractive index is reduced (increased) for both polarizations in comparison to the ideal helix. The result of this averaging is shown in Fig. 4.13(c) in the form of effective refractive index ellipses for  $H$  and  $V$  polarizations. It is also shown in a more standard way in Fig. 4.14(a), as two separate functions,  $n_H$  (pink) and  $n_V$  (green), representing the effective refractive indices inside the unit cell for  $H$  and  $V$  polarization, respectively. The polarization-dependent potentials created by these refractive index distributions are calculated as:

$$V_{H,V} = \frac{\pi \hbar c N}{n_{H,V} L} \propto \frac{1}{n_{H,V}}, \quad 4.22$$

with microcavity mode number  $N$ , and microcavity length  $L$ . These potentials are schematically depicted in Fig. 4.14(c). The periodic potential with half-pitch period  $p/2$  is present for  $H$  and absent for  $V$ . Naturally, a single potential well (the unit cell itself without periodicity) for  $H$  contains a localized state (shown as a dotted line in Fig. 4.14(c)), creating a band in the periodic system, exactly as in the experiment (Fig. 4.13(e)).

When the voltage is applied to the cavity along the  $z$  axis, molecules aligned closely to the electric field direction are the first to react on the field, and they realign with it even better, while molecules perpendicular to the field almost do not realign. This effect is often referred to as the dielectric effect of the electric field [267]. Thus, the uniformization of the director distribution along  $z$  happens for some regions (edges of the distribution in Fig. 4.13(b,d),  $y/p \approx 0$  or  $1/2$ ), while it does not happen for the others (middle of the distribution in Fig. 4.13(b,d),  $y/p \approx 1/4$ ). Therefore, the effective refractive index contrast is increasing for both polarizations: the highest refractive indices for  $H$  and  $V$  stay almost the same, while the lowest ones are decreasing, as shown in Fig. 4.14(b). Also, the narrowing of the central region (high refractive index region) happens (more red-colored directors appear in Fig. 4.13(b) with respect to Fig. 4.13(a)). In complete analogy with zero-voltage case, the potential is calculated by Eq. 4.22 and shown in Fig. 4.14(d). Now, the potential appears for  $V$  polarization, with a localized state inside a single well. For  $H$  polarization, the potential well deepens and allows now for two localized states. The continuum of states for both  $H$  and  $V$  is also shifted towards higher energy (shown by the pink and green colored rectangles, respectively).

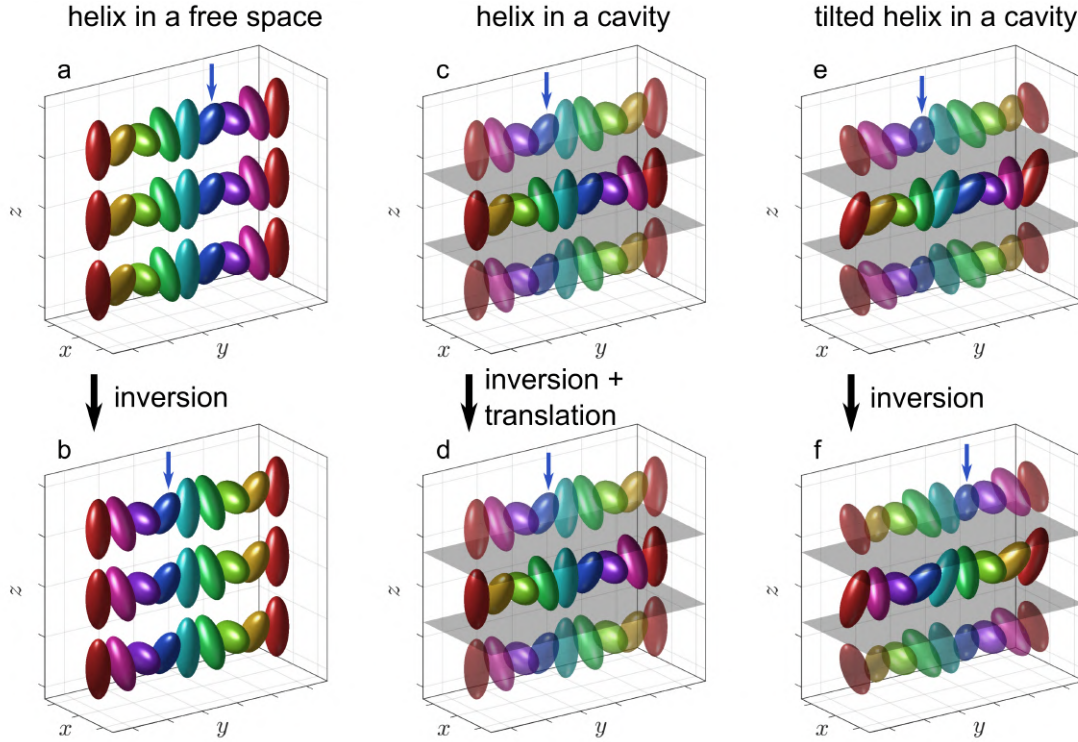


Figure 4.15: **Symmetry analysis of a cholesteric liquid crystal in the ULH configuration.** (a,b) Unbounded, (c,d) perfect bounded (sample A) and (e,f) tilted bounded (sample B) helix configurations; the first and the last break the inversion symmetry, while the second does not. Adopted from [235].

The presented analysis is performed in the assumption of normal incidence ( $k_y = 0$ ). By taking into account non-zero  $k_y$  components, we obtain mostly a quantitative difference, but not a qualitative one. The single case when the qualitative difference appears is the case of zero voltage. In this case,  $V$  polarization has a slight modulation of refractive index along  $y$  for non-zero incidence angles ( $k_y \neq 0$ ). This modulation is significantly less than the one for  $H$  polarization due to the small incidence angles in experiment, therefore, the size of the emerging gap is small, and it cannot be resolved in our experimental setup due to the mode broadening (Fig. 4.13(h)). The described qualitative behavior agrees perfectly with the experimental observations presented in Fig. 4.13(e-j).

#### 4.4.3 CLC-induced photonic spin-orbit coupling

It is important to stress that the strong *optical activity* ( $OA$ ) expected for a CLC helix and discussed in Sec. 3.2.4 does not show up for sample A. The unbounded medium with a cholesteric helix has no inversion symmetry from where its optical activity stems (see Fig. 4.15(a,b); in the following, for simplicity, one can simply track the position of the blue ellipsoid marked by the blue arrow). When a cholesteric helix is bounded by the cavity in the ULH configuration, the cavity volume can be unfolded to pave the whole space by building the reflection of the helix in the mirrors. In this case, the inversion symmetry (up to a supplementary translation by cavity width) is restored, preventing the appearance

of OA (Fig. 4.15(c,d)). However, this is not the case if an additional molecular tilt is introduced, as we show now for sample B (Fig. 4.15(e,f)).

Fig. 4.16(d-f) presents the angle-resolved reflectivity spectra measured for total intensity (Stokes parameter  $S_0$ ), horizontal  $H$ , and vertical  $V$  polarizations of detected light, respectively; the right parts of the panels are obtained by a semi-analytical model which we will not discuss here (if interested, see details in SM of [235]). The presence of a deeper photonic potential, compared to Fig. 4.13, leads to opening of a greater number of photonic bandgaps, as well as a deeper localization of light: a large effective mass of the trapped photons makes the lowest bands almost flat.

In a system with uncoupled  $H$  and  $V$  polarizations, each of them should possess a band structure with its own ladder of states. However, we observe that the states around 2 eV, expected to be  $H_p$  and  $V_s$ , show up in both polarizations. Fig. 4.16(g,h,i) show the corresponding Stokes parameters  $S_1$ ,  $S_2$ , and  $S_3$ , measured in the reflectivity in  $k$ -space (along  $k_y$ ). It is evident that each of these two coupled states contains both  $H$  and  $V$  contributions. Furthermore, in the circular polarization degree  $S_3$  in Fig. 4.16(i), these states form a non-zero check pattern. Stokes parameters of spatially-resolved ( $r$ -space) transmission spectrum are shown in Fig. 4.16(j-l). The lowest energy states in Fig. 4.16(j) portray the spatial periodicity of the refractive index corresponding to the half-pitch of ULH. The check pattern similar to that in Fig. 4.16(i) is visible in the Stokes parameter  $S_2$  (Fig. 4.16(k)) at energies around 2 eV. All these features prove the presence of spin-orbit coupling in the system.

#### 4.4.4 Spin-orbit coupling approximation by RDSOC

The trigger which forces the OA to reappear again, thus creating this spin-orbit coupling, is the molecular tilt, as was stated above. If the director is rotated (tilted) around  $x$  axis, the inversion symmetry breaks again, therefore, bringing back the OA which was suppressed by the mirrors. Turns out that the tilted ULH is one of the ULH stable configurations [269]. The particular choice of a stable configuration depends on the used LC, deposition techniques, anchoring strength, and other parameters, which explains the difference between samples A and B. The magnitude of the tilt (for small tilts) correlates with the strength of the SOC (see details in SM of [235]).

The polarization pattern which we observe for sample B reminds the one which RDSOC Hamiltonian 3.7 creates. Indeed, in  $k$ -space (Fig. 4.16(g-i)), the diagonal polarization is absent and the circular polarization forms two parabolas, which now just became discretized in energy (see Fig. 3.3(a,b) for comparison). In  $r$ -space, the dominant polarization is observed in  $S_1$  and  $S_2$  Stokes parameters (Fig. 4.16(j-l)), similar to the persistent spin-helix, or emergent optical activity, which creates linearly-polarized stripes in real space, as described in Secs. 3.2.3 and 3.2.4. By combining this remark with the fact that all measurements were done at small angles of incidence, we, actually, restore the similarity between OA of CLC and RDSOC which we extensively discussed in Sec. 3.2.4. Therefore, to reproduce results of the experiment, we can *approximate* the spin-orbit coupling term by RDSOC term. However, we should always keep in mind that the microscopic origin of

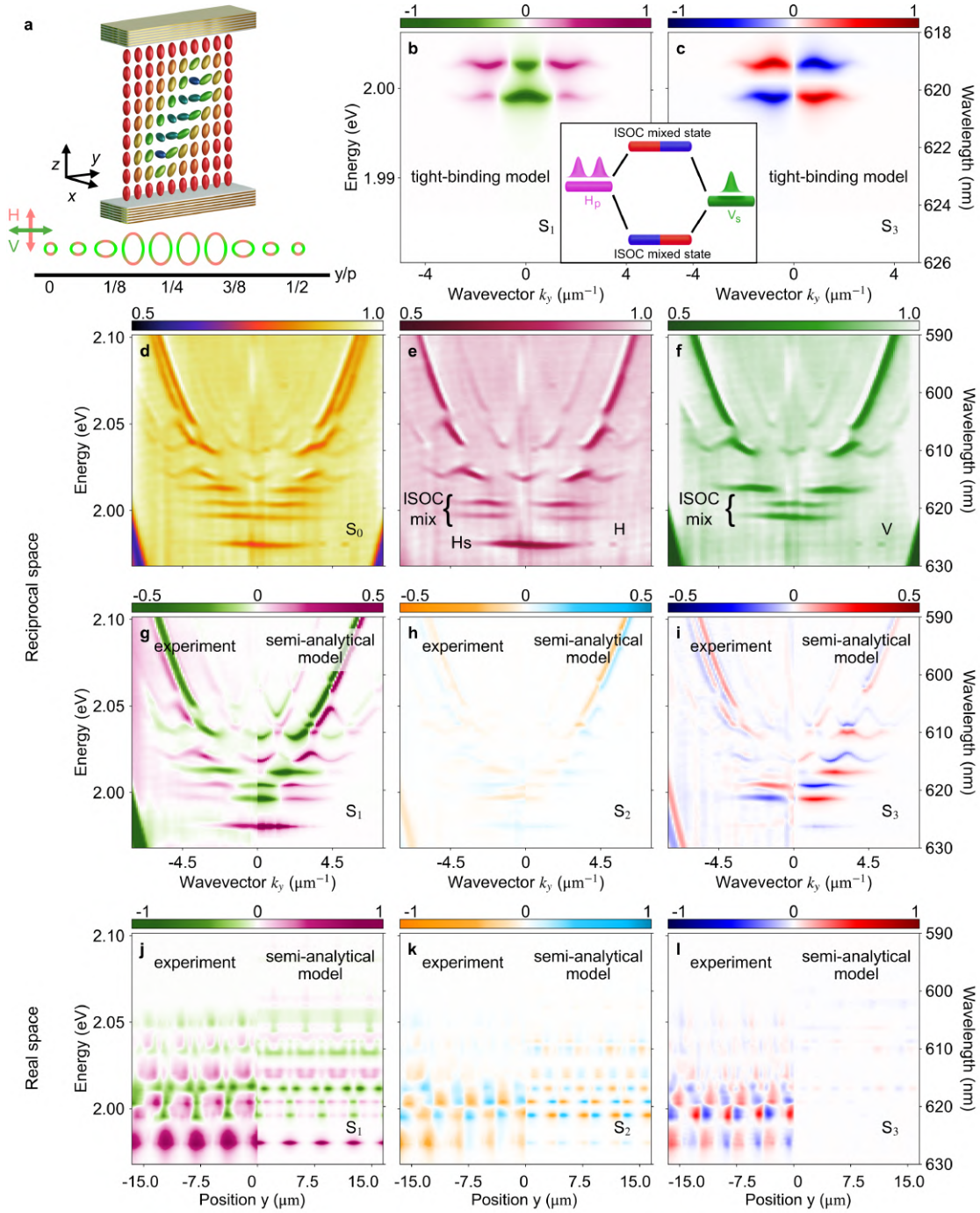


Figure 4.16: *Spin-orbit coupling in ULH LC microcavity (sample B)*. (a) (top) Illustration of the LC director distribution inside the microcavity and (bottom) effective refractive index ellipses;  $sp$ -hybridized bands obtained from the tight-binding Hamiltonian Eq. 4.24 with colors corresponding to (b)  $S_1$  and (c)  $S_3$  Stokes parameters ( $S_2 = 0$  everywhere); the inset shows a scheme of hybridization; the  $k$ -space reflectivity spectra measured for (d) total intensity ( $S_0$  Stokes parameter) and orthogonal linear (e) horizontal  $H$  and (f) vertical  $V$  polarization of light; Stokes parameters  $S_1$ ,  $S_2$ , and  $S_3$  in (g,h,i) reciprocal and (j,k,l) real space, respectively; the left halves of the Stokes parameter panels correspond to the experimental data, while the right halves represent the results of semi-analytical model (see details in SM of [235]); the SOC-mixed eigenstates appear near 2.0 eV as a result of coupling between  $p$  band of  $H$  polarization and  $s$  band of  $V$  polarization. Adopted from [235].

the SOC is different.

In this case, an effective Hamiltonian describing the cavity modes of two polarizations  $H$  and  $V$  in the polarization-dependent periodic potential created by the ULH in the  $(|H\rangle |V\rangle)^T$  basis in real space reads:

$$H_{cont} = \begin{pmatrix} -\frac{\hbar^2}{2m} \frac{\partial^2}{\partial y^2} + \frac{A_H}{2} [1 - \cos(2qy)] - \frac{\delta}{2} & -2i\alpha \frac{\partial}{\partial y} \\ -2i\alpha \frac{\partial}{\partial y} & -\frac{\hbar^2}{2m} \frac{\partial^2}{\partial y^2} + \frac{A_V}{2} [1 - \cos(2qy)] + \frac{\delta}{2} \end{pmatrix}, \quad 4.23$$

where  $m$  is the mass of a cavity photon moving along  $y$ ,  $\delta$  is the linear splitting, and  $q = 2\pi/p$  is the pitch wavevector of the ULH.  $A_{H,V}$  are potential amplitudes for  $H$  and  $V$  polarizations, respectively.

Now, we can derive from the continuous Hamiltonian 4.23 a tight-binding Hamiltonian reproducing in a transparent manner the coupling between the orthogonally  $H$ - and  $V$ -polarized bands of the periodic potential observed in the experiment. As we already discussed in Sec. 4.3 devoted to the tunneling control, the RDSOC term couples only localized states of opposite parity. The most pronounced coupling happens in the experiment around 2 eV between the  $s$ -band in  $V$  polarization ( $V_s$ ) and the  $p$ -band in  $H$  polarization ( $H_p$ ). By focusing exclusively on these two bands, we can write a 2x2 tight-binding Hamiltonian:

$$H = \begin{pmatrix} E_{H_p} - 2t_{pp} \cos(k_y p/2) & -i\alpha [t_{sp,0} - 2t_{sp,1} \cos(k_y p/2)] \\ c.c. & E_{V_s} - 2t_{ss} \cos(k_y p/2) \end{pmatrix}, \quad 4.24$$

where  $E_{H_p}$  and  $E_{V_s}$  are the onsite energies of  $H_p$  and  $V_s$ , respectively,  $t_{pp}$  and  $t_{ss}$  are the nearest-neighbor tunnelings between  $p$  states of  $H$  and  $s$  states of  $V$ , respectively,  $t_{sp,0}$  and  $t_{sp,1}$  are the onsite and nearest-neighbor cross-polarized couplings between  $H_p$  and  $V_s$ , respectively, and c.c. stands for complex conjugate. All terms are calculated from the Hamiltonian 4.23 using the standard perturbation theory on a trial basis of  $s$  and  $p$  states of a harmonic oscillator (see explicit expressions for terms and values used in App. B). In the limit of strongly localized modes ( $\alpha t_{sp,1}$ ,  $t_{ss}$ ,  $t_{pp} \ll \alpha t_{sp,0}$ ), which is our case, the spectrum of the Hamiltonian (4.24) is shown in Fig. 4.16(b,c), with color representing the Stokes parameters  $S_1$  and  $S_3$ . The resemblance between the theory (Fig. 4.16(b,c)) and experiment (Fig. 4.16(g,i)) is evident.

## 4.5 Perspectives for 2D lattice models

This short Section discusses 2D models that can be implemented with RDSOC. As was already mentioned in Sec. 3.1 and elaborated in Sec. 3.2.3, since RDSOC is a 1D SOC, the effects which it induces are few. Therefore, spatial modulation of its magnitude or direction can be used to achieve richer physics. We give two examples, HH and XY models, in order to emphasize the usefulness of both RDSOC lattice regimes, phase control and amplitude control.

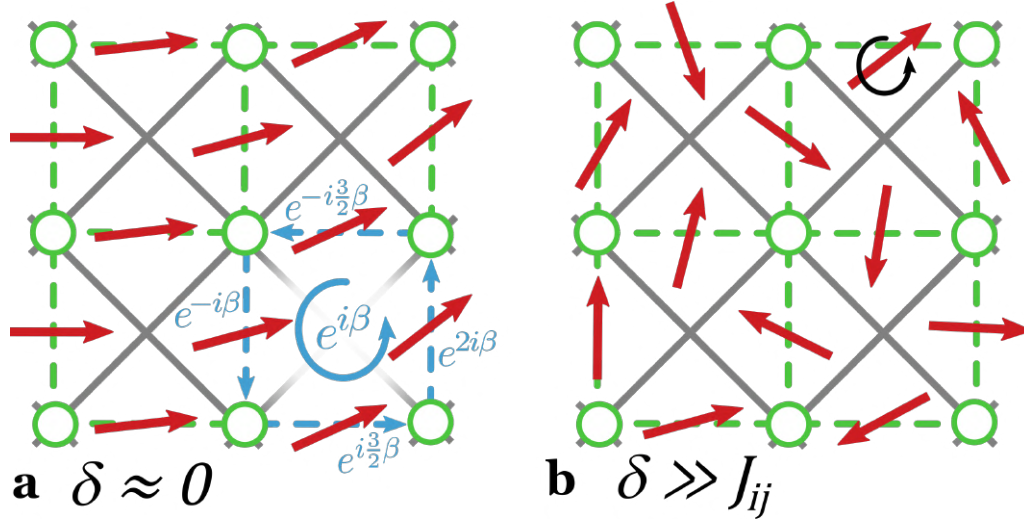


Figure 4.17: **2D lattice models.** Schemes of (a) Harper-Hofstadter and (b) XY models that can be realized with RDSOC; green circles are lattice sites; red arrows show the local direction of RDSOC; blue arrows indicate the total phase per plaquette for HH model (for one circular polarization). Adopted from [248].

#### 4.5.1 HH model in tunneling phase control regime

Following the approach of Sec. 3.2.3, we can consider the RDSOC with variation of orientation in real space. Let us focus on the case of RDSOC rotation with constant rate along  $x$  axis, and absent linear detuning  $\delta$ . Then, the angle of RDSOC orientation in real space with respect to  $x$  axis is  $\theta = \tau x$ , where  $\tau$  is a spatial rotation rate. The Hamiltonian 3.16 can then be rewritten as:

$$H = \frac{(p_x \sigma_0 - A_{RD,x}(x) \sigma_z)^2}{2m} + \frac{(p_y \sigma_0 - A_{RD,y}(x) \sigma_z)^2}{2m} + E_0 \sigma_0, \quad 4.25$$

$$A_{RD,x}(x) = \frac{2m\alpha}{\hbar} \cos \tau x, \quad A_{RD,y}(x) = \frac{2m\alpha}{\hbar} \sin \tau x.$$

The out-of-plane magnetic field (Eq. 3.21) acting on in-plane circular polarization currents  $J_{1,2}^3$  is, therefore:

$$\mathcal{B}_3^3(x) = \frac{2m\alpha}{\hbar} \tau \cos \tau x. \quad 4.26$$

This field is positive (along  $z$ ) for + polarization, and negative (counter  $z$ ) for - polarization. In the simplest case of small  $\theta$ , the field  $\mathcal{B}_3^3$  can be well-approximated by a constant field, which creates a spectrum of equidistant Landau levels, with the level spectral separation of  $\Delta E = \hbar \omega_c = 2\alpha\tau$ , where  $\omega_c$  is a cyclotron frequency. For a realistic value of RDSOC magnitude  $\alpha \approx 3.2 \text{ meV} \cdot \mu\text{m}$  [81] and spatial rotation rate  $\tau = 2\pi/40 \mu\text{m}$ , one gets  $\Delta E \approx 1 \text{ meV}$ , completely feasible to observe in experiment. If a square lattice is added to this picture, and it is located in the region of small  $\theta$ , the resulting model is equivalent to the *TRS-conserving HH model* (see Sec. 2.3.2 and Fig. 4.17(a)), where circular polarizations are uncoupled and each of them is described by the HH model with opposite chirality (edge state propagation direction). The similarity can be drawn here with the Quantum Spin Hall Effect in the context of the Kane-Mele model [197], which

can be viewed as two uncoupled spin-polarized copies of Haldane model [30] with opposite chirality. However, an important difference exists between HH and Haldane models, since the former breaks the TRS by non-zero total magnetic flux while the latter does it by a local magnetic field with the total flux of zero.

The nematic LC microcavity provides everything needed to implement this model. The square lattice can be patterned as was done in Sec. 4.3. The easiest way to realize a real-space variation of RDSOC direction is to deposit side-by-side two rubbing layers with different rubbing orientation defining LC director rotation plane, and, consequently, RDSOC orientation (Sec. 3.2). Inside the transition region between two layers, the LC director tends to continuously rotate in space from orientation defined by the first layer towards orientation defined by the second. The resulting RDSOC orientation in space should look like depicted in Fig. 4.17(a) by red arrows.

The same prediction of TRS-conserving HH model can be done with our formalism of phase control method. We know, that in the case of  $\delta \approx 0$ , opposite circular polarizations acquire opposite RDSOC phases Eq. 4.1. Therefore, for a 2D lattice with spatially varying RDSOC orientation shown in Fig. 4.17(a), we can assign an RDSOC phase for each link. If we trace now the total phase per lattice plaquette for one of circular polarizations (blue arrows), we get a non-zero value, exactly as discussed in Sec. 2.3.2. The phase per plaquette for an opposite circular polarization has an opposite sign.

## 4.5.2 XY Hamiltonian in tunneling amplitude control regime

In the amplitude control regime  $\delta \gg J_{ij}$ , the spatially-dependent orientation of the RDSOC allows to control the magnitudes and the signs of individual tunnelings according to the Eq. 4.4. By considering a square lattice with only nearest-neighbour tunnelings  $J$  (Fig. 4.17(b)), the Hamiltonian 4.4 can be mapped to the classical *XY Hamiltonian* [270]:

$$\hat{H}_{XY} = \sum_{i,j} J \cos \beta_{ij} \cos(\eta_i - \eta_j), \quad 4.27$$

where  $\eta_i$  is the orientation of the in-plane XY 'spin'  $i$ , encoded in the phase of the wavefunction  $\arg \psi_i$  at site  $i$ . This Hamiltonian allows to simulate complex spin-liquid phases, superfluids, superconductors, and solve some optimization problems [271, 270, 272, 273]. The dynamical version of XY model is also known as *Kuramoto network* [274], one of the simplest models describing synchronization and very important in the field of neural networks.

Contrary to the suggested HH model realization, this model requires control over RDSOC direction at the level of individual lattice tunnelings, which is very challenging. In LC microcavities, this can possibly be achieved with the use of more elaborated rubbing layer engineering [275]. Some studies even claim the in-plane control over LC director orientation by applied voltage [276]. If this possibility indeed exists, then by arranging individual electrodes in a lattice (grey squares in Fig. 4.17), the RDSOC in-plane direction can be controlled locally, therefore providing a full tunability for HH model (previous Section 4.5.1) in the phase control regime and for XY model in the amplitude control

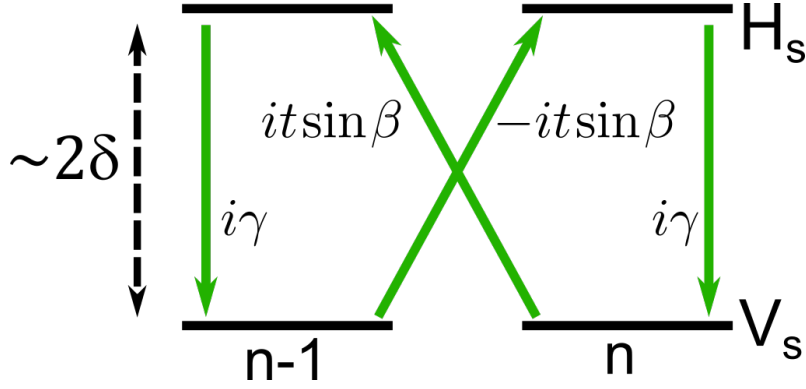


Figure 4.18: **Non-reciprocal tunneling.** Non-reciprocal tunneling (inequivalent forward and backward transitions) as the 2nd order perturbation correction which appears due to the combination of linear detuning  $\delta$ , RDSOC (phase  $\beta$ ), and circular dichroism  $\gamma$ ; green arrows mark allowed transitions.

regime. Such a LC-based simulator would be compact and benefit from high accessibility to the lattice state.

## 4.6 1D non-Hermitian models with RDSOC

In this Section we extend the results developed in Sec. 4.1 by introducing the spin-dependent lifetime of particles. This term is *non-Hermitian*, and it allows us to achieve *non-reciprocal tunneling coefficients* in amplitude control regime. As a consequence, we observe the effects of pure non-Hermitian nature: NHSE and anomalous bulk-boundary correspondence. We demonstrate these effects first in tight-binding model to gain a better understanding of physics behind, and then suggest their realistic implementations in photonics and electronics without need for any lattice potential. We will use the terminology of photonics everywhere, except the last Sec. 4.6.4. However, the results are generic and can be applied to any platform providing the same ingredients.

### 4.6.1 Hatano-Nelson tight-binding model

We start by considering a spin- $\frac{1}{2}$  particle in a 1D monomer chain of coupled potential wells, in the presence of the RDSOC (phase  $\beta$ ), linear detuning  $\delta$ , and spin-dependent loss  $\gamma$ , which is typically called *circular dichroism* in the case of photonics. The Hamiltonian of the system in the tight-binding approximation (Fig. 4.19(a)) is:

$$H_1 = \sum_n \delta \sigma_x a_n^\dagger a_n + i\gamma \sigma_z a_n^\dagger a_n + t e^{i\beta \sigma_z} a_{n+1}^\dagger a_n + t e^{-i\beta \sigma_z} a_n^\dagger a_{n+1}, \quad 4.28$$

where  $a_n$  ( $a_n^\dagger$ ) is an annihilation (creation) operator of a particle at lattice site  $n$ , and  $t$  is a tunneling coefficient. On-site circular dichroism  $\gamma$  is a new ingredient which was absent in our previous study of SSH model (Sec. 4.1) and which makes the Hamiltonian non-Hermitian. The average lifetime term  $-i\gamma_0 \sigma_0$  is not included in the Hamiltonian since it does not affect the physics related to the NHSE.

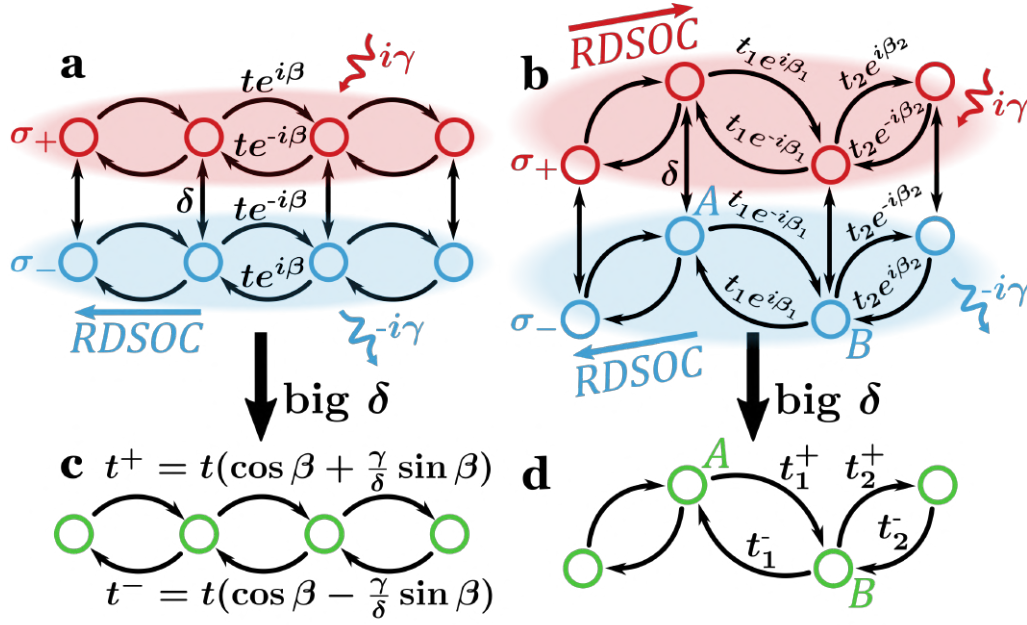


Figure 4.19: **Model transformations in the amplitude control regime.** (a) Spinful monomer and (b) SSH chains with RDSOC phases  $\beta_i$ , linear detuning  $\delta$  and circular dichroism  $\gamma$ , which in the amplitude control regime transform into (c) non-Hermitian HN and (d) SSH models. Adopted from [277].

We look at the tunneling amplitude control regime:  $|\delta| \gg |t|, |\gamma|$ . Contrary to the case of absent circular dichroism (Fig. 4.7(a)), where two-step transitions between neighboring sites were prohibited, here two-step transitions are allowed thanks to the one of the steps (previously prohibited) enabled by circular dichroism (Fig. 4.18). Also, as clearly seen from Fig. 4.18, the forward path ( $n-1 \rightarrow n$ ) and backward path ( $n \rightarrow n-1$ ) are not equivalent, therefore, producing a non-reciprocity in tunneling in the 2nd order perturbation theory. In this case, the effective Hamiltonian obtained from Eq. 4.28 (up to the 2nd order) in the linearly-polarized subspace  $a_n^\dagger |0\rangle \otimes |\sigma_x; -\rangle$  reads as:

$$\begin{aligned}
 H_1^{eff} &= H_{1,onsite}^{eff} + H_{1,NN}^{eff} + H_{1,NNN}^{eff}, \\
 H_{1,onsite}^{eff} &= \sum_n \left( -\delta + \frac{\gamma^2 - 2t^2 \sin^2 \beta}{2\delta} \right) a_n^\dagger a_n, \\
 H_{1,NN}^{eff} &= \sum_n t^- a_n^\dagger a_{n+1} + t^+ a_{n+1}^\dagger a_n, \\
 H_{1,NNN}^{eff} &= \sum_n \frac{t^2 \sin^2 \beta}{2\delta} (a_n^\dagger a_{n+2} + a_{n+2}^\dagger a_n), \\
 t^\pm &= t(\cos \beta \pm \frac{\gamma}{\delta} \sin \beta).
 \end{aligned} \tag{4.29}$$

where  $H_{1,onsite}^{eff}$ ,  $H_{1,NN}^{eff}$ ,  $H_{1,NNN}^{eff}$  stand for on-site, nearest neighbor (NN), and next-nearest neighbor (NNN) Hamiltonian contributions, respectively. As one can see from Eq. 4.29, forward and backward tunneling coefficients  $t^\pm$  differ by a factor  $\frac{\gamma}{\delta} \sin \beta$ . The

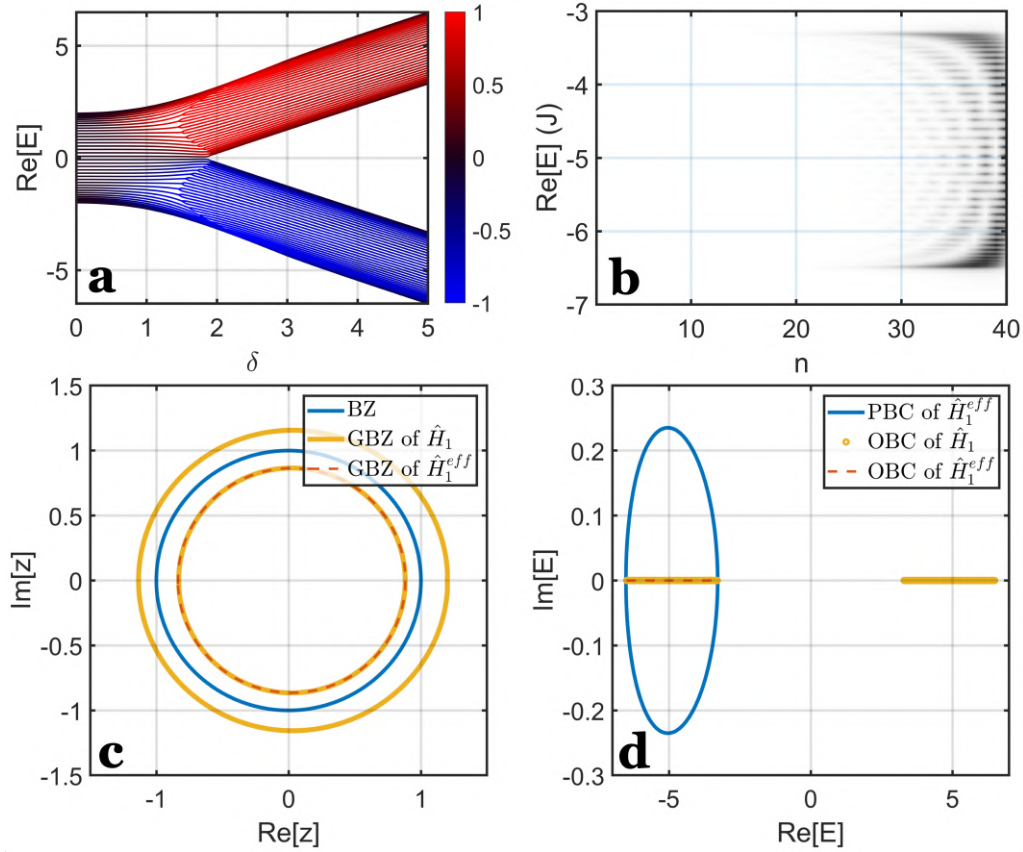


Figure 4.20: **NHSE in a monomer chain.** (a) Transition from the full Hamiltonian 4.28 to the effective Hamiltonian 4.29 for a 40-site chain with an increase of  $\delta$  displaying NHSE; blue (red) color shows the right (left) edge localization degree (similar to Eq. 2.3); (b) normalized density of eigenstates for the lower band of (a) depending on the real part of the energy  $\text{Re}[E]$  and site number  $n$ ; (c) BZ, GBZs of Eq. 4.28 and Eq. 4.29; (d) PBC spectrum of Eq. 4.28, OBC spectra of Eq. 4.28 and Eq. 4.29; parameters:  $t = 1$ ,  $\gamma = 1$ ,  $\delta = 5$ ,  $\beta = 0.2\pi$ . Adopted from [277].

chain is equivalent to the non-reciprocal HN model up to the NNN tunnelings (Fig. 4.19(c)).

We next consider a finite 40-site chain. Fig. 4.20(a) shows the real eigenenergies of the full Hamiltonian 4.28 versus  $\delta$ . With increasing  $\delta$ , a single band splits into two subbands ( $a_n^\dagger|0\rangle \otimes |\sigma_x; -\rangle$  and  $a_n^\dagger|0\rangle \otimes |\sigma_x; +\rangle$  for big  $\delta$ ). Each of the two subbands shows a strong localization of eigenstates on the edge of the chain (opposite edges for different subbands). Fig. 4.20(b) demonstrates for  $\delta/|t| = 5$  the spatial distribution of modes of the lowest band, which confirms the localization on the right edge.

The GBZs of the full Hamiltonian 4.28 and the effective Hamiltonian 4.29 are shown in Fig. 4.20(c) by yellow and red lines, respectively. The GBZ of the full Hamiltonian 4.28 consists of two closed lines, one inside the BZ (unit circle, blue) and one outside, corresponding to two subbands localized on the opposite edges. The GBZ of the reduced Hamiltonian 4.29 is in perfect agreement with the inner part of GBZ of the full Hamiltonian 4.28, confirming their equivalence in this limit. In contrast to a pure HN model, red and yellow circles are not centered at  $z = 0$  due to the presence of NNNs (4.29). As

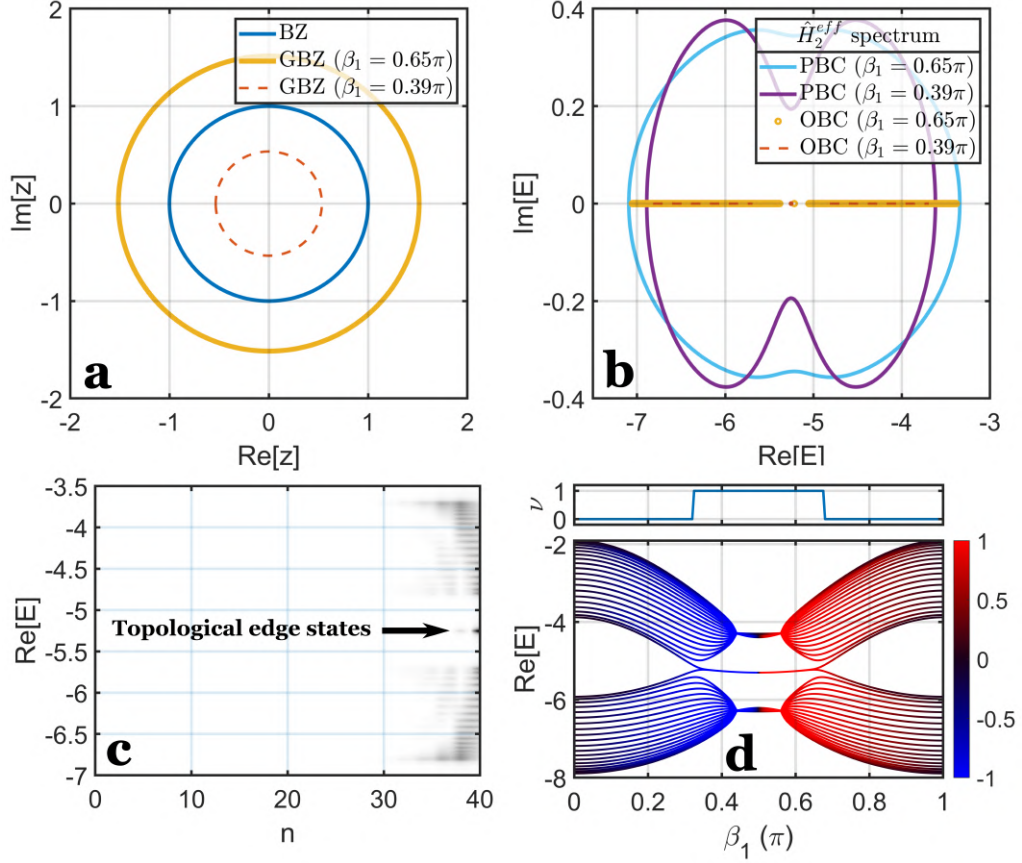


Figure 4.21: **NHSE in an SSH chain.** (a) BZ, GBZs of Hamiltonian 4.32 for two values of  $\beta_1$ ; (b) PBC spectra of 4.32, OBC spectra of 4.32 for two values of  $\beta_1$ , each showing two coinciding topological edge states; (c) normalized density of eigenstates of a 40-site chain depending on the real part of the energy  $\text{Re}[E]$  and site number  $n$ ; (d) real spectrum of Eq. 4.32 vs  $\beta_1$  displaying NHSE as well as a topological transition (bottom) confirmed by the winding number  $\nu$  (top); blue (red) color shows the right (left) edge localization (similar to Eq. 2.3); parameters:  $t_1 = 2$ ,  $t_2 = 1$ ,  $\gamma = 1$ ,  $\delta = 5$ ,  $\beta_2 = 0$ . Adopted from [277].

a result, the localization length is state-dependent (Fig. 4.20(b)).

Fig. 4.20(d) depicts the OBC spectra of Hamiltonians 4.28 (solid yellow line) and 4.29 (dashed red line) forming real-valued segments, and complex PBC spectrum of Hamiltonian 4.29 (blue solid line). One can see that the effective Hamiltonian 4.29 perfectly approximates the OBC spectrum of the lower energy band of the full Hamiltonian 4.28. The complex PBC spectrum can be used to compute a non-Hermitian spectral winding number (Eq. 2.25):

$$w_{E_b=-5} = -1. \quad 4.30$$

Therefore, the NHSE is confirmed by all approaches: GBZ, pronounced difference between PBC and OBC spectra, and spectral winding number.

### 4.6.2 Non-Hermitian SSH tight-binding model

We continue by considering the SSH model with the same ingredients: linear detuning  $\delta$ , RDSOC (phases  $\beta_{1,2}$ ), and circular dichroism  $\gamma$ . The Hamiltonian is written as (Fig. 4.19(b)):

$$H_2 = \sum_n \delta \sigma_x (a_{n,A}^\dagger a_{n,A} + a_{n,B}^\dagger a_{n,B}) + i\gamma \sigma_z (a_{n,A}^\dagger a_{n,A} + a_{n,B}^\dagger a_{n,B}) + (t_1 e^{i\beta_1 \sigma_z} a_{n,B}^\dagger a_{n,A} + t_2 e^{-i\beta_2 \sigma_z} a_{n,B}^\dagger a_{n+1,A} + h.c.), \quad 4.31$$

where  $t_1$  ( $t_2$ ) is an intra-(inter-)cell tunneling. By considering the amplitude control regime again ( $|\sigma_x; -\rangle$  polarization subspace), one can transform the Hamiltonian 4.31 to an effective Hamiltonian:

$$\begin{aligned} H_2^{eff} &= H_{2,onsite}^{eff} + H_{2,NN}^{eff} + H_{2,NNN}^{eff}, \\ H_{2,onsite}^{eff} &= \sum_n \left[ -\delta + \frac{\gamma^2 - (t_1^2 \sin^2 \beta_1 + t_2^2 \sin^2 \beta_2)}{2\delta} \right] (a_{n,A}^\dagger a_{n,A} + a_{n,B}^\dagger a_{n,B}), \\ H_{2,NN}^{eff} &= \sum_n t_1^+ a_{n,B}^\dagger a_{n,A} + t_1^- a_{n,A}^\dagger a_{n,B} + t_2^- a_{n,B}^\dagger a_{n+1,A} + t_2^+ a_{n+1,A}^\dagger a_{n,B}, \\ H_{2,NNN}^{eff} &= \sum_n \frac{t_1 t_2 \sin \beta_1 \sin \beta_2}{2\delta} (a_{n+1,A}^\dagger a_{n,A} + a_{n+1,B}^\dagger a_{n,B} + h.c.), \\ t_i^\pm &= t_i (\cos \beta_i \pm \frac{\gamma}{\delta} \sin \beta_i). \end{aligned} \quad 4.32$$

Analogously to the Hamiltonian 4.29, the effective Hamiltonian 4.32 contains on-site, NN, and NNN contributions. Up to the NNN terms, the Hamiltonian 4.32 is equivalent to the non-Hermitian SSH model described in Sec. 2.4.2 (Fig. 4.19(d)). Both intra- and inter-cell tunnelings become non-reciprocal, controlled by different RDSOC phases  $\beta_{1,2}$ . We investigate the case when  $\beta_2 = 0$  for simplicity. Consequently, the NNN terms vanish (see Eq. 4.32), and the chiral symmetry of the Hamiltonian 4.32 is restored. We stress that the NHSE is present for other values of  $\beta_2$  as well. The Hamiltonian 4.32 then can be transformed into the conventional SSH Hamiltonian by similarity transformation  $H_{SSH} = S H_2^{eff} S^{-1}$  with  $S = \text{diag}\{1, rs, r, r^2 s, \dots, r^{N-1}, r^N s\}$ ,  $r = \sqrt{t_1^- t_2^- / t_1^+ t_2^+}$ ,  $s = \sqrt{t_1^+ / t_1^-}$ , where  $2N$  defines the total number of lattice sites in the chain. The topology of the chain is then described by the Hermitian winding  $\nu$  (Sec. 2.3.1) such that  $\nu = 1$  for  $|t_2^+ t_2^-| > |t_1^+ t_1^-|$ , and  $\nu = 0$  otherwise. The biorthogonal polarization (Eq. 2.32) shows the same transition for the full Hamiltonian 4.31.

In Fig. 4.21(a) we show the GBZ for two different values of  $\beta_1$ :  $\beta_1 > \pi/2$  (solid yellow line) and  $\beta_1 < \pi/2$  (dashed red line). They indicate the NHSE with accumulation on different edges, which is also confirmed by Fig. 4.21(d), demonstrating finite chain spectrum for different values of  $\beta_1$  with a blue (red) color corresponding to the right (left) edge localization. The OBC spectra for the aforementioned values of  $\beta_1$  are depicted in Fig. 4.21(b) (solid yellow and dashed red lines) together with PBC spectra (solid blue and purple lines). The individual dots between two bands of each OBC spectrum are the topological states. These topological states are localized at the edge of the chain (as the

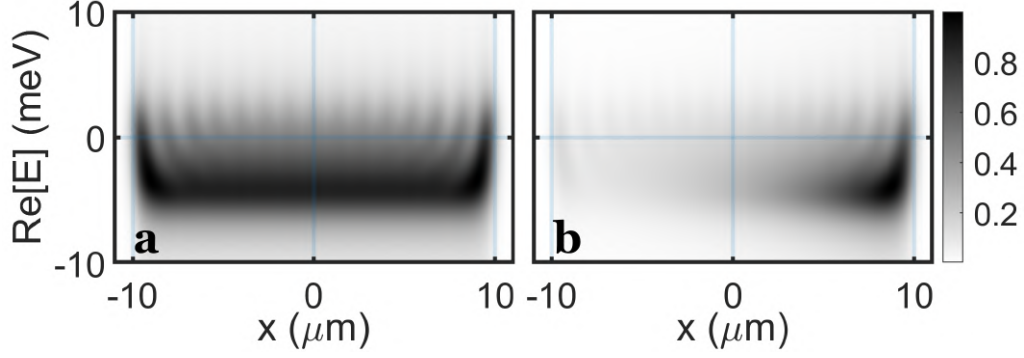


Figure 4.22: **NHSE in a photonic potential well.** Normalized eigenstate density for the lower energy states of the potential well depending on the real part of the energy  $\text{Re}[E]$  and real space coordinate  $x$ : (a) Hermitian and (b) non-Hermitian cases; parameters:  $d = 20 \mu\text{m}$ ,  $U_0 = 10 \text{ meV}$ ,  $m = 1.6 \cdot 10^{-5} m_e$ ,  $m_e$  is the electron mass,  $\alpha = 1 \text{ meV} \cdot \mu\text{m}$ ,  $\delta = 5 \text{ meV}$ , (a)  $\gamma = 0 \text{ meV}$  and (b)  $\gamma = 0.25 \text{ meV}$ . Adopted from [277].

bulk states), but they are located inside the real gap of the OBC spectrum. They appear in Fig. 4.21(c), where we plot the normalized density of eigenstates versus the lattice site number. In the Hermitian limit ( $\gamma \rightarrow 0$ ), the origin of the topological transition responsible for the formation of the edge states is the modulation of the tunneling amplitudes by the combination of RDSOC  $\beta$  with linear detuning  $\delta$ , as described in Sec. 4.2. Here, this transition is modified by non-Hermiticity and described by the invariant  $\nu$  plotted in the top panel of Fig. 4.21(d). This result is a realization of the anomalous bulk-boundary correspondence (Sec. 2.4.2).

### 4.6.3 NHSE in continuous realistic photonic model

Now, we show that the NHSE can be observed in a photonic potential well, without the use of a lattice. To do so, we consider a photonic microcavity filled with nematic LC and a potential, which can be a barrier or a well structured on a microcavity mirror, or even a strong enough defect. The presence of a chiral absorber or spin-dependent gain in a nonlinear system can create a polarization-dependent lifetime  $\gamma$ . To demonstrate the effect, we solve numerically the 1D spinor stationary Schrödinger equation with the Hamiltonian:

$$H_{ph}(x) = -\frac{\hbar^2}{2m} \frac{\partial^2}{\partial x^2} \sigma_0 - 2i\alpha \frac{\partial}{\partial x} \sigma_z + \delta \sigma_x - i\gamma_0 \sigma_0 + i\gamma \sigma_z + U(x) \sigma_0, \quad 4.33$$

where  $x$  is the real space coordinate,  $m$  is the microcavity photon mass,  $\gamma_0$  is the average loss,  $\gamma$  is the spin-dependent loss,  $\alpha$  is the RDSOC magnitude.  $U(x) = \{0, \text{ if } |x| < d; U_0, \text{ otherwise}\}$  is the real space potential. We plot the normalized eigenstate density for the Hermitian case  $\gamma = 0 \text{ meV}$  in Fig. 4.22(a) and for the non-Hermitian case  $\gamma = 0.25 \text{ meV}$  in Fig. 4.22(b). The parameters used correspond to a realistic LC microcavity. In particular, the broadening for every state is taken as  $\gamma_0 = 2 \text{ meV}$  in full-width half-maximum which exceeds the quantization energy, so the individual states are indistinguishable in Fig. 4.22. Nevertheless, it does not prevent a clear observation of NHSE: one can see that

the non-Hermiticity drives the density of all lowest eigenstates to the right edge of the well. The inversion of either the RDSOC direction ( $\alpha \rightarrow -\alpha$ ) or of the spin-dependent loss ( $\gamma \rightarrow -\gamma$ ) changes the NHSE so that the eigenstates localize at another edge. The continuous change of  $\delta$  also provides the tunability of the effect, with possibility to switch it on and off. A similar NHSE realization based on the spin-orbit coupling was also suggested for cold atoms [278, 279, 280].

This effect can be explained by considering again one polarization band (V) in the limit of large linear detuning  $\delta$ . Then, the Hamiltonian 4.33 is rewritten as:

$$\begin{aligned} H_{ph}^{eff}(x) &= E_0 + U(x) + \xi^2 (-i\partial_x - i\tau)^2, \\ E_0 &= -\delta + \frac{\gamma^2}{2\delta} + \left(\frac{\alpha\gamma}{\xi\delta}\right)^2, \quad \xi^2 = \frac{\hbar^2}{2m} - \frac{2\alpha^2}{\delta}, \quad \tau = \frac{\alpha\gamma}{\xi^2\delta}. \end{aligned} \quad 4.34$$

where  $E_0$  is a constant energy shift,  $\xi^2$  is a kinetic energy scaling,  $i\tau$  is an imaginary gauge potential [281]. By considering a wavefunction ansatz  $\psi(x) = \varphi(x)e^{-\tau x}$ , we arrive at a simple eigenvalue problem of a single spinless particle in a potential well with a wavefunction  $\varphi(x)$ :

$$H_{ph}^{eff}(x)\varphi(x) = \left(E_0 + U(x) - \xi^2\partial_x^2\right)\varphi(x). \quad 4.35$$

As one can see,  $\tau^{-1}$  is a localization length of a wavefunction  $\psi(x)$  and its finite value is a manifestation of NHSE. It is achieved only when  $\alpha, \gamma, \delta$  all have non-zero values, which confirms the necessity of each component in our model. The sign of  $\tau$  (the localization side) is controlled by the combination of signs of  $\alpha$  and  $\gamma$ .

The appearance of the NHSE can be also analyzed from the point of view of Hamiltonian symmetries. One can rewrite the Hamiltonian 4.33 without a potential ( $U(x) = 0$ ) in a reciprocal space as:

$$H_{ph}(k) = \frac{\hbar^2 k^2}{2m} \sigma_0 - 2\alpha k \sigma_z + \delta \sigma_x - i\gamma_0 \sigma_0 + i\gamma \sigma_z, \quad 4.36$$

where  $k$  stands for a wavevector along  $x$ . In the absence of RDSOC ( $\alpha = 0$ ), three symmetries simultaneously prevent the NHSE [119]: conjugated time-reversal symmetry (TRS<sup>†</sup>)  $\mathcal{C}_+$ , pseudo-Hermiticity (PH)  $\eta$  and parity (inversion, P)  $\mathcal{P}$ , which are defined as:

$$\mathcal{C}_+ H^T(k) \mathcal{C}_+^{-1} = H(-k), \quad 4.37$$

$$\eta H^\dagger(k) \eta^{-1} = H(k), \quad 4.38$$

$$\mathcal{P} H(k) \mathcal{P}^{-1} = H(-k). \quad 4.39$$

The symmetry operators in the case of Hamiltonian 4.36 are  $\mathcal{C}_+ = \mathcal{P} = \sigma_0$  and  $\eta = \sigma_x$ . When RDSOC is present ( $\alpha \neq 0$ ), all three aforementioned symmetries are simultaneously broken, giving rise to the NHSE. The single symmetry conserved for both cases is the time-reversal symmetry (TRS)  $\mathcal{T}_+$ , defined as:

$$\mathcal{T}_+ H^*(k) \mathcal{T}_+^{-1} = H(-k), \quad 4.40$$

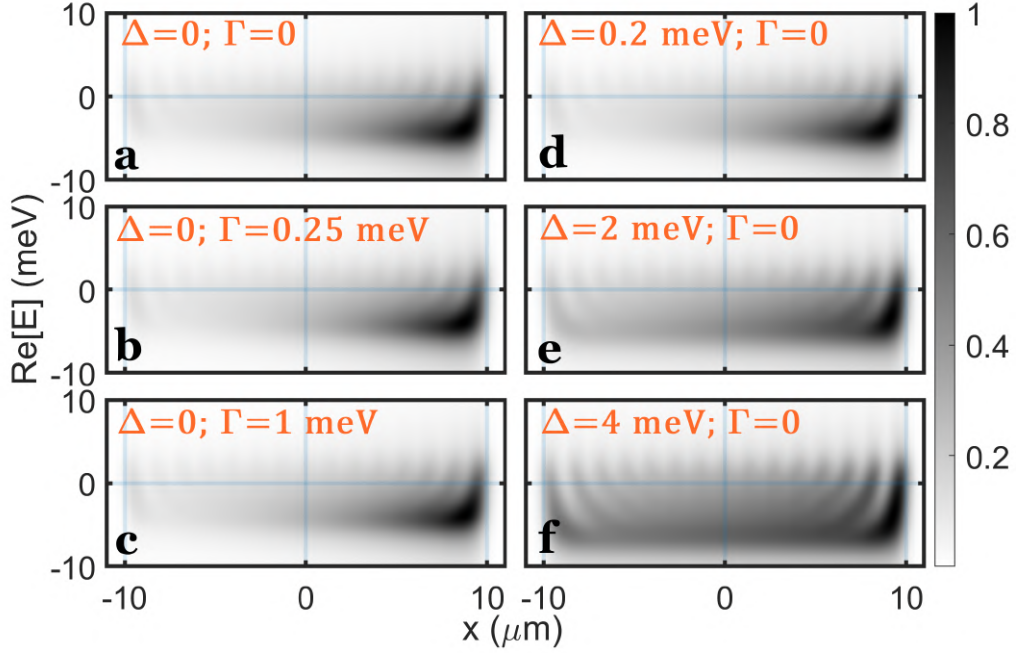


Figure 4.23: *NHSE in a photonic potential well with additional ingredients.* The NHSE obtained for the Hamiltonian [4.41](#) (a) without supplementary terms, (b,c) with linear polarization lifetime imbalance  $\Gamma$ , and (d,e,f) with effective Zeeman splitting  $\Delta$ ; all parameters that are not directly indicated in this Figure are taken from Fig. 4.22. Adopted from [\[277\]](#).

with the symmetry operator  $\mathcal{T}_+ = \sigma_x$ . TRS does not forbid the NHSE, and its conservation is natural since the RDSOC maintains it (Sec. 3.2).

We can also extend our analysis and investigate the effect introduced by two additional terms, typical for optical microcavities. These terms are (1) the effective Zeeman splitting  $\Delta\sigma_z$  and (2) linear polarization lifetime imbalance  $i\Gamma\sigma_x$ , or *linear dichroism*:

$$H_{ph}^{ext}(x) = -\frac{\hbar^2}{2m} \frac{\partial^2}{\partial x^2} \sigma_0 - 2i\alpha \frac{\partial}{\partial x} \sigma_z + (\delta + i\Gamma)\sigma_x + (\Delta + i\gamma)\sigma_z + U(x)\sigma_0. \quad 4.41$$

The first term  $\Delta\sigma_z$  represents the effective out-of-plane magnetic field acting on photon polarization. This term is often desirable in photonic microcavities in order to produce topologically nontrivial photonic states [\[73, 72\]](#). The interplay of effective Zeeman splitting with RDSOC has already been studied in the Hermitian case in a perovskite microcavity [\[231\]](#) and  $^{87}\text{Rb}$  atomic condensate [\[210\]](#). The results show a transition between RDSOC- and Zeeman-dominated regimes. A similar transition should also be present in the non-Hermitian case, and it, in general, can suppress the NHSE. However, the characteristic energy of RDSOC in LC microcavity  $\alpha Q_y$  is significantly bigger than a typical Zeeman splitting, therefore, making the RDSOC contribution dominant in most cases. In Fig. 4.23(a,d,e,f) we present the density of eigenstates of Hamiltonian [4.41](#) for several values of the Zeeman term  $\Delta$ . One can see, as Zeeman splitting amplitude grows, the delocalization of skin states occurs (Fig. 4.23(e,f)). However, the value realistic for a photonic system produces no visible effect on the localization (Fig. 4.23(d)).

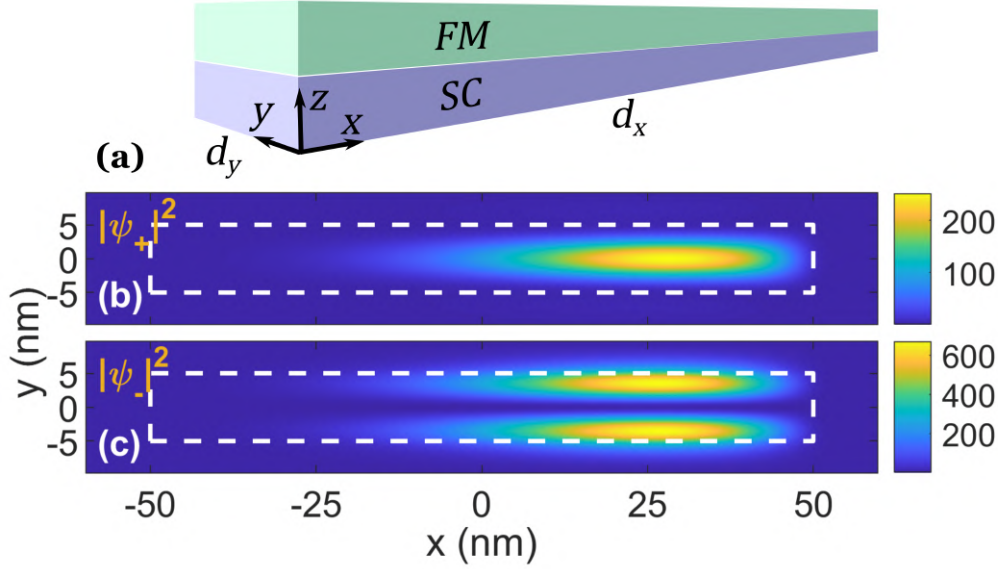


Figure 4.24: **NHSE in an electronic nanowire.** (a) The electronic system proposed to realize the non-Hermitian skin effect: a quantum wire composed of semiconductor (SC) and ferromagnetic (FM) layers; density of (b)  $|\psi_+|^2$  and (c)  $|\psi_-|^2$  spin components (in  $\sigma_y$  basis) of the lowest energy eigenstate with  $n_y = 2$ ; colorbars are in a.u. Adopted from [277].

The second term of interest, linear polarization lifetime imbalance  $i\Gamma\sigma_x$ , is natural for LC microcavity, and it has already been utilized to observe exceptional points creation and annihilation [242]. The magnitude of  $\Gamma$  experimentally measured in Ref. [242] is 0.25 meV. In Fig. 4.23(a,b,c) we present the density of eigenstates of Hamiltonian 4.41 for three different values of  $\Gamma$ . As the figure clearly illustrates, the NHSE always persists, even for a huge value of  $\Gamma$ .

Even in the presence of these additional terms, the role of RDSOC for the NHSE is still central. Without RDSOC ( $\alpha = 0$ ), in both cases ( $\Delta\sigma_z$  or  $i\Gamma\sigma_x$  term),  $\text{TRS}^+$  and  $\text{P}$  symmetries hold ( $\mathcal{C}_+ = \mathcal{P} = \sigma_0$ ), preventing the appearance of NHSE.

#### 4.6.4 NHSE in continuous realistic electronic model

We propose a 1D nanowire made of a semiconductor material with a deposited ferromagnetic material on top (scheme in Fig. 4.24(a)), as a possible system for NHSE realization. This kind of system has been already extensively studied experimentally [282, 283]. Additionally, a theoretical investigation of exceptional points in a planar configuration already exists [284].

We now show why this system is equivalent to our proposal (Eq. 4.33). We consider a semiconductor nanowire with massive electrons and Rashba SOC:  $H_R = \alpha_R(k_y\sigma_x - k_x\sigma_y)$ . The choice of considering either Rashba or Dresselhaus SOC is not crucial, and it depends on the material used and its growth configuration. The key point is that we have only one type of SOC out of two. Such a regime with one contribution dominant over another is easily achievable for InAs or GaAs [285, 207], for example. If the confinement along  $y$  direction is strong, and the corresponding energy quantization is much bigger than the

Rashba SOC along  $x$ , different spin projections of  $\sigma_x$  are only slightly mixed by  $\sigma_y$ . In this case, the effect of the  $k_y$  Rashba component is equivalent to the one of the linear splitting  $\delta$ , while the  $k_x$  Rashba component becomes equivalent to the RDSOC with  $\alpha_R = 2\alpha$ . The amplitude of the effective linear splitting  $\delta$  can be estimated as  $\delta = \alpha_R \langle |k_y| \rangle \approx \alpha_R \pi n_y / d_y$ , where  $n_y$  is the quantization number along  $y$ .

The presence of the ferromagnetic material magnetized along the axis forming  $45^\circ$  with  $x$  in the vicinity of the semiconductor creates an exchange splitting  $2\Delta$  (Zeeman splitting) and spin lifetime difference  $\gamma$ , both proportional to the  $\sigma_y$  Pauli matrix in the Hamiltonian [282, 283, 286, 287]. Therefore, the Hamiltonian of the system reads as:

$$H_{el}(x, y) = -\frac{\hbar^2}{2m} \nabla^2 \sigma_0 + i\alpha_R \frac{\partial}{\partial y} \sigma_x - i\alpha_R \frac{\partial}{\partial x} \sigma_y - i\gamma_0 \sigma_0 + (\Delta + i\gamma) \sigma_y + U(x, y) \sigma_0, \quad 4.42$$

where  $m$  is an effective electron mass,  $\gamma_0$  is an average electron loss, and  $U(x, y)$  is an electronic potential created by the nanowire. Taking into account the discussion above, this Hamiltonian is equivalent to the Hamiltonian 4.41 up to a (pseudo)spin basis transformation.

Finally, we calculate the eigenstate density distribution of Hamiltonian 4.42 in real space and show the results in Fig. 4.24(b,c). The quantum wire has width  $d_y = 5$  nm, length  $d_x = 100$  nm, and potential walls height  $U_0 = 100$  meV. The effective mass  $m = 0.1m_e$  and Rashba amplitude  $\alpha_R = 0.5$  eV·Å are typical for this type of combined semiconductor-ferromagnetic structure. The values of the exchange splitting  $2\Delta = 60$  meV and spin-dependent electron lifetime  $\gamma = 10$  meV are also taken according to the experimental data [286, 287, 288]. We consider the quantization number along  $y$  equal to  $n_y = 2$  since it produces stronger linear splitting  $\delta$  than  $n_y = 1$ , and hence stronger localization. The skin state is clearly visible in Fig. 4.24(b,c).

To conclude, we want to mention that the coupling between a ferromagnet and another material, not a semiconductor, can be also foreseen as a possible realization of the NHSE. For example, the Rashba ferromagnet, a ferromagnetic layer sandwiched between different materials creating an asymmetric confining potential and, consequently, Rashba SOC [289, 290, 291], or a coupled ferromagnet-graphene structure [292] are two systems to cite.



**Contents**

---

<b>5.1 Microcavity scheme and MeLPPP properties</b> . . . . .	<b>107</b>
<b>5.2 Strong coupling</b> . . . . .	<b>109</b>
5.2.1 Experimental results . . . . .	109
5.2.2 Photonic mass extraction . . . . .	111
5.2.3 Tavis-Cummings model with inhomogeneous broadening . . . . .	111
<b>5.3 Condensation</b> . . . . .	<b>115</b>
5.3.1 Condensate polarization control . . . . .	115
5.3.2 Polariton stripes . . . . .	118

---

In this Chapter, we study a system combining the RDSOC and the strong light-matter coupling regime [237]. The latter is realized through the coupling between microcavity photonic modes and excitons in the organic polymer called methyl-substituted ladder-type poly(p-phenylene), or shortly *MeLPPP*. In a thin microcavity, this material demonstrates a huge Rabi splitting in order of 115-145 meV [293, 294]. This allows us to achieve the room-temperature BEC of exciton-polaritons in the RDSOC regime by incorporating this polymer in a LC microcavity. We start by presenting the microcavity scheme and discussing the properties of MeLPPP in Sec. 5.1. We then turn to the confirmation of the strong coupling regime in Sec. 5.2. Next, we discuss the condensation of exciton-polaritons in this sample, and, specifically, the condensation polarization control in Sec. 5.3.1. Finally, we demonstrate a stripe phase in BEC of exciton-polaritons in Sec. 5.3.2, which is considered to be a hallmark of supersolidity. The results of this section were obtained in collaboration with the University of Warsaw, IBM Research–Zurich, Warsaw Military University of Technology, and University of Southampton.

**5.1 Microcavity scheme and MeLPPP properties**

A scheme of the fabricated sample is shown in Fig. 5.1. The microcavity thickness is approximately  $2 \mu m$ , therefore, it hosts plenty of longitudinal modes which we number with integers. The LC ordinary and extraordinary refractive indices are  $n_o \approx 1.57$  and  $n_e \approx 1.98$ , respectively. The LC director rotates in the  $yz$  plane. Modes polarized along  $y$  under normal incidence (H) are tunable by the LC rotation, while modes polarized along  $x$  (V) are not affected by the voltage. Therefore, the RDSOC will appear along  $k_x$ , contrary to Eq. 3.7, where it was along  $k_y$ . Two 35 nm-thick layers of MeLPPP surround the LC layer.

The absorption spectrum of MeLPPP layer deposited on a DBR shows several peaks (Fig. 5.2(a)). The lowest energy peak corresponds to the excitonic resonance, while higher energy peaks are vibronic resonances [293]. Vibrons play a crucial role in the condensation process in MeLPPP: the bottleneck excitons relax towards the bottom of the lower

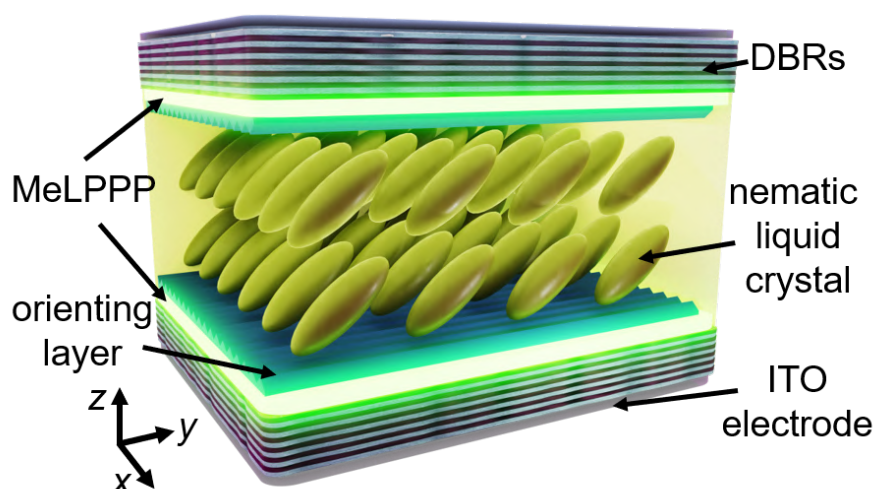


Figure 5.1: *Hybrid microcavity combining the organic polymer MeLPPP and a nematic LC. Thick LC layer sandwiched between two organic polymer layers, two DBRs, and two ITO electrodes. Adopted from [237].*

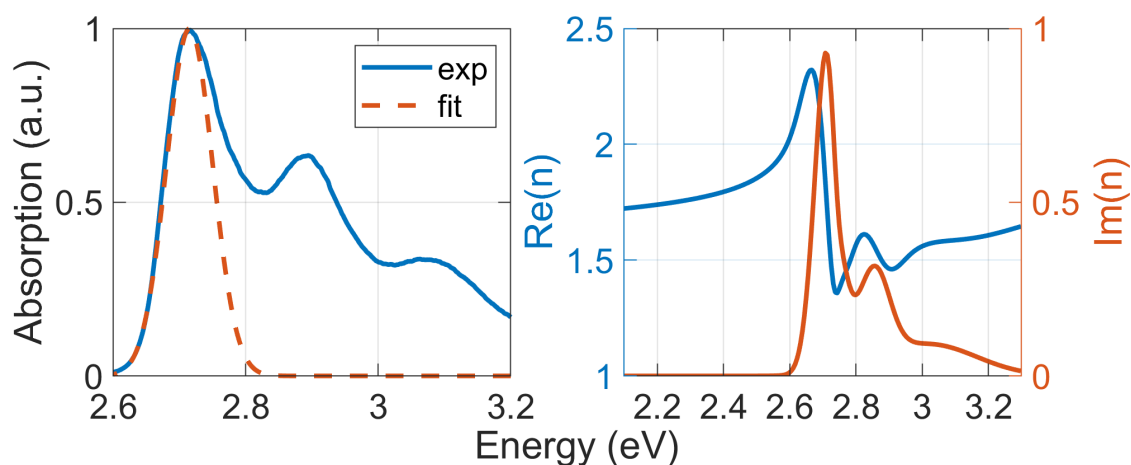


Figure 5.2: *MeLPPP absorption and complex refractive index. (a) Experimentally measured absorption of a single MeLPPP layer on the DBR (solid blue line); the fit of the main absorption peak by a Gaussian function representing the inhomogeneous broadening of excitons (dashed red line); (b) real ( $Re(n)$ , blue line) and imaginary ( $Im(n)$ , red line) parts of the MeLPPP complex refractive index obtained by the ellipsometry. Adopted from [237].*

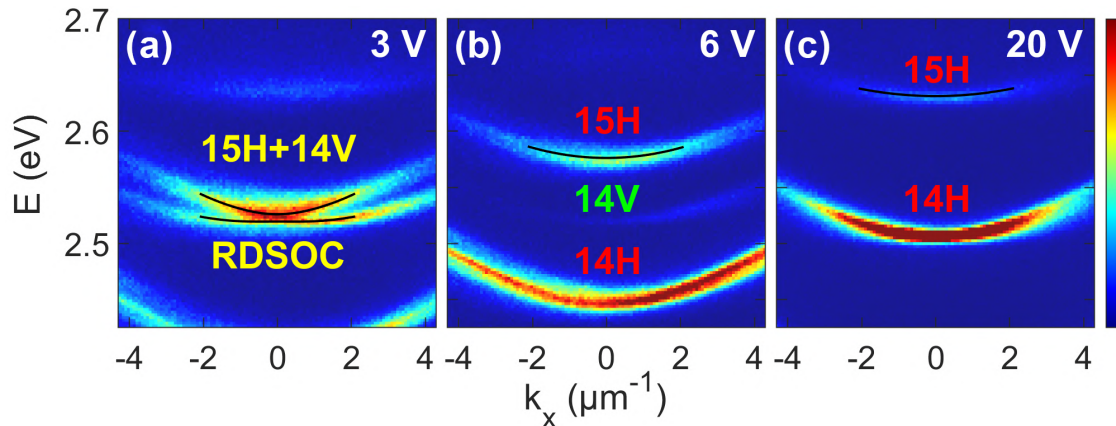


Figure 5.3: *LC microcavity PL spectra in the strong coupling regime.* Experimentally measured PL spectrum for different values of voltage, showing tunability of the H-polarized modes and (c) reach of the RDSOC regime; red, green and yellow text labels the longitudinal number and polarization of the mode(s); black solid lines show the fitting (c) by the Hamiltonian 3.7 and (d,e) by a parabola. Adopted from [237].

polariton branch through the stimulated scattering with vibrons. This scattering is particularly efficient at high temperatures, therefore, allowing for a room-temperature BEC. At the condensation threshold, typical features appear: BEC peak linewidth narrowing, nonlinear signal increase and the blueshift. At high pumping powers, the blueshift can become as large as 10 meV. This value is 2 orders of magnitude bigger than the typical blueshift in inorganic semiconductors. Though the size of Frenkel excitons is typically 1-2 orders smaller than the size of Wannier-Mott excitons, such a high blueshift for MeLPPP is achieved due to the 4-order increase in the condensation threshold and the 2-order increase in the exciton binding energy in comparison with inorganic semiconductors [293].

For our further analysis we will use several parameters of MeLPPP. The inhomogeneous broadening of MeLPPP excitonic resonance will play an important role for the next discussion, therefore, we performed its fit in the absorption spectrum Fig. 5.2(a) with a Gaussian function  $\exp[-(E - E_X)^2/2\sigma^2]$ , where  $E_X = 2.715$  eV is the central energy of the peak and  $\sigma = 35$  meV is the standard deviation of the exciton energy distribution. We will also utilize the complex refractive index of MeLPPP in order to perform the Berreman method simulation of the whole photonic structure presented in Fig. 5.2. The complex refractive index real and imaginary parts of MeLPPP are shown in Fig. 5.2(b). The background refractive index of MeLPPP extracted from  $\text{Re}(n)$  dependence is  $n_{BG} = 1.7$ . Finally, the bottleneck exciton lifetime at the condensation threshold is approximately 8 ps [293].

## 5.2 Strong coupling

### 5.2.1 Experimental results

Fig. 5.3 demonstrates the experimentally measured photoluminescence in H polarization. At 3V (Fig. 5.3(a)), the resonance between two longitudinal modes of opposite parity

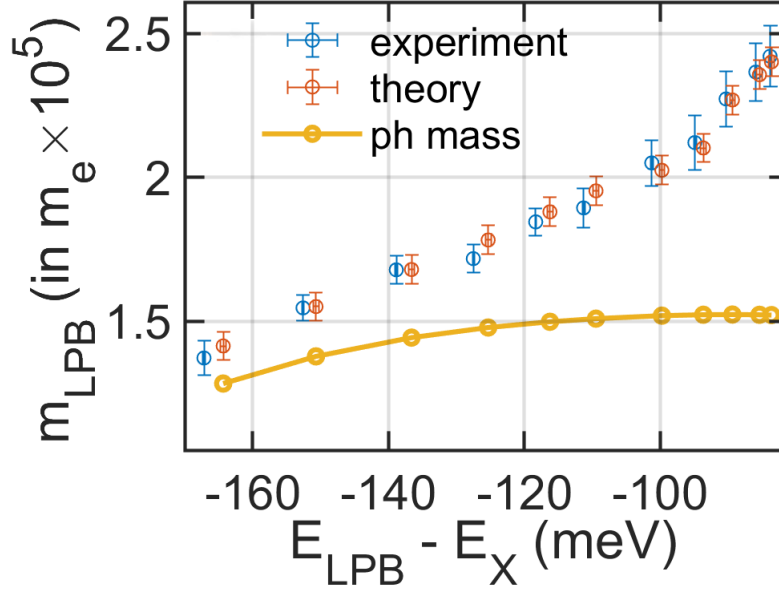


Figure 5.4: **Change of LPB mass depending on voltage.** The LPB mass  $m_{LPB}$  of the 15H mode as a function of the mode detuning  $E_{LPB} - E_X$ : experiment (blue dots) and theory (red dots) obtained by the model 5.1; the yellow solid line shows the change of photonic mass of the 15H mode obtained by the Berreman simulations (Sec. 5.2.2). Adopted from [237].

and polarization is observed, giving rise to the RDSOC spectrum, well described by the Hamiltonian 3.7 with the isotropic polarization-dependent mass difference  $\mu_x = \mu_y = \mu$ . At higher voltages, H-polarized modes move towards higher energies, therefore approaching the excitonic resonance at  $E_X = 2.715$  eV. While not in the RDSOC regime, H- and V-polarized modes are almost uncoupled, and H-polarized mode can be easily fitted by a parabola.

The typical way to prove the strong coupling in a microcavity system would be to observe an anticrossing either at high  $k_x$ , where a photonic mode crosses an excitonic resonance (Fig. 1.5(a)), or at  $k_x = 0$  with the linear detuning  $\delta$  changing with voltage (Fig. 1.5(b)). Both approaches are not applicable here since: (1) the excitonic resonance is significantly *inhomogeneously broadened* (Fig. 5.2(a)), and therefore the PL of the LPB vanishes before a bending of the mode appears; (2) the UPB is not visible due to the high MeLPPP absorption in this energy range (Fig. 5.2(a)). Though the strong coupling is not present for a photonic mode only slightly detuned with respect to the exciton, it shows up when the mode is significantly detuned, which is confirmed by the *LPB effective mass change*. This LPB mass change is clearly visible in Fig. 5.3(b,c) by looking at the parabolic fitting of the H-polarized mode (black solid lines). The curvature difference for these two lines is visible with a naked eye. We extract the LPB mass of one of the modes marked as 15H (the notation is explained later) for many voltages, and plot it in Fig. 5.4 (blue points) versus the LPB detuning  $E_{LPB}(k_x = 0) - E_X$ . The total mass change is approximately 70% of the initial mass.

As was captured by the Eq. 1.1, the mass change for a microcavity photon appears even without the strong coupling regime if the refractive index  $n_c$  of the mode changes,

which is exactly the case for a tunable H-polarized mode in our LC microcavity sample (see also Eq. 3.6). However, in the next two sections we prove that such a large mass change observed in the experiment can be only due to the strong coupling regime, and can not be explained solely by a photonic effect.

### 5.2.2 Photonic mass extraction

In order to prove this statement, we start by extracting the photonic mass of the mode of interest for all values of voltage. We first reproduce the whole band structure of the microcavity with the use of the *Berreman method* [295] (see the detailed description of the method in the context of nematic LC microcavities in Ref. [296]). We simulate the structure shown in Fig. 5.1 utilizing the MeLPPP refractive index depicted in Fig. 5.2(b) and tune the length of the LC layer and the angle of LC molecules in order to obtain a perfect correspondence between the measurement and the simulation at each voltage. The comparison for two values of voltage is shown in Fig. 5.5. In the experiment, the PL was measured in H polarization, which is why the H mode is well-visible for any voltage applied to the microcavity, while the V mode appears only when it couples to the H mode strongly enough (Fig. 5.5(a,c)). The numerical simulation (Fig. 5.5(b,d)) is represented by the first Stokes parameter  $S_1$  of the system (linear polarization degree) in order to easily distinguish between H and V modes, appearing as blue and red lines, respectively. After achieving the correspondence between the experiment and numerical simulation, we calculate once again the dispersion for every voltage and for the same structure, except that now the MeLPPP refractive index is constant and equal to the background one ( $n = n_{BG}$ ), thus eliminating the exciton from the calculation and making the system purely photonic. This allows us to extract the mass and the position of the photonic mode and plot them in Fig. 5.5(e). One can see that the total change of the photonic mass is approximately 19%. The photonic mass is also plotted together with the LPB mass in Fig. 5.4 for comparison. This result proves that the much bigger mode effective mass change observed in Fig. 5.3 can be explained solely by the exciton-photon coupling. We can also utilize the Berreman method simulation results to visualize the field distribution along the microcavity axis (Fig. 5.6). This allows us to verify that the photonic mode overlap with the MeLPPP layers is good enough to achieve the strong coupling regime and also to define the longitudinal numbers of modes for both polarizations by counting the number of field antinodes. These longitudinal numbers are utilized to label the modes in Fig. 5.3 and throughout this Chapter.

### 5.2.3 Tavis-Cummings model with inhomogeneous broadening

Now, to prove the strong coupling not only qualitatively, which was done in the previous Sec. 5.2.2, but also quantitatively, we need to take into account the inhomogeneous broadening of the excitonic resonance. The model which we construct should address two main features of the experimental data: (1) the LPB mass dependence on the LPB detuning shown in Fig. 5.4, and (2) the absence of the anticrossing for the LPB at the energies close to the exciton.

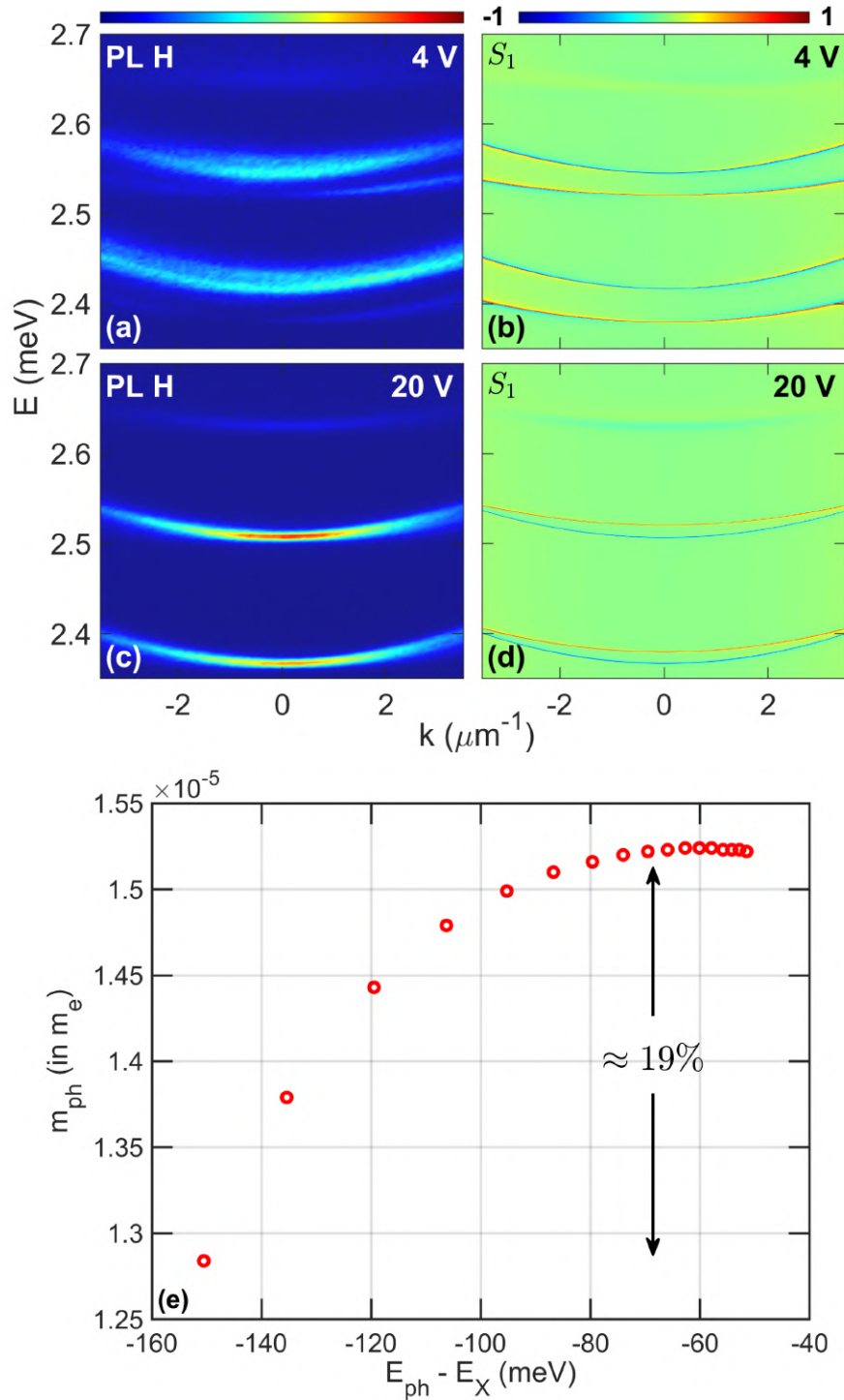


Figure 5.5: **Extraction of the photonic mass of the mode 15H.** Experimentally measured PL spectrum in H polarization for (a) 4 V and (c) 20 V; linear polarization degree  $S_1$  maps obtained by the Berreman method for the microcavity shown in Fig. 5.1 at (b) 4 V and (d) 20 V that fit well the experimental PL spectra; photonic mass vs photonic mode detuning extracted from the Berreman method calculations where MeLPPP layers were substituted by the constant refractive index layers. Adopted from [237].

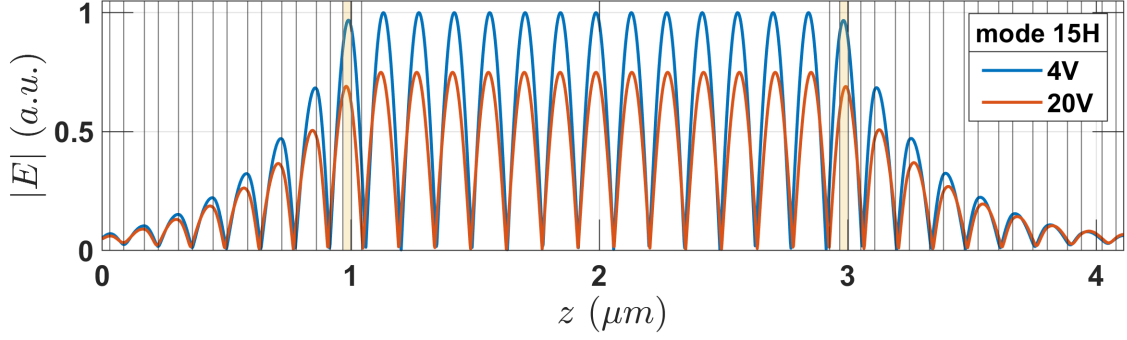


Figure 5.6: **Photonic mode field distribution.** The electric field distribution along the microcavity axis  $z$  ( $\mathbf{k}_\perp = 0$ ) for the 15H photonic mode at (a) 4 V and (b) 20 V; the number of field antinodes between the DBRs defines a longitudinal mode number; two MeLPPP layers are colored in yellow.

We apply the *Tavis-Cummings model* which describes the system consisting of a single cavity mode coupled to  $N$  two-level systems, excitons in our case. Usually, the model utilizes identical excitons, while in our case inhomogeneous broadening of the excitonic peak is taken into account. The model reads as:

$$H = \hbar(\omega_{ph} - i\gamma_{ph})a^\dagger a + \sum_{j=1}^N \hbar(\omega_{ex,j} - i\gamma_{ex})\sigma_j^+ \sigma_j^- + \hbar g (a\sigma_j^+ + a^\dagger\sigma_j^-), \quad 5.1$$

where  $\hbar\omega_{ph} = \hbar\omega_{ph,0} + \hbar^2 k_x^2 / 2m_{ph}$  is the dispersion of the photonic cavity mode 15H defined by  $\hbar\omega_{ph,0}$  energy at  $k_x = 0$  and the cavity photon mass  $m_{ph}$ ,  $\gamma_{ph}$  is the cavity mode decay,  $\hbar\omega_{ex,j}$  is the energy of  $j$ -th exciton taken from inhomogeneously broadened Gaussian distribution (Fig. 5.2(a)),  $\gamma_{ex}$  is the non-radiative decay of a single exciton,  $\hbar g$  is the exciton-photon coupling strength,  $a$  ( $a^\dagger$ ) is the cavity photon annihilation (creation) operator, and  $\sigma_j^+ = |e_j\rangle \langle g_j|$  ( $\sigma_j^- = |g_j\rangle \langle e_j|$ ) is the  $j$ -th two-level system raising (lowering) operator. For the big exciton-photon detunings, a photon "sees" the broadened excitonic peak as a single "strong" collective exciton located near  $E_X$ , and, consequently, the Rabi splitting can be estimated as  $\Omega = \hbar g \sqrt{N}$ . When the photonic mode approaches the excitonic resonance, a photon starts to "see" the internal structure of the broadened peak: individual excitons located closer to the photonic mode contribute significantly to the excitonic fraction (excitonic Hopfield coefficient Eq. 1.18) of the LPB, but induce only a weak Rabi splitting proportional to their individual coupling strength  $\hbar g$ . That is why when the LPB gets closer to the excitonic mode, the photonic Hopfield coefficient of the LPB and, consequently, the PL signal from the LPB disappears faster than the mode bends (anticrosses).

We confirm this intuition by performing numerical simulations with the model Eq. 5.1. Since the characteristic pump spot width ( $w_{pump} \approx 20 \mu\text{m}$ ) in the experiment (Fig. 5.3) is much larger than the estimated transverse cavity photon coherence length ( $l_{coh} \approx 1.5 \mu\text{m}$ ), we consider  $N_{ens} = w_{pump}^2 / l_{coh}^2$  different realizations of the Hamiltonian 5.1: each realization differs by the excitonic disorder (a corresponding ensemble of  $\hbar\omega_{ex,j}$ ) and a coupled photon. Using the photonic dispersion  $\hbar\omega_{ph}$  of the 15H mode obtained by the Berreman

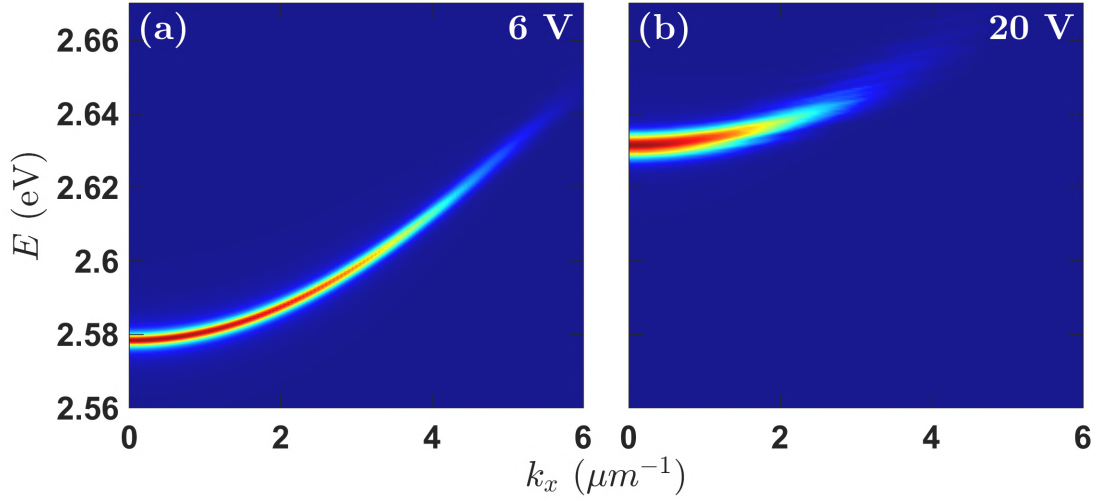


Figure 5.7: **Numerically calculated PL from the theoretical model.** The PL density produced with the use of the Tavis-Cummings model [5.1](#) by summing up the contributions from different exciton-photon ensembles and different eigenstates taking into account the luminosity (the photonic fraction) of each eigenstate: (a) 6 V and (b) 20 V.

method for every voltage (Fig. [5.5\(e\)](#)), we diagonalize each realization of the Hamiltonian [5.1](#) and for each realization we extract the photonic Hopfield coefficients of all eigenmodes. Next, we sum up the PL signal originating from these eigenmodes for all wavevectors and all realizations taking into account the eigenmode photonic fractions. After applying this procedure, we obtain a total PL signal similar to the experimental one (Fig. [5.7](#)). The LPB naturally appears under this procedure since it has the most pronounced photonic contribution. When the LPB approaches the excitonic resonance, it gradually vanishes, as expected.

The comparison with the model of a single "collective" exciton (two-oscillator model) with the exciton-photon coupling strength  $\Omega$  is shown in Fig. [5.8](#) as a PL spectrum dependence on the exciton-photon detuning  $E_{ph} - E_X$ . At high exciton-photon detunings, the two models converge, but while approaching the excitonic peak, the PL signal provided by the model [5.1](#) decays rapidly (Fig. [5.8\(a\)](#)). This is exactly what happens in the experiment (Fig. [5.3](#)), with the addition that the UPB is not visible at all. However, if we plot the same PL map in the logarithmic scale (Fig. [5.8\(b\)](#)), we see that an anticrossing is actually present, with a slightly higher splitting between the modes for the model including broadening (Eq. [5.1](#)).

We then extract the mass and the energy of the numerically obtained LPB, exactly like we do with the experimentally measured PL intensity maps, and plot the final results in Fig. [5.4](#) (red points). As one can see *both* LPB detuning and mass obtained by the numerical simulations correspond well to the experimental data when we choose Rabi splitting of  $\Omega = 93$  meV. The number of excitons used for every realization of Hamiltonian [5.1](#) is  $N_X = 200$ . In reality, the number of excitons per each coherent spot  $l_{coh}^2 \approx 2.25\mu m^2$  should be much bigger, but increasing this number very quickly makes the Hamiltonian diagonalization computationally heavy. That is why we first made sure that the simulation results slowly converge when we increase  $N_X$  up to 2000, then we performed all the

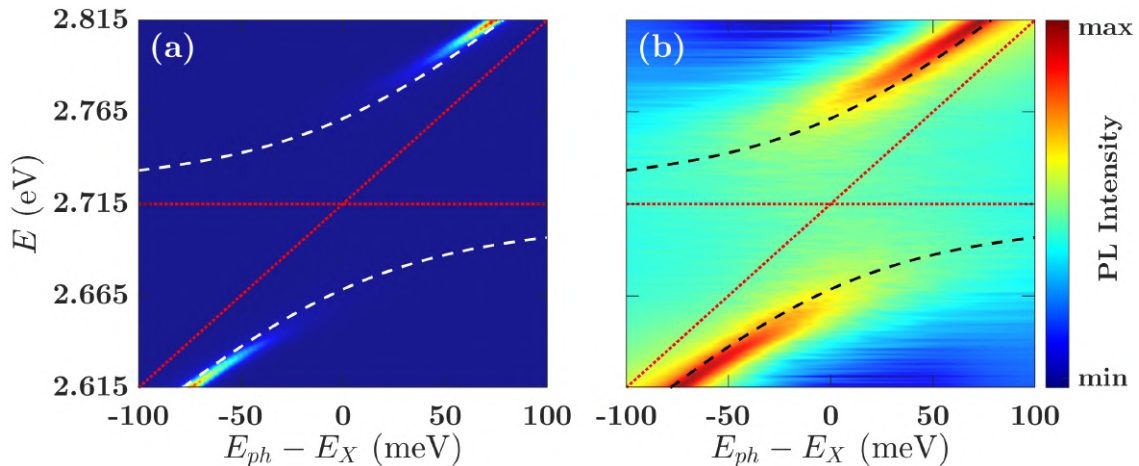


Figure 5.8: **Comparison between the model 5.1 and the two-oscillator model.** PL spectrum as a function of the exciton-photon detuning  $E_{ph} - E_x$  in the (a) linear and (b) logarithmic scales; dashed white and black lines represent the modes of the two-oscillator model with the Rabi splitting  $\Omega = 93$  meV; red dotted lines are the excitonic peak and the photonic mode energies; the PL signal (a) from the modes of the model 5.1 disappears before the modes start to bend (anticross); however, in the logarithmic scale (b) the anticrossing is more visible.

simulations for  $N_X = 200$  and included a typical difference between the two as a method error shown by red error bars in Fig. 5.4. We also extracted the LPB excitonic fraction of  $\approx 5.5\%$  at the RDSOC regime (Fig. 5.3(a)). The decay values used in the simulations are  $\hbar\gamma_{ph} = 3$  meV (obtained from the experimental reflectivity measurements, not shown here) and  $\hbar\gamma_{ex} = 0.1$  meV (which corresponds to the 8-ps bottleneck exciton decay time mentioned in Sec. 5.1). We can make a conclusion that the model 5.1 captures the dispersion behavior of the system with a high level of accuracy.

## 5.3 Condensation

### 5.3.1 Condensate polarization control

We now turn to the results obtained under the strong optical pumping, demonstrating the room-temperature exciton-polariton condensation. In the experiment, a pulsed non-resonant excitation was used, and the observations in real and reciprocal space are the result of averaging over 500-2500 pulses.

The verification of the condensation by measuring the dependencies of the emission intensity, linewidth and energy can be found in Ref. [237]. Here, we focus only on the experimental results that require a theoretical reproduction and explanation. Our cavity provides an independent control over the energy of the polarized polaritonic modes: for V and H through changing the position on the sample (cavity wedge) and for H with respect to V (linear detuning  $\delta$ ) through the applied voltage. We utilize these features to select the polariton condensate polarization.

When the non-resonant pump is circularly polarized, the mode at which the condensation occurs is the one closest to the maximum polariton gain located approximately at

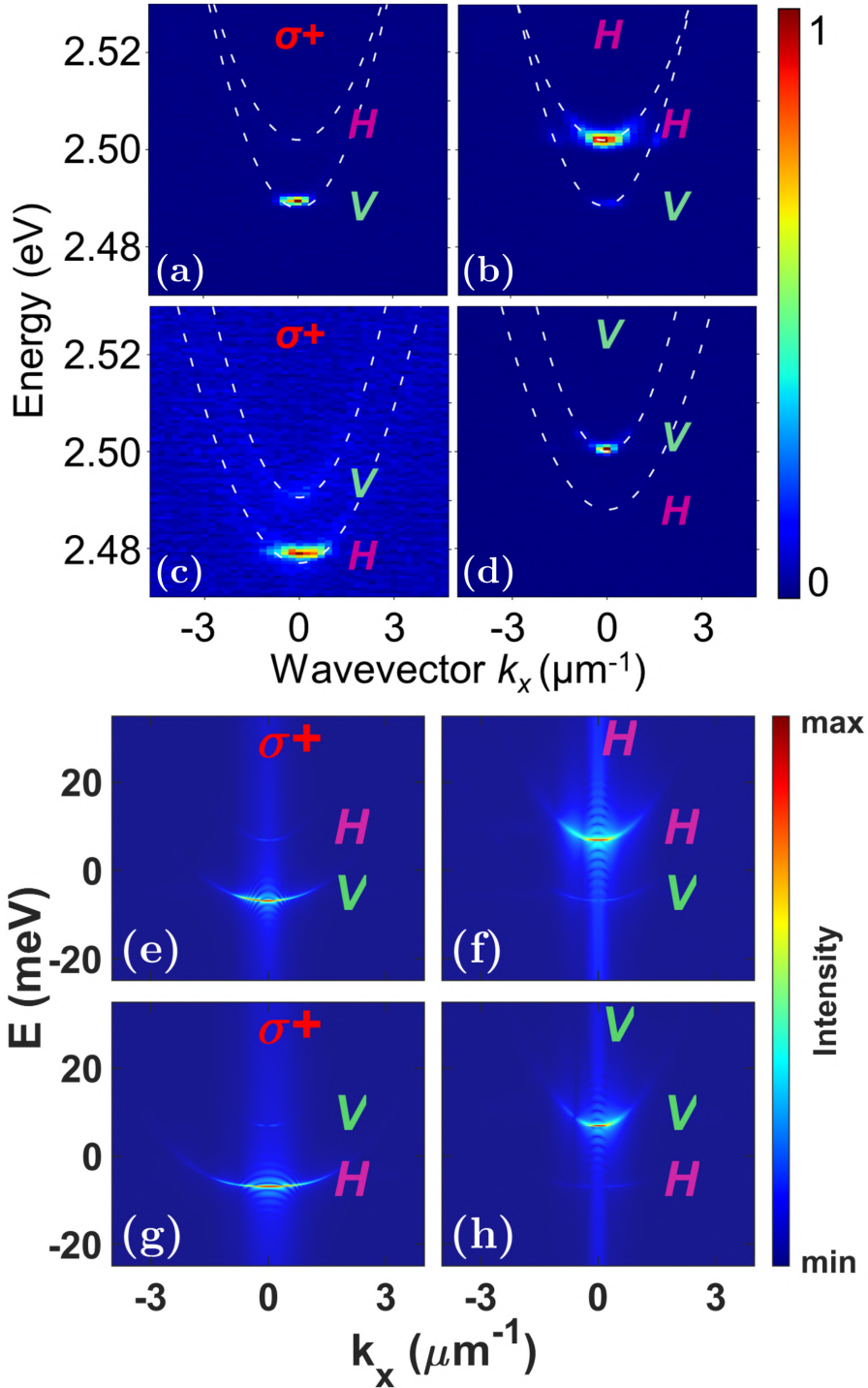


Figure 5.9: **Condensation polarization tuning.** (a-d) Experimental and (e-h) theoretical PL intensity demonstrating the polarization tuning; the polarization of the condensate is defined by the interplay of pump polarization and maximum polariton gain near 2.48 eV; linear H or V polarization of the pump is inherited by the condensate (b,d,f,h), while circular polarization of the pump is lost and the condensate shows up in the state with higher gain (a,c,e,g). Adopted from [237].

2.48 eV. By tuning voltage, the condensation switches from V-polarized to H-polarized mode (Fig. 5.9(a,c)). Under linearly-polarized pumping, the excitonic reservoir retains a part of pump polarization [293] due to the selective excitation of chromophores and slow depolarization through energy transfer. This favors the condensation in the polariton state with the same linear polarization as the pump (Fig. 5.9(b,d)).

In order to reproduce this result, we write the GPE equation analogous to Eq. 1.25, but with slight modifications [297]:

$$i\hbar \frac{\partial \psi_{H,V}}{\partial t} = (1 - i\Lambda) \left[ \left( -\frac{\hbar^2}{2m_{H,V}} \nabla^2 \pm \delta - E_0 \right) \psi_{H,V} + 2i\alpha \frac{\partial \psi_{V,H}}{\partial x} \right] + g_{H,V}(\psi_H, \psi_V) + \left[ U_{H,V}(n_{H,V}^R, \mathbf{r}, t) + iR_{H,V}(|\psi_{H,V}|^2, n_{H,V}^R, \mathbf{r}, t) + E_0 \right] \psi_{H,V} + \xi_{H,V}. \quad 5.2$$

This equation is written in  $HV$  basis in order to capture the linearly-polarized nature of excitonic reservoir and the transfer of this polarization towards the condensate. An additional energy-dependent relaxation towards the bottom of the dispersion is introduced by the term proportional to  $\Lambda$  [298], where  $E_0$  (Eq. 3.16) inside the brackets ensures that the relaxation is zero at the bottom of the dispersion. This modification of the model allows to obtain a linearized spectrum of condensate excitations (bogolons) [299], which is crucial for superfluidity studies. The polarization-dependent LPB effective masses  $m_{H,V}$  are related to the  $\mu$  (Eq. 3.7) as  $m_{H,V}^{-1} = m^{-1} \pm 2\mu/\hbar^2$ . The interaction term accounts for the repulsive interaction with the strength  $g_0$  between polaritons of the same spin (circular polarization), while the cross-spin interaction is negligible. The transformation to the linear basis makes the expressions for the interaction terms more bulky than in Eq. 1.25:  $g_H(\psi_H, \psi_V) = \frac{g_0}{\sqrt{2}} (\psi_H |\psi_H|^2 + 2\psi_H |\psi_V|^2 + \psi_H^* \psi_V^2)$  and  $g_V(\psi_H, \psi_V) = g_H(\psi_V, \psi_H)$ . The potential is created by the excitonic reservoir, and therefore it inherits the Gaussian pump profile and the reservoir lifetime:  $U_{H,V}(n_{H,V}^R, \mathbf{r}, t) = U_0(n_{H,V}^R) \exp[-r^2/2\sigma^2 - \gamma_{ex}t]$ , where  $\sigma$  is the pump profile width, and  $n_{H,V}^R$  is the excitonic reservoir density for H and V. The gain is due to the bottleneck exciton stimulated scattering towards the condensate, and therefore it has a saturation and also inherits the reservoir lifetime:

$$R_{H,V}(|\psi_{H,V}|^2, n_{H,V}^R, \mathbf{r}, t) = R_{H,V}^0(n_{H,V}^R) \exp\left[-r^2/2\sigma^2 - N_{H,V}^{tot}/N_{sat} - \gamma_{ex}t\right], \quad 5.3$$

where  $N_{H,V}^{tot} = \int |\psi_{H,V}|^2 d\mathbf{r}$  is the total condensate number of particles for H and V, and  $N_{sat}$  is the saturation number of particles. Contrary to the locally-saturated gain in Eq. 1.24, this term is an *integrally-saturated gain*. Finally,  $\xi_{H,V}$  is the noise term describing the spontaneous scattering from the excitonic reservoir towards the  $H$  and  $V$  condensate components.

To reproduce the experimental results under non-resonant pumping with circular polarization (Fig. 5.9(a,c)) several things are taken into account in the numerical simulations. First, it is the relaxation towards lower energy states (non-zero positive  $\Lambda$  term). Second, the pump laser excites equal amount of H and V chromophores ( $n_H^R = n_V^R$ ). And finally, the proximity to the maximum polariton gain creates a disbalance for the gain from the two reservoirs:  $R_H^0(n_H^R) \neq R_V^0(n_V^R)$ . The combination of these factors results in the

emission from the lower energy band as shown in Fig. 5.9(e,g).

In the case of H-(V-)polarized non-resonant pumping (Fig. 5.9(b,d)), one of the reservoirs can be considered empty:  $n_V^R = 0$  ( $n_H^R = 0$ ). This produces the gain  $R_H^0(n_V^R)$  ( $R_V^0(n_V^R)$ ) for the single polarization, coinciding with the pump polarization, and consequently triggers the condensation with well-defined H (V) polarization shown in Fig. 5.9(f,h).

### 5.3.2 Polariton stripes

Previous results were obtained for the case of high linear detuning  $\delta$ , and we were looking only on the spectrum and global condensation polarization. Now, we are interested in spatial structure of the condensate density and polarization, and especially in the differences that show up in the RDSOC regime. We start with the discussion of the experimental results. Fig. 5.10(a) shows the PL spectrum under non-resonant circular polarization above the condensation threshold at 0 V, when linear splitting  $\delta$  is big (as in Fig. 5.9). The real-space emission is shown in Fig. 5.10(d). It is affected by disorder, showing bright spots on a homogeneous Gaussian background of 25  $\mu\text{m}$ -width, comparable with the pump spot size. The emission is fully linearly polarized (Fig. 5.10(g)), with no circular polarization (Fig. 5.10(j)). The Fourier transform along  $x$  of the real space density (blue line in Fig. 5.10(m)) demonstrates the absence of any spatial periodicity.

By changing voltage on the same sample point, we approach the RDSOC regime (Fig. 5.10(b)). The dispersion is well described by the effective Hamiltonian 3.7 with  $m = 1.37 \cdot 10^{-5} m_e$ ,  $\delta = -1.3$  meV,  $\alpha = 2.7$  meV  $\cdot \mu\text{m}$  and  $\mu = -0.22$  meV  $\cdot \mu\text{m}^2$ . The bands show two minima at  $k_{\pm} \approx 1 \mu\text{m}^{-1}$  (see Eq. 3.13). Big part of the signal comes from the negative-mass state of the lower band at  $k_x = 0$ . This state demonstrates a high population since the negative-mass polaritons are attracted by the reservoir potential and they stay longer in the high gain region, while the positive-mass ones are repelled, and quit quickly the gain region. This is a typical behavior for exciton-polaritons [300, 301] and it can be considered as an additional proof of the strong coupling regime. The most interesting feature is observed in the real-space emission density (Fig. 5.10(e)). The condensate demonstrates a fragmentation due to the disorder and a periodic pattern along  $x$  axis, which is confirmed by the Fourier transform along this axis (red line in Fig. 5.10(m)). Contrary to 0 V case, a peak at  $k_x \approx 3 \mu\text{m}^{-1}$  is observed.

This spatial periodicity, or crystallinity, which we call the *density stripe phase*, can be considered as a hallmark of the *supersolidity*, supposing that the condensate is superfluid. This peculiar quantum phase combines two seemingly contradictory properties, the periodic ordering of a crystal and frictionless motion of a superfluid. The supersolidity can be interpreted as BEC at two finite-wavevector modes. Each mode independently demonstrates a spontaneous symmetry breaking by establishing a global mode-condensate phase. The interference between two modes creates density oscillations in real space with a spatial position defined by the relative phase of two modes. Combined with the superfluid properties of both mode-condensates, it gives rise to the supersolidity. This quantum phase was predicted more than 50 years ago [302, 303]. All the years after, many efforts have been done to observe it for a superfluid helium-4 [304, 305], but had no success so

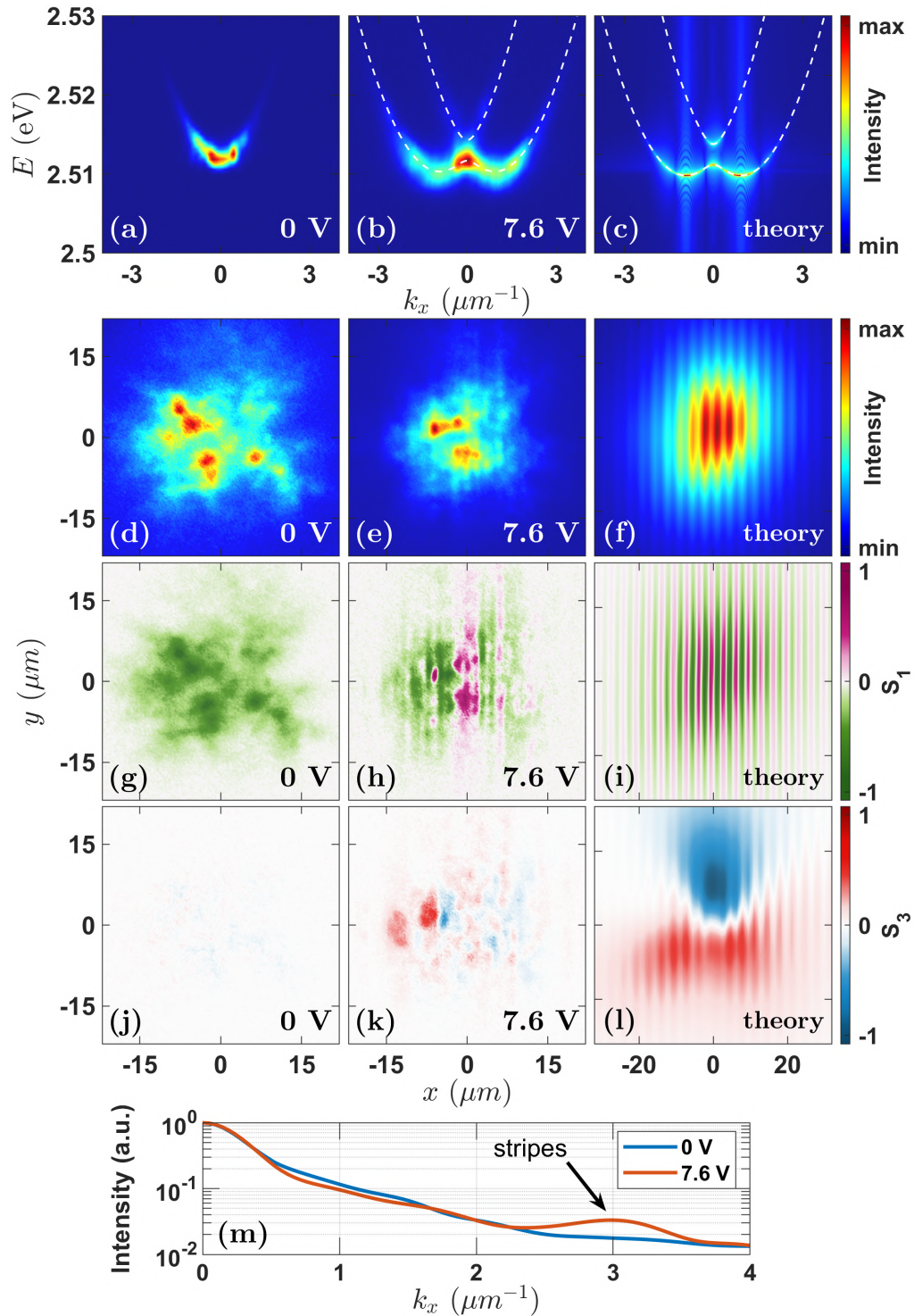


Figure 5.10: **Stripe phase in a polariton condensate.** PL measured at 0 V (first column), at 7.6 V (second column) and calculated numerically by the GPE Eq. 5.2 (third column); the first row (a-c) shows the  $k_x$ -dependent total emission with the RDSOC dispersion in (b,c); the second row (d-f) shows the real space total emission with density stripes absent in (d) and present in (e,f); the third (g-i) and fourth (j-l) rows show the real space distribution of the HV linear  $S_1$  and circular  $S_3$  polarization degrees, respectively; (m) Fourier transform along  $x$  of the experimental intensity from (d,e) with a marked stripes diffraction peak. Adopted with modifications from [237].

far [306]. BECs of atomic gases were then suggested as an alternative platform to catch this elusive quantum phase [307, 308]. The initial idea was to utilize atoms with a large magnetic dipole moment [309, 310, 311] or a field-induced electric dipole moment to realize long-range interactions. Such atomic condensates with properly tuned dipole-dipole and contact interactions placed in an appropriate non-uniform potential demonstrate a finite-wavevector "roton" minimum in their excitation spectrum associated with the supersolidity. In real space, their density demonstrates stripes, that is, a periodical atomic density modulation. However, the first two successful experiments that appeared simultaneously in 2017 were using different approaches. The first work utilized the long-range atomic interactions mediated by two cavities [312], while the second is very close to our system in study and it involves the RDSOC for atoms [313, 314] described in Sec. 3.1. The atomic BEC stays so far the single platform where the supersolid properties were observed.

While in this particular experiment that we demonstrate the physics of stripes establishment is very similar to the case of a spin-orbit coupled atomic condensate [313] (we describe this physics below), there are still some important differences. Typical experiments with atomic condensates utilize optical traps to control atoms. If any property of a condensate should be measured, for example, its distribution function, a condensate in most cases has to be released from the trap. Therefore, the process of measurement, basically, requires the destruction of a condensate. This is not the case for condensates of exciton-polaritons. The permanent leakage of photons through the cavity mirrors allows one, in principle, to continuously observe the condensate dynamics, including the superfluidity in the vicinity of a defect, stripes build-up, formation of vortices, disorder effect, etc. By demonstrating a stripe phase of exciton-polariton BEC, we, therefore, make a *step* towards supersolidity in a new platform. However, we would like to underline that this work is still far from the rigorous supersolidity demonstration, which requires a more detailed study of superfluidity, single-shot dynamics, disorder effect, and so on.

The observation of a stripe phase can be explained by considering the simplest case of BEC at absolute zero. In this case, the condensate wavefunction is fully defined by two degenerate points at the bottom of the RDSOC dispersion. The eigenstates at these two minima are elliptically-polarized with opposite circular polarization degree  $S_3$  and same linear polarization degree  $S_1$  (see Fig. 3.3 and Eq. 3.12). This linear polarization degree  $S_1$  is defined by Eq. 3.12 with a slight modification accounting for the presence of polarization-dependent mass term  $\mu$ :

$$S_1 = -\frac{\delta + \mu k_{\pm}^2}{\sqrt{4k_{\pm}^2\alpha^2 + (\delta + \mu k_{\pm}^2)^2}}. \quad 5.4$$

In this case, the spinor wavefunction of the condensate can be written as:

$$|\psi\rangle = \frac{1}{2} \begin{pmatrix} \cos \theta/2 \\ \sin \theta/2 \end{pmatrix} e^{ik_-x} + \frac{1}{2} \begin{pmatrix} \cos(\pi - \theta)/2 \\ \sin(\pi - \theta)/2 \end{pmatrix} e^{ik_+x}, \quad 5.5$$

where  $\theta$  ( $\pi - \theta$ ) is the polar angle of the Stokes vector  $\mathbf{S}$  of the first (second) valley state,

whereas they share the same azimuthal angle equal to  $\phi = 0$  (H polarization) or  $\phi = \pi$  (V polarization), depending on the linear detuning sign:  $\text{sign}(\delta)$ . The corresponding density reads:

$$\langle \psi | \psi \rangle = \frac{1}{2} (1 + \cos Q_x(\delta) x \cdot \sin \theta), \quad 5.6$$

where  $Q_x(\delta) = k_+ - k_-$  (Eq. 3.14), and we changed the notation  $Q_y \rightarrow Q_x$  since the RDSOC is along  $k_x$  now. This density exhibits the oscillations with spatial periodicity defined by  $Q_x$  and contrast defined by the absolute value of linear polarization degree common for two degenerate states  $|S_1| = |\sin \theta|$  (Eq. 5.4). This formula gives as a theoretical estimation for the contrast of 21%, while the experimental one extracted from Fig. 5.10(m) equals to 2.2%. This pronounced difference can be explained by accounting several effects. First of all, in the realistic case of non-zero-temperature BEC, the contrast is lowered due to the presence of higher energy states. Secondly, the experiment represents the averaging of many shots, therefore, any fluctuations of stripes position in real space reduce the total contrast. In the worst case, when no spatial pinning is present in the system, the averaging should completely destroy the stripes for an infinite number of repetitions. However, in our case, the stripes are pinned by inhomogeneity of the Gaussian pump profile: stripes tend to acquire the largest possible overlap with the gain from the excitonic reservoir, and, therefore, stripes density maximum overlaps with the center of the pump spot. Finally, the pattern can be also disturbed by the formation of vortices via the Kibble-Zurek mechanism [315] and their dynamics, which we will see also in the numerical simulations.

Another result which we observe in the experiment Fig. 5.10(h) is the persistent spin helix, or *polarization stripes*. Their contrast is defined by the magnitude of the circular polarization degree  $|S_3|$  common for two degenerate states. The theoretical estimation gives  $|S_3| = 1 - |S_1| = 79\%$ , while the experimental contrast is around 40%. This value sets a minimal mutual coherence degree between two condensate components located at different valleys  $k_{\pm}$ . If this coherence were absent, the averaging of many shots would result in a complete washing out of the persistent spin helix. Since the observed contrast is non-zero and significantly big, it demonstrates the presence of a phase locking mechanism between the two components.

In order to verify the experimental results, we perform the GPE numerical simulations with the model 5.2. Fig. 5.10(c) demonstrates the dispersion of the condensate. The reservoir-induced potential and relaxation are tuned in order to reproduce the population of the valleys and the negative-mass state. Real space density (Fig. 5.10(f)) shows the stripes obtained by averaging in time of a single "numerical shot". The pinning of the stripes maximum to the central point of the pump spot was verified by performing a series of simulations. In the linear *HV* polarization degree  $S_1$  (Fig. 5.10(i)), strong polarization stripes are present. The much better clarity of the theoretical stripes with respect to the experimental ones is explained by the absence of disorder in the simulations. Circular polarization degree  $S_3$  (Fig. 5.10(l)) demonstrates a non-zero pattern due to the rich dynamics of the system over a single realization, including the reservoir (gain) dynamics, the formation of vortices, and stripes establishment. Therefore, the numerical simulations

fully confirm our observations and interpretations.

In Ch. 4, we have demonstrated a variety of topological effects originating from the Rashba-Dresselhaus spin-orbit coupling in optical microcavities in the weak coupling regime. By writing a generic lattice Hamiltonian in Sec. 4.1, we demonstrated two distinct regimes of tunneling control via RDSOC, phase and amplitude control regimes. Both regimes are of importance, since some lattice models require a tunneling amplitude engineering, such as SSH chain or strained graphene, while others need a tunneling phase adjustment, such as Harper-Hofstadter or Haldane model. The significance of this result is what we tried to prove in further sections.

In Sec. 4.2, a zigzag SSH chain with RDSOC was studied in detail. We have shown how the topology of this chain is modified with the use of the RDSOC in the amplitude control regime. We confirmed this result by simulating a liquid crystal microcavity with an SSH potential: an initially trivial SSH patterned on top of the microcavity mirror becomes nontrivial when the RDSOC is turned on by applying voltage to the microcavity. We studied in detail the effect of TE-TM SOC in this system and demonstrated the edge state is robust for realistic magnitudes of the TE-TM SOC. We also investigated a peculiar structure of the edge state in real space where it is showing a period doubling of pseudospin and in reciprocal space where it demonstrates an interplay between three components with different wavevectors. Clearly, the next step is to demonstrate this SSH topology control in experiment.

In Sec. 4.3, we made a step back from a chain to an individual lattice site and their pairs in order to suggest a *continuously tunable* tunneling amplitude control contrary to the switching that we demonstrated in Sec. 4.2. In this study, we demonstrated a crucial role played by the symmetry of the RDSOC term and the number of localized states for the coupling between these localized states. We showed theoretically and experimentally, that the tunneling between two symmetric localized states can be continuously controlled via RDSOC by simply applying voltage to the microcavity. The total demonstrated tunneling change is more than 100%. At the end, we showed theoretically that once we are able to push the tunneling change even further down (suppress it), we can observe the topological transition characterized by the inversion of bands with different symmetry of eigenstates. One of the possible follow-ups of this work would be to produce a cavity with a different LC material and observe this topological transition in experiment. The proposed method of tunneling tunability is actually more generic than it seems at first glance and it can simply go beyond microcavity realizations, since it has only two, relatively loose requirements: (1) selection rules which allow some transitions and prohibit the others, and (2) tunability of energy separation between the states of interest and intermediate states. The continuous *in-situ* tunability is highly desirable in photonics, therefore, this technique can certainly be further used for band structure reconfigurability in more complicated lattices.

In Sec. 4.4, we switched our focus to a slightly different and more complicated system of a *cholesteric* liquid crystal microcavity. We provided a detailed explanation of the electrically-induced band structure tunability in this system by considering a combination of cholesteric-induced periodic potential, dielectric effect and liquid crystal molecular fluc-

tuations. After this, we explained first the disappearance and then reemergence of the *optical activity* in this system from the symmetry considerations. We drew the analogy between optical activity and RDSOC, and verified it on the experimental data. This analogy is quite remarkable, in our opinion, since it allows us to link the RDSOC-based effects and optical activity-based effects, therefore, on one hand, enriching our understanding of these phenomena by considering them from two different points of view, and, on the other hand, allowing us to establish clear differences between them. This work demonstrates the versatility of microcavities filled with liquid crystals as a platform. In perspective, we can study both theoretically and experimentally other configurations provided by the cholesteric phase [316]: hopfions, heliknotons, skyrmions and torons. These defects of the cholesteric phase are both Abelian and non-Abelian, and they are topological themselves, which makes it interesting to study their interplay with light in optical microcavities, both in form of individual defects and defects arranged in chains or lattices by self-organization.

In Sec. 4.5, we briefly reviewed how the amplitude and phase control techniques can be extended towards 2D lattice models. We suggested a feasible way to construct a time-reversal-symmetry-conserving Harper-Hofstadter model by using the phase control regime. In the assumption of spatially adjustable orientation of the RDSOC, we suggested a realization of the XY Hamiltonian in the amplitude control regime. XY model is interesting because of its dynamic capturing the swarm synchronization phenomenon and its mapping with various optimization problems. Such a LC-based simulator would be compact and benefit from high accessibility to the lattice state. An interesting theoretical continuation would be to study the Harper-Hofstadter model in more detail, and in particular, to go beyond the Harper-Hofstadter Hamiltonian by reducing the number of constraints we use, to study the impact of additional terms, especially in the context of non-Abelian gauge fields, and to explore the potential tunability of this system.

In Sec. 4.6, we extended our formalism of tunneling amplitude control to non-Hermitian systems. We first demonstrated that by adding a proper non-Hermitian term, the circular dichroism, we make available some cross-polarized transitions which were prohibited before. The effect is two-fold: (1) the second-order correction to the tunneling coefficient emerges, and (2) this correction is non-reciprocal due to the non-Hermitian nature of the added term. As a result, the monomer chain transforms into the Hatano-Nelson model and the SSH chain transforms into the non-Hermitian SSH chain in the amplitude control regime. On the level of the continuous-space Hamiltonian, this gives rise to an imaginary gauge potential responsible for the localization of *all* eigenstates of the system on the edge, demonstrating, therefore, the effect called the non-Hermitian skin effect. We suggested realistic realizations of this effect in photonic and electronic systems. We also studied in detail symmetries of the system and the effect of additional terms to prove the robustness of the effect. Certainly, realization of this effect in experiment would be a great step forward, since there is still a few demonstrations in photonics, with most of them operating in synthetic dimensions. From theoretical point of view, it would be nice to explore other non-Hermitian terms naturally provided by liquid crystal microcavities [242], such as linear polarization lifetime difference and non-Hermitian TE-TM SOC. They can give rise to non-Hermitian singularities, such as exceptional points [54], and trigger interesting

non-Hermitian topological phases and transitions.

In Ch. 5, we switched to the description of a hybrid microcavity combining an organic emitter and a nematic liquid crystal layer, and operating in the strong-coupling regime. First, we verified that the strong coupling regime is achieved in this system. To do this, we constructed a model taking into account the inhomogeneous broadening of the excitonic resonance. Contrary to the standard strong coupling verification by observing the anticrossing, we suggested an alternative way profiting from the microcavity spectrum tunability. Though this approach requires a more rigorous analysis of the system, it provides a powerful alternative to the standard anticrossing fitting, and also enriches our understanding of the strong coupling in a system with a broadened resonance. Then, we considered the exciton-polariton Bose-Einstein condensation in this system at room temperature and under non-resonant pumping. We demonstrated the persistent spin helix and the density stripes in the RDSOC regime. We provided the theoretical explanation for both these effects. The latter is considered to be a hallmark of supersolidity *if we assume* that the condensate is superfluid. Therefore, we make here a step towards this peculiar quantum phase of matter.

From the theoretical point of view, the next logical step is to study the effect of disorder in this system, and, especially, how it affects the condensation and stripes contrasts. Then, in order to get closer to the statement of supersolidity, the weak excitations of the condensate can be studied for the RDSOC dispersion. This analysis can be reinforced by the numerical GPE simulations of the superfluid behavior in the vicinity of a defect, as was done for the first experimental demonstrations of polariton superfluidity (Fig. 1.6). All these analytical derivations and numerical simulations can be performed for different parameter ranges in order to search for distinct condensation regimes. Especially, the dependence on the linear detuning  $\delta$  should receive a special attention, since this control knob is available in the experiment. Some additional ingredients can be added to the theoretical model 5.2, such as Zeeman splitting, for example, since it is easy to induce it for polaritons through an applied magnetic field. Finally, a special attention should be devoted to establish differences between polariton and atomic supersolidity in order to fully understand and further utilize the advantages which polaritons are able to provide. One of such potential advantages of polaritons is the access to the non-equilibrium condensation which is not the case for atomic condensates. Therefore, studying the rich non-equilibrium dynamics of the stripe phase in a polariton condensate would be a reasonable next step.

In general, all the models discussed in Ch. 4 can be pushed to a nonlinear regime by combining a liquid crystal material with an emitter as it is done in Ch. 5. This is exactly the goal of the TopoLight project, as a part of which this Thesis has been realized. This project aims to build photonic devices profiting from topological robustness and tunability of liquid crystals: lasers, isolators, modulators, optical gates, etc. These nonlinear and non-Hermitian systems and devices form the most broad domain for future studies.



## Appendices



In the basis  $(|H_s^l\rangle |H_s^r\rangle |V_s^l\rangle |V_s^r\rangle |H_p^l\rangle |H_p^r\rangle |V_p^l\rangle |V_p^r\rangle)^T$  the DT Hamiltonian reads:

$$H_{DT,lr}^{(8)} = \begin{pmatrix} E_{H_s} & -J_{0,H_s} & 0 & i\beta'_1 & 0 & 0 & -i\beta'_2 & i\beta'_3 \\ -J_{0,H_s} & E_{H_s} & -i\beta'_1 & 0 & 0 & 0 & i\beta'_3 & -i\beta'_2 \\ 0 & i\beta'_1 & E_{V_s} + \delta & -J_{0,V_s} & -i\beta'_4 & i\beta'_5 & 0 & 0 \\ -i\beta'_1 & 0 & -J_{0,V_s} & E_{V_s} + \delta & i\beta'_5 & -i\beta'_4 & 0 & 0 \\ 0 & 0 & i\beta'_4 & -i\beta'_5 & E_{H_p} & J_{0,H_p} & 0 & i\beta'_6 \\ 0 & 0 & -i\beta'_5 & i\beta'_4 & J_{0,H_p} & E_{H_p} & -i\beta'_6 & 0 \\ i\beta'_2 & -i\beta'_3 & 0 & 0 & 0 & i\beta'_6 & E_{V_p} + \delta & J_{0,V_p} \\ -i\beta'_3 & i\beta'_2 & 0 & 0 & -i\beta'_6 & 0 & J_{0,V_p} & E_{V_p} + \delta \end{pmatrix}, \quad \text{A.1}$$

with  $l$  ( $r$ ) standing for the left (right) trap in DT,  $J_{0,\varphi} > 0$  tunneling between left  $|\varphi^l\rangle$  and right  $|\varphi^r\rangle$  ST states in the absence of RDSOC, and  $\beta'_i = |\langle \varphi^l | 2\alpha k_x | \varphi \rangle|$  RDSOC transition matrix elements between corresponding states  $|\varphi^l\rangle$  and  $|\varphi\rangle$ . Here, we utilized the fact that the unperturbed tunneling coefficients between  $p$  states are positive:  $J_{0,H_p}, J_{0,V_p} > 0$ . Since in our experiment for both polarizations only even (symmetric)  $p$  states are present, we need to transform the basis of  $p$  states from left-right ST states to even-odd DT states, which is done by transformation matrix  $T = \text{diag}(\sigma_0, \sigma_0, U, U)$ , where  $U = (\sigma_0 - i\sigma_y)/\sqrt{2}$ . The transformed Hamiltonian reads in the basis  $(|H_s^l\rangle |H_s^r\rangle |V_s^l\rangle |V_s^r\rangle |H_p^e\rangle |H_p^o\rangle |V_p^e\rangle |V_p^o\rangle)^T$ :

$$H_{DT,eo}^{(8)} = \begin{pmatrix} E_{H_s} & -J_{0,H_s} & 0 & i\beta_{DT,1} & 0 & 0 & -i\beta_{DT,2} & -i\beta_{DT,3} \\ -J_{0,H_s} & E_{H_s} & -i\beta_{DT,1} & 0 & 0 & 0 & i\beta_{DT,2} & -i\beta_{DT,3} \\ 0 & i\beta_{DT,1} & E_{V_s} + \delta & -J_{0,V_s} & -i\beta_{DT,4} & -i\beta_{DT,5} & 0 & 0 \\ -i\beta_{DT,1} & 0 & -J_{0,V_s} & E_{V_s} + \delta & i\beta_{DT,4} & -i\beta_{DT,5} & 0 & 0 \\ 0 & 0 & i\beta_{DT,4} & -i\beta_{DT,4} & E_{H_p^e} & 0 & 0 & i\beta_{DT,6} \\ 0 & 0 & i\beta_{DT,5} & i\beta_{DT,5} & 0 & E_{H_p^o} & -i\beta_{DT,6} & 0 \\ i\beta_{DT,2} & -i\beta_{DT,2} & 0 & 0 & 0 & i\beta_{DT,6} & E_{V_p^e} + \delta & 0 \\ i\beta_{DT,3} & i\beta_{DT,3} & 0 & 0 & -i\beta_{DT,6} & 0 & 0 & E_{V_p^o} + \delta \end{pmatrix}, \quad \text{A.2}$$

where  $\beta_{DT,1/6} = \beta'_{1/6}$ ,  $\beta_{DT,2/3} = (\beta'_2 \pm \beta'_3)/\sqrt{2}$ ,  $\beta_{DT,4/5} = (\beta'_4 \pm \beta'_5)/\sqrt{2}$  are transformed matrix elements,  $E_{H_p^{e/o}} = E_{H_p} \mp J_{0,H_p}$ ,  $E_{V_p^{e/o}} = E_{V_p} \mp J_{0,V_p}$  are energies of even/odd DT  $p$  states.

After applying the 2nd order perturbation theory in the limit  $|\delta| > \max |\Delta E_{ij}| \gg \beta$ ,  $J_{0,\varphi}$ , where  $\Delta E_{ij}$  is the difference between  $i$ th and  $j$ th localized states, we reduce Hamiltonian [A.2](#) to an effective 2x2 Hamiltonian including only  $(|H_s^l\rangle |H_s^r\rangle)^T$  basis states:

$$H_{DT} = \begin{pmatrix} E'_{H_s}(\delta) & -J(\delta) \\ -J(\delta) & E'_{H_s}(\delta) \end{pmatrix},$$

$$E'_{H_s}(\delta) = E_{H_s} - \frac{\beta_{DT,1}^2}{E_{V_s} - E_{H_s} + \delta} - \frac{\beta_{DT,2}^2 + \beta_{DT,3}^2}{E_{V_p} - E_{H_s} + \delta}, \quad \text{A.3}$$

$$J(\delta) = J_{0,H_s} - \frac{\beta_{DT,2}^2 - \beta_{DT,3}^2}{E_{V_p} - E_{H_s} + \delta},$$

where  $E'_{H_s}(\delta)$  is a detuning-dependent modified energy of ST states  $|H_s^{l,r}\rangle$ ,  $J(\delta)$  is a detuning-dependent effective tunneling, and  $J_{0,H_s} \equiv J_0$  used in the main text. As one can see, the contributions  $\beta_{DT,2}$  and  $\beta_{DT,3}$  from different intermediate states  $|V_p^e\rangle$  and  $|V_p^o\rangle$ ,

respectively, are additive for on-site energy shift  $E'_{H_s}(\delta)$  and subtractive for the tunneling change  $J(\delta)$ . Therefore, the absence of the state  $|V_p^o\rangle$  in the experiment ( $\beta_{DT,3} = 0$ ) maximizes the absolute value of tunneling change.

We use  $s$  and  $p$  eigenstates of a harmonic oscillator as trial basis states:  $|0(y), V\rangle$  and  $|1(y), H\rangle$ , respectively. In this basis, the terms of tight-binding Hamiltonian [4.24](#) are written as:

$$E_{H_p} = \langle 1(y), H | \left( -\frac{\hbar^2}{2m} \frac{\partial^2}{\partial y^2} + \frac{A_H}{2} [1 - \cos(2qy)] - \frac{\delta}{2} \right) | 1(y), H \rangle, \quad \text{B.1}$$

$$E_{V_s} = \langle 0(y), V | \left( -\frac{\hbar^2}{2m} \frac{\partial^2}{\partial y^2} + \frac{A_V}{2} [1 - \cos(2qy)] + \frac{\delta}{2} \right) | 0(y), V \rangle, \quad \text{B.2}$$

$$t_{pp} = \langle 1(y + p/2), H | \left( -\frac{\hbar^2}{2m} \frac{\partial^2}{\partial y^2} + \frac{A_H}{2} [1 - \cos(2qy)] - \frac{\delta}{2} \right) | 1(y), H \rangle, \quad \text{B.3}$$

$$t_{ss} = \langle 0(y + p/2), V | \left( -\frac{\hbar^2}{2m} \frac{\partial^2}{\partial y^2} + \frac{A_V}{2} [1 - \cos(2qy)] + \frac{\delta}{2} \right) | 0(y), V \rangle, \quad \text{B.4}$$

$$t_{sp,0} = \langle 1(y), H | 2\partial_y | 0(y), V \rangle, \quad \text{B.5}$$

$$t_{sp,1} = \langle 1(y + p/2), H | 2\partial_y | 0(y), V \rangle, \quad \text{B.6}$$

with  $E_{H_p}$  and  $E_{V_s}$  onsite energies of  $H_p$  and  $V_s$ , respectively,  $t_{pp}$  and  $t_{ss}$  nearest-neighbour couplings between  $p$  states of  $H$  and  $s$  states of  $V$ , respectively,  $t_{sp,0}$  and  $t_{sp,1}$  onsite and nearest-neighbour cross-polarized couplings between  $H_p$  and  $V_s$ , respectively. The RDSOC onsite coupling term  $\alpha t_{sp,0}$  is dominant over other coupling terms ( $t_{pp}$ ,  $t_{ss}$ ,  $\alpha t_{sp,1}$ ), which is confirmed by efficient mixing of polarizations (high  $S_3$  values in Fig. [4.16\(i\)](#)), and large band splitting with respect to the band size. The parameters used for Fig. [4.16\(b,c\)](#):  $E_{H_p} = 24.24$  meV,  $E_{V_s} = 23.27$  meV,  $t_{pp} = 0.12$  meV,  $t_{ss} = 0.10$  meV,  $\alpha = 1.1$  meV $\cdot\mu\text{m}$ ,  $t_{sp,0} = 1.71$   $\mu\text{m}^{-1}$ ,  $t_{sp,1} = 0.06$   $\mu\text{m}^{-1}$ ,  $p = 8$   $\mu\text{m}$ .



- Z. Zhang, I. Septembre, Z. Liu, P. Kokhanchik, S. Liang, F. Liu, C. Li, H. Wang, M. Liu, Y. Zhang et al., “Beam dynamics induced by the quantum metric of exceptional rings,” *arXiv preprint* arXiv:2410.14428, 2024.
- M. Muszynski, P. Kokhanchik, D. Urbonas, P. Kapuscinski, P. Oliwa, R. Mirek, I. Georgakilas, T. Stoferle, R. F. Mahrt, M. Forster et al., “Observation of a stripe phase in a spin-orbit coupled exciton-polariton Bose-Einstein condensate,” *arXiv preprint* arXiv:2407.02406, 2024.
- M. Muszyński, P. Oliwa, P. Kokhanchik, P. Kapuściński, E. Oton, R. Mazur, P. Morawiak, W. Piecek, P. Kula, W. Bardyszewski et al., “Electrically tunable spin-orbit coupled photonic lattice in a liquid crystal microcavity,” *arXiv preprint* arXiv:2407.07161, 2024.
- R. Mirek, P. Kokhanchik, D. Urbonas, I. Georgakilas, P. Morawiak, W. Piecek, P. Kula, D. Solnyshkov, G. Malpuech, R. Mahrt et al., “In-situ tunneling control in photonic potentials by Rashba-Dresselhaus spin-orbit coupling,” *arXiv preprint* arXiv:2408.08582, 2024.
- P. Kokhanchik, D. Solnyshkov, and G. Malpuech, “Non-Hermitian skin effect induced by Rashba-Dresselhaus spin-orbit coupling,” *Physical Review B*, vol. 108, no. 4, p. L041403, 2023.
- P. Kokhanchik, D. Solnyshkov, T. Stöferle, B. Piętka, J. Szczytko, and G. Malpuech, “Modulated Rashba-Dresselhaus spin-orbit coupling for topology control and analog simulations,” *Physical Review Letters*, vol. 129, no. 24, p. 246801, 2022.



- *Poster presentation* “Non-Hermitian skin effect induced by Rashba-Dresselhaus spin-orbit coupling,” PEPS 2024, 6–10 August 2024, Reykjavík, Iceland
- *Poster presentation* “Non-Hermitian skin effect induced by Rashba-Dresselhaus spin-orbit coupling,” NHTOP 2023, 14–18 August 2023, Dresden, Germany
- *Oral presentation* “Modulated Rashba-Dresselhaus spin-orbit coupling for topology control,” Topological Photonics 2023, 31 May – 2 June 2023, Madrid, Spain
- *Poster presentation* “Non-Hermitian skin effect in 1D systems with Rashba-Dresselhaus spin-orbit coupling,” Out-of-equilibrium physics with photons and atoms, 5–10 March 2023, Les Houches, France
- *Poster presentation* “Modulated Rashba-Dresselhaus spin-orbit coupling for topology control and analog simulations,” PQIP 2023, 21–27 January 2023, Trento, Italy
- *Oral presentation* “Control of SSH chain topology by Rashba-Dresselhaus spin-orbit coupling,” PLMCN 2022, 10–16 April 2022, Varadero, Cuba  
Award for the best student talk (2nd place)



- [1] K. J. Vahala, “Optical microcavities,” *Nature*, vol. 424, no. 6950, pp. 839–846, 2003.
- [2] A. V. Kavokin, J. J. Baumberg, G. Malpuech, and F. P. Laussy, *Microcavities*. Oxford University Press, 2017, vol. 21.
- [3] Y.-F. Xiao and F. Vollmer, “Special Issue on the 60th anniversary of the first laser – series I: Microcavity Photonics – from fundamentals to applications,” *Light: Science & Applications*, vol. 10, no. 1, p. 141, 2021.
- [4] G. Panzarini, L. C. Andreani, A. Armitage, D. Baxter, M. Skolnick, V. Astratov, J. Roberts, A. V. Kavokin, M. R. Vladimirova, and M. Kaliteevski, “Cavity-polariton dispersion and polarization splitting in single and coupled semiconductor microcavities,” *Physics of the Solid State*, vol. 41, pp. 1223–1238, 1999.
- [5] D. D. Solnyshkov, G. Malpuech, P. St-Jean, S. Ravets, J. Bloch, and A. Amo, “Microcavity polaritons for topological photonics,” *Optical Materials Express*, vol. 11, no. 4, pp. 1119–1142, 2021.
- [6] A. Kavokin, G. Malpuech, and M. Glazov, “Optical Spin Hall Effect,” *Physical Review Letters*, vol. 95, no. 13, p. 136601, 2005.
- [7] I. Carusotto and C. Ciuti, “Quantum fluids of light,” *Reviews of Modern Physics*, vol. 85, no. 1, pp. 299–366, 2013.
- [8] E. T. Jaynes and F. W. Cummings, “Comparison of quantum and semiclassical radiation theories with application to the beam maser,” *Proceedings of the IEEE*, vol. 51, no. 1, pp. 89–109, 1963.
- [9] J. Hopfield, “Theory of the contribution of excitons to the complex dielectric constant of crystals,” *Physical Review*, vol. 112, no. 5, p. 1555, 1958.
- [10] M. H. Anderson, J. R. Ensher, M. R. Matthews, C. E. Wieman, and E. A. Cornell, “Observation of Bose-Einstein condensation in a dilute atomic vapor,” *Science*, vol. 269, no. 5221, pp. 198–201, 1995.
- [11] K. B. Davis, M.-O. Mewes, M. R. Andrews, N. J. van Druten, D. S. Durfee, D. Kurn, and W. Ketterle, “Bose-Einstein condensation in a gas of sodium atoms,” *Physical Review Letters*, vol. 75, no. 22, p. 3969, 1995.
- [12] L. Keldysh and A. Kozlov, “Collective properties of excitons in semiconductors,” in *Selected papers of Leonid V Keldysh*. World Scientific, 2024, pp. 79–86.
- [13] J. Kasprzak, M. Richard, S. Kundermann, A. Baas, P. Jeambrun, J. M. J. Keeling, F. Marchetti, M. Szymańska, R. André, J. Staehli *et al.*, “Bose-Einstein condensation of exciton polaritons,” *Nature*, vol. 443, no. 7110, pp. 409–414, 2006.

- [14] L. Pitaevskii and S. Stringari, *Bose-Einstein Condensation*, ser. International Series of Monographs on Physics. Clarendon Press, 2003.
- [15] H. Deng, G. Weihs, D. Snoke, J. Bloch, and Y. Yamamoto, “Polariton lasing vs. photon lasing in a semiconductor microcavity,” *Proceedings of the National Academy of Sciences*, vol. 100, no. 26, pp. 15 318–15 323, 2003.
- [16] J. F. Allen and A. Misener, “Flow of liquid helium II,” *Nature*, vol. 141, no. 3558, pp. 75–75, 1938.
- [17] P. Kapitza, “Viscosity of liquid helium below the  $\lambda$ -point,” *Nature*, vol. 141, no. 3558, pp. 74–74, 1938.
- [18] L. Landau, “Theory of the Superfluidity of Helium II,” *Physical Review*, vol. 60, pp. 356–358, Aug 1941.
- [19] A. Amo, J. Lefrère, S. Pigeon, C. Adrados, C. Ciuti, I. Carusotto, R. Houdré, E. Giacobino, and A. Bramati, “Superfluidity of polaritons in semiconductor microcavities,” *Nature Physics*, vol. 5, no. 11, pp. 805–810, 2009.
- [20] A. Amo, D. Sanvitto, F. Laussy, D. Ballarini, E. d. Valle, M. Martin, A. Lemaitre, J. Bloch, D. Krizhanovskii, M. Skolnick *et al.*, “Collective fluid dynamics of a polariton condensate in a semiconductor microcavity,” *Nature*, vol. 457, no. 7227, pp. 291–295, 2009.
- [21] I. Carusotto and C. Ciuti, “Probing microcavity polariton superfluidity through resonant Rayleigh scattering,” *Physical Review Letters*, vol. 93, no. 16, p. 166401, 2004.
- [22] C. Ciuti and I. Carusotto, “Quantum fluid effects and parametric instabilities in microcavities,” *Physica Status Solidi (B)*, vol. 242, no. 11, pp. 2224–2245, 2005.
- [23] M. Wouters and I. Carusotto, “Superfluidity and critical velocities in nonequilibrium Bose-Einstein condensates,” *Physical Review Letters*, vol. 105, no. 2, p. 020602, 2010.
- [24] S. Pigeon, I. Carusotto, and C. Ciuti, “Hydrodynamic nucleation of vortices and solitons in a resonantly excited polariton superfluid,” *Physical Review B – Condensed Matter and Materials Physics*, vol. 83, no. 14, p. 144513, 2011.
- [25] E. P. Gross, “Structure of a quantized vortex in boson systems,” *Il Nuovo Cimento (1955-1965)*, vol. 20, no. 3, pp. 454–477, 1961.
- [26] L. P. Pitaevskii, “Vortex lines in an imperfect bose gas,” *Soviet Physics JETP*, vol. 13, no. 2, pp. 451–454, 1961.
- [27] M. Wouters and I. Carusotto, “Excitations in a nonequilibrium Bose-Einstein condensate of exciton polaritons,” *Physical Review Letters*, vol. 99, no. 14, p. 140402, 2007.

- [28] K. v. Klitzing, G. Dorda, and M. Pepper, “New method for high-accuracy determination of the fine-structure constant based on quantized hall resistance,” *Physical Review Letters*, vol. 45, no. 6, p. 494, 1980.
- [29] D. J. Thouless, M. Kohmoto, M. P. Nightingale, and M. den Nijs, “Quantized Hall conductance in a two-dimensional periodic potential,” *Physical Review Letters*, vol. 49, no. 6, p. 405, 1982.
- [30] F. D. M. Haldane, “Model for a quantum Hall effect without Landau levels: Condensed-matter realization of the "parity anomaly",” *Physical Review Letters*, vol. 61, no. 18, p. 2015, 1988.
- [31] L. Lu, J. D. Joannopoulos, and M. Soljačić, “Topological photonics,” *Nature Photonics*, vol. 8, no. 11, pp. 821–829, 2014.
- [32] T. Ozawa, H. M. Price, A. Amo, N. Goldman, M. Hafezi, L. Lu, M. C. Rechtsman, D. Schuster, J. Simon, O. Zilberberg *et al.*, “Topological photonics,” *Reviews of Modern Physics*, vol. 91, no. 1, p. 015006, 2019.
- [33] H. Price, Y. Chong, A. Khanikaev, H. Schomerus, L. J. Maczewsky, M. Kremer, M. Heinrich, A. Szameit, O. Zilberberg, Y. Yang *et al.*, “Roadmap on topological photonics,” *Journal of Physics: Photonics*, vol. 4, no. 3, p. 032501, 2022.
- [34] F. D. M. Haldane and S. Raghu, “Possible realization of directional optical waveguides in photonic crystals with broken time-reversal symmetry,” *Physical Review Letters*, vol. 100, no. 1, p. 013904, 2008.
- [35] S. Raghu and F. D. M. Haldane, “Analogues of quantum-Hall-effect edge states in photonic crystals,” *Physical Review A – Atomic, Molecular, and Optical Physics*, vol. 78, no. 3, p. 033834, 2008.
- [36] Y. Hatsugai, “Edge states in the integer quantum Hall effect and the Riemann surface of the Bloch function,” *Physical Review B*, vol. 48, no. 16, p. 11851, 1993.
- [37] —, “Chern number and edge states in the integer quantum Hall effect,” *Physical Review Letters*, vol. 71, pp. 3697–3700, 1993.
- [38] Z. Wang, Y. Chong, J. D. Joannopoulos, and M. Soljačić, “Reflection-free one-way edge modes in a gyromagnetic photonic crystal,” *Physical Review Letters*, vol. 100, no. 1, p. 013905, 2008.
- [39] Z. Wang, Y. Chong, J. D. Joannopoulos, and M. Soljačić, “Observation of unidirectional backscattering-immune topological electromagnetic states,” *Nature*, vol. 461, no. 7265, pp. 772–775, October 2009.
- [40] M. C. Rechtsman, J. M. Zeuner, Y. Plotnik, Y. Lumer, D. Podolsky, F. Dreisow, S. Nolte, M. Segev, and A. Szameit, “Photonic Floquet topological insulators,” *Nature*, vol. 496, no. 7444, pp. 196–200, 2013.

- [41] J. Noh, S. Huang, D. Leykam, Y. D. Chong, K. P. Chen, and M. C. Rechtsman, “Experimental observation of optical Weyl points and Fermi arc-like surface states,” *Nature Physics*, vol. 13, no. 6, pp. 611–617, 2017.
- [42] M. Kremer, T. Biesenthal, L. J. Maczewsky, M. Heinrich, R. Thomale, and A. Szameit, “Demonstration of a two-dimensional PT-symmetric crystal,” *Nature Communications*, vol. 10, no. 1, p. 435, 2019.
- [43] L. J. Maczewsky, J. M. Zeuner, S. Nolte, and A. Szameit, “Observation of photonic anomalous Floquet topological insulators,” *Nature Communications*, vol. 8, no. 1, p. 13756, 2017.
- [44] S. Mukherjee, A. Spracklen, M. Valiente, E. Andersson, P. Öhberg, N. Goldman, and R. R. Thomson, “Experimental observation of anomalous topological edge modes in a slowly driven photonic lattice,” *Nature Communications*, vol. 8, no. 1, p. 13918, 2017.
- [45] S. Stützer, Y. Plotnik, Y. Lumer, P. Titum, N. H. Lindner, M. Segev, M. C. Rechtsman, and A. Szameit, “Photonic topological Anderson insulators,” *Nature*, vol. 560, no. 7719, pp. 461–465, 2018.
- [46] T. Kitagawa, M. A. Broome, A. Fedrizzi, M. S. Rudner, E. Berg, I. Kassal, A. Aspuru-Guzik, E. Demler, and A. G. White, “Observation of topologically protected bound states in photonic quantum walks,” *Nature Communications*, vol. 3, no. 1, p. 882, 2012.
- [47] T. Ozawa, H. M. Price, N. Goldman, O. Zilberberg, and I. Carusotto, “Synthetic dimensions in integrated photonics: From optical isolation to four-dimensional quantum Hall physics,” *Physical Review A*, vol. 93, no. 4, p. 043827, 2016.
- [48] L. Yuan, Y. Shi, and S. Fan, “Photonic gauge potential in a system with a synthetic frequency dimension,” *Optics Letters*, vol. 41, no. 4, pp. 741–744, 2016.
- [49] E. Lustig, S. Weimann, Y. Plotnik, Y. Lumer, M. A. Bandres, A. Szameit, and M. Segev, “Photonic topological insulator in synthetic dimensions,” *Nature*, vol. 567, no. 7748, pp. 356–360, 2019.
- [50] X.-W. Luo, X. Zhou, J.-S. Xu, C.-F. Li, G.-C. Guo, C. Zhang, and Z.-W. Zhou, “Synthetic-lattice enabled all-optical devices based on orbital angular momentum of light,” *Nature Communications*, vol. 8, no. 1, p. 16097, 2017.
- [51] X.-F. Zhou, X.-W. Luo, S. Wang, G.-C. Guo, X. Zhou, H. Pu, and Z.-W. Zhou, “Dynamically manipulating topological physics and edge modes in a single degenerate optical cavity,” *Physical Review Letters*, vol. 118, no. 8, p. 083603, 2017.
- [52] H. M. Price, “Four-dimensional topological lattices through connectivity,” *Physical Review B*, vol. 101, no. 20, p. 205141, 2020.

- [53] D. Smirnova, D. Leykam, Y. Chong, and Y. Kivshar, “Nonlinear topological photonics,” *Applied Physics Reviews*, vol. 7, no. 2, 2020.
- [54] E. J. Bergholtz, J. C. Budich, and F. K. Kunst, “Exceptional topology of non-Hermitian systems,” *Reviews of Modern Physics*, vol. 93, no. 1, p. 015005, 2021.
- [55] Y. Lumer, Y. Plotnik, M. C. Rechtsman, and M. Segev, “Self-localized states in photonic topological insulators,” *Physical Review Letters*, vol. 111, no. 24, p. 243905, 2013.
- [56] D. Leykam and Y. D. Chong, “Edge solitons in nonlinear-photonic topological insulators,” *Physical Review Letters*, vol. 117, no. 14, p. 143901, 2016.
- [57] Y. Lumer, M. C. Rechtsman, Y. Plotnik, and M. Segev, “Instability of bosonic topological edge states in the presence of interactions,” *Physical Review A*, vol. 94, no. 2, p. 021801, 2016.
- [58] S. Mukherjee and M. C. Rechtsman, “Observation of Floquet solitons in a topological bandgap,” *Science*, vol. 368, no. 6493, pp. 856–859, 2020.
- [59] L. J. Maczewsky, M. Heinrich, M. Kremer, S. K. Ivanov, M. Ehrhardt, F. Martinez, Y. V. Kartashov, V. V. Konotop, L. Torner, D. Bauer *et al.*, “Nonlinearity-induced photonic topological insulator,” *Science*, vol. 370, no. 6517, pp. 701–704, 2020.
- [60] Y. Hadad, A. B. Khanikaev, and A. Alu, “Self-induced topological transitions and edge states supported by nonlinear staggered potentials,” *Physical Review B*, vol. 93, no. 15, p. 155112, 2016.
- [61] D. Dobrykh, A. Yulin, A. Slobozhanyuk, A. Poddubny, and Y. S. Kivshar, “Nonlinear control of electromagnetic topological edge states,” *Physical Review Letters*, vol. 121, no. 16, p. 163901, 2018.
- [62] F. Zangeneh-Nejad and R. Fleury, “Nonlinear second-order topological insulators,” *Physical Review Letters*, vol. 123, no. 5, p. 053902, 2019.
- [63] S. Weimann, M. Kremer, Y. Plotnik, Y. Lumer, S. Nolte, K. G. Makris, M. Segev, M. C. Rechtsman, and A. Szameit, “Topologically protected bound states in photonic parity-time-symmetric crystals,” *Nature Materials*, vol. 16, no. 4, pp. 433–438, 2017.
- [64] L. Xiao, X. Zhan, Z. Bian, K. Wang, X. Zhang, X. Wang, J. Li, K. Mochizuki, D. Kim, N. Kawakami *et al.*, “Observation of topological edge states in parity-time-symmetric quantum walks,” *Nature Physics*, vol. 13, no. 11, pp. 1117–1123, 2017.
- [65] H. Zhou, C. Peng, Y. Yoon, C. W. Hsu, K. A. Nelson, L. Fu, J. D. Joannopoulos, M. Soljačić, and B. Zhen, “Observation of bulk Fermi arc and polarization half charge from paired exceptional points,” *Science*, vol. 359, no. 6379, pp. 1009–1012, 2018.

- [66] B. Peng, Ş. K. Özdemir, M. Liertzer, W. Chen, J. Kramer, H. Yilmaz, J. Wiersig, S. Rotter, and L. Yang, “Chiral modes and directional lasing at exceptional points,” *Proceedings of the National Academy of Sciences*, vol. 113, no. 25, pp. 6845–6850, 2016.
- [67] L. Feng, Z. J. Wong, R.-M. Ma, Y. Wang, and X. Zhang, “Single-mode laser by parity-time symmetry breaking,” *Science*, vol. 346, no. 6212, pp. 972–975, 2014.
- [68] H. Hodaei, M.-A. Miri, M. Heinrich, D. N. Christodoulides, and M. Khajavikhan, “Parity-time-symmetric microring lasers,” *Science*, vol. 346, no. 6212, pp. 975–978, 2014.
- [69] D. D. Solnyshkov, A. V. Nalitov, and G. Malpuech, “Kibble-Zurek mechanism in topologically nontrivial zigzag chains of polariton micropillars,” *Physical Review Letters*, vol. 116, no. 4, p. 046402, 2016.
- [70] P. St-Jean, V. Goblot, E. Galopin, A. Lemaître, T. Ozawa, L. Le Gratiet, I. Sagnes, J. Bloch, and A. Amo, “Lasing in topological edge states of a one-dimensional lattice,” *Nature Photonics*, vol. 11, no. 10, pp. 651–656, 2017.
- [71] O. Bleu, G. Malpuech, Y. Gao, and D. Solnyshkov, “Effective theory of nonadiabatic quantum evolution based on the quantum geometric tensor,” *Physical Review Letters*, vol. 121, no. 2, p. 020401, 2018.
- [72] A. Gianfrate, O. Bleu, L. Dominici, V. Ardizzone, M. De Giorgi, D. Ballarini, G. Lerario, K. West, L. Pfeiffer, D. Solnyshkov, D. Sanvitto, and G. Malpuech, “Measurement of the quantum geometric tensor and of the anomalous Hall drift,” *Nature*, vol. 578, no. 7795, pp. 381–385, 2020.
- [73] A. Nalitov, D. Solnyshkov, and G. Malpuech, “Polariton Z topological insulator,” *Physical Review Letters*, vol. 114, no. 11, p. 116401, 2015.
- [74] C.-E. Bardyn, T. Karzig, G. Refael, and T. C. Liew, “Topological polaritons and excitons in garden-variety systems,” *Physical Review B*, vol. 91, no. 16, p. 161413, 2015.
- [75] S. Klemmt, T. Harder, O. Egorov, K. Winkler, R. Ge, M. Bandres, M. Emmerling, L. Worschech, T. Liew, M. Segev *et al.*, “Exciton-polariton topological insulator,” *Nature*, vol. 562, no. 7728, pp. 552–556, 2018.
- [76] O. Bleu, G. Malpuech, and D. Solnyshkov, “Robust quantum valley Hall effect for vortices in an interacting bosonic quantum fluid,” *Nature Communications*, vol. 9, no. 1, p. 3991, 2018.
- [77] C.-E. Bardyn, T. Karzig, G. Refael, and T. C. Liew, “Chiral Bogoliubov excitations in nonlinear bosonic systems,” *Physical Review B*, vol. 93, no. 2, p. 020502, 2016.

- [78] H. Sigurdsson, G. Li, and T. C. H. Liew, “Spontaneous and superfluid chiral edge states in exciton-polariton condensates,” *Physical Review B*, vol. 96, no. 11, p. 115453, 2017.
- [79] O. Bleu, D. Solnyshkov, and G. Malpuech, “Photonic versus electronic quantum anomalous Hall effect,” *Physical Review B*, vol. 95, no. 11, p. 115415, 2017.
- [80] ———, “Interacting quantum fluid in a polariton Chern insulator,” *Physical Review B*, vol. 93, no. 8, p. 085438, 2016.
- [81] K. Rechcińska, M. Król, R. Mazur, P. Morawiak, R. Mirek, K. Łempicka, W. Bardyszewski, M. Matuszewski, P. Kula, W. Piecek *et al.*, “Engineering spin-orbit synthetic Hamiltonians in liquid-crystal optical cavities,” *Science*, vol. 366, no. 6466, pp. 727–730, 2019.
- [82] M. Aidelsburger, S. Nascimbene, and N. Goldman, “Artificial gauge fields in materials and engineered systems,” *Comptes Rendus Physique*, vol. 19, no. 6, pp. 394–432, 2018.
- [83] Y. Aharonov and D. Bohm, “Significance of electromagnetic potentials in the quantum theory,” *Physical Review*, vol. 115, no. 3, p. 485, 1959.
- [84] Y. Chen, R.-Y. Zhang, Z. Xiong, Z. H. Hang, J. Li, J. Q. Shen, and C. T. Chan, “Non-Abelian gauge field optics,” *Nature Communications*, vol. 10, no. 1, p. 3125, 2019.
- [85] A. B. Khanikaev, S. Hossein Mousavi, W.-K. Tse, M. Kargarian, A. H. MacDonald, and G. Shvets, “Photonic topological insulators,” *Nature Materials*, vol. 12, no. 3, pp. 233–239, 2013.
- [86] R. Umucalılar and I. Carusotto, “Artificial gauge field for photons in coupled cavity arrays,” *Physical Review A*, vol. 84, no. 4, p. 043804, 2011.
- [87] M. Hafezi, E. A. Demler, M. D. Lukin, and J. M. Taylor, “Robust optical delay lines with topological protection,” *Nature Physics*, vol. 7, no. 11, pp. 907–912, 2011.
- [88] M. Hafezi, S. Mittal, J. Fan, A. Migdall, and J. Taylor, “Imaging topological edge states in silicon photonics,” *Nature Photonics*, vol. 7, no. 12, pp. 1001–1005, 2013.
- [89] P. G. Harper, “Single band motion of conduction electrons in a uniform magnetic field,” *Proceedings of the Physical Society. Section A*, vol. 68, no. 10, p. 874, 1955.
- [90] D. R. Hofstadter, “Energy levels and wave functions of Bloch electrons in rational and irrational magnetic fields,” *Physical Review B*, vol. 14, no. 6, p. 2239, 1976.
- [91] M. C. Rechtsman, J. M. Zeuner, A. Tünnermann, S. Nolte, M. Segev, and A. Szameit, “Strain-induced pseudomagnetic field and photonic Landau levels in dielectric structures,” *Nature Photonics*, vol. 7, no. 2, pp. 153–158, 2013.

- [92] G. Salerno, T. Ozawa, H. M. Price, and I. Carusotto, “Propagating edge states in strained honeycomb lattices,” *Physical Review B*, vol. 95, no. 24, p. 245418, 2017.
- [93] O. Jamadi, E. Rozas, G. Salerno, M. Milićević, T. Ozawa, I. Sagnes, A. Lemaître, L. Le Gratiet, A. Harouri, I. Carusotto *et al.*, “Direct observation of photonic Landau levels and helical edge states in strained honeycomb lattices,” *Light: Science & Applications*, vol. 9, no. 1, p. 144, 2020.
- [94] R. Barczyk, L. Kuipers, and E. Verhagen, “Observation of Landau levels and chiral edge states in photonic crystals through pseudomagnetic fields induced by synthetic strain,” *Nature Photonics*, vol. 18, no. 6, p. 574–579, Apr. 2024.
- [95] K. Fang, Z. Yu, and S. Fan, “Realizing effective magnetic field for photons by controlling the phase of dynamic modulation,” *Nature Photonics*, vol. 6, no. 11, pp. 782–787, 2012.
- [96] G. Jotzu, M. Messer, R. Desbuquois, M. Lebrat, T. Uehlinger, D. Greif, and T. Esslinger, “Experimental realization of the topological Haldane model with ultracold fermions,” *Nature*, vol. 515, no. 7526, pp. 237–240, 2014.
- [97] D. Hey and E. Li, “Advances in synthetic gauge fields for light through dynamic modulation,” *Royal Society Open Science*, vol. 5, no. 4, p. 172447, 2018.
- [98] A. Dutt, Q. Lin, L. Yuan, M. Minkov, M. Xiao, and S. Fan, “A single photonic cavity with two independent physical synthetic dimensions,” *Science*, vol. 367, no. 6473, pp. 59–64, 2020.
- [99] M. Wimmer, H. M. Price, I. Carusotto, and U. Peschel, “Experimental measurement of the Berry curvature from anomalous transport,” *Nature Physics*, vol. 13, no. 6, pp. 545–550, 2017.
- [100] K. Wang, B. A. Bell, A. S. Solntsev, D. N. Neshev, B. J. Eggleton, and A. A. Sukhorukov, “Multidimensional synthetic chiral-tube lattices via nonlinear frequency conversion,” *Light: Science & Applications*, vol. 9, no. 1, p. 132, 2020.
- [101] X.-L. Qi, T. L. Hughes, and S.-C. Zhang, “Topological field theory of time-reversal invariant insulators,” *Physical Review B – Condensed Matter and Materials Physics*, vol. 78, no. 19, p. 195424, 2008.
- [102] A. Slobozhanyuk, S. H. Mousavi, X. Ni, D. Smirnova, Y. S. Kivshar, and A. B. Khanikaev, “Three-dimensional all-dielectric photonic topological insulator,” *Nature Photonics*, vol. 11, no. 2, pp. 130–136, 2017.
- [103] Y. Yang, Z. Gao, H. Xue, L. Zhang, M. He, Z. Yang, R. Singh, Y. Chong, B. Zhang, and H. Chen, “Realization of a three-dimensional photonic topological insulator,” *Nature*, vol. 565, no. 7741, pp. 622–626, 2019.

- [104] Y. Lumer, M. A. Bandres, M. Heinrich, L. J. Maczewsky, H. Herzig-Sheinfux, A. Szaimeit, and M. Segev, “Light guiding by artificial gauge fields,” *Nature Photonics*, vol. 13, no. 5, pp. 339–345, 2019.
- [105] H. Chalabi, S. Barik, S. Mittal, T. E. Murphy, M. Hafezi, and E. Waks, “Guiding and confining of light in a two-dimensional synthetic space using electric fields,” *Optica*, vol. 7, no. 5, pp. 506–513, 2020.
- [106] Y. Yang, B. Zhen, J. D. Joannopoulos, and M. Soljačić, “Non-Abelian generalizations of the Hofstadter model: spin-orbit-coupled butterfly pairs,” *Light: Science & Applications*, vol. 9, no. 1, p. 177, 2020.
- [107] X. Ni, D. Purtseladze, D. A. Smirnova, A. Slobozhanyuk, A. Alù, and A. B. Khanikaev, “Spin- and valley-polarized one-way Klein tunneling in photonic topological insulators,” *Science Advances*, vol. 4, no. 5, p. eaap8802, 2018.
- [108] L. Lu, Z. Wang, D. Ye, L. Ran, L. Fu, J. D. Joannopoulos, and M. Soljačić, “Experimental observation of Weyl points,” *Science*, vol. 349, no. 6248, pp. 622–624, 2015.
- [109] A. Cerjan, S. Huang, M. Wang, K. P. Chen, Y. Chong, and M. C. Rechtsman, “Experimental realization of a Weyl exceptional ring,” *Nature Photonics*, vol. 13, no. 9, pp. 623–628, 2019.
- [110] A. Nalitov, G. Malpuech, H. Terças, and D. Solnyshkov, “Spin-orbit coupling and the optical spin Hall effect in photonic graphene,” *Physical Review Letters*, vol. 114, no. 2, p. 026803, 2015.
- [111] C. Whittaker, T. Dowling, A. Nalitov, A. Yulin, B. Royall, E. Clarke, M. Skolnick, I. Shelykh, and D. Krizhanovskii, “Optical analogue of Dresselhaus spin-orbit interaction in photonic graphene,” *Nature Photonics*, vol. 15, no. 3, pp. 193–196, 2021.
- [112] H. Terças, H. Flayac, D. Solnyshkov, and G. Malpuech, “Non-Abelian gauge fields in photonic cavities and photonic superfluids,” *Physical Review Letters*, vol. 112, no. 6, p. 066402, 2014.
- [113] L. Polimeno, A. Fieramosca, G. Lerario, L. De Marco, M. De Giorgi, D. Ballarini, L. Dominici, V. Ardizzone, M. Pugliese, C. Prontera *et al.*, “Experimental investigation of a non-Abelian gauge field in 2D perovskite photonic platform,” *Optica*, vol. 8, no. 11, pp. 1442–1447, 2021.
- [114] H.-T. Lim, E. Togan, M. Kroner, J. Miguel-Sanchez, and A. Imamoğlu, “Electrically tunable artificial gauge potential for polaritons,” *Nature Communications*, vol. 8, no. 1, p. 14540, 2017.
- [115] W.-P. Su, J. R. Schrieffer, and A. J. Heeger, “Solitons in polyacetylene,” *Physical Review Letters*, vol. 42, no. 25, p. 1698, 1979.

- [116] J. K. Asbóth, L. Oroszlány, and A. Pályi, “A short course on topological insulators,” *Lecture notes in physics*, vol. 919, no. 1, 2016.
- [117] S. Ryu and Y. Hatsugai, “Topological origin of zero-energy edge states in particle-hole symmetric systems,” *Physical Review Letters*, vol. 89, no. 7, p. 077002, 2002.
- [118] A. Altland and M. R. Zirnbauer, “Nonstandard symmetry classes in mesoscopic normal-superconducting hybrid structures,” *Physical Review B*, vol. 55, no. 2, p. 1142, 1997.
- [119] K. Kawabata, K. Shiozaki, M. Ueda, and M. Sato, “Symmetry and topology in non-Hermitian physics,” *Physical Review X*, vol. 9, no. 4, p. 041015, 2019.
- [120] P. Delplace, D. Ullmo, and G. Montambaux, “Zak phase and the existence of edge states in graphene,” *Physical Review B – Condensed Matter and Materials Physics*, vol. 84, no. 19, p. 195452, 2011.
- [121] J. Zak, “Berry’s phase for energy bands in solids,” *Physical Review Letters*, vol. 62, no. 23, p. 2747, 1989.
- [122] T. H. Harder, M. Sun, O. A. Egorov, I. Vakulchyk, J. Beierlein, P. Gagel, M. Emmerling, C. Schneider, U. Peschel, I. G. Savenko *et al.*, “Coherent topological polariton laser,” *ACS Photonics*, vol. 8, no. 5, pp. 1377–1384, 2021.
- [123] M. Dusel, S. Betzold, T. H. Harder, M. Emmerling, J. Beierlein, J. Ohmer, U. Fischer, R. Thomale, C. Schneider, S. Hofling *et al.*, “Room-temperature topological polariton laser in an organic lattice,” *Nano Letters*, vol. 21, no. 15, pp. 6398–6405, 2021.
- [124] R. Su, S. Ghosh, T. C. Liew, and Q. Xiong, “Optical switching of topological phase in a perovskite polariton lattice,” *Science Advances*, vol. 7, no. 21, p. eabf8049, 2021.
- [125] P. Gagel, O. A. Egorov, F. Dzimira, J. Beierlein, M. Emmerling, A. Wolf, F. Jabeen, S. Betzold, U. Peschel, S. Hofling *et al.*, “An electrically pumped topological polariton laser,” *Nano Letters*, vol. 24, no. 22, pp. 6538–6544, 2024.
- [126] L. Pickup, H. Sigurdsson, J. Ruostekoski, and P. Lagoudakis, “Synthetic band-structure engineering in polariton crystals with non-Hermitian topological phases,” *Nature Communications*, vol. 11, no. 1, p. 4431, 2020.
- [127] N. Malkova, I. Hromada, X. Wang, G. Bryant, and Z. Chen, “Observation of optical Shockley-like surface states in photonic superlattices,” *Optics Letters*, vol. 34, no. 11, pp. 1633–1635, 2009.
- [128] F. Cardano, A. D’Errico, A. Dauphin, M. Maffei, B. Piccirillo, C. de Lisio, G. De Filippis, V. Cataudella, E. Santamato, L. Marrucci *et al.*, “Detection of Zak phases and topological invariants in a chiral quantum walk of twisted photons,” *Nature Communications*, vol. 8, no. 1, p. 15516, 2017.

- [129] I. S. Sinev, I. S. Mukhin, A. P. Slobozhanyuk, A. N. Poddubny, A. E. Miroschnichenko, A. K. Samusev, and Y. S. Kivshar, “Mapping plasmonic topological states at the nanoscale,” *Nanoscale*, vol. 7, no. 28, pp. 11 904–11 908, 2015.
- [130] A. P. Slobozhanyuk, A. N. Poddubny, I. S. Sinev, A. K. Samusev, Y. F. Yu, A. I. Kuznetsov, A. E. Miroschnichenko, and Y. S. Kivshar, “Enhanced photonic spin Hall effect with subwavelength topological edge states,” *Laser & Photonics Reviews*, vol. 10, no. 4, pp. 656–664, 2016.
- [131] S. Kruk, A. Slobozhanyuk, D. Denkova, A. Poddubny, I. Kravchenko, A. Miroschnichenko, D. Neshev, and Y. Kivshar, “Edge states and topological phase transitions in chains of dielectric nanoparticles,” *Small*, vol. 13, no. 11, p. 1603190, 2017.
- [132] Q. Cheng, Y. Pan, Q. Wang, T. Li, and S. Zhu, “Topologically protected interface mode in plasmonic waveguide arrays,” *Laser & Photonics Reviews*, vol. 9, no. 4, pp. 392–398, 2015.
- [133] F. Bleckmann, Z. Cherpakova, S. Linden, and A. Alberti, “Spectral imaging of topological edge states in plasmonic waveguide arrays,” *Physical Review B*, vol. 96, no. 4, p. 045417, 2017.
- [134] Z. Fedorova, C. Jörg, C. Dauer, F. Letscher, M. Fleischhauer, S. Eggert, S. Linden, and G. von Freymann, “Limits of topological protection under local periodic driving,” *Light: Science & Applications*, vol. 8, no. 1, p. 63, 2019.
- [135] A. Blanco-Redondo, I. Andonegui, M. J. Collins, G. Harari, Y. Lumer, M. C. Rechtsman, B. J. Eggleton, and M. Segev, “Topological optical waveguiding in silicon and the transition between topological and trivial defect states,” *Physical Review Letters*, vol. 116, no. 16, p. 163901, 2016.
- [136] Y. Wang, Y.-H. Lu, F. Mei, J. Gao, Z.-M. Li, H. Tang, S.-L. Zhu, S. Jia, and X.-M. Jin, “Direct observation of topology from single-photon dynamics,” *Physical Review Letters*, vol. 122, no. 19, p. 193903, 2019.
- [137] C. Poli, M. Bellec, U. Kuhl, F. Mortessagne, and H. Schomerus, “Selective enhancement of topologically induced interface states in a dielectric resonator chain,” *Nature Communications*, vol. 6, no. 1, p. 6710, 2015.
- [138] M. B. On, F. Ashtiani, D. Sanchez-Jacome, D. Perez-Lopez, S. B. Yoo, and A. Blanco-Redondo, “Programmable integrated photonics for topological Hamiltonians,” *Nature Communications*, vol. 15, no. 1, p. 629, 2024.
- [139] B. A. Bernevig, *Topological insulators and topological superconductors*. Princeton University Press, 2013.
- [140] M. V. Berry, “Quantal phase factors accompanying adiabatic changes,” *Proceedings of the Royal Society of London. A. Mathematical and Physical Sciences*, vol. 392, no. 1802, pp. 45–57, 1984.

- [141] N. Moiseyev, P. Certain, and F. Weinhold, “Resonance properties of complex-rotated hamiltonians,” *Molecular Physics*, vol. 36, no. 6, pp. 1613–1630, 1978.
- [142] C. M. Bender and S. Boettcher, “Real spectra in non-Hermitian Hamiltonians having  $pt$  symmetry,” *Physical Review Letters*, vol. 80, no. 24, p. 5243, 1998.
- [143] A. Ruschhaupt, F. Delgado, and J. Muga, “Physical realization of  $pt$ -symmetric potential scattering in a planar slab waveguide,” *Journal of Physics A: Mathematical and General*, vol. 38, no. 9, p. L171, 2005.
- [144] R. El-Ganainy, K. Makris, D. Christodoulides, and Z. H. Musslimani, “Theory of coupled optical  $pt$ -symmetric structures,” *Optics Letters*, vol. 32, no. 17, pp. 2632–2634, 2007.
- [145] J. Wiersig, “Enhancing the sensitivity of frequency and energy splitting detection by using exceptional points: application to microcavity sensors for single-particle detection,” *Physical Review Letters*, vol. 112, no. 20, p. 203901, 2014.
- [146] W. Chen, Ş. Kaya Özdemir, G. Zhao, J. Wiersig, and L. Yang, “Exceptional points enhance sensing in an optical microcavity,” *Nature*, vol. 548, no. 7666, pp. 192–196, 2017.
- [147] H. Hodaei, A. U. Hassan, S. Wittek, H. Garcia-Gracia, R. El-Ganainy, D. N. Christodoulides, and M. Khajavikhan, “Enhanced sensitivity at higher-order exceptional points,” *Nature*, vol. 548, no. 7666, pp. 187–191, 2017.
- [148] A. Regensburger, C. Bersch, M.-A. Miri, G. Onishchukov, D. N. Christodoulides, and U. Peschel, “Parity-time synthetic photonic lattices,” *Nature*, vol. 488, no. 7410, pp. 167–171, 2012.
- [149] L. Feng, Y.-L. Xu, W. S. Fegadolli, M.-H. Lu, J. E. Oliveira, V. R. Almeida, Y.-F. Chen, and A. Scherer, “Experimental demonstration of a unidirectional reflectionless parity-time metamaterial at optical frequencies,” *Nature Materials*, vol. 12, no. 2, pp. 108–113, 2013.
- [150] B. Peng, Ş. K. Özdemir, F. Lei, F. Monifi, M. Gianfreda, G. L. Long, S. Fan, F. Nori, C. M. Bender, and L. Yang, “Parity-time-symmetric whispering-gallery microcavities,” *Nature Physics*, vol. 10, no. 5, pp. 394–398, 2014.
- [151] S. Yao and Z. Wang, “Edge states and topological invariants of non-Hermitian systems,” *Physical Review Letters*, vol. 121, no. 8, p. 086803, 2018.
- [152] Z. Gong, Y. Ashida, K. Kawabata, K. Takasan, S. Higashikawa, and M. Ueda, “Topological phases of non-Hermitian systems,” *Physical Review X*, vol. 8, no. 3, p. 031079, 2018.
- [153] N. Hatano and D. R. Nelson, “Localization transitions in non-Hermitian quantum mechanics,” *Physical Review Letters*, vol. 77, no. 3, p. 570, 1996.

- [154] K. Yokomizo and S. Murakami, “Non-Bloch band theory of non-Hermitian systems,” *Physical Review Letters*, vol. 123, no. 6, p. 066404, 2019.
- [155] K. Zhang, Z. Yang, and C. Fang, “Correspondence between winding numbers and skin modes in non-Hermitian systems,” *Physical Review Letters*, vol. 125, no. 12, p. 126402, 2020.
- [156] X. Zhang, Y. Tian, J.-H. Jiang, M.-H. Lu, and Y.-F. Chen, “Observation of higher-order non-Hermitian skin effect,” *Nature Communications*, vol. 12, no. 1, p. 5377, 2021.
- [157] L. Zhang, Y. Yang, Y. Ge, Y.-J. Guan, Q. Chen, Q. Yan, F. Chen, R. Xi, Y. Li, D. Jia *et al.*, “Acoustic non-Hermitian skin effect from twisted winding topology,” *Nature Communications*, vol. 12, no. 1, p. 6297, 2021.
- [158] M. Brandenbourger, X. Locsin, E. Lerner, and C. Coulais, “Non-reciprocal robotic metamaterials,” *Nature Communications*, vol. 10, no. 1, p. 4608, 2019.
- [159] A. Ghatak, M. Brandenbourger, J. Van Wezel, and C. Coulais, “Observation of non-Hermitian topology and its bulk-edge correspondence in an active mechanical metamaterial,” *Proceedings of the National Academy of Sciences*, vol. 117, no. 47, pp. 29 561–29 568, 2020.
- [160] Y. Chen, X. Li, C. Scheibner, V. Vitelli, and G. Huang, “Realization of active metamaterials with odd micropolar elasticity,” *Nature Communications*, vol. 12, no. 1, p. 5935, 2021.
- [161] W. Wang, X. Wang, and G. Ma, “Non-Hermitian morphing of topological modes,” *Nature*, vol. 608, no. 7921, pp. 50–55, 2022.
- [162] T. Helbig, T. Hofmann, S. Imhof, M. Abdelghany, T. Kiessling, L. Molenkamp, C. Lee, A. Szameit, M. Greiter, and R. Thomale, “Generalized bulk-boundary correspondence in non-Hermitian topoelectrical circuits,” *Nature Physics*, vol. 16, no. 7, pp. 747–750, 2020.
- [163] T. Hofmann, T. Helbig, F. Schindler, N. Salgo, M. Brzezińska, M. Greiter, T. Kiessling, D. Wolf, A. Vollhardt, A. Kabaši *et al.*, “Reciprocal skin effect and its realization in a topoelectrical circuit,” *Physical Review Research*, vol. 2, no. 2, p. 023265, 2020.
- [164] S. Liu, R. Shao, S. Ma, L. Zhang, O. You, H. Wu, Y. J. Xiang, T. J. Cui, and S. Zhang, “Non-Hermitian skin effect in a non-Hermitian electrical circuit,” *Research*, 2021.
- [165] D. Zou, T. Chen, W. He, J. Bao, C. H. Lee, H. Sun, and X. Zhang, “Observation of hybrid higher-order skin-topological effect in non-Hermitian topoelectrical circuits,” *Nature Communications*, vol. 12, no. 1, p. 7201, 2021.

- [166] Q. Liang, D. Xie, Z. Dong, H. Li, H. Li, B. Gadway, W. Yi, and B. Yan, “Dynamic signatures of non-Hermitian skin effect and topology in ultracold atoms,” *Physical Review Letters*, vol. 129, no. 7, p. 070401, 2022.
- [167] S. Longhi, D. Gatti, and G. D. Valle, “Robust light transport in non-Hermitian photonic lattices,” *Scientific Reports*, vol. 5, no. 1, pp. 1–12, 2015.
- [168] X. Zhu, H. Wang, S. K. Gupta, H. Zhang, B. Xie, M. Lu, and Y. Chen, “Photonic non-Hermitian skin effect and non-Bloch bulk-boundary correspondence,” *Physical Review Research*, vol. 2, no. 1, p. 013280, 2020.
- [169] Y. Song, W. Liu, L. Zheng, Y. Zhang, B. Wang, and P. Lu, “Two-dimensional non-Hermitian skin effect in a synthetic photonic lattice,” *Physical Review Applied*, vol. 14, no. 6, p. 064076, 2020.
- [170] H. Gao, H. Xue, Z. Gu, L. Li, W. Zhu, Z. Su, J. Zhu, B. Zhang, and Y. Chong, “Anomalous Floquet non-Hermitian skin effect in a ring resonator lattice,” *Physical Review B*, vol. 106, no. 13, p. 134112, 2022.
- [171] S. Mandal, R. Banerjee, E. A. Ostrovskaya, and T. C. H. Liew, “Nonreciprocal transport of exciton polaritons in a non-Hermitian chain,” *Physical Review Letters*, vol. 125, no. 12, p. 123902, 2020.
- [172] H. Xu, K. Dini, X. Xu, R. Banerjee, S. Mandal, and T. C. Liew, “Nonreciprocal exciton-polariton ring lattices,” *Physical Review B*, vol. 104, no. 19, p. 195301, 2021.
- [173] S. Mandal, R. Banerjee, and T. C. Liew, “From the topological spin-Hall effect to the non-Hermitian skin effect in an elliptical micropillar chain,” *ACS Photonics*, vol. 9, no. 2, pp. 527–539, 2022.
- [174] X. Xu, R. Bao, and T. C. Liew, “Non-Hermitian topological exciton-polariton corner modes,” *Physical Review B*, vol. 106, no. 20, p. L201302, 2022.
- [175] M. Yang, L. Wang, X. Wu, H. Xiao, D. Yu, L. Yuan, and X. Chen, “Concentrated subradiant modes in a one-dimensional atomic array coupled with chiral waveguides,” *Physical Review A*, vol. 106, no. 4, p. 043717, 2022.
- [176] J. Zhong, K. Wang, Y. Park, V. Asadchy, C. C. Wojcik, A. Dutt, and S. Fan, “Nontrivial point-gap topology and non-Hermitian skin effect in photonic crystals,” *Physical Review B*, vol. 104, no. 12, p. 125416, 2021.
- [177] “Non-Hermitian skin effect and delocalized edge states in photonic crystals with anomalous parity-time symmetry,” *Progress In Electromagnetics Research*, vol. 172, pp. 33–40, 2021.
- [178] K. Yokomizo, T. Yoda, and S. Murakami, “Non-Hermitian waves in a continuous periodic model and application to photonic crystals,” *Physical Review Research*, vol. 4, no. 2, p. 023089, 2022.

- [179] Z. Fang, M. Hu, L. Zhou, and K. Ding, “Geometry-dependent skin effects in reciprocal photonic crystals,” *Nanophotonics*, vol. 11, no. 15, pp. 3447–3456, 2022.
- [180] S. Weidemann, M. Kremer, T. Helbig, T. Hofmann, A. Stegmaier, M. Greiter, R. Thomale, and A. Szameit, “Topological funneling of light,” *Science*, vol. 368, no. 6488, pp. 311–314, 2020.
- [181] L. Xiao, T. Deng, K. Wang, G. Zhu, Z. Wang, W. Yi, and P. Xue, “Non-Hermitian bulk-boundary correspondence in quantum dynamics,” *Nature Physics*, vol. 16, no. 7, pp. 761–766, 2020.
- [182] Q. Lin, T. Li, L. Xiao, K. Wang, W. Yi, and P. Xue, “Observation of non-Hermitian topological Anderson insulator in quantum dynamics,” *Nature Communications*, vol. 13, no. 1, p. 3229, 2022.
- [183] Q. Lin, W. Yi, and P. Xue, “Manipulating directional flow in a two-dimensional photonic quantum walk under a synthetic magnetic field,” *Nature Communications*, vol. 14, no. 1, p. 6283, 2023.
- [184] K. Wang, A. Dutt, K. Y. Yang, C. C. Wojcik, J. Vučković, and S. Fan, “Generating arbitrary topological windings of a non-Hermitian band,” *Science*, vol. 371, no. 6535, pp. 1240–1245, 2021.
- [185] K. Wang, A. Dutt, C. C. Wojcik, and S. Fan, “Topological complex-energy braiding of non-Hermitian bands,” *Nature*, vol. 598, no. 7879, pp. 59–64, 2021.
- [186] Y. G. Liu, Y. Wei, O. Hemmatyar, G. G. Pyrialakos, P. S. Jung, D. N. Christodoulides, and M. Khajavikhan, “Complex skin modes in non-Hermitian coupled laser arrays,” *Light: Science & Applications*, vol. 11, no. 1, p. 336, 2022.
- [187] Y. Li, C. Liang, C. Wang, C. Lu, and Y.-C. Liu, “Gain-loss-induced hybrid skin-topological effect,” *Physical Review Letters*, vol. 128, no. 22, p. 223903, 2022.
- [188] T. E. Lee, “Anomalous edge state in a non-Hermitian lattice,” *Physical Review Letters*, vol. 116, no. 13, p. 133903, 2016.
- [189] D. C. Brody, “Biorthogonal quantum mechanics,” *Journal of Physics A: Mathematical and Theoretical*, vol. 47, no. 3, p. 035305, 2013.
- [190] F. K. Kunst, E. Edvardsson, J. C. Budich, and E. J. Bergholtz, “Biorthogonal bulk-boundary correspondence in non-Hermitian systems,” *Physical Review Letters*, vol. 121, no. 2, p. 026808, 2018.
- [191] G. Dresselhaus, “Spin-orbit coupling effects in zinc blende structures,” *Physical Review*, vol. 100, no. 2, p. 580, 1955.
- [192] E. I. Rashba and S. V. I., “Symmetry of energy bands in crystals of wurtzite type: II. Symmetry of bands including spin-orbit interaction,” *Fizika Tverdogo Tela: Collected Papers*, vol. 2, pp. 162–176, 1959.

- [193] G. Bihlmayer, O. Rader, and R. Winkler, “Focus on the Rashba effect,” *New Journal of Physics*, vol. 17, no. 5, p. 050202, 2015.
- [194] Y. A. Bychkov and É. I. Rashba, “Properties of a 2D electron gas with lifted spectral degeneracy,” *JETP Letters*, vol. 39, no. 2, pp. 78–81, 1984.
- [195] I. Žutić, J. Fabian, and S. D. Sarma, “Spintronics: Fundamentals and applications,” *Reviews of Modern Physics*, vol. 76, no. 2, p. 323, 2004.
- [196] M. I. Dyakonov, “Possibility of orienting electron spins with current,” *JETP Letters*, vol. 13, p. 467, 1971.
- [197] C. L. Kane and E. J. Mele, “Quantum spin Hall effect in graphene,” *Physical Review Letters*, vol. 95, no. 22, p. 226801, 2005.
- [198] J. D. Sau, R. M. Lutchyn, S. Tewari, and S. Das Sarma, “Generic new platform for topological quantum computation using semiconductor heterostructures,” *Physical Review Letters*, vol. 104, no. 4, p. 040502, 2010.
- [199] J. Alicea, “Majorana fermions in a tunable semiconductor device,” *Physical Review B – Condensed Matter and Materials Physics*, vol. 81, no. 12, p. 125318, 2010.
- [200] J. Alicea, Y. Oreg, G. Refael, F. Von Oppen, and M. P. Fisher, “Non-Abelian statistics and topological quantum information processing in 1D wire networks,” *Nature Physics*, vol. 7, no. 5, pp. 412–417, 2011.
- [201] V. Mourik, K. Zuo, S. M. Frolov, S. R. Plissard, E. P. A. M. Bakkers, and L. P. Kouwenhoven, “Signatures of Majorana fermions in hybrid superconductor-semiconductor nanowire devices,” *Science*, vol. 336, no. 6084, pp. 1003–1007, 2012.
- [202] B. A. Bernevig, J. Orenstein, and S.-C. Zhang, “Exact SU(2) symmetry and persistent spin helix in a spin-orbit coupled system,” *Physical Review Letters*, vol. 97, no. 23, p. 236601, 2006.
- [203] Y. Ohno, R. Terauchi, T. Adachi, F. Matsukura, and H. Ohno, “Spin relaxation in GaAs (110) quantum wells,” *Physical Review Letters*, vol. 83, no. 20, p. 4196, 1999.
- [204] N. Averkiev and L. Golub, “Giant spin relaxation anisotropy in zinc-blende heterostructures,” *Physical Review B*, vol. 60, no. 23, p. 15582, 1999.
- [205] J. Schliemann, J. C. Egues, and D. Loss, “Nonballistic spin-field-effect transistor,” *Physical Review Letters*, vol. 90, no. 14, p. 146801, 2003.
- [206] K. C. Hall, W. H. Lau, K. Gündoğdu, M. E. Flatté, and T. F. Boggess, “Nonmagnetic semiconductor spin transistor,” *Applied Physics Letters*, vol. 83, no. 14, pp. 2937–2939, 2003.
- [207] J. D. Koralek, C. P. Weber, J. Orenstein, B. A. Bernevig, S.-C. Zhang, S. Mack, and D. Awschalom, “Emergence of the persistent spin helix in semiconductor quantum wells,” *Nature*, vol. 458, no. 7238, pp. 610–613, 2009.

- [208] M. Walser, C. Reichl, W. Wegscheider, and G. Salis, “Direct mapping of the formation of a persistent spin helix,” *Nature Physics*, vol. 8, no. 10, pp. 757–762, 2012.
- [209] X.-J. Liu, M. F. Borunda, X. Liu, and J. Sinova, “Effect of induced spin-orbit coupling for atoms via laser fields,” *Physical Review Letters*, vol. 102, no. 4, p. 046402, 2009.
- [210] Y.-J. Lin, K. Jiménez-García, and I. B. Spielman, “Spin-orbit-coupled Bose-Einstein condensates,” *Nature*, vol. 471, no. 7336, pp. 83–86, 2011.
- [211] P. Wang, Z.-Q. Yu, Z. Fu, J. Miao, L. Huang, S. Chai, H. Zhai, and J. Zhang, “Spin-orbit coupled degenerate Fermi gases,” *Physical Review Letters*, vol. 109, no. 9, p. 095301, 2012.
- [212] L. W. Cheuk, A. T. Sommer, Z. Hadzibabic, T. Yefsah, W. S. Bakr, and M. W. Zwierlein, “Spin-injection spectroscopy of a spin-orbit coupled Fermi gas,” *Physical Review Letters*, vol. 109, no. 9, p. 095302, 2012.
- [213] K. Jiménez-García, L. J. LeBlanc, R. A. Williams, M. C. Beeler, C. Qu, M. Gong, C. Zhang, and I. Spielman, “Tunable spin-orbit coupling via strong driving in ultracold-atom systems,” *Physical Review Letters*, vol. 114, no. 12, p. 125301, 2015.
- [214] C. Qu, C. Hamner, M. Gong, C. Zhang, and P. Engels, “Observation of Zitterbewegung in a spin-orbit-coupled Bose-Einstein condensate,” *Physical Review A – Atomic, Molecular, and Optical Physics*, vol. 88, no. 2, p. 021604, 2013.
- [215] L. J. LeBlanc, M. Beeler, K. Jimenez-Garcia, A. R. Perry, S. Sugawa, R. Williams, and I. B. Spielman, “Direct observation of zitterbewegung in a Bose-Einstein condensate,” *New Journal of Physics*, vol. 15, no. 7, p. 073011, 2013.
- [216] S.-L. Zhu, H. Fu, C.-J. Wu, S.-C. Zhang, and L.-M. Duan, “Spin Hall effects for cold atoms in a light-induced gauge potential,” *Physical Review Letters*, vol. 97, no. 24, p. 240401, 2006.
- [217] J. Vaishnav, J. Ruseckas, C. W. Clark, and G. Juzeliūnas, “Spin field effect transistors with ultracold atoms,” *Physical Review Letters*, vol. 101, no. 26, p. 265302, 2008.
- [218] M. C. Beeler, R. A. Williams, K. Jimenez-Garcia, L. J. LeBlanc, A. R. Perry, and I. B. Spielman, “The spin Hall effect in a quantum gas,” *Nature*, vol. 498, no. 7453, pp. 201–204, 2013.
- [219] S.-C. Ji, J.-Y. Zhang, L. Zhang, Z.-D. Du, W. Zheng, Y.-J. Deng, H. Zhai, S. Chen, and J.-W. Pan, “Experimental determination of the finite-temperature phase diagram of a spin-orbit coupled Bose gas,” *Nature Physics*, vol. 10, no. 4, pp. 314–320, 2014.
- [220] D. Hügél and B. Paredes, “Chiral ladders and the edges of quantum Hall insulators,” *Physical Review A*, vol. 89, no. 2, p. 023619, 2014.

- [221] Y. Yao, M. Sato, T. Nakamura, N. Furukawa, and M. Oshikawa, “Theory of electron spin resonance in one-dimensional topological insulators with spin-orbit couplings: Detection of edge states,” *Physical Review B*, vol. 96, no. 20, p. 205424, 2017.
- [222] Z.-H. Liu, O. Entin-Wohlman, A. Aharony, J. You, and H. Xu, “Topological states and interplay between spin-orbit and Zeeman interactions in a spinful Su-Schrieffer-Heeger nanowire,” *Physical Review B*, vol. 104, no. 8, p. 085302, 2021.
- [223] J. Ren, Q. Liao, F. Li, Y. Li, O. Bleu, G. Malpuech, J. Yao, H. Fu, and D. Solnyshkov, “Nontrivial band geometry in an optically active system,” *Nature Communications*, vol. 12, no. 1, p. 689, 2021.
- [224] T. Long, X. Ma, J. Ren, F. Li, Q. Liao, S. Schumacher, G. Malpuech, D. Solnyshkov, and H. Fu, “Helical polariton lasing from topological valleys in an organic crystalline microcavity,” *Advanced Science*, vol. 9, no. 29, p. 2203588, 2022.
- [225] J. Jia, X. Cao, X. Ma, J. De, J. Yao, S. Schumacher, Q. Liao, and H. Fu, “Circularly polarized electroluminescence from a single-crystal organic microcavity light-emitting diode based on photonic spin-orbit interactions,” *Nature Communications*, vol. 14, no. 1, p. 31, 2023.
- [226] Y. Li, X. Ma, X. Zhai, M. Gao, H. Dai, S. Schumacher, and T. Gao, “Manipulating polariton condensates by Rashba-Dresselhaus coupling at room temperature,” *Nature Communications*, vol. 13, no. 1, p. 3785, 2022.
- [227] K. Łempicka-Mirek, M. Król, H. Sigurdsson, A. Wincukiewicz, P. Morawiak, R. Mazur, M. Muszyński, W. Piecek, P. Kula, T. Stefaniuk *et al.*, “Electrically tunable Berry curvature and strong light-matter coupling in liquid crystal microcavities with 2D perovskite,” *Science Advances*, vol. 8, no. 40, p. eabq7533, 2022.
- [228] J. Liang, W. Wen, F. Jin, Y. G. Rubo, T. C. Liew, and R. Su, “Polariton spin Hall effect in a Rashba-Dresselhaus regime at room temperature,” *Nature Photonics*, vol. 18, no. 4, pp. 357–362, 2024.
- [229] M. Król, K. Rechcińska, H. Sigurdsson, P. Oliwa, R. Mazur, P. Morawiak, W. Piecek, P. Kula, P. G. Lagoudakis, M. Matuszewski *et al.*, “Realizing optical persistent spin helix and Stern-Gerlach deflection in an anisotropic liquid crystal microcavity,” *Physical Review Letters*, vol. 127, no. 19, p. 190401, 2021.
- [230] M. Muszyński, M. Król, K. Rechcińska, P. Oliwa, M. Kędziora, K. Łempicka-Mirek, R. Mazur, P. Morawiak, W. Piecek, P. Kula *et al.*, “Realizing persistent-spin-helix lasing in the regime of Rashba-Dresselhaus spin-orbit coupling in a dye-filled liquid-crystal optical microcavity,” *Physical Review Applied*, vol. 17, no. 1, p. 014041, 2022.
- [231] L. Polimeno, G. Lerario, M. De Giorgi, L. De Marco, L. Dominici, F. Todisco, A. Coriolano, V. Ardizzone, M. Pugliese, C. T. Prontera *et al.*, “Tuning of the Berry curvature in 2D perovskite polaritons,” *Nature Nanotechnology*, vol. 16, no. 12, pp. 1349–1354, 2021.

- [232] P. Kokhanchik, H. Sigurdsson, B. Piętka, J. Szczytko, and P. G. Lagoudakis, “Photonic Berry curvature in double liquid crystal microcavities with broken inversion symmetry,” *Physical Review B*, vol. 103, no. 8, p. L081406, 2021.
- [233] K. Łempicka-Mirek, M. Król, L. De Marco, A. Coriolano, L. Polimeno, I. Viola, M. Kędziora, M. Muszyński, P. Morawiak, R. Mazur *et al.*, “Electrical polarization switching of perovskite polariton laser,” *Nanophotonics*, vol. 13, no. 14, pp. 2659–2668, 2024.
- [234] Y. Deng, T. Long, P. Wang, H. Huang, Z. Deng, C. Gu, C. An, B. Liao, G. Malpuech, D. Solnyshkov *et al.*, “Spin-valley-locked electroluminescence for high-performance circularly polarized organic light-emitting diodes,” *Journal of the American Chemical Society*, 2024.
- [235] M. Muszyński, P. Oliwa, P. Kokhanchik, P. Kapuściński, E. Oton, R. Mazur, P. Morawiak, W. Piecek, P. Kula, W. Bardyszewski *et al.*, “Electrically tunable spin-orbit coupled photonic lattice in a liquid crystal microcavity,” *arXiv preprint arXiv:2407.07161*, 2024.
- [236] W. Wen, J. Liang, H. Xu, F. Jin, Y. G. Rubo, T. C. Liew, and R. Su, “Trembling motion of exciton polaritons close to the Rashba-Dresselhaus regime,” *Physical Review Letters*, vol. 133, no. 11, p. 116903, 2024.
- [237] M. Muszynski, P. Kokhanchik, D. Urbonas, P. Kapuscinski, P. Oliwa, R. Mirek, I. Georgakilas, T. Stoferle, R. F. Mahrt, M. Forster *et al.*, “Observation of a stripe phase in a spin-orbit coupled exciton-polariton Bose-Einstein condensate,” *arXiv preprint arXiv:2407.02406*, 2024.
- [238] X. Zhai, Y. Gao, X. Ma, C. Xing, X. Wang, A. Pan, M. Assmann, S. Schumacher, and T. Gao, “Observation of sub-Poissonian correlation in spin-orbit coupled polariton vortex pairs at room temperature,” *arXiv preprint arXiv:2403.15133*, 2024.
- [239] J. Ren, Q. Liao, X. Ma, S. Schumacher, J. Yao, and H. Fu, “Realization of exciton-mediated optical spin-orbit interaction in organic microcrystalline resonators,” *Laser & Photonics Reviews*, vol. 16, no. 1, p. 2100252, 2022.
- [240] K. Lekenta, M. Król, R. Mirek, K. Łempicka, D. Stephan, R. Mazur, P. Morawiak, P. Kula, W. Piecek, P. G. Lagoudakis *et al.*, “Tunable optical spin Hall effect in a liquid crystal microcavity,” *Light: Science & Applications*, vol. 7, no. 1, p. 74, 2018.
- [241] M. Król, H. Sigurdsson, K. Rehcńska, P. Oliwa, K. Tyszka, W. Bardyszewski, A. Opala, M. Matuszewski, P. Morawiak, R. Mazur *et al.*, “Observation of second-order meron polarization textures in optical microcavities,” *Optica*, vol. 8, no. 2, pp. 255–261, 2021.
- [242] M. Król, I. Septembre, P. Oliwa, M. Kędziora, K. Łempicka-Mirek, M. Muszyński, R. Mazur, P. Morawiak, W. Piecek, P. Kula *et al.*, “Annihilation of exceptional

- points from different Dirac valleys in a 2D photonic system,” *Nature Communications*, vol. 13, no. 1, p. 5340, 2022.
- [243] F. Liu, S. Wang, S. Xiao, Z. H. Hang, and J. Li, “Polarization-dependent optics using gauge-field metamaterials,” *Applied Physics Letters*, vol. 107, no. 24, 2015.
- [244] F. Liu, T. Xu, S. Wang, Z. H. Hang, and J. Li, “Polarization beam splitting with gauge field metamaterials,” *Advanced Optical Materials*, vol. 7, no. 12, p. 1801582, 2019.
- [245] K. Rechcińska, “The spin-orbit interaction of light in tunable liquid crystal microcavities,” Ph.D. dissertation, University of Warsaw, 2023.
- [246] P.-Q. Jin, Y.-Q. Li, and F.-C. Zhang, “ $Su(2) \times u(1)$  unified theory for charge, orbit and spin currents,” *Journal of Physics A: Mathematical and General*, vol. 39, no. 22, p. 7115, 2006.
- [247] P.-G. De Gennes and J. Prost, *The physics of liquid crystals*. Oxford University Press, 1993.
- [248] P. Kokhanchik, D. Solnyshkov, T. Stöferle, B. Piętka, J. Szczytko, and G. Malpuech, “Modulated Rashba-Dresselhaus spin-orbit coupling for topology control and analog simulations,” *Physical Review Letters*, vol. 129, no. 24, p. 246801, 2022.
- [249] P. De Gennes, “Collective motions of hydrogen bonds,” *Solid State Communications*, vol. 1, no. 6, pp. 132–137, 1963.
- [250] P. Pfeuty, “The one-dimensional Ising model with a transverse field,” *Annals of Physics*, vol. 57, no. 1, pp. 79–90, 1970.
- [251] P. Jordan and E. P. Wigner, *Über das paulische äquivalenzverbot*. Springer, 1993.
- [252] F. Scafirimuto, D. Urbonas, M. A. Becker, U. Scherf, R. F. Mahrt, and T. Stöferle, “Tunable exciton-polariton condensation in a two-dimensional Lieb lattice at room temperature,” *Communications Physics*, vol. 4, no. 1, pp. 1–6, 2021.
- [253] R. Mirek, P. Kokhanchik, D. Urbonas, I. Georgakilas, P. Morawiak, W. Piecek, P. Kula, D. Solnyshkov, G. Malpuech, R. Mahrt *et al.*, “In-situ tunneling control in photonic potentials by Rashba-Dresselhaus spin-orbit coupling,” *arXiv preprint arXiv:2408.08582*, 2024.
- [254] B. A. Bernevig, T. L. Hughes, and S.-C. Zhang, “Quantum spin Hall effect and topological phase transition in HgTe quantum wells,” *Science*, vol. 314, no. 5806, pp. 1757–1761, 2006.
- [255] R. Jackiw and C. Rebbi, “Solitons with fermion number  $\frac{1}{2}$ ,” *Physical Review D*, vol. 13, pp. 3398–3409, 1976.
- [256] M. Z. Hasan and C. L. Kane, “Colloquium: topological insulators,” *Reviews of Modern Physics*, vol. 82, no. 4, pp. 3045–3067, 2010.

- [257] S. Michaelis de Vasconcellos, A. Calvar, A. Dousse, J. Suffczyński, N. Dupuis, A. Lemaître, I. Sagnes, J. Bloch, P. Voisin, and P. Senellart, “Spatial, spectral, and polarization properties of coupled micropillar cavities,” *Applied Physics Letters*, vol. 99, no. 10, 2011.
- [258] V. Sala, D. Solnyshkov, I. Carusotto, T. Jacqmin, A. Lemaître, H. Terças, A. Nalitov, M. Abbarchi, E. Galopin, I. Sagnes *et al.*, “Spin-orbit coupling for photons and polaritons in microstructures,” *Physical Review X*, vol. 5, no. 1, p. 011034, 2015.
- [259] J. D. Töpfer, I. Chatzopoulos, H. Sigurdsson, T. Cookson, Y. G. Rubo, and P. G. Lagoudakis, “Engineering spatial coherence in lattices of polariton condensates,” *Optica*, vol. 8, no. 1, pp. 106–113, 2021.
- [260] M. Mrejen, H. Suchowski, T. Hatakeyama, C. Wu, L. Feng, K. O’Brien, Y. Wang, and X. Zhang, “Adiabatic elimination-based coupling control in densely packed sub-wavelength waveguides,” *Nature Communications*, vol. 6, no. 1, p. 7565, 2015.
- [261] N. V. Vitanov, T. Halfmann, B. W. Shore, and K. Bergmann, “Laser-induced population transfer by adiabatic passage techniques,” *Annual Review of Physical Chemistry*, vol. 52, no. 1, pp. 763–809, 2001.
- [262] X. Piao, S. Yu, and N. Park, “Programmable photonic time circuits for highly scalable universal unitaries,” *Physical Review Letters*, vol. 132, p. 103801, 2024.
- [263] W. Song, T. Li, S. Wu, Z. Wang, C. Chen, Y. Chen, C. Huang, K. Qiu, S. Zhu, Y. Zou, and T. Li, “Dispersionless coupling among optical waveguides by artificial gauge field,” *Physical Review Letters*, vol. 129, p. 053901, 2022.
- [264] L. Komitov, G. Bryan-Brown, E. Wood, and A. Smout, “Alignment of cholesteric liquid crystals using periodic anchoring,” *Journal of Applied Physics*, vol. 86, no. 7, pp. 3508–3511, 1999.
- [265] E. Oton and E. Netter, “Wide tunable shift of the reflection band in dual frequency cholesteric liquid crystals,” *Optics Express*, vol. 25, no. 12, pp. 13 314–13 323, 2017.
- [266] H. K. Bisoyi, T. J. Bunning, and Q. Li, “Stimuli-driven control of the helical axis of self-organized soft helical superstructures,” *Advanced Materials*, vol. 30, no. 25, p. 1706512, 2018.
- [267] P. Rudquist, L. Komitov, and S. Lagerwall, “Linear electro-optic effect in a cholesteric liquid crystal,” *Physical Review E*, vol. 50, no. 6, p. 4735, 1994.
- [268] J. Martinand and G. Durand, “Electric field quenching of thermal fluctuations of orientation in a nematic liquid crystal,” *Solid State Communications*, vol. 10, no. 9, pp. 815–818, 1972.
- [269] Z. Jia, T. Pawale, G. I. Guerrero-García, S. Hashemi, J. A. Martínez-González, and X. Li, “Engineering the uniform lying helical structure in chiral nematic liquid

- crystals: From morphology transition to dimension control,” *Crystals*, vol. 11, no. 4, p. 414, 2021.
- [270] N. G. Berloff, M. Silva, K. Kalinin, A. Askitopoulos, J. D. Töpfer, P. Cilibrizzi, W. Langbein, and P. G. Lagoudakis, “Realizing the classical XY Hamiltonian in polariton simulators,” *Nature Materials*, vol. 16, no. 11, pp. 1120–1126, 2017.
- [271] I. M. Georgescu, S. Ashhab, and F. Nori, “Quantum simulation,” *Reviews of Modern Physics*, vol. 86, no. 1, p. 153, 2014.
- [272] M. Parto, W. Hayenga, A. Marandi, D. N. Christodoulides, and M. Khajavikhan, “Realizing spin Hamiltonians in nanoscale active photonic lattices,” *Nature Materials*, vol. 19, no. 7, pp. 725–731, 2020.
- [273] R. Tao, K. Peng, L. Haeberlé, Q. Li, D. Jin, G. R. Fleming, S. Kéna-Cohen, X. Zhang, and W. Bao, “Halide perovskites enable polaritonic XY spin Hamiltonian at room temperature,” *Nature Materials*, vol. 21, no. 7, pp. 761–766, 2022.
- [274] J. A. Acebrón, L. L. Bonilla, C. J. Pérez Vicente, F. Ritort, and R. Spigler, “The Kuramoto model: A simple paradigm for synchronization phenomena,” *Reviews of Modern Physics*, vol. 77, no. 1, pp. 137–185, 2005.
- [275] A. Muravsky and A. Murauski, “Q&A of liquid crystal alignment: theory and practice,” *Frontiers in Soft Matter*, vol. 4, p. 1382925, 2024.
- [276] A. Mochizuki, “Molecular tilting effect on smectic liquid crystal sub-phase stability from its retardation switching behavior,” *Journal of Molecular Liquids*, vol. 267, pp. 456–468, 2018.
- [277] P. Kokhanchik, D. Solnyshkov, and G. Malpuech, “Non-Hermitian skin effect induced by Rashba-Dresselhaus spin-orbit coupling,” *Physical Review B*, vol. 108, no. 4, p. L041403, 2023.
- [278] S. Guo, C. Dong, F. Zhang, J. Hu, and Z. Yang, “Theoretical prediction of a non-Hermitian skin effect in ultracold-atom systems,” *Physical Review A*, vol. 106, no. 6, p. L061302, 2022.
- [279] L. Zhou, H. Li, W. Yi, and X. Cui, “Engineering non-Hermitian skin effect with band topology in ultracold gases,” *Communications Physics*, vol. 5, no. 1, p. 252, 2022.
- [280] H. Li, X. Cui, and W. Yi, “Non-Hermitian skin effect in a spin-orbit-coupled Bose-Einstein condensate,” *JUSTC*, vol. 52, no. 8, p. 2, 2022.
- [281] S. Longhi, “Non-Hermitian skin effect beyond the tight-binding models,” *Physical Review B*, vol. 104, no. 12, p. 125109, 2021.
- [282] S. Vaitiekėnas, Y. Liu, P. Krogstrup, and C. Marcus, “Zero-bias peaks at zero magnetic field in ferromagnetic hybrid nanowires,” *Nature Physics*, vol. 17, no. 1, pp. 43–47, 2021.

- [283] Y. Liu, S. Vaitiekėnas, S. Martí-Sánchez, C. Koch, S. Hart, Z. Cui, T. Kanne, S. A. Khan, R. Tanta, S. Upadhyay *et al.*, “Semiconductor-ferromagnetic insulator-superconductor nanowires: Stray field and exchange field,” *Nano Letters*, vol. 20, no. 1, pp. 456–462, 2019.
- [284] J. Cayao, “Exceptional degeneracies in non-Hermitian Rashba semiconductors,” *Journal of Physics: Condensed Matter*, vol. 35, no. 25, p. 254002, 2023.
- [285] S. Giglberger, L. E. Golub, V. Bel’kov, S. Danilov, D. Schuh, C. Gerl, F. Rohlfing, J. Stahl, W. Wegscheider, D. Weiss *et al.*, “Rashba and Dresselhaus spin splittings in semiconductor quantum wells measured by spin photocurrents,” *Physical Review B*, vol. 75, no. 3, p. 035327, 2007.
- [286] F. Passek, M. Donath, K. Ertl, and V. Dose, “Longer living majority than minority image state at Fe (110),” *Physical Review Letters*, vol. 75, no. 14, p. 2746, 1995.
- [287] M. Aeschlimann, M. Bauer, S. Pawlik, W. Weber, R. Burgermeister, D. Oberli, and H. Siegmann, “Ultrafast spin-dependent electron dynamics in fcc Co,” *Physical Review Letters*, vol. 79, no. 25, p. 5158, 1997.
- [288] M. Donath, C. Math, M. Pickel, A. Schmidt, and M. Weinelt, “Realization of a spin-polarized two-dimensional electron gas via image-potential-induced surface states,” *Surface Science*, vol. 601, no. 24, pp. 5701–5706, 2007.
- [289] I. Mihai Miron, G. Gaudin, S. Auffret, B. Rodmacq, A. Schuhl, S. Pizzini, J. Vogel, and P. Gambardella, “Current-driven spin torque induced by the Rashba effect in a ferromagnetic metal layer,” *Nature Materials*, vol. 9, no. 3, pp. 230–234, 2010.
- [290] X. Wang and A. Manchon, “Diffusive spin dynamics in ferromagnetic thin films with a Rashba interaction,” *Physical Review Letters*, vol. 108, no. 11, p. 117201, 2012.
- [291] D. Pesin and A. MacDonald, “Quantum kinetic theory of current-induced torques in Rashba ferromagnets,” *Physical Review B*, vol. 86, no. 1, p. 014416, 2012.
- [292] H. Yang, G. Chen, A. A. Cotta, A. T. N’Diaye, S. A. Nikolaev, E. A. Soares, W. A. Macedo, K. Liu, A. K. Schmid, A. Fert *et al.*, “Significant Dzyaloshinskii-Moriya interaction at graphene-ferromagnet interfaces due to the Rashba effect,” *Nature Materials*, vol. 17, no. 7, pp. 605–609, 2018.
- [293] J. D. Plumhof, T. Stöferle, L. Mai, U. Scherf, and R. F. Mahrt, “Room-temperature Bose-Einstein condensation of cavity exciton-polaritons in a polymer,” *Nature Materials*, vol. 13, no. 3, pp. 247–252, 2014.
- [294] A. V. Zasedatelev, A. V. Baranikov, D. Urbonas, F. Scafrimuto, U. Scherf, T. Stöferle, R. F. Mahrt, and P. G. Lagoudakis, “A room-temperature organic polariton transistor,” *Nature Photonics*, vol. 13, no. 6, pp. 378–383, 2019.
- [295] D. W. Berreman, “Optics in stratified and anisotropic media:  $4 \times 4$ -matrix formulation,” *JOSA*, vol. 62, no. 4, pp. 502–510, 1972.

- [296] P. Kokhanchik, “Photonic Berry curvature in double liquid crystal microcavities with broken inversion symmetry,” Master’s thesis, Skolkovo Institute of Science and Technology, 2021.
- [297] E. Wertz, A. Amo, D. Solnyshkov, L. Ferrier, T. C. H. Liew, D. Sanvitto, P. Senellart, I. Sagnes, A. Lemaître, A. Kavokin *et al.*, “Propagation and amplification dynamics of 1D polariton condensates,” *Physical Review Letters*, vol. 109, no. 21, p. 216404, 2012.
- [298] L. Pitaevskii, “Phenomenological theory of superfluidity near the Lambda point,” *Soviet Physics JETP*, vol. 8, p. 282, 1959.
- [299] D. Solnyshkov, H. Tercas, K. Dini, and G. Malpuech, “Hybrid Boltzmann-Gross-Pitaevskii theory of Bose-Einstein condensation and superfluidity in open driven-dissipative systems,” *Physical Review A*, vol. 89, no. 3, p. 033626, 2014.
- [300] D. Tanese, H. Flayac, D. Solnyshkov, A. Amo, A. Lemaître, E. Galopin, R. Braive, P. Senellart, I. Sagnes, G. Malpuech *et al.*, “Polariton condensation in solitonic gap states in a one-dimensional periodic potential,” *Nature Communications*, vol. 4, no. 1, p. 1749, 2013.
- [301] T. Jacqmin, I. Carusotto, I. Sagnes, M. Abbarchi, D. Solnyshkov, G. Malpuech, E. Galopin, A. Lemaître, J. Bloch, and A. Amo, “Direct observation of Dirac cones and a flatband in a honeycomb lattice for polaritons,” *Physical Review Letters*, vol. 112, no. 11, p. 116402, 2014.
- [302] A. Andreev and I. Lifshits, “Quantum theory of defects in crystals,” *Soviet Physics JETP*, vol. 56, no. 6, pp. 2057–2068, 1969.
- [303] G. Chester, “Speculations on Bose-Einstein condensation and quantum crystals,” *Physical Review A*, vol. 2, no. 1, p. 256, 1970.
- [304] E. Kim and M. H. Chan, “Probable observation of a supersolid helium phase,” *Nature*, vol. 427, no. 6971, pp. 225–227, 2004.
- [305] —, “Observation of superflow in solid helium,” *Science*, vol. 305, no. 5692, pp. 1941–1944, 2004.
- [306] D. Y. Kim and M. H. Chan, “Absence of supersolidity in solid helium in porous vycor glass,” *Physical Review Letters*, vol. 109, no. 15, p. 155301, 2012.
- [307] D. O’dell, S. Giovanazzi, and G. Kurizki, “Roton in gaseous Bose-Einstein condensates irradiated by a laser,” *Physical Review Letters*, vol. 90, no. 11, p. 110402, 2003.
- [308] L. Santos, G. Shlyapnikov, and M. Lewenstein, “Roton-maxon spectrum and stability of trapped dipolar Bose-Einstein condensates,” *Physical Review Letters*, vol. 90, no. 25, p. 250403, 2003.

- [309] L. Tanzi, E. Lucioni, F. Famà, J. Catani, A. Fioretti, C. Gabbanini, R. N. Bisset, L. Santos, and G. Modugno, “Observation of a dipolar quantum gas with metastable supersolid properties,” *Physical Review Letters*, vol. 122, no. 13, p. 130405, 2019.
- [310] F. Böttcher, J.-N. Schmidt, M. Wenzel, J. Hertkorn, M. Guo, T. Langen, and T. Pfau, “Transient supersolid properties in an array of dipolar quantum droplets,” *Physical Review X*, vol. 9, no. 1, p. 011051, 2019.
- [311] L. Chomaz, D. Petter, P. Ilzhöfer, G. Natale, A. Trautmann, C. Politi, G. Durastante, R. Van Bijnen, A. Patscheider, M. Sohmen *et al.*, “Long-lived and transient supersolid behaviors in dipolar quantum gases,” *Physical Review X*, vol. 9, no. 2, p. 021012, 2019.
- [312] J. Léonard, A. Morales, P. Zupancic, T. Esslinger, and T. Donner, “Supersolid formation in a quantum gas breaking a continuous translational symmetry,” *Nature*, vol. 543, no. 7643, pp. 87–90, 2017.
- [313] J.-R. Li, J. Lee, W. Huang, S. Burchesky, B. Shteynas, F. Ç. Top, A. O. Jamison, and W. Ketterle, “A stripe phase with supersolid properties in spin-orbit-coupled Bose-Einstein condensates,” *Nature*, vol. 543, no. 7643, pp. 91–94, 2017.
- [314] Y. Li, L. P. Pitaevskii, and S. Stringari, “Quantum tricriticality and phase transitions in spin-orbit coupled Bose-Einstein condensates,” *Physical Review Letters*, vol. 108, no. 22, p. 225301, 2012.
- [315] C. N. Weiler, T. W. Neely, D. R. Scherer, A. S. Bradley, M. J. Davis, and B. P. Anderson, “Spontaneous vortices in the formation of Bose-Einstein condensates,” *Nature*, vol. 455, no. 7215, pp. 948–951, 2008.
- [316] J.-S. Wu and I. I. Smalyukh, “Hopfions, heliknotons, skyrmions, torons and both abelian and nonabelian vortices in chiral liquid crystals,” *Liquid Crystals Reviews*, vol. 10, no. 1-2, pp. 34–68, 2022.



DBR	Distributed Bragg reflector
SOC	Spin-orbit coupling
OSHE	Optical Spin Hall Effect
HV	Horizontal-vertical (basis)
DA	Diagonal-antidiagonal (basis)
+−	Positive-negative circular (basis)
LPB	Lower polariton branch
UPB	Upper polariton branch
BEC	Bose-Einstein condensation
GPE	Gross-Pitaevskii equation
TRS	Time-Reversal Symmetry
PHS	Particle-Hole Symmetry
CS	Chiral Symmetry
SLS	Sublattice Symmetry
OBC	Open Boundary Condition
PBC	Periodic Boundary Condition
BZ	Brillouin zone
HH	Harper-Hofstadter (model)
NHSE	Non-Hermitian skin effect
HN	Hatano-Nelson (model)
GBZ	generalized Brillouin zone
RDSOC	Rashba-Dresselhaus spin-orbit coupling
LC	Liquid crystal
CLC	Cholesteric liquid crystal
TFIM	Transverse-field Ising model
ST	Single trap (potential)
DT	Double trap (potential)
ULH	Uniformly lying helix
OA	Optical activity
NN	nearest neighbor
NNN	next nearest neighbor
MeLPPP	Methyl-substituted ladder-type poly(p-phenylene)
PL	Photoluminescence



- amplitude control regime, 67  
 anomalous bulk-boundary  
     correspondence, 46  
 artificial gauge field, 34  
 BEC, 25  
 Berreman method, 111  
 Berry connection, 43  
 Berry curvature, 34, 43  
 Berry phase, 43  
 biorthogonal polarization, 46  
 birefringence, 20  
 bottleneck region, 28  
 bottleneck reservoir, 28  
 bulk inversion asymmetry (BIA), 49  
 bulk-boundary correspondence, 37  
 Chern number, 31, 43  
 chiral symmetry, 37  
 cholesteric liquid crystal, 59  
 cholesteric pitch, 59  
 circular dichroism, 96  
 coherent pumping, 28  
 complex Ginzburg-Landau equation, 29  
 complex spectral winding number, 44  
 composite boson, 22  
 condensate order parameter  
     (wavefunction), 25  
 detuning (linear polarization splitting),  
     55  
 Dirac points, 21  
 distributed Bragg reflector, 14  
 Dresselhaus spin-orbit coupling, 49  
 edge states, 37  
 effective magnetic field, 16  
 electron hole, 22  
 emergent optical activity, 61  
 energy flueshift, 25  
 exciton, 22  
 exciton-polariton, 22, 24  
 extraordinary refractive index, 20  
 Frenkel excitons, 22  
 gap Chern number, 43  
 generalized Brillouin zone, 45  
 Gross-Pitaevskii equation, 28  
 Harper-Hofstadter model, 35, 40  
 Hatano-Nelson model, 44  
 Hofstadter butterfly, 42  
 Hopfield coefficients, 24  
 Hopfield transformation, 24  
 incoherent (non-resonant) pumping, 28  
 Jaynes-Cummings model, 23  
 Landau superfluidity criterion, 26  
 MeLPPP, 107  
 microcavity, 13  
 minimal coupling Hamiltonian, 34  
 molecular director, 20  
 nematic liquid crystal, 52  
 non-Abelian vector potential, 57  
 non-Hermitian skin effect, 44  
 open boundary condition, 38  
 optical activity, 61  
 Optical Spin Hall Effect, 20  
 ordinary refractive index, 20  
 particle-hole symmetry, 37  
 Peierls phase, 34  
 Peierls substitution, 41  
 periodic boundary condition, 38  
 persistent spin helix, 58  
 pesistent spin helix, 51  
 phase control regime, 66  
 phase space filling, 26  
 photon-exciton detuning, 24  
 photonic RDSOC Hamiltonian, 53

- photonic spin-orbit coupling, [17](#)
- Poincaré sphere, [16](#)
- polarization, [15](#)
- pseudospin, [16](#)
- Purcell effect, [13](#)
  
- Quantum Spin Hall Effect, [35](#)
  
- Rabi frequency, [13](#), [23](#)
- Rashba spin-orbit coupling, [49](#)
- Rashba-Dresselhaus spin-orbit coupling,  
[51](#)
- RDSOC phase, [66](#)
  
- spontaneous symmetry breaking, [25](#)
- Stokes vector, [16](#)
- strong coupling, [13](#), [24](#)
- structure inversion symmetry (SIA), [49](#)
- sublattice symmetry, [38](#)
- subsonic regime, [26](#)
- superfluidity, [26](#)
  
- supersolidity, [118](#)
- supersonic regime, [26](#)
- Su–Schrieffer–Heeger model, [36](#)
  
- Tavis-Cummings model, [113](#)
- TE-TM SOC, [18](#)
- time-reversal symmetry, [37](#)
- TKNN formula, [42](#)
- topology, [31](#)
- transverse-field Ising model, [70](#)
  
- uniformly lying helix, [86](#)
- uniformly lying helix (ULH), [61](#)
  
- Wannier-Mott excitons, [22](#)
- winding number, [39](#)
  
- XY Hamiltonian, [95](#)
  
- Zak phase, [39](#)
- Zitterbewegung, [58](#)